

Controlled Resolution Reconstruction of One-Dimensional Permittivity Profiles

Dissertation

zur Erlangung des akademischen Grades

**Doktoringenieur
(Dr.-Ing.)**

von M.Eng. Md. Jaleel Akhtar
geb. am 26 März 1971 in Gaya, Indien

genehmigt durch
die Fakultät für Elektrotechnik und Informationstechnik
der Otto-von-Guericke-Universität Magdeburg

Gutachter:

Prof. Dr.-Ing. A. S. Omar

Prof. Dr.-Ing. habil. Bernd Michaelis

Prof. Dr. V. F. Hanna

Promotionskolloquium am: 03. September 2003

Acknowledgements

Seldom is anything accomplished without the assistance or encouragement of others. This thesis would also not have been in its present form without the support of many people who, in one way or other, provided help to me. It is my humble duty to thank all those people at this stage.

First and foremost, I would like to thank my supervisor, Prof. Dr.-Ing. A. S. Omar, for his kind guidance throughout this research work. Apart from being an excellent supervisor, he has also been my mentor and a great source of inspiration. His positive attitude towards younger researchers, and his unquenchable curiosity and love for the subject are probably some of the things, which I really admired in him. I am also grateful to Prof. Dr.-Ing. habil. Bernd Michaelis, University of Magdeburg, and Prof. Dr. V. F. Hanna, University of Pierre et Marie Curie, Paris, for kindly agreeing to be referees for this thesis in spite of their hectic schedules.

I would like to thank Deutsche Forschungsgemeinschaft for sponsoring a project to carry out this research work.

I am also thankful to my host institutions in India, Central Electronics Engineering Research Institute, Pilani, and the Council of Scientific and Industrial Research, New Delhi, for granting me study leave to pursue the Dr.-Ing. degree.

Thanks are due to all colleagues of my institute, who were always quite helpful during my stay. I would specially like to thank Dr.-Ing. Jstingmeier and Dipl.-Ing. T. Meyer for many thoughtful discussions and useful suggestions. I am also thankful to Dr.-Ing. Holub for providing the logistic support throughout my stay at this institute.

Finally, I express my appreciation to my family specially my parents, whose kind blessings and support have always been with me. I would also like to thank my wife for being patient enough over the whole period.

(Md. Jaleel Akhtar)

Table of Contents

Zusammenfassung	V
Abstract	VI
List of Symbols	VII
1 Introduction	1
1.1 Objective	1
1.2 The direct problem: electromagnetic scattering theory	6
1.3 The inverse problem: microwave inverse scattering	8
1.4 State of the Art	9
2 Microwave Inverse Scattering Theory	18
2.1 Basic formulas and definitions	18
2.1.1 The electromagnetic field in free space	18
2.1.2 Interaction of electromagnetic waves with dielectric materials .	19
2.1.2.1 The electric dipole moment	20
2.1.2.2 The macroscopic electric field due to polarized di-	
electric molecules	21
2.1.2.3 The concept of general electric flux density and the	
local electric field	22
2.1.2.4 The electronic polarization	24
2.1.2.5 The ionic polarization	25
2.1.2.6 The orientational polarization	27
2.1.2.7 The concept of relative permittivity	28
2.1.2.8 The effect of time-varying electromagnetic field . . .	29
2.1.3 The scattering parameters	30
2.1.4 The multiple reflections from inhomogeneous transmission lines	33
2.1.5 The integral transform	37
2.2 The inverse problem from the mathematical point of view	40
2.3 The common methods for solving inverse scattering problems	45
2.3.1 The Born approximation	45
2.3.2 The distorted Born approximation	48
2.3.3 Numerical methods	49
2.3.4 The Riccati-equation approach	52
3 The Direct Problem Formulation	54
3.1 The planar geometry	54
3.1.1 TEM illumination	54

3.1.1.1	The discontinuous structure	56
3.1.1.2	The continuous media	59
3.1.2	TE-mode illumination	61
3.1.3	TM-mode illumination	63
3.2	The cylindrical geometry	65
3.2.1	Radial transmission line approach	66
3.2.1.1	The stratified media	72
3.2.1.2	The continuous media	75
3.2.2	Higher order mode illuminations	78
3.3	The spherical geometry	85
3.3.1	Higher order mode illuminations	87
3.3.2	Lower order mode illuminations	93
4	The Inverse Solution	95
4.1	The planar geometry	95
4.1.1	TEM illumination	95
4.1.1.1	The special case with a continuity at the air-dielectric interface	98
4.1.1.2	The general case with a discontinuity at the air-dielectric interface	100
4.1.1.3	Numerical algorithm for transforming the virtual space variable into the actual physical distance	103
4.1.1.4	Determination of the permittivity at the air-dielectric interface	104
4.1.2	<i>TE</i> -mode illumination	105
4.1.3	<i>TM</i> -mode illumination	106
4.2	The <i>RDE</i> technique applied to non-planar structures	107
4.2.1	Generalization of the one dimensional Fourier transform technique	108
4.2.2	Extending the validity of the analysis to a general one-dimensional case	112
4.3	The cylindrical geometry	113
4.3.1	Radial transmission line approach	114
4.3.2	Higher order mode illuminations	122
4.4	The spherical geometry	130
5	Reconstructed Examples	137
5.1	Simulated results	137
5.1.1	Planar geometry	137
5.1.2	Cylindrical geometry	146
5.1.3	Spherical geometry	158
5.2	Experimental results	164
5.2.1	Coaxial airline measurements	165
5.2.2	Free-space measurements	174
6	Summary	187

A	The solution of two simultaneous differential equations having a common factor	190
B	The derivatives of the spherical Hankel functions	191
B.1	The first order derivative	191
B.2	The second order derivative	191
C	Integral containing two Hankel functions	193
C.1	The cylindrical Hankel functions	193
C.2	The spherical Hankel functions	193
D	The spherical Fourier-Bessel transform	195
	Bibliography	197
	Curriculum Vitae	206

Zusammenfassung

Diese Arbeit beschreibt einen neuen Ansatz für die Rekonstruktion von eindimensionalen tiefenabhängigen Permittivitätsprofilen von planen, zylindrischen und kugelförmigen Objekten, die von einer beliebigen TE oder TM polarisierten Welle beleuchtet werden. Die Rekonstruktion von Permittivitätsprofilen von planen und nicht planen Objekten bildet die Basis für die Darstellung von beliebig geformten dielektrischen Körpern, wenn Antennen hoher Direktivität für die laterale Abtastung verwendet werden. Die Hauptvorteile der neuen von uns vorgeschlagenen Technik sind, dass eine eindeutige Lösung erreicht wird und dass die Darstellung stark streuender Objekte möglich wird. Ein weiterer Vorteil ist, dass die Auflösung des Bildes im Raumbereich durch die Wahl der Bandbreite der gemessenen Reflektionsdaten exakt eingestellt werden kann.

Für ein planes Objekt werden zunächst die Riccati-Differentialgleichungen, welche das direkte Problem für den Fall von TE, TM und TEM Beleuchtung beschreiben, untersucht. Diese Differentialgleichungen werden mit der von uns vorgeschlagenen nichtlinearen Normierung invertiert, was einen Ausdruck für das tiefenabhängige Permittivitätsprofil als Funktion der inversen Fourier-Transformation der gemessenen Reflektionskoeffizienten im Frequenzbereich ergibt. Für zylindrische und kugelförmige Objekte werden die der nichtlinearen Riccati-Differentialgleichung ähnlichen Gleichungen für das direkte Problem für die Fälle der Beleuchtung mit TE- oder TM-Wellen in den entsprechenden Koordinatensystemen abgeleitet. Die Formulierung in Zylinderkoordinaten beziehungsweise Kugelkoordinaten ist vorteilhaft wenn Antennen mit geringerer Direktivität zum Scannen verwendet werden, da zylindrische und kugelförmige Geometrien die eindimensionale oder zweidimensionale Krümmung des Objekts berücksichtigen können und damit die Genauigkeit der Abbildung verbessern. Um die für den planen Fall vorgeschlagene Methode für nicht plane Strukturen anwenden zu können, wird die Fourier-Transformationstechnik, die für plane Objekte gültig ist, verallgemeinert und ihre Anwendbarkeit durch Veränderung der Form des Transformationskerns auf beliebige Koordinatensysteme ausgedehnt. Diese allgemeine Theorie für die Rekonstruktion wird dann auf die Fälle zylindrischer und kugelförmiger Koordinaten angewendet, um die hergeleiteten Riccati-ähnlichen Differentialgleichungen zu invertieren. Diese Inversion ergibt einen geschlossenen Ausdruck für das radial variierende Permittivitätsprofil zylindrischer Objekte in Form einer Hankel-Transformation der frequenzabhängigen Reflektionsdaten. Im Fall kugelförmiger Objekte ist der geschlossene Ausdruck für das radial variierende Permittivitätsprofil durch eine sphärische Fourier-Bessel-Transformation der Frequenzbereichsreflektionsdaten gegeben.

Ein experimenteller Aufbau für die Darstellung inhomogener dielektrischer Körper wird vorgestellt, der zerstörungsfrei arbeitet, da nur die Platzierung des Objektes im Freiraum direkt vor der Antenne erforderlich ist. Mehrere simulierte und experimentelle Beispiele wurden untersucht, um die Gültigkeit der vorgeschlagenen Technik nachzuweisen. Die Abweichung zwischen wahren und rekonstruierten Permittivitätsprofilen ist für den Fall planer Objekte kleiner als 2% und beträgt für den Fall nicht planer Objekte zwischen 1% und 5%. Der Einfluss von Rauschen wurde ebenfalls untersucht, und es konnte festgestellt werden, dass sogar Fehler von 2–5% in den Reflektionsdaten eine recht genaue Abbildung erlauben, was die Stabilität der von uns vorgeschlagenen Methode beweist.

Abstract

The present thesis describes a new approach for reconstructing one-dimensional depth-dependent permittivity profiles of planar, cylindrical and spherical objects illuminated by any arbitrary order TE or TM polarized wave. The reconstruction of permittivity profiles of planar and non-planar objects forms the basis for the general active microwave imaging of arbitrary shaped dielectric bodies if high directivity antennas are used for the lateral scanning. The main advantages of our proposed technique, as compared to previous approaches, are that it gives a unique solution, and it is able to image the dielectric objects of higher contrast as well. Another advantage of our proposed method is that the resolution of the imaging in the spatial domain can precisely be controlled by varying the bandwidth of the measured spectral domain reflection coefficient data.

For a planar medium, the non-linear Riccati differential equations describing the direct problem for TEM , TE , and TM illuminations are first revised, and then these equations are inverted using our proposed renormalization technique to obtain an expression for the depth-dependent permittivity profile in terms of an inverse Fourier transform of the spectral domain reflection coefficient data.

For the cylindrical and spherical objects, the non-linear Riccati-similar differential equations describing the direct problem formulation for any arbitrary order TE and TM illumination are derived in their respective coordinate systems. The formulation in the cylindrical and spherical coordinate system is advantageous if less directive antennas are used for the scanning, as these cylindrical and spherical geometries can take the $1 - D$ and $2 - D$ curvature of the object into account thus improving the accuracy of the image. To apply our proposed method in case of non-planar structures, the Fourier-transform technique valid for planar objects is generalized and its applicability is extended to any arbitrary coordinate system by changing the functional form of the transform kernel. The general theory of reconstruction is then applied in the case of cylindrical and spherical coordinate system to invert the derived non-linear Riccati-similar differential equations. This inversion gives us a closed-form expression for the radially varying permittivity profile of cylindrical objects in terms of a Hankel transform of the frequency-dependent reflection coefficient data. In case of spherical objects, the closed form expression of the radially varying permittivity profile is obtained in terms of a spherical Fourier-Bessel transform of the spectral domain reflection coefficient data.

An experimental setup is developed for the imaging of inhomogeneous dielectric bodies, which is completely non-destructive in nature requiring the dielectric object to be placed in free-space directly in front of the antenna. Several simulated and experimental examples are considered to validate our proposed technique. The deviation between the actual and reconstructed permittivity profile is less than 2% in case of planar media, while it is around 1 – 5% in case of non-planar structures. The effect of noise is also considered and it is observed that even a 2 – 5% error in the scattering data provides a reasonably accurate reconstructed image, which proves the stability of our proposed method.

List of Symbols

$\ \cdot\ $	Norm of a quantity
α_c	Ratio of the inward to outward wave impedance for the cylindrical media
α_e	Electronic polarizability
α_i	Ionic polarizability
α_o	Orientalional polarizability
α_r	Ratio of the inward to outward characteristic impedance for a radial line
α_s	Ratio of the inward to outward wave impedance for the spherical media
β	Propagation phase constant
γ	Internal field constant
Γ	Reflection coefficient
$\hat{\Gamma}$	Virtual reflection coefficient
$\delta(x - x')$	Dirac delta function
δ	A constant in the cylindrical dielectric media
$\Delta\varepsilon_r(x)$	Permittivity profile variation about the ambient value
$\Delta\rho$	Incremental distance in the ρ -direction
Δx	Incremental distance in the x -direction
ε	Total permittivity
ε_0	Permittivity of free-space
ε_r	Relative permittivity
ε_{r0}	Relative permittivity at the air-dielectric interface
$\varepsilon_r(\rho)$	Radially varying permittivity profile of the cylindrical media
$\tilde{\varepsilon}_r(\rho)$	Effective value of the permittivity profile in the cylindrical media
$\varepsilon_r(r)$	Radially varying permittivity profile of the spherical media
ε_{rb}	Relative permittivity of the background medium

$\varepsilon_r(x)$	One-dimensional permittivity profile of the Cartesian media
$\tilde{\varepsilon}_r(x)$	Effective permittivity profile of the planar media
$\varepsilon_{rp}(x)$	<i>A priori</i> knowledge of the permittivity profile
η_0	Free-space intrinsic impedance
μ	Total permeability; Permanent dipole moment
μ_0	Permeability of free-space
μ_r	Relative permeability
λ	Free-space wavelength
ρ_0	Inner radius of the cylindrical dielectric object
ρ_c	Electric charge density
ρ, ϕ, z	Coordinates of the cylindrical geometry
σ	Conductivity
Φ_n	Electric potential
χ	Dielectric susceptibility
Ψ	Wave function
ω	Angular frequency
a	Outer radius of the spherical dielectric object
a_m	Incident wave amplitude at the m^{th} port
\hat{a}_m	Normalized incident wave amplitude at the m^{th} port
A	Magnetic vector potential
b	Outer radius of the cylindrical dielectric object
b_m	Reflected wave amplitude from the m^{th} port
\hat{b}_m	Normalized reflected wave amplitude from the m^{th} port
B	Magnetic flux density
c	velocity of light
d	Linear distance; An element of the data set D
D	Data set
D	Electric flux density
$D(t, t')$	Sampling function in t -domain

DFT	Discrete Fourier transform
e	Charge of an electron
\mathbf{E}	Total electric field
\mathbf{E}^i	Incident electric field
\mathbf{E}_{loc}	Local electric field
\mathbf{E}^{ref}	Reflected electric field
\mathbf{E}^s	Scattered electric field
\mathbf{E}^{tran}	Transmitted electric field
f	Frequency
\mathbf{F}	Electric vector potential
F, F^{-1}	Mapping and its inverse
$F(s), f(r)$	Hankel transform pair
FFT	Fast Fourier transform
$g(x, x')$	Green's function in x -domain
$G_1(t)$	Permittivity profile function
$G(k_0, x')$	Green's function in k_0 -domain
$h(t)$	Inverse Fourier transform
\mathbf{H}	Total magnetic field
\mathbf{H}^i	Incident magnetic field
\mathbf{H}^s	Scattered magnetic field
$H(\omega)$	Fourier transform
$H_n^{(p)}(k_\rho \rho)$	Hankel function of order n and of type p
$H_n^{(p)'}(k_\rho \rho)$	First order derivative of the Hankel function
$\hat{H}_n^{(p)}(kr)$	Spherical Hankel function of order n and of type p
$\hat{H}_n^{(p)'}(kr)$	First order derivative of the spherical Hankel function
$IFFT$	Inverse fast Fourier transform
I	Current
I^-	Inward travelling current wave

I^+	Outward travelling current wave
j	Imaginary unit
\mathbf{J}	Electric current density
k	Wave number of the dielectric media
k_0	Free-space wavenumber; Boltzman's constant
\bar{k}_0	Normalized value of the free-space wavenumber
k_ρ	Radial propagation constant in the cylindrical dielectric media
k_b	Wave number of the background medium
k_z	Propagation constant in the z -direction
$K(\omega, t)$	Kernel of the general integral transform
$K(s, y)$	Auxiliary or Kernel function
l	Electrical length
MUT	Material under test
N	Number of ports; Density of molecules
o	An element of the object set O
O	Object set
\mathbf{p}	Total dipole moment
\mathbf{P}	Polarization
$P_n^m(\cos \theta)$	Associated Legendre function of the first kind
$P_n^{m'}(\cos \theta)$	First order derivative of the Associated Legendre function
Q	Total charge
r, θ, ϕ	Coordinates of the spherical geometry
r_0	Inner radius of the spherical dielectric object
rl	Reflection coefficient in the virtual space domain
$R(k_b)$	Back-scattered reflection coefficient
$R(k_0)$	Spectral-domain reflection coefficient
$RAND$	Uniformly distributed random number whose value lies between 0 and 1
RDE	Riccati differential equation
$[S]$	Scattering matrix

t	Time; Virtual time domain
\bar{t}	Normalized time variable
$[T]$	Transmission matrix
T	Transmission coefficient; Temperature
TDR	Time-domain reflectometer
TEM	Transverse electromagnetic
TE	Transverse electric
TM	Transverse magnetic
$\mathbf{u}_\rho, \mathbf{u}_\phi, \mathbf{u}_z$	Unit vectors in $\rho, \phi,$ and z directions respectively
$\mathbf{u}_r, \mathbf{u}_\theta, \mathbf{u}_\phi$	Unit vectors in $r, \theta,$ and ϕ directions respectively
V	Voltage
V^-	Inward travelling voltage wave
V^+	Outward travelling voltage wave
$V(s)$	Potential function
VNA	Vector network analyzer
x, y, z	Coordinates of the planar (Cartesian) geometry
\bar{Z}	Normalized impedance
Z_{0m}	Characteristic impedance of the m^{th} line
Z_0^-	Characteristic impedance of the radial line for inward travelling waves
Z_0^+	Characteristic impedance of the radial line for outward travelling waves
Z_L	Load impedance

Chapter 1

Introduction

1.1 Objective

In recent years the use of microwaves for the imaging of materials and biological bodies, and for the remote sensing of underground metallic/non-metallic objects has gained much attention. The microwaves refer to electromagnetic waves, whose frequency lies in the range of 0.3 GHz to 300 GHz and they offer the access to information related to electrical properties of the medium without making *in situ* measurements. This electrical property is generally expressed as the permittivity, whose accurate determination in materials and biological tissues leads to much other useful informations. Some of the practical applications of imaging using microwaves include, e.g., environmental studies of water content, aging and possible detection of diseases in trees and forests [1, 2, 3], the nondestructive evaluation and characterization of different food grains [4], geological investigations of the earth structure as being seen from an exploration well in oil fields [5], and imaging of human organs in biomedical microwave tomography [6, 7, 8]. The microwaves have also got application in the field of remote sensing e.g., for the detection of anti-personnel mines [9, 10]. In all of these applications, the determination of the permittivity profile leads to the imaging of the corresponding medium or material.

In case of trees or forests, any vegetation canopy is composed of different components, such as leaves, stems, branches, and trunks. Each of these components has its own geometric and biophysical characteristics. Any disease in trees affects these biophysical characteristics (such as water content and water potential), and these characteristic have a strong influence on the permittivity values of the components. It is, therefore, in principle possible to detect the disease in trees once the permittivity of different vegetation layer is determined. Similarly, in case of materials and different kinds of food grains, the determination of permittivity helps in finding the moisture content. The moisture content in grains can favorably or adversely affect both their quality and price and its accurate determination helps in the characterization of these food grains.

In the areas of geophysical prospecting, oil can be distinguished from rock and water by its permittivity value, and hence the accurate reconstruction of permittivity profile as a function of position in the earth will indicate the location of oil.

In case of biological bodies, different soft tissues can in principle be imaged once their permittivity profile is determined as the dielectric properties of these tissues vary over a wide range (permittivity ranges from 5 to 50, compared to the varia-

tion of only a few percent of densities in soft tissues). The soft tissues such as fat, lungs etc. present lower microwave absorption whereas the ultrasound energy suffers the greatest attenuation in these tissues [11]. Similarly in the case of chest cavity large discontinuities at lung surfaces limit the use of ultrasound, and low densities limit the use of X-rays [12]. Hence these soft tissues can be imaged more appropriately using microwaves rather than using e.g. the ultrasound or X-rays. There is also a possibility of detecting cancerous tissues using microwaves [13], as the dielectric properties of these tissues, depending upon their water content, are quite different from normal ones. Another advantage of using microwaves for biomedical applications is that the photon energy of these radiations is too low to cause any ionization to occur in biological tissues at ordinary intensity levels, and hence it allows a virtually safe exploration of living tissues giving a possibility of even continuous monitoring [6, 14].

For the remote sensing application, different underground metallic and non-metallic objects can be characterized by different values of permittivity. As a matter of fact, the use of microwaves helps in detecting anti-personnel mines, which are sometimes non-metallic in nature and hence can not be detected by a simple metal detector [9, 10]. It is also advantageous to use microwaves for the remote sensing applications because they are able to penetrate more deeply into vegetation and the ground than visible and infrared radiations, and hence they can yield better information about the lower layers and the ground beneath. Sometimes, the use of microwaves can give information, which is in addition to that available from visible and near-infrared regions. For example, the visible and near-infrared regions give information about the molecular-resonance properties of the surface layer of the vegetation or soil, while the microwave region allows a study of geometric and bulk-dielectric properties.

As obvious from the above discussion, a primary objective in the field of imaging and remote sensing using microwaves is the reconstruction of inhomogeneous permittivity profiles of planar and non-planar objects and of layered media. The common method for accomplishing this goal is to illuminate the object with electromagnetic waves, and measure the scattered fields (or some of their characteristics) interacting with the medium, in order to obtain the image of the distribution of the properties of the object from these measured fields. The overall process of imaging using microwaves can be well understood with the help of Fig. 1.1, where we have shown its application in the field of remote sensing. We assume that three different layers of plastic mines exist inside the earth's surface and our job is to detect and reconstruct them. We illuminate the whole area with an electromagnetic plane wave and measure the reflected signal with the help of a vector network analyzer as shown in this figure. We then apply some kind of *reconstruction algorithm* to reconstruct these different layers. The most difficult part in the overall imaging process is generally the development of an efficient reconstruction algorithm, and this thesis mainly deals with this problem. This whole method of imaging or reconstruction using microwaves is called the *microwave inverse scattering process*, and it comes under the general category of the so-called *inverse problems*. The name inverse comes from the fact that the imaging or reconstruction is *not* achieved by any conventional or *direct* procedure. As a matter of fact, even the scattered fields, which are needed for reconstructions, are measured outside the medium, for instance on its boundary because one does not have any access inside the medium. Inverse problems are en-

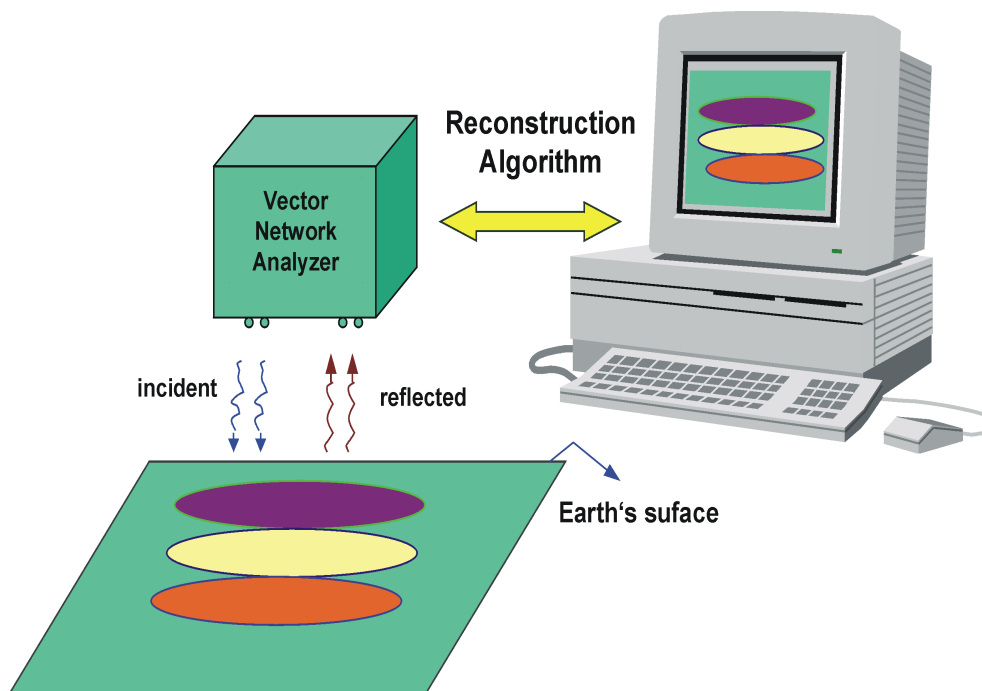


Figure 1.1: A typical example of imaging

countered in several areas of applied sciences and engineering and can be defined in a number of ways. Probably one of the best definitions could be as follows

The solution of an inverse problem entails determining unknown *causes* based on observation of their *effects*. This is in contrast to the corresponding direct problem, whose solution involves finding *effects* based on a complete description of their *causes*.

The above definition can be well understood in our context of wave scattering, where the electrical or physical properties of the medium are the causes, and the scattered fields (or some of their characteristics) are the effects. Typically, inverse problems emerge when one has indirect observations of a quantity, and one needs some computational methods to determine this quantity. For the solution of any inverse problem, it is however, very important to first formulate the corresponding direct problem in a very precised way. This direct problem is then inverted using some specialized imaging algorithms to obtain the desired parameter. In the case of electromagnetic wave scattering, the two problems can be defined as follows

The direct problem This problem is concerned with determining the scattering or reflection coefficient data from the knowledge of the incident field and properties of the scattering object.

The inverse problem Here one tries to determine the properties of the scatterer (e.g. the permittivity profile) from the measurement of the scattering data for a number of incident fields having varying characteristics.

One good distinction between the direct and inverse problems of wave scattering, which is meaningful in remote sensing problems, was given by W.-M. Boerner *et al.* [15].

Whereas, on the one hand, in the direct problem of electromagnetic scattering total *a priori* information on the size, shape and material constituents of an object, together with the relative geometry of the incident field vector and the object coordinate system, are given and the scattered field vector is to be determined everywhere over the total frequency or time domain; on the other hand, the inverse problem is to reconstruct the size, shape and material characteristics of an *a priori* unknown scattering object from the knowledge of the incident field vector and the resulting scattered field data.

The main objective of this thesis is to propose a new approach for the reconstruction of permittivity profiles of planar and non-planar objects, which is a basic problem in the field of microwave imaging and remote sensing as discussed in previous paragraphs. We have mainly dealt with the depth-dependent (one-dimensional) part of the reconstruction process, because these measurements can not generally be carried out *in situ*. The main reason for this is that one does not have any direct access *inside* the geometry of these objects, and hence it is not possible to go with some kind of probe and carry out any *direct* measurement at each and every point along depth of the object. On the other hand, lateral part of the reconstruction can be obtained using high directivity antennas and moving them mechanically in two directions. These directive antennas can provide very narrow beam width and hence it is, in principle, possible to focus the beam at large number of points by means of some mechanical movement and scan the whole lateral (say $X - Y$) plane. If these directive antennas are able to provide very narrow beam in both X and Y directions, then this lateral scanning along with the proposed method for reconstruction of depth-dependent permittivity profiles in the Cartesian coordinate system should provide us enough information for the imaging of any planar shaped dielectric object. Now imagine a situation, where the available antenna is highly directive in only one direction (say along X axis), and we want to image an object having a curved boundary with this kind of antenna. Under this kind of situation, if we carry out the analysis in the simple Cartesian coordinate system then we may lose some detailed information of the object specially along the direction in which the beam is not highly directional. However, for these cases if we formulate the whole problem in the cylindrical coordinate system, then low directivity of the antenna in a particular direction (say along Y axis) can be compensated by taking the one-dimensional curvature of the object into account along that direction. Hence, the formulation of the problem under these circumstances will yield a more accurate image in the cylindrical coordinate system than using e.g. a planar or Cartesian coordinate system. Similarly we might have a situation, where the antenna is *not* able to provide the directive beam in both the lateral (X and Y) directions. For this case, we will have to take into account the curvature of the object in both X and Y directions and this can be achieved in a better way by analyzing the whole problem in the spherical coordinate system. The formulation of the problem in the spherical coordinate system can compensate for low directivity of the antenna in both the lateral directions by taking the two-dimensional curvature of the object into account and thus providing a better image under these situations. Hence, it can be said that formulations in the cylindrical and spherical coordinate system are quite helpful and provide a reasonably accurate image of the dielectric object under

situations where the directivity of the available antenna is not very high.

It follows from the above discussion that a practical problem in case of imaging of arbitrary shaped dielectric objects is the reconstruction of one-dimensional permittivity profiles in the planar, cylindrical, and spherical coordinate system, and this was the motivation behind our present research work. The one-dimensional scattering model is also an idealized example that possesses a complete exact solution; and the physical insight into the relations between the scattering data and the permittivity profile can be obtained by considering this model. We have developed in this work new algorithms to reconstruct the one-dimensional depth-dependent permittivity profile of planar, cylindrical and spherical objects quite accurately from the measurement of wide-band reflection coefficient data. As compared to previous approaches, our proposed method is having the advantage of providing a stable solution of both low and high contrast dielectric object, and the resolution of the reconstruction in each case can be increased by simply increasing the bandwidth over which spectral domain reflection coefficient data are measured. From the practical point of view, we have proposed an experimental setup for the imaging of inhomogeneous dielectric bodies, which is completely non-destructive in nature. The procedure generally requires placing the dielectric objects directly in front of the antenna for the measurement of spectral domain reflection coefficient data. The dielectric image of the object is obtained from the measured scattering data using our proposed reconstruction algorithm.

The proposed reconstruction algorithm is quite general in nature and its applicability can be easily extended to any arbitrary coordinate system. It may be mentioned that for all the cases considered here the relative permittivity is assumed to be lossless and dispersionless, as our basic aim in this work is to obtain a stable and unique solution in the closed-form for the *inhomogeneous* permittivity profiles in different coordinate systems using an analytical and quasi-linear approach. The lossy dielectric objects are generally frequency dependent, and determining both the frequency and space-dependence of permittivity profiles will be too complicated to handle analytically and that is the main reason for considering only lossless case in this thesis.

This thesis is organized as follows. In the next two sections of this chapter, the direct and inverse scattering problems are briefly discussed. The last section of this chapter provides a state of the art of methods used for solving the general electromagnetic inverse scattering problems. The second chapter gives outline of the basic electromagnetic theory and explains the interaction phenomenon of electromagnetic waves with dielectric materials. The mathematical aspects of the inverse problem are discussed, and some of the most common methods for solving inverse problems are also briefly described. In the third chapter, the direct problem is formulated for the planar, cylindrical, and spherical coordinate system in order to find an accurate relationship between the one-dimensional depth-dependent permittivity profile of planar and non-planar objects and the reflection coefficient measured at the outer air-dielectric boundary. The fourth chapter describes in detail the proposed technique for solving the one-dimensional inverse scattering problem, and accordingly the direct equations derived in the third chapter are inverted in order to find a closed-form expression for the one-dimensional permittivity profile of planar and non-planar objects in terms of an appropriate integral transform of the wide-band reflection coefficient data. In the fifth chapter, we have reconstructed a number

of permittivity profiles using both simulated and experimental reflection coefficient data to validate our technique. This chapter also describes the effect of noise on the overall reconstruction process by adding a few percent of random error to the simulated reflection data at each frequency, and then using our algorithm to determine the unknown permittivity profile from these noisy data. Finally, a summary of the overall work is given in the sixth chapter.

1.2 The direct problem: electromagnetic scattering theory

The term scattering literally means throwing arbitrarily in all possible directions. When an electromagnetic wave encounters any obstacle or object in its path, then the original path of wave propagation changes and the wave scattering takes place. In this process of wave scattering, the total field associated with the wave also gets modified. Suppose that initially, when there is no obstacle present, a set of sources in the homogeneous medium are emitting waves, which are described by the incident electric and magnetic fields \mathbf{E}^i and \mathbf{H}^i respectively. Now, when some form of obstacle is introduced into this field as shown in Fig. 1.2, then the total field \mathbf{E} or \mathbf{H} is modified and is given by [16]

$$\mathbf{E} = \mathbf{E}^i + \mathbf{E}^s \quad \mathbf{H} = \mathbf{H}^i + \mathbf{H}^s \quad (1.1)$$

where, E^s and H^s are defined as the scattered electric and magnetic fields respectively.

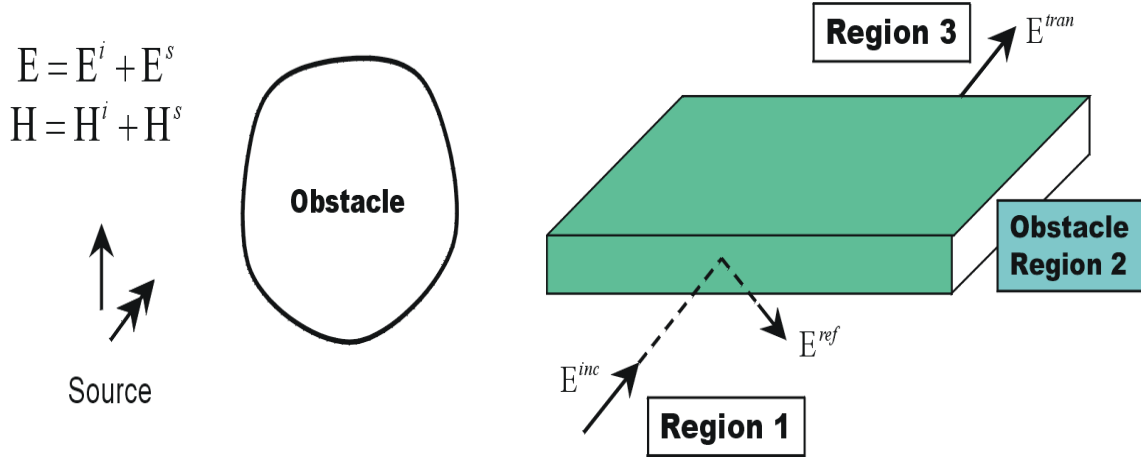


Figure 1.2: The effect of an obstacle on the incident field

Figure 1.3: The reflection and transmission of waves

These scattered fields are fields external to the obstacle and can be thought of as fields produced by the charges inside the object. Usually, in an electrically neutral object, the algebraic sum of the positive and negative charges inside the object is zero, and these positive and negative charges are so close that the net fields produced by them cancel on the macroscopic scale in the absence of an incident field. However, after application of an incident field on the obstacle, the internal positive and negative charges get separated and the net fields produced by these charges are

no longer zero on the macroscopic scale. These fields are called scattered fields and they combine with the incident fields to produce a new total field, which further affects the internal charges. This process continues until an equilibrium is reached, resulting in some net value of the total field and the scattered field. Thus we can say that in the presence of any obstacle, the total field is estimated by the vector sum of the incident field and scattered field and the characteristics of the scattered field will depend upon the physical properties of the scatterer. The direct problem or the electromagnetic scattering theory is associated with the determination of the scattered fields or some of their characteristics from the knowledge of the incident fields and physical properties of the obstacle or medium through which they travel. In the process of electromagnetic scattering, some of the incident wave gets reflected from the obstacle and comes back towards the source; while the rest of it passes through the obstacle and gets transmitted in the forward direction as shown in Fig. 1.3. To account for the reflection and transmission properties of the medium, the concept of reflection and transmission coefficients can be introduced as follows. In Fig. 1.3, the total field in the region 1 can be considered as the sum of incident and reflected fields, i.e.,

$$\mathbf{E} = \mathbf{E}^i + \mathbf{E}^r = \mathbf{E}^i(1 + \Gamma) \quad (1.2)$$

where, Γ is being interpreted as the reflection coefficient due to the scattering object or the obstacle. Similarly in the region 3, the total field is given by $\mathbf{E}_3 = \mathbf{E}^{tran}$, and the transmission coefficient T will be defined as

$$\mathbf{E}^t = T \mathbf{E}^i \quad (1.3)$$

assuming that the obstacle is lossless. The reflection and transmission coefficients are generally called as scattering coefficients, and these are in general vector quantities being functions of wave number, position and properties of the scattering object. It may be mentioned here that it is sometimes more convenient to work with the scattering coefficients rather than the absolute field components because these coefficients also have transmission line analogy and they can easily be measured in the r.f and microwave frequency range using a vector network analyzer.

One of the basic aims of the scattering theory is to develop a *forward* or *direct* model describing a relationship between the field components or scattering coefficients, which can be easily determined or measured, and physical or electrical properties (e.g. the dielectric permittivity) of the object, which are generally not directly measurable. It may be mentioned here that the electromagnetic waves are able to penetrate deeply into the inhomogeneous dielectric medium and hence the reflection coefficient measured at the outer air-dielectric interface is the result of multiple reflections between the top surface and various layers as well as internal reflections between various layers. Because of these multiple reflections, the whole process becomes nonlinear and any simple linear relationship between the scattering parameter and the physical properties will not give the exact formulation. It is also worth mentioning here that because of the vector nature of electromagnetic waves, the direct problem formulation is also strongly dependent on the polarization of incident waves, both in planar and non-planar structures. We have taken both of these phenomenon, i.e. multiple reflections and the dependence on the wave polarization,

into account to formulate the direct problem in planar and non-planar structures, which is described in detail in the third chapter of this thesis.

1.3 The inverse problem: microwave inverse scattering

It was mentioned in the last section that introduction of a dielectric object in the path of an electromagnetic field augments the total field, and this increase in field is mainly attributed to the polarization of charges inside the dielectric object after the application of an incident field. The fields produced by charges inside the dielectric object are called scattered fields, and the scattering theory is mainly concerned with finding these scattered fields from a knowledge of physical or electrical properties of the dielectric object which interacts with the incident field. The inverse scattering theory, on the other hand, is mainly concerned with finding the physical or electrical properties of the object from a knowledge of scattered fields interacting with the medium. These scattered wave fields are generally measured outside the object, and the name inverse comes from the fact that the desired physical or electrical parameters are *not directly* measurable in this case. When an electromagnetic wave of the microwave frequency range is used to explore the internal structure of the object, then the overall process may be termed as the microwave inverse scattering. The microwaves interact with electrical properties of an object normally expressed as the permittivity, and one of the basic aims of the microwave inverse scattering process is to determine the spatial distribution of permittivity function from a knowledge of scattering parameters. As mentioned earlier, the microwave inverse scattering theory finds applications in the field of imaging, remote sensing, and non-destructive evaluation of materials and tissues, as in all these cases it is not possible to *directly* measure the required parameters inside the object or media at each and every point.

The microwave inverse scattering may be considered as opposite to the direct electromagnetic scattering theory described in the last section. Hence the solution of an inverse scattering problem can be achieved by inverting the *direct* or *forward* scattering model. This inversion, in principle, should give an expression of the electrical properties of the object in terms of the measured scattered field (or some of its characteristics). However, this inversion procedure is generally not very straightforward and does not always give a unique solution. The problem mainly arises because the whole process of electromagnetic scattering is generally a non-linear phenomenon, and hence the inversion of any accurate direct scattering model may give rise to unstable solution unless special care is taken. The solution of the inverse scattering problem is often ill-posed and gives rise to ill-conditioned matrices if some numerical methods are used to solve the problem. But as the inverse scattering problems occur quite frequently in many areas of practical importance, hence some special types of algorithms have been developed with the passage of time to solve these problems under some special conditions. For example, the researchers who have used numerical method to solve these inverse problems employ some special routines in order to reduce the ill-conditioning of matrices. However, till now, no method exists in the literature which is quite versatile in nature and works under all situations. Hence, the field of microwave inverse scattering is still a grey area for research, and many researchers have been working in this field to develop some

accurate methods. In this thesis, we have proposed some new algorithms to obtain a *unique* solution of the inverse scattering problem in different coordinate systems. Our proposed method is quite versatile in the sense that it gives a reasonably accurate image of dielectric objects of both low and high contrasts, and it is also *not* very sensitive to the presence of noise in the measured scattering data. As our method is based on an analytical formulation, hence we do not have to deal with the problem of ill-posedness and ill-conditioning of matrices. Although our emphasis in this work is mainly the solution of *microwave* inverse scattering problem, but the proposed technique as such is quite general in nature and can be extended to solve the inverse problems in other areas of research as well.

1.4 State of the Art

Over the last few decades, much research has been done in the field of inverse scattering in general, and in the field of microwave inverse scattering in particular. One of the early works in the field of inverse scattering was probably carried out by Rutherford [17] in 1911, which ultimately led to the discovery of atomic nucleus. Rutherford studied the path of the back-scattered α -particles from thin gold foils, and showed that the only model of the atom which could account for these back-scattered radiations is a small positively charged nucleus surrounded by negatively charged cloud of electrons. After Rutherford's experiment, the Schrödinger's wave equation was evolved in 1926 which provided a way of relating the state of a particle to the potential influencing it at any time [18]. It was mainly due to the Rutherford's experiment and the invent of Schrödinger equation, that some early research in the field of inverse scattering was related to the area of quantum mechanics where many researchers tried to obtain an approximate inverse solution of the Schrödinger equation. One of the pioneering works in this regard was done by Born in 1926, who showed that provided the scattering interaction was weak, a particularly simple relationship existed between the scattered field and the scattering potential. As the Schrödinger equation can be transformed into an electromagnetic wave equation [17], hence all concepts applied to the quantum mechanics problem also have relevance to the microwave inverse scattering problem. As a matter of fact, many of the methods used to solve microwave inverse scattering problems find roots in the quantum inverse scattering as will be evident from the discussion in following paragraphs, where we provide a brief historical survey of commonly used methods for solving microwave inverse scattering problems.

Most of the methods available today to solve the microwave inverse scattering problem could be broadly classified into two major categories. The first category includes linear approximation methods, which are applicable for dielectric objects with very low contrast only. The second category of methods use some numerical iterative techniques, which are computationally quite intense and are often associated with a non-uniqueness and uncertainty of the achieved solution, but are accurate enough to reconstruct higher permittivity objects as well. An overview of the most common inverse methods applied to electromagnetic problems was given in a special issue of *IEEE – AP* [15]. In this special issue, many papers including some review articles relating to various aspects of the electromagnetic inverse scattering were reported. Another review article concerning the inverse scattering problem was

written by Habashy *et al.* [5, 19], where they have described some early methods used to solve mainly the one-dimensional inverse scattering problem.

The linear approximation methods are based on the assumption that the scattered field is very weak as compared to the incident field, and hence these methods are only valid for very weak scattering objects. This assumption is generally called the Born approximation, which was probably named after the famous scientist Born who proposed this kind of approximation in the field of quantum mechanics as mentioned above. In one of very early papers, Wolf [20] showed that under Born approximation and plane wave illumination, a two-dimensional tomographic image of the dielectric object function could be reconstructed from the scattering data collected by a linear array using *angular diversity* techniques in forward scattering. This statement is generally known as the Fourier diffraction projection theorem, and it forms the basis of the first-order diffraction tomography to find the approximate tomographic or cross-sectional image of objects using microwaves [21, 22]. In the year 1984, Slaney *et al.* [23] provided some simulated results to determine the domains of applicability of this diffraction tomography method for the cross-sectional imaging of dielectric objects. They established the fact that the first-order Born approximations are only valid for objects where the product of the change in refractive index and the diameter of the object is less than 0.35λ , where λ is the wavelength of the interrogating plane wave. They introduced this restriction on the dimension of the object to consider the fact that for Born approximation to be valid, the change in phase between the incident field and the wave propagating through the object should be less than π . After few years Chu *et al.* [24] proposed the *frequency diversity* technique for the microwave diffraction tomography in both forward and backward scattering to reduce the number of angular views. In their paper, they mentioned that the wide-band microwave measurements in the backward scattering are more suitable for reconstructing the edges of a scattering object than the space diversity forward scattering method. They also argued that only a total of four views in the backward scattering frequency diversity method could provide a reasonably better quality of image than the forward scattering angular diversity method which generally requires large number of views over 360° angle. For the solution of one-dimensional inverse scattering problem, one of the early papers applying the linearization technique was reported by Tabbara *et al.* [25, 26]. In their papers, they used the Born approximation to arrive at some simple analytical relations for reconstructing the one-dimensional permittivity profile from the multifrequency reflecting coefficient data. After some years, Ge *et al.* [27] used perturbational and high-frequency methods for the approximate reconstruction of dielectric permittivity from reflection coefficient data. They observed that in the high frequency region, the reflection coefficient was small and hence the approximate perturbational methods could work quite well in cases where only the general shape of the dielectric profile was required. Later on, the inverse Born solution was exemplified with experimental data of scattering by Carter *et al.* [28], and some other researchers [29] tried to qualitatively reconstruct cylindrical dielectric objects from the multi-frequency and multi-view scattering field data by making use of the linear Born approximation. In the year 1989, Hopcraft *et al.* [30] used the geometrical structure of the back-scattered fields to obtain an inverse solution of the one dimensional inverse scattering problem. They reported that plotting the real and imaginary parts of the backscattered field as a function of the wavenumber in the

complex plane yields a circle, and from the radius and intercept of this circle some properties of the scatterer could be deduced without any ambiguity. The method presented by these authors is specially useful to find the value of permittivity at the air-dielectric interface of inhomogeneous dielectric objects from the measurement of spectral domain reflection coefficient data. In the early 90's, many researchers developed some algorithms along with prototype models based on the Born approximation for the active microwave imaging of biological tissues. Broquetas *et al.* [14] in 1991 presented a prototype model based on a cylindrical array of antennas to measure the scattered field without any mechanical movement of either the body or the antenna. Their algorithm was based on the bidimensional scalar formulation of fields and they were able to image some weak scattering bodies using their setup. In the year 1992, the same group of authors [11] presented algorithms for the active microwave imaging of biomedical systems based on both planar and cylindrical array configurations. In this paper, they mentioned that the planar system was better from the point of view of stability of the reconstructed image and algorithm simplicity, while the cylindrical geometry could give better resolution. It may be, however, mentioned here that nowadays with the advent of many new methods and due to the availability of high computational power, the inversion based upon the first order Born approximations are not used quite often except probably in the case of some imaging devices where they can easily give the qualitative sketch of the scatterer's structure.

The numerical methods, either in frequency or in time domain, are generally used to solve the inverse scattering problem in a more exact way, and in most of the cases they are able to reconstruct the objects with high contrast and with very high value of permittivity. However, the problem with these methods is that they generally take lot of computational time, and often may give rise to a non-unique or unstable solution. The accurate solution of the inverse scattering problem was, however, first developed by Gelfand, Levitan, and Marchenko [31] in the early 1950's for the inverse solution of Schrödinger equation in the field of the quantum-wave mechanics. The method proposed by them is generally called the *GLM* method, which is actually based on the analytical formulation and hence it cannot be called a numerical method in the real sense. The *GLM* method is of significance because it was the first method ever proposed to find an exact solution of the inverse scattering problem, and many researchers used this analytical method in past in order to avoid a strong dependence on the computational power. The *GLM* method is based on the formulation of an integral equation relating the scattered potential to the non-scattered one via some kernel or auxiliary function. This integral equation is solved to construct the kernel from the scattered data, and from this kernel the profile of the inhomogeneous object is determined. Some of the early papers using the *GLM* technique in the field of electromagnetic inverse scattering were reported by Jordan *et al.* [32, 33], who generally assumed the complex reflection coefficient as a rational function of the wavenumber. However, the main problem with the *GLM* method is that the integral equation in this case is solved by a differential-operator technique, which generally leads to inaccurate results whenever the scattered data are imprecise or incomplete [17]. The inversion scheme introduced by Balanis [34] tried to avoid the step of differentiation, when he formulated the whole problem directly in terms of the reduced electromagnetic wave equation rather than in terms of the Schrödinger equation. The Balanis method was used by Jaggard *et al.* to

reconstruct the one-dimensional refractive index profile of a dispersionless dielectric, where they also mentioned that the numerical implementation of this method was better than that of *GLM* and it was also robust with respect to noise [35, 36]. It may be, however, mentioned, that the *GLM* method gives an analytical solution only for a very small class of reflection coefficients in case of quantum inverse scattering, hence this method can not be called an exact method for solving the microwave inverse scattering problem in a more general sense [33, 37].

For obtaining a numerical solution, many researchers have tried to use some iterative methods based on a second order Born method, which generally gives an accuracy of one order more than the simple Born method and is generally called the distortive Born approximation. The distorted Born approximation can be basically thought of as a linear method with some added form of standard regularization [17]. In one of very early papers, Roger [38] described the Newton-kantorovitch algorithm which forms the basis of many distorted Born methods. As mentioned in [38], the Newton-kantorovitch algorithm is a step-by-step procedure, which generally converges to the exact solution provided a good estimate of *a priori* information is available. Many researchers have used the iterative methods based on the distortive Born approximation for determining the one-dimensional permittivity profiles of both continuous and discontinuous objects from the spectral domain reflection data [39, 40], and results for different polarizations using this method have also been reported [41]. Habashy *et al.* [42] have used the distorted Born approximation method to obtain the radially varying permittivity profile in a cylindrically stratified medium. The iterative technique using distorted Born approximation has the advantage that a closed form solution can be obtained in some special cases, and hence the computational requirement might be less as compared to other numerical methods [39, 40]. The other advantage of using the distortive Born approach methods is that one might not need a very large number of *a priori* parameters because of the linear approximation of the functional operator locally [38]. However, as previously mentioned, the inverse problems often give rise to ill-conditioned matrices and hence most of the numerical methods used to solve these problems try to make some special strategy to reduce the ill-conditioning. Joachimowicz *et al.* have proposed that the ill-conditioning of the iterative procedure based on the Newton-kantorovitch algorithm can be reduced by incorporating *a priori* information such as an outer boundary of the object and upper and lower bounds of the permittivity into these algorithms [28]. These authors have validated their reconstruction algorithms with the real experimental data, and they have reported that their iterative algorithms in the spatial domain provides an accurate image of even high scattering objects with a very reasonable number of iterations [8]. The iterative Born approach was used in the time-domain by Moghaddam *et al.* [43], where they reported that this method gives accurate inversion and converges quite fast even for objects of higher electrical dimensions and of higher contrast. In recent years many researchers have used the iterative routines based on the the distorted Born method or the Newton-kantorovitch algorithm [44, 45, 46] to improve the quality of the reconstructed image in case of biomedical applications. Recently some researchers have applied the first and second order Born approximation to solve the inverse scattering problem in the field of remote sensing [47], where they have reconstructed the rotationally symmetric permittivity profile from multi-frequency scattering data.

Some researchers have also implemented the numerical scheme in time domain to

facilitate the iterative determination of constitutive parameters of inhomogeneous dielectric objects from the reflected data [48, 49]. Their method is based upon a space-time discretization of the integral equation for the reflected field, and for the inversion they have mainly tried to utilize those values that can be determined most accurately in the associate direct scattering problem [48]. In the year 1991, Caorsi *et al.* presented an experimental imaging system making use of the multi-view scattering data [50], where they measured the electric field at many angular positions by rotating the region under test with respect to the measurement setup. From the theoretical point of view, they subdivided the nonlinear problem into two linear steps. In the first step, they expressed the equivalent current density inside the region to be investigated in terms of the permittivity function. The second step involved the formulation of a linear integral equation representing the scattering field in terms of the equivalent current density and a known Green function. They applied the moment method to transform the integral equation into a linear algebraic system. To reduce the ill-conditioning problem, these authors solved the matrix equations via a pseudoinverse transformation [51], which is a tool for regularizing such problems. These authors reported that pseudoinverse matrices can be computed offline for a given measurement setup resulting in an computationally inexpensive method. In 1990's, many researchers have used the conjugate gradient method and its modified version for the imaging of dielectric objects [52, 45]. They have converted the inverse scattering problem into a nonlinear optimization problem, which is based on the minimization of a functional defined as the norm of discrepancy between the measured and calculated scattering data for an estimated object function. The conjugate gradient method involves the search for the minimum of a functional in a direction suggested by its negative gradient and it is a nonlinear iterative method in the sense that its new estimate is not a linear function of the past estimate. This method has the advantage of having a rate of convergence practically insensitive to the initial guess and it is well suited for ill-conditioned matrices [51]. It has been reported that the gradient method is also effective in reconstructing strong scattering objects, where the Newton-kantorovitch approach might not give very accurate result [52]. Recently, a number of researchers have used numerical techniques based on the spectral-domain moment method [53, 54] for both quantitative and qualitative microwave imaging of biological objects. This method is based on expanding the unknown object function in a set of spatially shifted Gaussian basis function, and ultimately the inverse scattering problem is formulated as a nonlinear optimization problem, which is then solved by employing the modified gradient method. These authors have reported a substantial reduction of the number of optimization variables for a given problem size thus enabling the implementation of this method for electrically large object.

The microwave imaging has recently been applied to the detection of breast cancer, where the high contrast in permittivity between the normal breast tissues and tumors is exploited. In [55], authors have used a number of small antennas to scan the breast area, and the finite-difference-time-domain (FDTD) method has been used to simulate the behavior of the antennas, with and without the breast model present. In this paper, an algorithm has been presented to subtract the dominant reflections from the outer skin of the breast, resulting in successful detection of tumors. A clinical prototype for microwave imaging of the breast has also been developed [56], where the breast is illuminated by a 16 element antenna array through

a water-coupled interface. These authors have reported that their configuration setup is a practical comfortable approach, and initial results of microwave-breast-examinations performed on five volunteers were encouraging. It is worth mentioning here that most of the iterative methods mentioned above linearize the exact integral equation in order to solve the direct problem numerically. Because of this local linearization mechanism, these methods are not really able to reconstruct the objects of very high contrast. The other point to be noted here is that these numerical methods generally use some kind of regularization parameter to obtain the stable solution of the inverse problem. This additional constraint of regularization is quite often achieved by putting the higher order derivatives of the object function to zero, which is an indirect way of reconstructing only smooth kinds of profiles.

Most of the methods discussed in previous paragraphs to solve the inverse scattering problems are based on the scattering integral equation (*SIE*), which basically relates the incident field with the scattered field and properties of the scatterer [25, 54]. For obtaining the inverse solution, the *SIE* is either solved using a Born approximation, or discretized for a numerical solution. Apart from this *SIE* approach, other category of methods also exist in the literature for solving inverse scattering problems, which are based on the nonlinear Riccati-differential equation (*RDE*) relating the spectral domain reflection coefficient data with properties of the scatterer [17]. The main advantage of *RDE* based method is that the formulation is carried out in terms of the reflection coefficient (rather than the field component), which also has a transmission line analogy and can easily be measured (both magnitude and phase) in the *rf* and microwave frequency range using a vector network analyzer. The *RDE* method was originally introduced in the field of electromagnetic inverse scattering about 50 years ago [57] for the approximate reconstruction of impedance profiles with low contrast within *TEM* structures with an axially independent propagation constant. As the impedance can also be expressed in terms of the material properties such as the relative permittivity [58], hence the reconstruction of impedance profiles also leads to the determination of inhomogeneous permittivity profiles. However, the *RDE* approach was initially able to reconstruct dielectric objects of very low contrast only, as the original nonlinear differential equation was simply linearized after ignoring the non-linear term, and the axial dependence of the propagation constant was also not taken into account. After some years, it was tried to take the axial dependence of the propagation constant into account but the corresponding differential equation was still considered to be linear. This new formulation helped in obtaining the permittivity profiles of somewhat higher contrast, but still the dielectric objects of high values of permittivity could not be reconstructed and also the method did not work if the variation in the permittivity was very large. The situation was same for quite long time until the so called "Renormalization technique" was introduced by some researchers [59] to tackle the nonlinearity of this differential equation in a different way. The overall idea of using this renormalization technique was to solve the linear differential equation in terms of an inverse hyperbolic tangent of the reflection coefficient function rather than in terms of the reflection coefficient itself. Recently Cui *et al.* [60] used the microwave networking technique to derive the nonlinear Riccati-differential equation, and then later on they used the renormalization methods described above to obtain a solution in a closed form [61] for the one-dimensional permittivity profile of planar objects in terms of the Fourier transform of the reflection coefficient data. This idea somewhat

relaxed the constraint that the variations in the permittivity of the material should be very small, and the overall process also worked for strong scattering objects. But for the quantitative reconstruction of permittivity profiles using this method, a higher deviation between the exact and reconstructed values was observed if either the depth of reconstruction or the variation in material properties was high.

In this thesis, we have extended the whole concept of renormalization techniques and *RDE* approach to solve the one-dimensional inverse scattering problems applied to the field of imaging and remote sensing. We have mainly put our attention on reconstruction of the one-dimensional depth-dependent part of the inhomogeneity, as this is generally the most difficult part of the overall imaging process since these measurements can not be carried out *in situ*. Moreover, the general problem of imaging of $3 - D$ inhomogeneous dielectric objects reduces to this one-dimensional part, if a number of high directivity antennas are used to scan the objects in other two directions. Hence our proposed technique in combination with a lateral scanning mechanism can, in principle, provide the standard image of any dielectric object. Our approach is based on solving the exact non-linear Riccati differential equation in a more flexible way than it has been done in past (see e.g. [59, 61]). The basic idea is to solve the corresponding linear differential equation in terms of an arbitrary function of the reflection coefficient [62] rather than using the inverse hyperbolic tangent function as was done in previous papers. The exact form of this arbitrary function is determined and optimized by means of an algebraic nonlinear transformation. The main advantage of our approach as compared to previously proposed methods is that we isolate the nonlinearity of the associated inverse problem into a nonlinear algebraic transformation, which can be optimized in a flexible way to obtain a very accurate and *unique* image of both low and high contrast dielectric objects in all cases.

Our other major contribution in this thesis is to generalize the above mentioned *RDE* approach so that they could be applied to any arbitrary coordinate system. This is really a new work in this field, as to the best of our knowledge, the *RDE* approach have till now been applied only to objects in the Cartesian coordinate system. The formulation of the problem in a non-Cartesian coordinate system will clearly help to image the dielectric object of any arbitrary shape in a more accurate way. To achieve our goal, the Fourier transform of the planar geometry is replaced by a general kind of integral transform whose exact form of kernel is decided by the particular geometry. This replacement is based on the fact that any pair of adjoint kernels can be used for the direct and inverse transforms provided they satisfy certain completeness properties over the spectral or spatial band of interest [63]. The new pair of transform kernels replace the ideal delta sampling function (of the Fourier transform) by a more flexible pulse-shaped pencil function. It has been observed that this pencil function can be used to sample the unknown permittivity function of any arbitrary shaped dielectric object provided it satisfies certain properties such as its movability in the desired spatial band with minimum distortion. These properties are, however, quite general ones and are found to be achievable in most of the practical cases.

To validate the proposed theory of reconstruction, we have implemented it in case of cylindrical and spherical coordinate systems. The formulation of the problem in cylindrical and spherical coordinate systems helps to reconstruct the radially-dependent permittivity profiles of those dielectric objects whose boundary coincides

with these non-planar coordinate systems. These formulations in the non-planar coordinate system also facilitates the use of less directive antennas by taking the curvature of the object into account. The cylindrical coordinate system e.g. can take the $1 - D$ curvature into account, while the $2 - D$ curvature is better dealt with in the spherical coordinate system, if the available antennas are not highly directional.

In order to formulate the problem in the cylindrical and spherical coordinate system, the non-linear *Riccati-similar* differential equations in both coordinate systems for any arbitrary order TE and TM polarization are derived. These equations, which basically relate an appropriately defined reflection coefficient to the radially varying permittivity profile, do not exist in the literature and are new contributions to this field. The formulation of the problem for any arbitrary order TE or TM mode illumination becomes necessary as the practical antenna arrangements for illumination (transmitters) or measurement of scattering data (receivers) are not generally able to excite or measure a single wave mode. An arbitrary illuminating or scattered electromagnetic field can, however, be expanded into an infinite sum of modes due to their completeness property (see e.g. [64]). A multiple illumination / multiview scenario can then be used to extract the necessary information on the scattering of a certain TE or TM mode. After deriving the differential equations for any arbitrary order mode, these equations are inverted using our proposed technique to reconstruct the one-dimensional depth-dependent permittivity profile in the respective coordinate system in terms of an appropriate integral transform of the wide-band spectral domain reflection coefficient data. We have started our work with a cylindrical geometry illuminated by a lowest order mode and in the initial stage the dependence of wave-number on the permittivity profile is ignored to simplify the overall process [65, 66]. In a later stage, a coordinate transformation is employed in order to achieve the better accuracy for reconstructing the dielectric objects of higher contrast [67, 68]. The overall formulation is finally extended to higher order TE and TM modes [69]. In the cylindrical coordinate system, the lowest order mode is equivalent to a transmission line mode [16] and this property is exploited to analyze the one-dimensional radial structure using the classical transmission line theory [70]. For the spherical geometry, we start with lower order illuminations to simplify the analysis [71, 72] and then generalize our formulation for higher order modes. The effects of noise on the overall reconstruction are also considered, and the quality of the reconstructed image in each case is *not* found to be much sensitive with respect to noise [73, 74].

The main advantages of our technique as compared to previously proposed methods to solve the microwave inverse scattering problems may be stated as follows. The first advantage is that our method does not use any kind of linearization or Born approximation, and hence dielectric objects of relative permittivity of as high as 100 can be reconstructed. The second advantage is that our method always provides a closed-form solution, and hence it does not require high computational time. The third major advantage is that both continuous and discontinuous permittivity profiles can be reconstructed using our proposed technique, as we do not have to put any additional regularization constraint in our algorithm which is normally the case in iterative methods as mentioned earlier. From the practical point of view, we have proposed an experimental setup for the imaging of inhomogeneous dielectric bodies, which is completely non-destructive and which does not require the mate-

rial or medium to be confined inside some closed structures. This is in contrast to other experimental prototypes developed in past by some researchers for the microwave imaging purposes, which are generally based on placing the target to be imaged inside a water tank (to increase the lateral resolution) [8, 14]. We do not always require the object under test to be placed inside a water tank or some other medium having a high permittivity, as our proposed reconstruction algorithm allows the resolution of the image in the spatial domain to be increased by simply increasing the bandwidth of the measured spectral domain reflection coefficient data. Our proposed setup of placing the dielectric object directly in front of the antenna has also an advantage under situations, where it might be inconvenient or sometimes even impossible to place the material under test (MUT) inside some tank or other confined structures.

The details of our proposed technique for all three coordinate systems (Cartesian, spherical and cylindrical) along with several reconstructed examples are presented in subsequent chapters of this thesis. Here it may just be pointed out that after combining results of all three major coordinate systems proposed in this thesis, it is in principle possible to obtain a dielectric image of any arbitrary shaped inhomogeneous dielectric object in terms of an appropriate integral transform of the wide-band reflection coefficient data.

Chapter 2

Microwave Inverse Scattering Theory

2.1 Basic formulas and definitions

2.1.1 The electromagnetic field in free space

The electromagnetic theory is mainly concerned with interrelated or coupled electric and magnetic fields and this coupling effect occurs when the two fields are time varying. Generally at lower frequencies i.e. when dimensions of the device or system are small compared to the wavelength ($L \ll \lambda$), the spatial distribution of the electromagnetic fields over the extent of the device is same as that of static fields even when the actual fields vary with time. The electric and magnetic fields can, therefore, be considered as uncoupled in this lower frequency range and hence the electric circuit theory, which is much simpler than the complicated electromagnetic theory, can be used for the analysis in this case. However, in the microwave frequency range where the wavelength is of the order of the dimensions of the component ($L \approx \lambda$), the electric and magnetic fields are strongly coupled and the lumped circuit element approximation of the standard circuit theory cannot be used for the analysis in this case. The reason is that at such a high frequency, the phase of the voltage or current changes significantly over the physical extent of the device. Hence the electromagnetic field theory and the distributed element approximation is used for the analysis in the microwave frequency range. The modern electromagnetic field theory is based on the mathematical equations proposed by Maxwell in 1873 [75], who hypothesized them solely from mathematical considerations. These Maxwell's equations, which are basically coupled equations involving electric and magnetic fields, were validated experimentally by Hertz during the period 1887-1891 [58]. The general form of time-varying Maxwell's equations in differential form can be written as follows

$$\nabla \times \mathbf{E} = -\frac{\partial \mathbf{B}}{\partial t} \quad (2.1a)$$

$$\nabla \times \mathbf{H} = \frac{\partial \mathbf{D}}{\partial t} + \mathbf{J} \quad (2.1b)$$

$$\nabla \cdot \mathbf{E} = \frac{\rho_c}{\epsilon_0} \quad (2.1c)$$

$$\nabla \cdot \mathbf{B} = 0 \quad (2.1d)$$

where \mathbf{E} is the electric field intensity in V/m , \mathbf{H} is the magnetic field intensity in A/m , \mathbf{D} is the electric flux density in $Coul./m^2$, \mathbf{B} is the magnetic flux density in Wb/m^2 , \mathbf{J} is the electric current density in A/m^2 and ρ_c is the electric charge density in $Coul./m^3$. It may be mentioned here that bold-faced letters in this thesis always denote vector quantities. The meaning of all the above equations are briefly described below.

The first equation (2.1a) means that a time-varying magnetic flux density $\frac{\partial \mathbf{B}}{\partial t}$ will act as a source for the electric field \mathbf{E} and that the \mathbf{E} field produced by changing \mathbf{B} encircles it. The second equation (2.1b) implies that a time-changing electric flux density $\frac{\partial \mathbf{D}}{\partial t}$ and an electric current \mathbf{J} are both sources for the magnetic field \mathbf{H} and the \mathbf{H} -field lines produced by these two sources encircle \mathbf{J} and $\frac{\partial \mathbf{D}}{\partial t}$. The third equation (2.1c) means that the electric charge ρ_c is a source of \mathbf{E} and that the \mathbf{E} lines begin and end on charges. Finally, the last equation (2.1d) implies that there are no magnetic charges analogous to electric ones and that the \mathbf{B} -field lines always occur in closed loops. It may be concluded from the above discussion that the ultimate source of electromagnetic field is the electric charge density ρ_c , but because of coupling nature of (2.1) both \mathbf{E} and \mathbf{H} also act as source of each other.

The electric and magnetic field intensities in free-space are related with the current density and flux densities by the following simple relationships

$$\mathbf{B} = \mu_0 \mathbf{H} \quad (2.2a)$$

$$\mathbf{D} = \varepsilon_0 \mathbf{E} \quad (2.2b)$$

where $\mu_0 = 4\pi \times 10^{-7} \text{ henry}/m$ is the permeability of free-space, and $\varepsilon_0 = 8.854 \times 10^{-12} \text{ farad}/m$ is the free-space permittivity. If the electromagnetic wave is passing through any media other than the free space, then the behavior of passing wave will be influenced and accordingly these parameters will be modified as discussed in the next section.

Today, most of the analysis using the electromagnetic field theory involves the solution of Maxwell's equations with appropriate boundary conditions. It is mainly because of the complexity and coupled nature of these Maxwell's equations that the electromagnetic field theory approach becomes more complicated and involved than the circuit theory approach. However, nowadays because of the availability of high computational power, these Maxwell's equations can be solved quite accurately for any arbitrary geometry using some numerical techniques. The numerical solution gives the value of the electric and magnetic fields at any point inside the body of an arbitrary shape, provided the boundary conditions are properly defined.

2.1.2 Interaction of electromagnetic waves with dielectric materials

When the electromagnetic waves pass through certain material or medium, then the characteristics of these waves get changed depending upon the properties of the medium. The properties of any media or materials are described by the permeability μ , permittivity ε , and conductivity σ . Materials having large values of σ are called

conductors and those having small values of σ are called insulators or dielectrics. Our main concern here is the interaction of electromagnetic waves with non-magnetic dielectric materials, which are characterized by $\mu_r = 1$, $\varepsilon > \varepsilon_0$ and having $\sigma \simeq 0$. An ideal dielectric material possesses no free charges and thus completely inhibits the passage of steady electric current. The vacuum is also one example of dielectric.

In this section, different aspects of the interaction of electromagnetic waves with dielectric materials are discussed. As the electric and magnetic fields basically represent the forces among charges, the fundamental interaction of electromagnetic field with materials is due to the exertion of force by the applied fields on the charges in the material. The dielectric as a whole is electrically neutral, but it is composed of molecules, which in turn are composed of charged particles (nuclei and electrons), and these particles are usually affected by the presence of an electric field. The applied field influences the positively and negatively charged parts of a molecule oppositely, and these parts are displaced in opposite directions from their equilibrium positions, thus causing the molecule to become *polarized*. These displacements are, however, limited by strong repulsive forces, caused by the altered charge distribution within the molecule, so that the net shift is just a small fraction of the molecular diameter. The molecule in such cases may be viewed as an electric dipole and when the contribution from all such dipoles are summed up, then this changes the original field distribution. The dipole behavior of a molecule can be attributed to three main causes namely electronic, ionic and orientational polarization, which are explained in detail in later part of this section. These three polarization mechanisms in materials are generally used as the basis for an explanation of their dielectric behavior.

2.1.2.1 The electric dipole moment

A fundamental concept associated with the phenomenon of polarization is the *electric dipole moment* p , which is defined as follows

$$\mathbf{p} = (\mathbf{r}_1 - \mathbf{r}_2)Q = Q\mathbf{d} \quad (2.3)$$

where \mathbf{r}_1 and \mathbf{r}_2 are the position vectors of the total positive and negative charges Q and $-Q$, and \mathbf{d} is the directed distance from the center of negative charge to the center of positive charge associated with the electrically neutral atom. The above formulation is also applicable to a pair of ions, in which case \mathbf{d} is drawn from the center of charge of the negative ion to the center of charge of the positive ion. The presence of an electric dipole generally alters the electric field, which would have otherwise existed. From the practical point of view, the effect of a single polarized atom on the total electric field may be rather small (sometimes, it may be negligible). However, if we consider the cumulative effect of large numbers of such polarized atoms or ions, then the electric field created by these systems of charges may be quite appreciable. If several neutral systems of charges are considered jointly, then their combined electric moment may be written as [76]

$$\mathbf{p} = \sum_j \mathbf{p}_j \quad (2.4)$$

where $\mathbf{p}_j = q_j\mathbf{d}_j$ is the dipole moment of the j^{th} system, with q_j as the total positive charge of this j^{th} system, and \mathbf{d}_j as the directed distance from the center of negative charge to the center of positive charge of this system.

2.1.2.2 The macroscopic electric field due to polarized dielectric molecules

The matter as a whole may be considered as consisting of electrons and positively charged nuclei, and these elementary particles are quite small as compared to inter-atomic spacings. The electric and magnetic fields associated with these particles are called *microscopic* fields and these fields are generally not of much interest because of their rapid variations in space and time. For this reason, the local average values of fields known as *macroscopic* \mathbf{E} and \mathbf{H} are often considered, and in this thesis we will mainly deal with these fields components, which satisfy Maxwell's equations for all types of materials [76].

In an ideal dielectric, we can assume that there is no *free* charge and all of the electrical charges present are associated with electric dipoles, which are usually called *bound charges*. One key feature of these bound charges associated with electrically neutral atoms in a dielectric is that their total sum is generally zero as these kinds of charges arise from electrically neutral dipoles. These electrically neutral dipoles are better described by the term *molecule*, which is considered to be the fundamental building block of any dielectric material. If we consider any n^{th} molecule, and if a center of subgroup of positive charges q_{n1} is displaced by a distance \mathbf{d}_{n1} from a center of subgroup of negative charges $-q_{n1}$ within this molecule, then it will contribute an electric dipole moment, $\mathbf{p}_{n1} = q_{n1}\mathbf{d}_{n1}$ according to (2.3). The n^{th} molecule may consist of many subgroups of displaced charges $(q_{ni}, -q_{ni})$ displaced by a distance \mathbf{d}_{ni} , and hence the total dipole moment for the molecule in this case will be given by, $\mathbf{p}_n = \sum_i q_{ni}\mathbf{d}_{ni}$ according to (2.4). This dipole moment \mathbf{p}_n causes a potential at any distant point (x, y, z) , as shown in Fig. 2.1, which is given by

$$\Phi_n = \frac{\mathbf{p}_n \cdot \tilde{\mathbf{r}}_n}{4\pi\epsilon_0\tilde{r}_n^3} \quad (2.5)$$

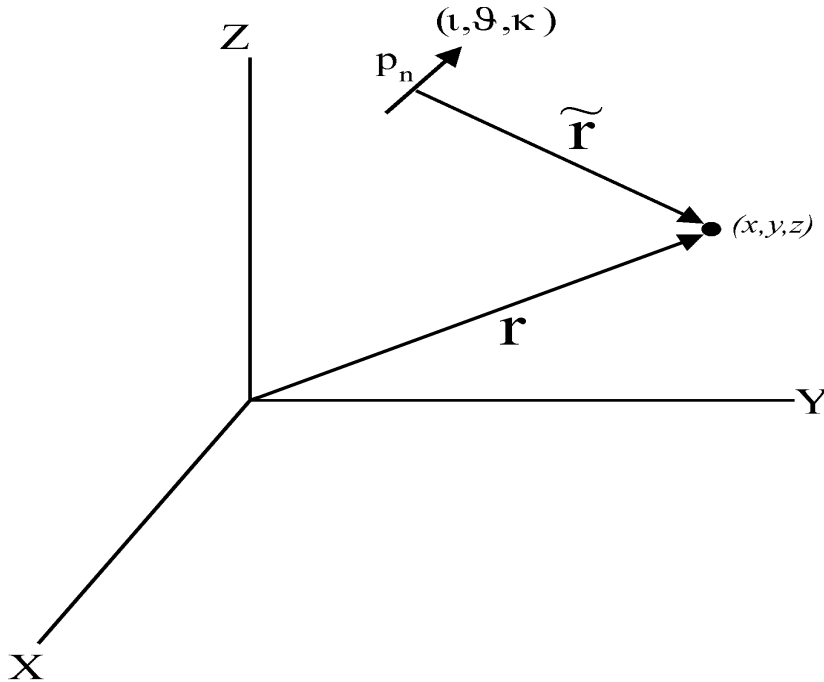


Figure 2.1: The dipole moment

Now, the volume V of the dielectric material is generally large enough, so that it can be divided into N number of *macroscopic* volume elements dV , with each dV containing M molecules. In this case, the vector sum of all the dipole moments in dV can be written as

$$\sum_{n=1}^M \mathbf{p}_n = \mathbf{P} dV \quad (2.6)$$

where \mathbf{P} is called the polarization density, or sometimes simply the *Polarization*. Accordingly, making use of (2.5) and (2.6), the potential at any arbitrary point (x, y, z) due to all the elementary dipoles in the entire volume of the dielectric material is given by the following expression [76]

$$\Phi(x, y, z) = \int_V \frac{\mathbf{P}(\iota, \vartheta, \kappa) \cdot \tilde{\mathbf{r}} d\iota d\vartheta d\kappa}{4\pi\epsilon_0 \tilde{r}^3} \quad (2.7)$$

where $(\iota, \vartheta, \kappa)$ are coordinates of the source point, $\tilde{\mathbf{r}}$ is a vector drawn from the source point to the observation point as shown in Fig. 2.1, and the observation point (x, y, z) is assumed to be quite far away from each of dipoles in V ($\tilde{r} \gg d_{ni}$). The above expression for the total potential can be mathematically manipulated to obtain the following form as given in [76]

$$\Phi(x, y, z) = \int_S \frac{\mathbf{P} \cdot d\mathbf{S}}{4\pi\epsilon_0 \tilde{r}} + \int_V \frac{(-\nabla_S \cdot \mathbf{P}) dV}{4\pi\epsilon_0 \tilde{r}} \quad (2.8)$$

where, ∇_s is the conventional del operator at the source point $(\iota, \vartheta, \kappa)$, and S is the bounding surface of the dielectric material. The potential expression (2.8) will cause an electric field, which is given by the following expression [76]

$$\mathbf{E}(x, y, z) = -\nabla_O \left[\int_S \frac{\mathbf{P} \cdot d\mathbf{S}}{4\pi\epsilon_0 \tilde{r}} + \int_V \frac{(-\nabla_S \cdot \mathbf{P}) dV}{4\pi\epsilon_0 \tilde{r}} \right] \quad (2.9)$$

where, ∇_O is the del operator at the observation point. The above expression basically represents the macroscopic electric field at any point external to the dielectric material. However, it has been verified in [76] that the macroscopic electric field is always given by the same formula (2.9), irrespective of whether the observation point (x, y, z) is internal or external to the dielectric material. Meanwhile, equations (2.8) and (2.9) can also be interpreted in terms of the equivalent charges. The first term on the right hand side of this equation can be considered as a surface density of bound electric charge $\rho_P = P_n$ distributed over S , while the second term may be viewed as a volume density of bound electric charge $\rho_P = -\nabla_S \cdot \mathbf{P}$ distributed throughout V .

2.1.2.3 The concept of general electric flux density and the local electric field

In this section, we make use of the concept of equivalent charges given by (2.9) to derive a general expression for the electric flux density. For this purpose, let us first distinguish between the primary charges and the equivalent charges. The primary charges may be regarded as charges present in *a vacuum*, while the equivalent charges are defined for dielectric materials to take into the account the effect of polarization

in order to consider these dipole moments as some sort of actual charges in *a vacuum*. This means that in case of *a vacuum* or free-space only primary charges will be present, while in dielectric materials both primary and equivalent charges might be present. Now, let us consider a general electrostatic system consisting of two parts; the volume V_1 is occupied by the primary charges having density ρ_c , and the volume V_2 (bounded by the surface S_2) is occupied by the electric dipoles representing the dielectric materials. These volumes V_1 and V_2 may overlap as shown in Fig. 2.2. The electric field in the first region (V_1) will be simply the field intensity due to the

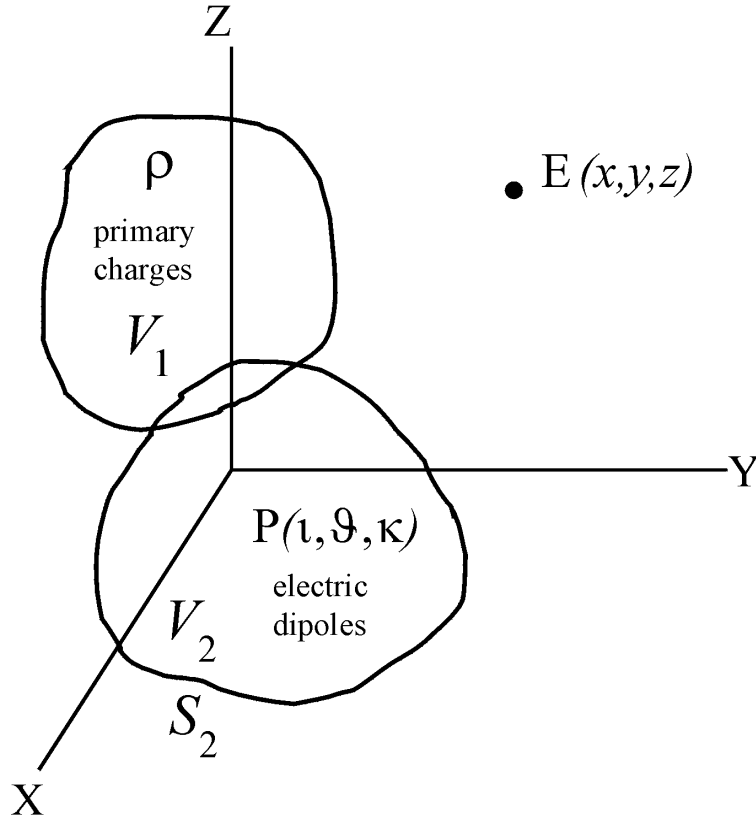


Figure 2.2: The primary charges and the electric dipoles

volume charge density ρ_c , while the electric field in the second region (V_2) will be given by the expression (2.9) with S and V replaced by S_2 and V_2 respectively. Now, if the entire electrostatic system, including dielectric materials, is viewed as a distribution of primary charges of density ρ_c and equivalent bound charges of density $\rho_P = -\nabla \cdot \mathbf{P}$ in *a vacuum*, then a total macroscopic electric flux density may be defined as follows

$$\begin{aligned} \mathbf{D}_0(x, y, z) &= \varepsilon_0 \mathbf{E}(x, y, z) \\ &= \varepsilon_0 \mathbf{E}_1(x, y, z) + \varepsilon_0 \mathbf{E}_2(x, y, z) \\ &= \mathbf{D}_{01}(x, y, z) + \mathbf{D}_{02}(x, y, z) \end{aligned} \quad (2.10)$$

where \mathbf{E} is the total macroscopic electric field of the medium at the observation point as shown in Fig. 2.2, and \mathbf{D}_{01} and \mathbf{D}_{02} are electric flux densities associated with the primary charge distribution ρ_c and the *equivalent* charge distribution ρ_P respectively. Both the flux densities satisfy Gauss' law and hence the expression involving these two quantities can be written as follows

$$\begin{aligned}\nabla \cdot \mathbf{D}_{01} &= \rho_c \\ \nabla \cdot \mathbf{D}_{02} &= -\nabla \cdot \mathbf{P}\end{aligned}\tag{2.11}$$

Now, under most of the practical situations, we are generally interested in the *total* electric field \mathbf{E} , and the electric flux density \mathbf{D}_{01} associated with the primary charges ρ_c . Keeping this in mind, equations (2.10) and (2.11) can be solved to give the following expression for the *macroscopic* electric flux density

$$\begin{aligned}\mathbf{D} &= \mathbf{D}_{01} = \varepsilon_0 \mathbf{E} - \mathbf{D}_{02} \\ &= \varepsilon_0 \mathbf{E} + \mathbf{P}\end{aligned}\tag{2.12}$$

where \mathbf{E} is the total macroscopic electric field of the medium, and \mathbf{P} represents the macroscopic volume density of electric dipole moments associated with dielectric materials. It may be noted here that (2.12) is basically an expression for the generalized electric flux density \mathbf{D} , wherein the macroscopic \mathbf{E} represents the electric field both *inside* and *outside* the materials. Equation (2.12) is quite general in the sense that in the absence of dielectric materials, the polarization density \mathbf{P} simply becomes zero, and the expression (2.12) reduces to that of fields due to system of primary charges only. This expression, however, represents the fields at the macroscopic level and to have the physical interpretation of the dielectric theory, it is quite useful to relate the macroscopic \mathbf{P} with its causes, which generally occur at the microscopic level. To obtain a relationship between \mathbf{P} and its real causes at the microscopic level, the concept of *local electric field* \mathbf{E}_{loc} is introduced, which is basically the average field intensity acting on a given molecule within the dielectric. This local field \mathbf{E}_{loc} is usually determined by removing the molecule in question, maintaining all other molecules in their time-averaged polarized positions, and calculating the space-averaged electrostatic field in the space previously occupied by the removed molecule. Following this procedure, the local field may be derived to have the following expression [76]

$$\mathbf{E}_{loc} = \mathbf{E} + \left(\frac{\gamma}{\varepsilon_0} \right) \mathbf{P}\tag{2.13}$$

where \mathbf{E} is the macroscopic electric field and γ , which is basically the constant of proportionality between the average local field and the total dipole moment, is called the internal field constant. The formulation of the local electric field as in (2.13), can be used to obtain a relationship between \mathbf{P} and its causes for all three types of polarization, as will be shown in following paragraphs.

2.1.2.4 The electronic polarization

This type of polarization occurs due to shifting of the electron cloud of an atom relative to its nucleus in the presence of an electric field. Let us assume that the nucleus is shifted by a distance d with respect to the center of the electron cloud, due to the presence of a local electric field \mathbf{E}_{loc} as shown below in Fig. 2.3. It is assumed that the electrons originally form a cloud of constant charge density around the nucleus, confined to a sphere of the radius r_0 . Now, if Ze is the total charge on the nucleus, with Z being the atomic number and e the charge, then the force

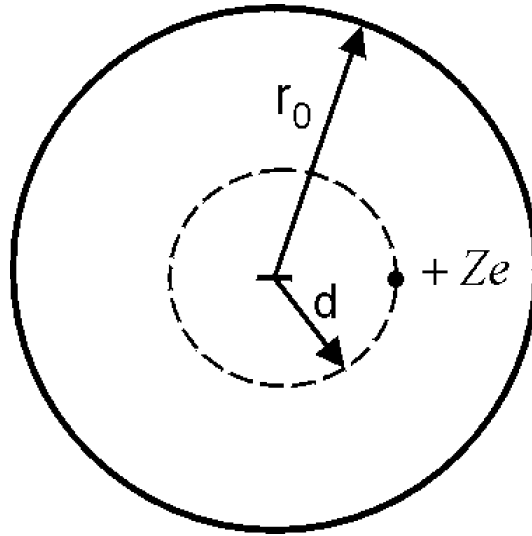


Figure 2.3: The electronic polarization

on this nucleus due to all other charges except its own electron cloud will be given by $Ze\mathbf{E}_{loc}$. This force on the nucleus should be balanced by the restoring force due to the electron cloud distribution $Q_d = Zed^3/r_0^3$ within the radius d as shown in Fig. 2.3. The expression for this restoring force can be derived using Coulomb's law, and is given by $(Ze)^2 \frac{d^3/r_0^3}{4\pi\epsilon_0 d^2}$ [76]. Under equilibrium condition, these both forces will be equal, and this leads to the following expression for the electronic dipole moment $p_e = Zed$ of the atom [77]

$$\mathbf{p}_e = \alpha_e \mathbf{E}_{loc} \quad (2.14)$$

where,

$$\alpha_e = 4\pi\epsilon_0 r_0^3 \quad (2.15)$$

is called the *electronic polarizability* of the atom. Sometimes, it may be difficult to find an exact expression for α_e in complicated cases, however its average value could always be deduced, which would generally differ from (2.15) only by some scaling factor. This implies that the induced electronic dipole moment in dielectric materials is proportional to the local electric field as given by (2.14) in most of the cases.

2.1.2.5 The ionic polarization

Sometimes, a molecule may consist of two different atoms which are joined together by a chemical bond as shown in Fig 2.4(a). These kinds of molecules, in which two distinct atoms A and B are arranged *in-line*, have generally a net dipole moment of zero. However, the presence of an electric field in such molecules causes a relative displacement of these charged atoms resulting in a net dipole moment $2\delta p$ as shown in Fig 2.4(b). The effect of inducing dipole moment in these kinds of molecules is called the *ionic polarization*. Suppose that d_0 is the average interatomic spacing between the centers of A and either of the B atoms and $2q$ is the net time-average charge on the A atom. Now, if the the ions in Fig 2.4(a) are separated by a distance

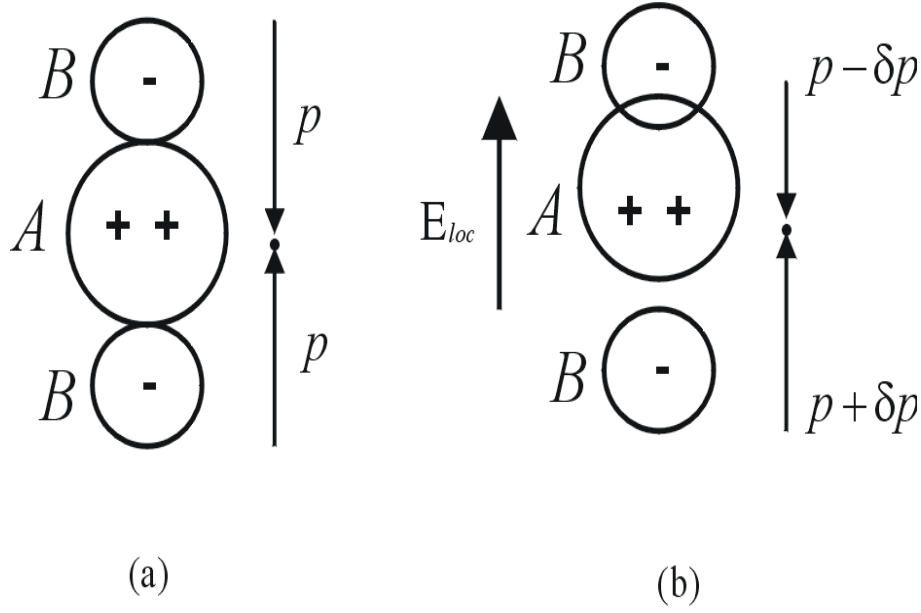


Figure 2.4: The ionic polarization

r in the absence of any electric field, then the net force on the lower B ion due to the positive ion A and the other negative ion B is given by the following expression [76]

$$F_{n0} = \frac{(2q)(q)}{4\pi\epsilon_0 r^2} + \frac{(-q)(q)}{4\pi\epsilon_0 (2r)^2} - \frac{7q^2 d_0^{n-1}}{16\pi\epsilon_0 r^{n+1}} \quad (2.16)$$

where n is a constant, whose value depends on the ions being considered. The first two terms on the right hand side of (2.16) represent the Coulomb's attractive forces between ions, while the third term indicates the net repulsive force due to the electron clouds of adjacent ions. Under equilibrium, $r = d_0$ and the net force given by (2.16) would be zero. Now, suppose that the presence of an electric field \mathbf{E}_{loc} shifts the ion A by a distance δd closer to the upper B ion as shown in Fig 2.4(b). The net force experience by the lower B ion in this case can be calculated using (2.16), provided the distances d_0 , and r are replaced by $d_0 + \delta d$. After this substitution, this equation may be further simplified to obtain the following expression [76]

$$F_{nd} = \frac{q^2 \delta d}{16\pi\epsilon_0 d_0^3} [7(n+1) - 16] \quad (2.17)$$

This force should be balanced by the external force $-qE_{loc}$ on the lower B ion under the equilibrium condition. Making this equality and noting that $p_i = 2q\delta d$ is basically the induced dipole moment for the entire molecule, we obtain the following expression for the average induced dipole moment [76]

$$\mathbf{p}_i = \alpha_i \mathbf{E}_{loc} \quad (2.18)$$

where,

$$\alpha_i = \frac{32\pi\epsilon_0 d_0^3}{[7(n+1) - 16]} \quad (2.19)$$

is called the *ionic polarizability* of the molecule. Equation (2.18) is in general applicable to all kinds of non-polar molecules as well as the ionic crystals except that some times a slight change in the magnitude of α_i may be observed. It may be noted here that the above analysis assumes that the major axis of orientation of all the molecules is in a direction parallel to the applied electric field. However, when the molecules are randomly oriented and this condition is not satisfied, then the component of electric field which is in the direction of the major axis of crystal should be considered.

2.1.2.6 The orientational polarization

The molecules having a permanent dipole moment are called *polar* molecules and in the absence of an electric field, these moments are randomly oriented. The application of an electric field exerts a torque on these polar molecules tending to align them with the field and this effect is called the *orientational polarization*. However, because of the thermal agitation effect, the molecules keep on colliding with each other and break up this orientational pattern. The net result is that the all the molecules are never completely aligned, except at very low temperatures. For a quantitative description of this effect, consider a permanent dipole $\mu = qd$ making an angle β with respect to the electric field \mathbf{E}_{loc} as shown in Fig. 2.5. The potential

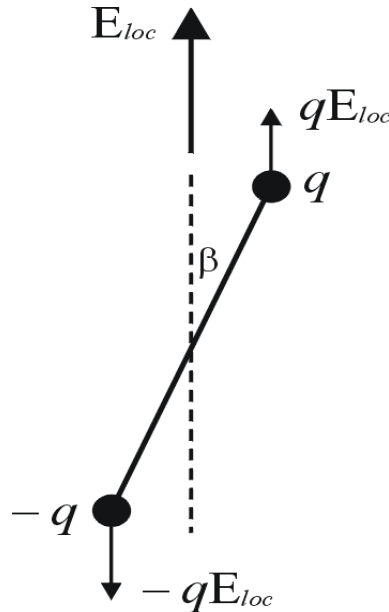


Figure 2.5: The orientational polarization

energy of the whole system here consisting of the dipole and the electric field is given by the following expression [76]

$$\mathbf{W} = -\mu \cdot \mathbf{E}_{loc} \quad (2.20)$$

It is observed from the above equation that the energy is minimum when the angle between the dipole and the field is zero and it is maximum when this angle becomes π . Hence it may be deduced that the preferred orientation for the dipoles is in the direction of the applied field. At very low temperatures, the effect of thermal

agitation will be negligible and all the permanent dipole moments can be considered to be aligned with the field resulting in the value of orientational dipole moment per molecule p_0 approximately equal to μ . However, at normal temperatures the orientation will never be complete, and the expression for the orientational dipole moment per unit molecule is given by the following expression [76]

$$\mathbf{p}_o = \alpha_o \mathbf{E}_{loc} \quad (2.21)$$

where, $\alpha_o = \mu^2/3kT$ is called the *orientational polarizability* of the molecule, with k and T being the Boltzmann's constant and the temperature respectively.

2.1.2.7 The concept of relative permittivity

As can be easily seen from (2.14), (2.18), and (2.21), the dipole moment in all three types of polarization is proportional to the local field. Hence for the materials exhibiting all three types of polarizability, we may define an average polarization per molecule as follows

$$\mathbf{p} = \alpha \mathbf{E}_{loc} \quad (2.22)$$

where,

$$\mathbf{p} = \mathbf{p}_e + \mathbf{p}_i + \mathbf{p}_o \quad (2.23)$$

is the sum of all the three individual dipole moments, and

$$\alpha = \alpha_e + \alpha_i + \alpha_o \quad (2.24)$$

is the total polarizability, being sum of all three contributions. Now, if N is the density of molecules per cubic meter, then the volume density of dipole moments will be given by

$$\mathbf{P} = N\mathbf{p} = N\alpha \mathbf{E}_{loc} \quad (2.25)$$

This equation may be combined with (2.13) to obtain the following expression for the total polarization

$$\mathbf{P} = \chi \varepsilon_0 \mathbf{E} \quad (2.26)$$

where, χ is a dimensionless quantity, known as the *dielectric susceptibility* and is given by the following expression [76]

$$\chi = \frac{N\alpha/\varepsilon_0}{1 - \gamma N\alpha/\varepsilon_0} \quad (2.27)$$

where γ is called the internal field constant as used in (2.13), and α is defined by (2.24). The expression for \mathbf{P} as given by (2.26) may be used in (2.12) to express the total electric flux density as follows

$$\mathbf{D} = \varepsilon_0(1 + \chi)\mathbf{E} = \varepsilon_0 \varepsilon_r \mathbf{E} = \varepsilon \mathbf{E} \quad (2.28)$$

where,

$$\varepsilon_r = (1 + \chi) \quad (2.29)$$

is also a dimensionless quantity, and is called the *relative permittivity* or the *relative dielectric constant* of the medium. The quantity $\varepsilon = \varepsilon_0\varepsilon_r$ in (2.28) is called the *total permittivity* of the medium. As the field \mathbf{E} and the flux density \mathbf{D} are both macroscopic quantities, the relative permittivity ε_r can be thought of as representing the macroscopic electric behavior of the dielectric. The value of relative dielectric constant will depend upon the value of polarization density P per unit field. In case of gases, the molecules are generally far enough and so they cause a very low polarization density resulting in a value of the relative dielectric constant close to unity. In case of solids and liquids, however, the high density of molecules results in a considerable value of P per unit applied field and so the value of the dielectric constant as given by (2.27) and (2.29) should be taken into account to find the total electric flux density in (2.28). When we use the expression given by (2.27), then we may have to use one, two or three terms of (2.24) and (2.25) depending upon whether the material under consideration consists of single type of atom, more than one type of atoms, and whether its molecules contain permanent dipole moments. As the distance between atoms in non-polar solids and liquids is generally not much affected by the temperature, the relative dielectric constant in these cases can be considered to be constant over a wide temperature range. However, in case of polar solids and liquids, whose molecules possess permanent dipole moment, the susceptibility or the relative permittivity can show a temperature dependence over some range. In this thesis, we mainly deal with dielectric materials at around room temperature and hence the temperature-dependence of the relative permittivity is not of much relevance to us.

2.1.2.8 The effect of time-varying electromagnetic field

All the discussion so far in this section assumed that dielectric materials were under the influence of *static* electric fields. In this section the results given earlier will be extended to the *time-harmonic* case. However, we will limit our discussion to *linear* and *isotropic* materials, as most of materials of our interest fall under this category. In *linear* media, the polarization density \mathbf{P} and the applied electric field \mathbf{E} are linearly related and the permittivity does not depend upon the strength of the applied electric field. The *isotropic* materials are characterized by the scalar value of permittivity so that \mathbf{P} and \mathbf{E} are parallel and point in the same direction. For anisotropic materials, permittivity will have to be defined by a tensor relating the three components of electric flux density \mathbf{D} to the three components of \mathbf{E} [78]. When a time-harmonic \mathbf{E} is applied to linear and isotropic dielectric materials, then it will result in a time-harmonic \mathbf{P} . But, the induced \mathbf{P} may not be in phase with the local field because of the inertia exhibited by displaced charges and so we may have to consider the phase factor of \mathbf{P} . After a careful analysis, it has been observed that for materials exhibiting only electronic and the ionic polarization, the permittivity may be considered to be real and frequency independent in the microwave and millimeter-wave range [76]. However, materials having strong orientational polarization (which is basically frequency dependent), exhibit complex permittivity and also have dielectric losses in the microwave frequency range. Some common examples of such kind of materials, which fall under this category are some liquids such as water

and some crystalline solids. In this thesis, however, only lossless dielectric materials having *real* values of permittivities will be considered. The reason being that our main aim in this thesis is, basically, to propose analytical methods for the reconstruction of *inhomogeneous* permittivity profiles in different coordinate systems. And it will be quite complicated and sometimes even impossible to consider both position and frequency dependence of permittivity (lossy materials have generally strong frequency dependence because of the orientational polarization phenomenon), specially if some analytical method is used. Also the dielectric materials having low loss can be considered as lossless for many practical applications. Meanwhile, the concept of relative permittivity as given by (2.29) and the general electric flux density given by (2.28) can be used to generalize Maxwell's equations (2.1) and (2.2) with ϵ_0 replaced by ϵ . This is definitely an advantage because then the situation looks like as if no polarized molecules were present and all the basic formulas and definitions applicable in free space can be applied to dielectric media as well with just this replacement of ϵ_0 by the total ϵ . It may be mentioned here that if the material is conductive, then the electric current density \mathbf{J} in (2.1b) may be replaced by $\mathbf{J} = \sigma\mathbf{E}$ where σ is conductivity of the material. This factor σ may be combined with the imaginary part of the ϵ to account for the losses in dielectrics. Similarly, for magnetic materials, the free-space permittivity μ_0 in (2.2a) may be replaced by a more general $\mu = \mu_0\mu_r$, where μ_r is the relative permeability of the medium. However, as mentioned earlier, only non-magnetic lossless dielectric materials will be considered in this thesis, and hence $\sigma = 0$ and $\mu_r = 1$ would be taken for all future reference.

2.1.3 The scattering parameters

At low frequencies, where the wavelength is large compared to the circuit dimensions, lumped equivalent circuit approach can be used and the voltage and current can be defined uniquely at each and every point. These low frequency circuits can be analyzed in a variety of ways and many sets of parameters such as impedance or admittance parameters can be defined and accurately measured. However, at microwave frequencies, where the circuits dimensions become comparable to the wavelength, the lumped circuit approach does not work as the phase of the wave may change along the line. The best way to analyze the circuits at microwave frequencies would be to solve Maxwell's equations along with the appropriate boundary condition to obtain the field at each and every point in space. However, this analysis is usually quite complicated and time-consuming and sometimes is not worth doing for some simple structures. Generally, for circuits having two-conductors and supporting *TEM* waves (such as coaxial cables), the voltage and current can be defined uniquely even at higher frequencies, and many network concepts can be applied to them by treating them as distributed components. If we are able to define equivalent voltages and currents at some terminal pairs or *ports* for these transmission lines at higher frequencies, then impedance or admittance matrices of the circuit theory concept can be used to characterize these networks. However, for transmission lines supporting non-TEM waves (such as waveguides), it is very difficult or rather impossible to define the voltage and current uniquely at any point [58]. As a matter of fact, even for TEM-lines, the direct measurement of voltage and current waves (both magnitude and phase) travelling in a given direction, is practically not feasible

at microwave frequencies. Hence the whole definition of voltages and currents and the formulation of impedance and admittance matrices at microwave frequencies remains a mere theoretical concept. At microwave frequencies, a set of parameters known as *scattering parameters*, which basically relate the incident waves on the ports with the reflected and transmitted waves from the ports, are commonly used for the analysis. The port may be any type of transmission line or transmission line equivalent of a single propagating waveguide mode, and this may be thought of like a "two-terminal pair" of the conventional circuits [58]. The scattering parameters (both magnitude and phase) can be very accurately measured over a wide band of frequencies using e.g. a vector network analyzer, and they are also uniquely defined for both *TEM* and *non-TEM* lines at a given reference plane. Let us consider an N -port microwave network as shown below in Fig. 2.6, with the terminal plane t_n defined at a reference point on the n th port. The scattering parameters for this

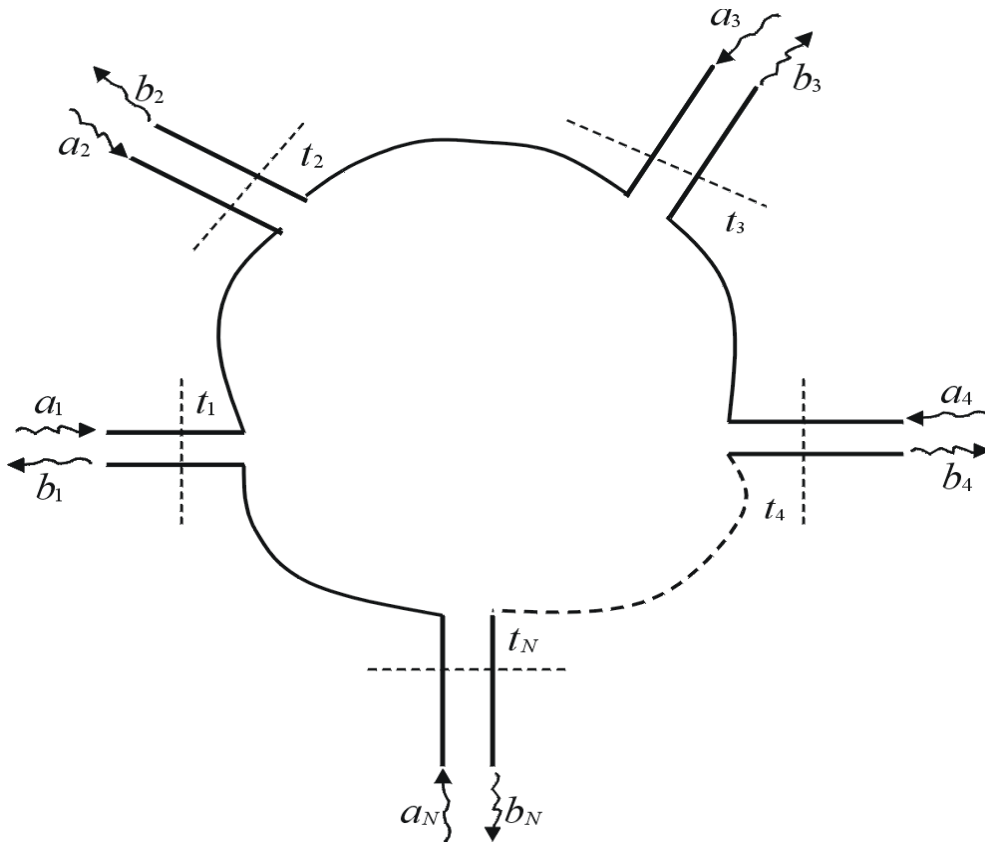


Figure 2.6: The N -port microwave network

N -port network will be defined by a $N \times N$ scattering matrix as follows [79]

$$\begin{bmatrix} b_1 \\ b_2 \\ \vdots \\ b_N \end{bmatrix} = \begin{bmatrix} S_{11} & S_{12} & \dots & S_{1N} \\ S_{21} & S_{22} & \dots & S_{2N} \\ \vdots & \vdots & \ddots & \vdots \\ S_{N1} & S_{N2} & \dots & S_{NN} \end{bmatrix} \begin{bmatrix} a_1 \\ a_2 \\ \vdots \\ a_N \end{bmatrix} \quad (2.30)$$

where a_n is the amplitude of the incident wave at the n th port, while b_n represents the scattered wave amplitude from the port n . Each port in Fig. 2.6 may represent a transmission line or its equivalent corresponding to a single propagating waveguide

mode. The scattering parameter S_{ii} may be considered as the reflection coefficient at the port i provided all other ports are matched, and the parameter S_{ij} is the transmission coefficient from port j to port i when all other ports are terminated in matched loads. In a more concise form, (2.30) can also be written as follows

$$[b] = [S] [a] \quad (2.31)$$

As the $[S]$ -parameters defined by (2.30) and (2.31) relate both magnitude and phase of the incident waves with that of reflected and transmitted waves, the location of a phase reference plane t_n is crucial for each port n as shown in Fig. 2.6. However, if the reference plane is moved from the original positions, then we do not need to measure or calculate the S parameters again, rather they may be easily modified using simple mathematical relationships [58]. If we assume that the reference plane in port m is shifted by a distance l_m away from the original position, then the original S parameters are modified as follows

$$S'_{mm} = e^{-2j\beta_m l_m} S_{mm} \quad (2.32)$$

where S_{mm} / S'_{mm} basically represent the reflection coefficients at the port m provided all other ports are matched, and $\beta_m = 2\pi/\lambda_m$ is the propagation phase constant for the m th line. A similar kind of relationship can be developed for generalized scattering parameters S_{mn} [79]. It may be noted here that the above formulation (2.32) holds good only if the frequency is constant throughout this operation. It may be also mentioned here that in deriving (2.30) and (2.31), it is assumed that all ports have the same characteristic impedance so that the power is directly proportional to the square of the wave amplitude. The identical characteristic impedance also helps in obtaining a symmetric S matrix for reciprocal networks. However, if this is not the case, and if the port m is having its characteristic impedance as Z_{0m} , then the normalized wave amplitudes may be defined as follows

$$\begin{aligned} \hat{a}_m &= a_m / \sqrt{Z_{0m}} \\ \hat{b}_m &= b_m / \sqrt{Z_{0m}} \end{aligned} \quad (2.33)$$

These normalized wave amplitudes may then be used along with (2.30) to obtain the S parameters for the multi-port network with unequal characteristic impedances of each port. The normalization of wave amplitudes as in (2.33) is quite useful for the analysis of non-uniform transmission lines as will be shown in the later part of this thesis.

In equation (2.30), the S parameters are defined for an arbitrary number of ports. However, the two-port networks shown in Fig. 2.7 are most commonly used at microwave frequencies. It is also very common to have a cascade of two or more of these types of two-port networks representing various microwave circuits. Under these circumstances, when we have a cascade of two port junctions, it is more convenient to represent each junction by a wave-amplitude transmission matrix $[T]$ as shown in Fig. 2.7. The transmission matrix $[T]$ relates the incident and reflected waves on the input port to those on the output port as follows

$$\begin{bmatrix} a_1 \\ b_1 \end{bmatrix} = \begin{bmatrix} T_{11} & T_{12} \\ T_{21} & T_{22} \end{bmatrix} \begin{bmatrix} b_2 \\ a_2 \end{bmatrix} \quad (2.34)$$

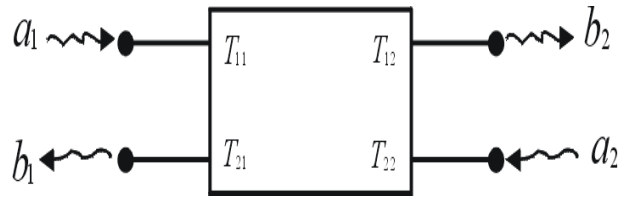


Figure 2.7: A 2-port microwave network

The main advantage of this type of formulation defined by (2.34) is that the transmission matrix $[T]$ of the cascade connection of two or more two-port networks shown in Fig. 2.7 can simply be found by multiplying the $[T]$ -matrices of the individual two-ports. The transmission matrix $[T]$ can be easily transformed into the scattering matrix $[S]$ using simple mathematical relationships [79].

2.1.4 The multiple reflections from inhomogeneous transmission lines

In the last section, it was briefly mentioned that the scattering coefficient S_{mm} basically represents the reflection coefficient at the port m , provided all the other ports in network are matched. If we have a junction of two transmission lines of characteristic impedances Z_1 and Z_2 as shown in Fig. 2.8, then this junction behaves like a 2-port network and the scattering parameter at the input port S_{11} will be equal

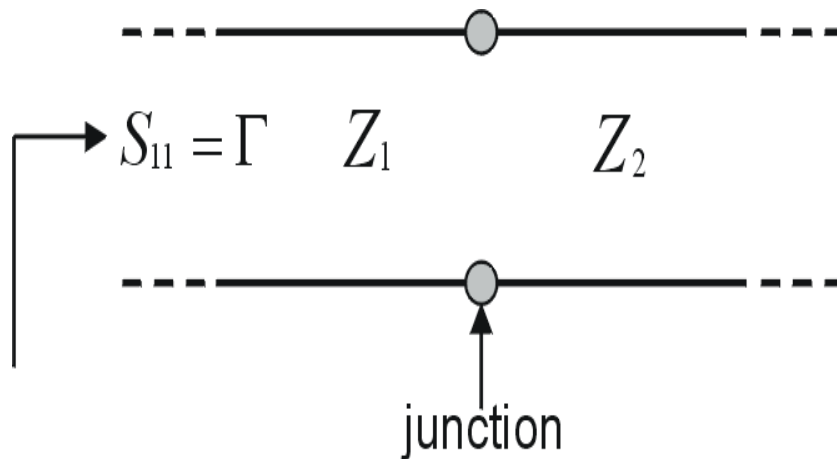


Figure 2.8: Reflection at the junction of two transmission lines

to the reflection coefficient Γ provided the second port is matched, i.e.,

$$\Gamma = S_{11} = \frac{Z_2 - Z_1}{Z_2 + Z_1} \quad (2.35)$$

Now, suppose that the second transmission line of electrical length $\theta = \beta l$ and of the characteristic impedance Z_2 , is terminated in a load impedance $Z_L \neq Z_2$. This situation is depicted in Fig. 2.9, where it has also been shown that there will be multiple reflections at both first and second junctions due to mismatching. The total reflection coefficient Γ at the input line will basically be infinite sum of all the partial reflections and transmissions. However, it is easily shown that for small

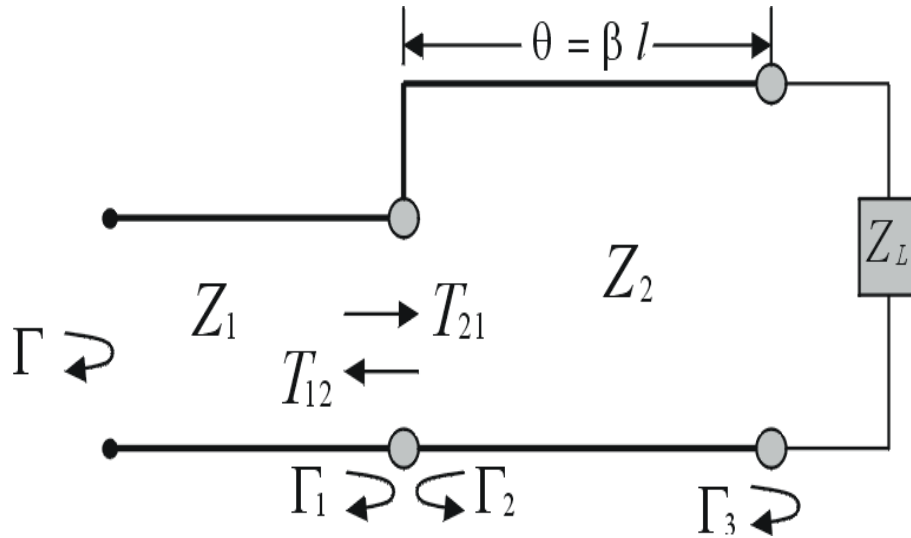


Figure 2.9: Multiple reflections in a circuit with two junctions

reflections, the resultant reflection coefficient Γ can be found by considering only first order reflections from both the junctions, i.e.

$$\Gamma = \Gamma_1 + \Gamma_3 e^{-2j\theta} \quad (2.36)$$

where the term $e^{-2j\theta}$ is introduced to take into account the total phase shift 2θ , which the incident wave undergoes in travelling the line up and down. It may be noted here that the above approximation is valid only when the discontinuity between the impedances Z_1, Z_2 and Z_2, Z_L is small [58]. This concept of small reflection theory can be extended to analyze a multi-layered transmission line shown in Fig. 2.10, where the impedance in each layer is assumed to be constant. In the

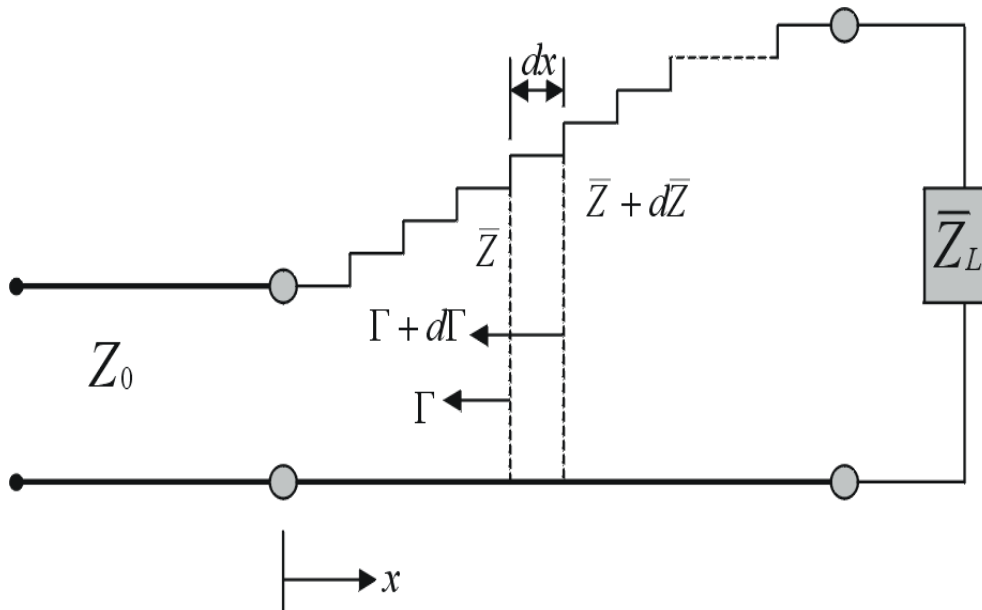


Figure 2.10: A multi-layered transmission line having a large number of homogeneous layers

limiting case, i.e., when the number of layers is quite large and the change in the

impedance from one step to another $d\bar{Z}$ is small, this multi-layered transmission line approaches a continuously tapered line shown in Fig. 2.11. The normalized

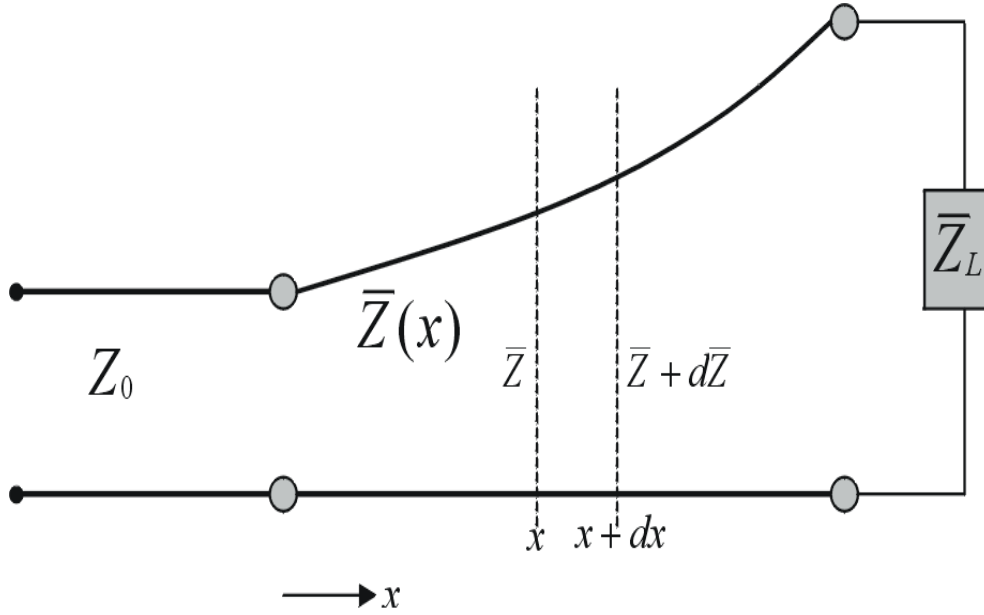


Figure 2.11: A tapered transmission line

characteristic impedance of this tapered line

$$\bar{Z}(x) = Z(x)/Z_0 \quad (2.37)$$

changes continuously over the length of the line, and it can basically represent any general type of inhomogeneous transmission line. The incremental change in the impedance $d\bar{Z}$ in Figs. 2.10 and 2.11 will produce a local differential reflection coefficient given by the following expression

$$d\Gamma_l = \frac{\bar{Z} + d\bar{Z} - \bar{Z}}{\bar{Z} + d\bar{Z} + \bar{Z}} \simeq \frac{d\bar{Z}}{2\bar{Z}} \quad (2.38)$$

where it is assumed that $d\bar{Z}$ is sufficiently small so that the higher order terms such as $d\bar{Z}^2, d\bar{Z}^3, \dots$ can be neglected. Now, as mentioned earlier, the total reflection coefficient at the input $x = 0$ can be *approximately* estimated by summing up all the individual terms such as (2.38) after taking into account their proper phase shifts, as was done for the two-junction transmission line in (2.36). However, this formulation will neglect all multiple reflections between individual differential sections in Fig. 2.10. To take into account these multiple reflections, an *exact* differential equation for the reflection coefficient Γ can be derived using the concept of microwave network theory [79]. The region between x and $x + dx$ in Fig. 2.10 can be considered as a transmission line of length dx followed by a two-port network $[\partial S]$ representing the junction between two impedances \bar{Z} and $\bar{Z} + d\bar{Z}$ as shown in Fig. 2.12. The total reflection coefficients at points x and $x + dx$ are supposed to be given by Γ and $\Gamma + d\Gamma$ respectively as shown in Fig. 2.10. If the circuit is assumed to be lossless, then the S parameters of the junction in Fig. 2.12 is given by the following expression

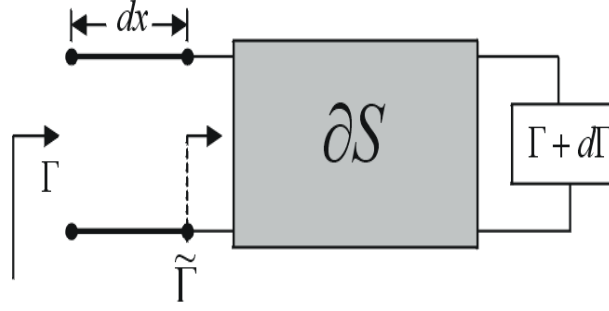


Figure 2.12: A single section of the tapered transmission line

$$[\partial S] = \begin{bmatrix} S_{11} & S_{12} \\ S_{21} & S_{22} \end{bmatrix} = \begin{bmatrix} d\Gamma_l & \sqrt{1 - d\Gamma_l^2} \\ \sqrt{1 - d\Gamma_l^2} & -d\Gamma_l \end{bmatrix} \quad (2.39)$$

where the unitary property of the 2-port $[S]$ matrix is used. As can be seen from Fig 2.12, the second port of the junction $[\partial S]$ is not fully matched rather it is terminated into an impedance characterized by the reflection coefficient $\Gamma + d\Gamma$. This mismatching at the output port will modify the input reflection coefficient $\hat{\Gamma}$ in Fig. 2.12 as follows [79]

$$\tilde{\Gamma} = S_{11} - \frac{S_{12}S_{21}(\Gamma + d\Gamma)}{S_{22}(\Gamma + d\Gamma) - 1} = d\Gamma_l + \frac{[1 - d\Gamma_l^2](\Gamma + d\Gamma)}{1 + d\Gamma_l(\Gamma + d\Gamma)} \quad (2.40)$$

Now, equation (2.32) can be used to relate this intermediate parameter $\hat{\Gamma}$ with the reflection coefficient Γ in Fig. 2.12 as follows:

$$\Gamma = \tilde{\Gamma} e^{-2j\beta dx} \quad (2.41)$$

Equations (2.40) and (2.41) can be combined together to arrive at the following equation

$$\begin{aligned} \Gamma e^{2j\beta dx} &\simeq \Gamma [1 + j2\beta dx] \\ &= d\Gamma_l + \frac{[1 - d\Gamma_l^2](\Gamma + d\Gamma)}{1 + d\Gamma_l(\Gamma + d\Gamma)} \simeq d\Gamma_l + \frac{[(\Gamma + d\Gamma)]}{1 + \Gamma d\Gamma_l} \end{aligned} \quad (2.42)$$

where the exponential function is expanded into Taylor's series and the higher order infinitesimals such as dx^2 , $d\Gamma_l^2$, $d\Gamma d\Gamma_l$, $dx d\Gamma_l$, \dots etc. are neglected. Equation (2.42) can be further simplified after neglecting the higher order terms of differentials, and using (2.38) to arrive at the following exact differential equation involving the reflection coefficient

$$\frac{d\Gamma}{dx} = 2j\beta\Gamma - \frac{1}{2}(1 - \Gamma^2) \frac{d(\ln \bar{Z})}{dx} \quad (2.43)$$

The above equation is called the *Riccati* equation and it is the exact equation, which takes into account the multiple reflections within the inhomogeneous transmission line. However, this equation is non-linear because of the presence of Γ^2 term and hence does not have any general solution. But, this equation can always be solved numerically provided that we are able to specify the impedance $\bar{Z}(x)$ along the line. The more complicated problem is of synthesis, where we are required to determine

$\bar{Z}(x)$ for some given values of reflection coefficient data taking into account the non-linearity of (2.43). As the normalized impedance can generally be related with the permittivity profile, so the synthesis problem is of main concern to us in this thesis. It will be shown in subsequent chapters of this thesis that these kinds of non-linear synthesis problems can be solved using our proposed technique.

2.1.5 The integral transform

Integral transforms find application in many areas of science and engineering. The basic aim of the integral transform method is to transform a given problem into one that is easier to solve. They are, for example, very convenient tools for solving initial-value and boundary-value problems in an easy way. A problem involving derivatives can be reduced to a simpler problem involving only multiplication by polynomials in the transform variable by taking an integral transform, solving the problem in the transform domain, and then finding an inverse transform. There are many basic theorems and quite involved theory regarding the integral transform, which can be found in many books such as [63]. However, the conditions and criteria described in these theorems are generally broad enough so that they are generally applicable to most of the functions that arise in the field of science and engineering. Hence we discuss here the use of the integral transform only from the application point of view. In very general terms, an *integral transform* may be defined by the following relationship [80]

$$H(s) = \int_{-\infty}^{\infty} h(t)K(s, t) dt \quad (2.44)$$

where a given function $h(t)$ of domain t is said to have been transformed into another function $H(s)$ of domain s by this integral. The function $H(s)$ is called the integral transform of $h(t)$, and $K(s, t)$ is called the *kernel* of this transformation. The function $h(t)$ and the kernel $K(s, t)$ must satisfy certain conditions to ensure the existence and uniqueness of the transform $H(s)$. There are a variety of kernels that may be used in (2.44) to define a particular kind of integral transform. However, two most widely used transforms, which would also be used in this thesis, are the *Fourier transform* and the *Hankel transform*.

If a function $h(t)$ is absolutely integrable in the interval $(-\infty, \infty)$ i.e. $\int_{-\infty}^{\infty} |h(t)| dt < \infty$, then its *Fourier transform* is defined as follows [63]

$$H(\omega) = \mathfrak{F}[h(t); \omega] = \int_{-\infty}^{\infty} h(t)e^{-j\omega t} dt \quad (2.45)$$

where t and ω may be referred to as time and frequency domains respectively. The domains t and ω are chosen arbitrarily and may be replaced by another pair of domains, e.g. d and k known as *distance* and *wavenumber* domains respectively. The only restriction is that the two domains should have dimensions opposite to each other. In many practical cases, it is also required to determine the function $h(t)$ when its transform $H(\omega)$ is known. This is called the *inverse Fourier transform* and is defined as follows

$$h(t) = \mathfrak{F}^{-1}[H(\omega); t] = \frac{1}{2\pi} \int_{-\infty}^{\infty} H(\omega)e^{j\omega t} d\omega \quad (2.46)$$

The inclusion of the constant factor $1/2\pi$ in (2.45) is arbitrary and it depends on the convention used in definition of the Fourier transform and its corresponding inverse. But once any particular convention is chosen, then it should be adhered to throughout the analysis. One very easy way to test the correctness of a particular definition of a Fourier transform pairs is by means of the following equation

$$h(t) = \mathfrak{S}^{-1} \{ \mathfrak{S} [h(t); \omega] ; t \} \quad \text{and} \quad H(\omega) = \mathfrak{S} \{ \mathfrak{S}^{-1} [H(\omega); t] ; \omega \} \quad (2.47)$$

The above equation means that for the correct definition of transform pairs, if we take the Fourier transform of any function $h(t)$ and afterwards take its inverse transform, then it should yield the original function. This statement also holds true for the function $H(\omega)$ except that the order of transform and its inverse should be interchanged. A physical process can be described either in *time domain* or in *frequency domain*, and hence $h(t)$ and $H(\omega)$ may be considered as two different representations of the same function. Equations (2.45) and (2.46) are generally applicable to continuous functions, i.e. when $h(t)$ is given as a continuous function in the time domain, then (2.45) can be used to transform this function into frequency domain or vice-versa. However, in many practical situations, the functions $h(t)$ (or $H(\omega)$) are sampled, i.e. their values are specified over a finite number of discrete intervals. Generally, the signals which are band-limited, can be sampled at fixed intervals of time and the complete signal can be reconstructed from these samples provided the sampling rate is at least twice the highest frequency component of the signal. It is worth mentioning here that the same concept can be applied for sampling time-limited frequency-domain signals, which generally forms the basis for taking inverse Fourier transform of discrete frequency-domain samples. Once the signals are sampled, then the formulas (2.45) and (2.46) are modified so that they are valid for discrete signals. Since in real situations, we can only have *finite* number of sampled values, hence the infinite limit integrals in (2.45) and (2.46) are replaced by a finite discrete sum [63]. In our proposed work, we carry out measurements of the reflection coefficient data at a number of points over a wide frequency-domain and use inverse discrete transform to convert these values into the real-space or virtual-time domain. We, therefore, formulate here the definition of discrete Fourier transform and its inverse from our perspective, in accordance with the theory given in many standard books such as [63].

Let us suppose that we have N consecutive sampled values of a frequency-domain function $H(\omega)$, which represent the measured values in a given frequency range, as follows

$$H_m \equiv H(2\pi f_m), \quad f_m \equiv m\Delta f, \quad m = 0, 1, 2, \dots, N-1 \quad (2.48)$$

Now, we can assume that these N number of inputs will not be able to produce more than N number of outputs and hence the function $h(t)$ can be estimated at N discrete values from N discrete values of $F(\omega)$ as follows

$$t_n \equiv \frac{n}{N\Delta f} \quad n = 0, 1, 2, \dots, N-1 \quad (2.49)$$

The next step is to substitute (2.48) and (2.49) in (2.46) and approximate the infinite integral by a finite discrete sum

$$\begin{aligned}
h(t_n) &\simeq \frac{1}{2\pi} \sum_{m=0}^{N-1} H_m e^{j2\pi t_n f_m} 2\pi \Delta f = \sum_{m=0}^{N-1} H_m e^{j2\pi \frac{n}{N\Delta f} m \Delta f} \Delta f \\
&= \Delta f \sum_{m=0}^{N-1} H_m e^{j2\pi \frac{mn}{N}} = \Delta f h_n
\end{aligned} \tag{2.50}$$

where the summation

$$h_n = \sum_{m=0}^{N-1} H_m e^{j2\pi \frac{mn}{N}} \tag{2.51}$$

is called the *inverse discrete Fourier transform*, which maps N complex numbers (the H_m 's) into another N complex numbers (the h_n 's) and does not depend on any dimensional parameter such as Δf . The corresponding *direct discrete Fourier transform* can be similarly derived after combining (2.48), (2.49), and (2.45) and is given by the following expression

$$H_m = \frac{1}{N} \sum_{n=0}^{N-1} h_n e^{-j2\pi \frac{mn}{N}} \tag{2.52}$$

which is of the same form as (2.51) except a change of sign in the exponential function and a constant factor $1/N$. Hence the routines for calculating discrete Fourier transform and its inverse are not much different from each other and they can always be interchanged with slight modifications. If we look closely at (2.50) and (2.51), then it is observed that to compute the DFT (discrete Fourier transform) of N points, N^2 complex multiplications are required, which is substantially high especially for higher N . However, in mid-1960s, Cooley and Tukey developed an algorithm that, under certain conditions, reduces the number of computations required to compute a DFT for N points from N^2 to $N \log_2 N$ [81]. This algorithm is known as the *fast Fourier transform (FFT)*, and today there are several variations of this algorithm, but they all are based on the same principle [80]. As a matter of fact, nowadays many standard packages such as MATLAB already have pre-built routines for calculating *FFT* and *IFFT*, hence one does not need to spend much time in writing the whole routine from scratch.

After Fourier transform, probably the another most popular transform is the *Hankel transform of order ν* , which is defined as follows

$$F(s) \equiv H_\nu[f(r)] \equiv \int_0^\infty f(r) r J_\nu(sr) dr \tag{2.53}$$

where, $f(r)$ is a function defined for $r \geq 0$ in the r -domain, $F(s)$ is the corresponding function in the s -domain, and $J_\nu(sr)$ is the Bessel function of the first type and of the order ν . The Hankel transform is quite useful when we are dealing with problems that show circular symmetry, and it is the natural transform to be used in cylindrical coordinate systems. The *inverse* transform corresponding to (2.53) is described by the following relationship

$$f(r) \equiv H_\nu^{-1}[F(s)] \equiv \int_0^\infty F(s) s J_\nu(sr) ds \tag{2.54}$$

As can be easily seen from (2.53) and (2.54), the Hankel transform and its inverse are quite symmetrical in nature. The most common cases of the Hankel transform generally correspond to $\nu = 0$ and $\nu = 1$. As a matter of fact, the Hankel transform of order $\nu = 0$ can be considered as the two-dimensional Fourier transform of a circularly symmetric function [80]. For discrete or sampled values of a function, we can define the discrete Hankel transforms in a way similar to that of discrete Fourier transforms defined earlier. However, for discrete values of functions, equations (2.53) and (2.54) can always be integrated numerically provided the number of points N is not very high and the time required for the operation is within reasonable limit.

Finally, it may be noted here that besides Fourier and Hankel transforms, many other types of kernels which satisfy certain conditions can also be chosen in (2.44) to formulate other transforms according to our convenience. As a matter of fact, the definition of integral transform as given by (2.44) can be made quite general so that it is applicable to many complicated functions, as will be shown in the later part of this thesis.

2.2 The inverse problem from the mathematical point of view

The inverse problem was defined in the previous chapter as the one, which mainly deals with finding the causes of a known consequence. It was also mentioned very briefly that under normal circumstances it is difficult to obtain a very stable and unique solution of an inverse problem. In this section, some mathematical implications of solving an inverse problem are discussed. We start the section with some common examples of inverse problems, which occur in mathematics and other branches of science and engineering.

In basic mathematics, the direct problem is generally the multiplication of given two numbers. The corresponding inverse problem may be to find a pair of factors of a given number. It is interesting to note that like many inverse problems, the factorization does not always seem to have a unique solution. As a matter of fact, the whole notion of prime numbers is introduced to impose uniqueness on the solution of this inverse problem. We can also explain the inverse problem with reference to an example associated with the electromagnetic scattering. Assume that the behavior of a field is described by a differential equation $Pu = f$, where f is a source and u is the measuring parameter. Now suppose that we are able to measure u outside M , where M is a region occupied by the medium. It is conventional in mathematics to consider the problem of finding u in the case when P and f are given and hence it is called the *direct* problem. With this convention in mind, the problem of determination of f (which is basically the source) from u may be regarded as the inverse problem, as it is exactly opposite to the one described previously. The mathematical models of many physical phenomenon are described as inverse problems and they always come paired with direct problems. We mainly discuss here the mathematical concepts associated with the electromagnetic scattering problem. However, these concepts are quite general and can be applied to other applications of inverse problems as well. Because of the non-conventional nature of inverse problems in mathematical terms, their solution is also sometimes uncertain and unstable.

Mathematically, the scattering problem can be considered as a mapping between two sets of functions [17]. One set of functions d form the elements of a data set D , which basically represents the scattered field (or some of its characteristics). The other set is represented by the object set O , which comprises of a set of functions o , describing properties of the inhomogeneous object or medium. The direct scattering problem consists of finding how the object set functions o are mapped to the data set functions d . The mapping F is basically an operator which acts on the elements $o \in O$ to produce an element of a data set $d \in D$ or $F : O \rightarrow D$. If the operator and properties of the medium are known, then the forward mapping from the object set to data set is represented in mathematical terms as follows

$$D = \{d : F(o) \rightarrow d\} \quad (2.55)$$

The above mathematical equation basically means that the set D is the collection of elements d such that the operator F maps o to d . The solution of an inverse problem involves finding the inverse mapping or inverse operator $F^{-1} : D \rightarrow O$ which constructs the object set from the data set. The inverse operator can thus be considered as one which reconstructs the properties of the object, and if the data set and this operator is known, then the object set can be defined as follows

$$O = \{o : F^{-1}(d) \rightarrow o\} \quad (2.56)$$

The above equation basically means that if the inverse operator and the data sets are known, then the object set can be reconstructed. The schematic diagram of both forward and inverse mappings, which are given by (2.55) and (2.56) respectively is shown below in Fig. 2.13. The complicated nature of inverse scattering problems

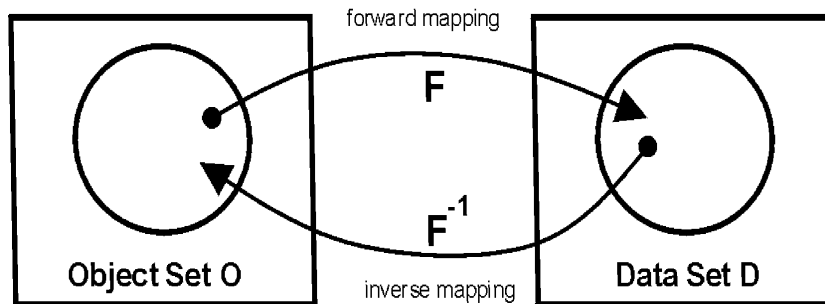


Figure 2.13: The forward and inverse scattering problems as mappings between two sets

can be better understood, if the above relationship between the mapping and the respective sets are related to the real scattering experiment. The object set O may be regarded as a collection of points, where each point corresponds to a particular value of the physical or electrical properties of the object. The data set D represents a collection of points in such a way that each point corresponds to a complete set of measured scattered field (or some of its characteristics) for a given object. This means that if we are measuring the scattering parameters in frequency domain, then each point of D represents a complete set of spectral domain scattering data corresponding to any given dielectric object. It is in this sense that one element of object set corresponds to a single element of the data set and vice-versa. The mapping itself can be considered to be a model representing the real scattering phenomenon

which is obtained from the wave propagation characteristics, and this information is usually expressed in the form of either a differential or an integral equation. The forward and inverse mapping between the object and data sets can be nonlinear in many cases. As a matter of fact, the inverse scattering process is a nonlinear process because of the multiple scattering phenomenon as discussed previously. For the inverse mapping case, one critical aspect is to study the effect of noise, as it becomes sometimes very difficult to avoid some error in the measured scattering data under practical situations. This noise consideration is important regarding stability of the inverse solution. The other two important aspects regarding the solution of an inverse problem are uniqueness and existence. It may be mentioned here that many inverse problems lead to a non-unique solution, because of the nonlinearity and complexity involved in the whole process of mapping as explained above. The concept of existence and uniqueness from the mathematical point of view was first studied well by Hadamard [82] when he was working on differential equations, and in this process he introduced the notion of *well-posed* and *ill-posed* problems. Hadamard postulated that a mathematical model for a physical problem has to be well-posed or properly posed in the sense that it had following three properties

1. There exists a solution of the problem (existence).
2. There is at most one solution of the problem (uniqueness).
3. The solution depends continuously on the data (stability).

The above definition means that any mathematical model, for which (*at least*) one of the above properties does not hold, is called *ill-posed* [83]. Mathematically, the existence of a solution requires that the inverse mapping should map elements from the data set to those elements which are proper members of the object set, and it can sometimes be enforced by enlarging the solution space. The inverse solution should be unique in the sense that one point in the data set D corresponds to a single point of the object set O . If a problem has more than one solution, then some information about the model may be missing and in this case, additional properties such as sign conditions can be built into the model. The requirement of stability is the most important one, as this factor is associated with the effect of noise on the overall reconstruction and a few percent of noise is almost unavoidable under practical measuring situations. A stable inversion is one in which an infinitesimally small change in the measured data gives rise to a correspondingly small change in the physical or electrical properties of the object. If the changes in the reconstructed properties of the object are large with even a small error in the measured scattering data, then the inversion is considered to be unstable. The concept of non-uniqueness, instability, and non-existence in an *ill-posed* problem is shown schematically in Fig. 2.14. As can be seen from this figure, the inversion of the data here does not always yield a unique point in the object set O (non-unique). The points, which are very close to each other in the data set, do not map to points close to each other in object set O (unstable). The inversion also sometimes maps data to points, which lie outside the legitimate object set O (nonexistent). So, it is obvious from the above discussion that it is very difficult or sometimes impossible to solve an ill-posed problem. For a long time, research on ill-posed problems was neglected since they were not considered relevant to the proper treatment of applied problems. However, many

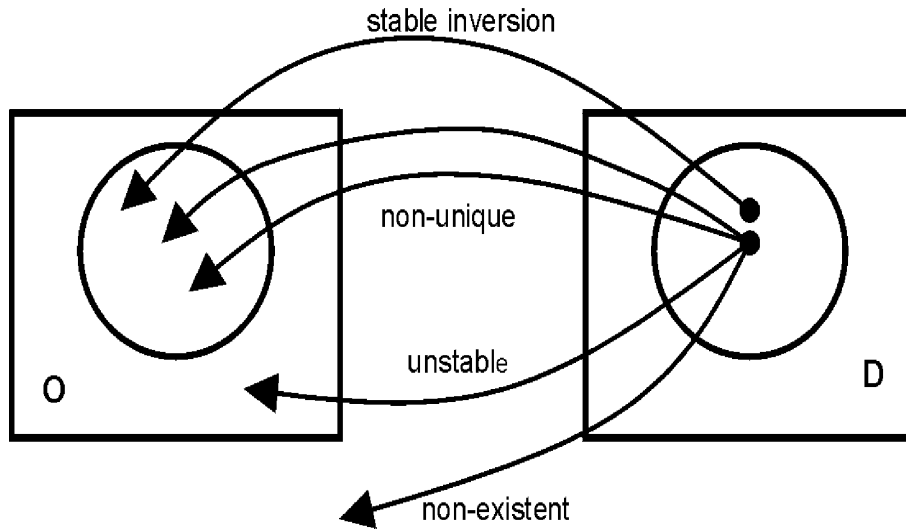


Figure 2.14: The concept of non-uniqueness, instability and non-existence in an ill-posed problem

inverse problems in the field of electromagnetic scattering and other relevant fields are ill-posed under some circumstances [84]. In this sense, there is a close linkage and interaction between research on inverse problems and ill-posed problems.

An ill-posed problem in the linear algebra is defined by a system of equations

$$Ax = y \tag{2.57}$$

where x and y are vectors and A is a matrix with a huge condition number [85]. This can be easily verified as follows. We assume that a unique solution exists for each y , i.e. A is an invertible matrix. Our aim is to know the relative change in the solution x with a small error in y . Suppose \tilde{y} is a perturbation of the right hand side y . The size of the perturbation relative to the size of y , measured in terms of a given norm $\|\cdot\|$, is $\|y - \tilde{y}\|/\|y\|$. Let x be the unique solution of the system corresponding to the right-hand side y , and let \tilde{x} be that corresponding to the right hand side \tilde{y} . Then

$$\|x - \tilde{x}\| = \|A^{-1}y - A^{-1}\tilde{y}\| \leq \|A^{-1}\| \|y - \tilde{y}\| \tag{2.58}$$

Hence the matrix norm $\|A^{-1}\|$ gives a bound for the change in the solution arising from a perturbation in the right-hand side. A relative measure of this change is obtained as follows

$$\|x - \tilde{x}\| \leq \|A^{-1}\| \|y\| \frac{\|y - \tilde{y}\|}{\|y\|} \leq \|A^{-1}\| \|A\| \|x\| \frac{\|y - \tilde{y}\|}{\|y\|} \tag{2.59}$$

From the above equation, we get

$$\frac{\|x - \tilde{x}\|}{\|x\|} \leq \text{cond}(A) \frac{\|y - \tilde{y}\|}{\|y\|} \tag{2.60}$$

Where $\text{cond}(A) = \|A\| \|A^{-1}\|$ is called the *condition number* of the matrix A (with respect to the norm $\|\cdot\|$). The condition number therefore gives an upper bound for the relative error in the solution caused by a given relative error in the right hand side.

For matrices with large condition numbers, i.e. *ill-conditioned* matrices, relatively small perturbations in the right hand side gives rise to relatively large changes in the solution. It is in this sense that ill-conditioned systems are said to be unstable. The solution of such ill-conditioned systems is particularly challenging as the data of the problem, which is represented on the right hand side of (2.57), invariably contains errors. Sometimes a severely ill-conditioned matrix can give very unpleasant effects even due to errors resulting from the representation of real numbers in a computer in floating-point form. In general terms it can be said that a set of equations of the form (2.57) is ill-conditioned when the matrix A is 'nearly singular'. An ill-posed problem is quite often ill-conditioned and neither a simple nor a complicated reformulation of the problem will improve the ill-conditioned problem significantly. In a strict mathematical setting we are not able to solve an ill-posed problem and get the correct solution. However, using *a priori* knowledge we are able to get an answer, that hopefully is close to the correct solution. The study of ill-posed solutions in a practical context has thus led to the development of techniques which incorporate constraints in the inversion or reconstruction operation which have some physical relevance to the problem being considered. These constraints are also referred to as *prior knowledge* because they consist of information which is independent of data set and therefore should be known *a priori*. A priori knowledge is quite useful as this information is used to confine the reconstruction to solutions which are considered acceptable or sensible. Typical prior knowledge about the object can include boundary conditions, smoothness conditions, positivity constraints or conformity to certain statistical distributions of the scattering parameters [84]. The inclusion of prior knowledge, which is shown in Fig. 2.15, helps in finding a stable solution in many cases and is also commonly termed as *regularization*. There are many regu-

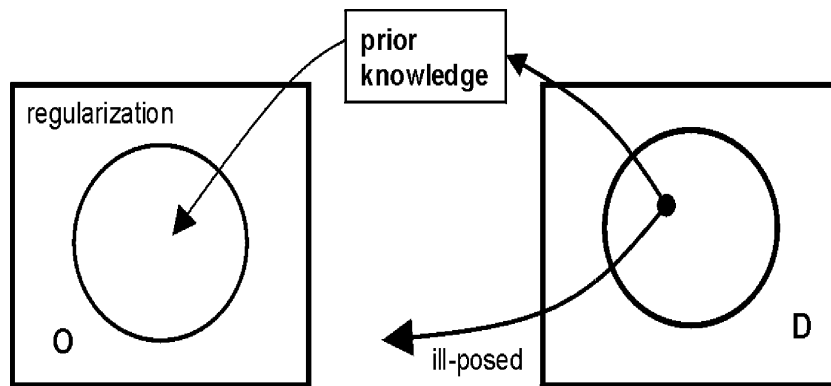


Figure 2.15: The effect of *prior knowledge* on the inversion

larization schemes available in literature [83] for solving operator equations of the form (2.57). Many of these schemes define a regularization parameter in one way or other in order to incorporate some prior information to obtain a stable solution. The regularization parameter helps in reformulating the error function corresponding to (2.57), which is then minimized to yield a stable inversion. There are many techniques presently available to determine the correct value of the regularization parameter for a given problem. The classical strategy, due to Morozov [86] e.g., determines the regularization parameter by solving numerically a nonlinear scalar equation. There are some iterative algorithms such as the Landweber's method [87],

and the conjugant gradient method [83] to solve linear (or nonlinear) equations numerically by making use of some regularization theory. One very common method for adding a regularization parameter is to assume the object function to be smooth, and thereby putting all the higher derivatives of this function equal to zero. The details about all these methods of regularization is beyond the scope of this thesis and can be found in many books such as [83]. However, it is worth mentioning here that the general regularization theory plays a very significant role in the solution of inverse problems, especially when the numerical approach is used.

2.3 The common methods for solving inverse scattering problems

It was mentioned in previous sections that the solution of inverse problems is generally a complicated process because of non-linearity and non-uniqueness associated with them. However, many methods exist today to solve these kinds of problems and the choice of a particular solution depends upon the particular application and on the availability of different resources. For example, linearized methods may be used for simple geometries, where we just need an approximate solution. For complicated geometries, we may turn to numerical methods, which require quite high amount of computational power but give reasonably accurate results. In this section, we briefly describe some of the most common methods used to solve inverse scattering problems.

2.3.1 The Born approximation

It was mentioned in the previous chapter that the total electric field \mathbf{E} can be written as a linear sum of incident field \mathbf{E}^{inc} and the scattered field \mathbf{E}^{scat} . When we seek scattered field solution of Maxwell's equations, then under certain conditions the difference between the incident and scattered fields may be assumed to be small compared with the incident field, i.e. $|\mathbf{E}^{inc} - \mathbf{E}^{scat}| \ll |\mathbf{E}^{inc}|$ and in this case the total field may be approximated by the incident field. This assumption is generally called the *Born approximation* and leads to *linearization* of the scattering interaction phenomenon. This approximation holds as long as the intrinsic parameters (e.g. permittivity, conductivity, permeability) of the scatterer are not much different from the surrounding medium, i.e., the intrinsic parameters are a small perturbation about the homogeneous surrounding medium. The solution of an inverse problem using the Born approximation has mainly become popular because of the ease of its implementation, its simple physical interpretation, and a simple linear relationship between the scattered field and the scattering object parameters. We derive here the basic formula of inversion using the Born approximation assuming that the medium is having a variation of its intrinsic property (permittivity) in one-dimension only (say, in the direction x).

Let us consider here the one-dimensional scalar Helmholtz equation, which gives a plane wave solution of the electromagnetic fields. The wave is assumed to be travelling in the direction x and a time-variation of $e^{j\omega t}$ is considered. If we consider any rectangular component Ψ of this wave, then it will satisfy the following second-order scalar wave equation [16]

$$\frac{d^2\Psi}{dx^2} + k_0^2\varepsilon_r(x)\Psi = 0 \quad (2.61)$$

where k_0 is the free-space wave number, and $\varepsilon_r(x)$ represents the variation of relative permittivity in the direction x . According to Born approximation, the permittivity $\varepsilon_r(x)$ is just a small perturbation about the background homogeneous relative permittivity ε_{rb} , i.e.

$$\varepsilon_r(x) = \varepsilon_{rb} + \Delta\varepsilon_r(x) \quad (2.62)$$

where $\Delta\varepsilon_r(x)$ is the variation of the relative permittivity of the scatterer about the ambient value and its value is zero outside the scatterer. Now, after combining (2.61) and (2.62), one obtains the following scalar wave equation in one-dimension

$$\frac{d^2\Psi}{dx^2} + k_b^2\Psi = -k_0^2\Delta\varepsilon_r(x)\Psi \quad (2.63)$$

where $k_b = k_0\sqrt{\varepsilon_{rb}}$ is the wave number of the background medium. Equation (2.63) is basically a one-dimensional non-homogeneous differential equation, whose homogeneous part describes the propagation of waves through the uniform medium and whose homogeneous solution is called the *incident field*, which is given by the following expression

$$\Psi^{inc} = e^{\pm jk_b x} \quad (2.64)$$

where the incident amplitude is normalized to unity, and the plus and minus signs represent plane waves travelling in left and right directions respectively. The total field is generally given by the sum of the incident field, and the scattered field which is the solution of the non-homogeneous part of (2.63). Equation of type (2.63) can be solved using the Green's function $g(x, x')$ method [88], which is defined as the solution of (2.63) after placing a point source at the point x' and is mathematically expressed as

$$\frac{d^2g(x, x')}{dx^2} + k_b^2g(x, x') = -\delta(x - x') \quad (2.65)$$

where $\delta(x - x')$ is the dirac delta function [63], which is very commonly used in the engineering analysis. This function is singular at $x = x'$, but has a distinct sampling property, i.e.,

$$\int_x f(x)\delta(x - x_0)dx = f(x_0) \quad (2.66)$$

The above property of the delta function can be exploited to express the asymptotic integral representation of the wave function in terms of the Green's function, i.e. the non-homogeneous solution of (2.63) will be given as

$$\Psi^{scat}(x) = k_0^2 \int_{x'} \Delta\varepsilon_r(x')\Psi(x')g(x, x')dx' \quad (2.67)$$

where the Ψ appearing inside the integral is the sum of the incident field and the scattered field in the presence of a scatterer. Now, the Fourier transform method can be used to solve (2.63) for the Green's function in k_0 domain to obtain the following expression [17]

$$G(k_0, x') = \int_{-\infty}^{\infty} g(x, x') e^{-jk_0 x} dx = \frac{e^{-jk_0 x'}}{k^2 - k_b^2} \quad (2.68)$$

where the delta function's property (2.66) is used in order to arrive at the above equation. We then take the inverse Fourier transform of (2.68) and use the residue property of integral to obtain an expression for $g(x, x')$ as follows

$$g(x, x') = \frac{j}{2k_b} e^{jk_b(x-x')} \quad (2.69)$$

where it is assumed that the scattered field is measured in the region $x < x'$. This expression can now be combined with (2.67) to represent the scattering field as

$$\Psi^{scat}(x) = \frac{jk_b}{2} e^{jk_b x} \int_{-\infty}^{\infty} \frac{\Delta \varepsilon_r(x')}{\varepsilon_{rb}} \Psi(x') e^{-jk_b x'} dx' \quad (2.70)$$

The above equation according to (2.64) represents a wave propagating towards the left and hence this expression gives the value of back-scattered reflection coefficient as follows

$$R(k_b) = \frac{jk_b}{2} \int_{-\infty}^{\infty} \frac{\Delta \varepsilon_r(x')}{\varepsilon_{rb}} \Psi(x') e^{-jk_b x'} dx' \quad (2.71)$$

As mentioned previously the Ψ inside the integral in (2.71) represents the total field, which is the sum of incident field and the scattered field. However, according to Born approximation the field inside the integral can be approximated by the incident field as given by (2.64) provided the scattering is weak and this gives rise to the following simple expression for the reflection coefficient

$$R(k_b) = \frac{jk_b}{2} \int_{-\infty}^{\infty} \frac{\Delta \varepsilon_r(x')}{\varepsilon_{rb}} e^{-j2k_b x'} dx' \quad (2.72)$$

If we define a new parameter $\zeta = 2k_b$, then (2.64) can be rewritten as

$$\frac{R(\zeta)}{j\zeta} = \frac{1}{4} \int_{-\infty}^{\infty} \frac{\Delta \varepsilon_r(x)}{\varepsilon_{rb}} e^{-j\zeta x} dx \quad (2.73)$$

It can be clearly seen from (2.73) that $R(\zeta)/j\zeta$ and $\frac{\Delta \varepsilon_r(x)}{\varepsilon_{rb}}$ form a Fourier-transform pair. Hence the unknown permittivity profile can be reconstructed by taking the inverse Fourier transform of (2.73) as follows

$$\frac{\Delta \varepsilon_r^{rec}(x)}{\varepsilon_{rb}} = \frac{2}{\pi} \int_{-\infty}^{\infty} \frac{R(\zeta)}{j\zeta} e^{j\zeta x} d\zeta \quad (2.74)$$

which is the expression for the reconstructed permittivity profile in terms of the measured reflection coefficient $R(\zeta)$ using the Born approximation. The main advantage of this inversion formula is that it can be written in closed form and only requires inverse Fourier transform of the measured reflection coefficient data. We can clearly observe from (2.73) and (2.74) that $\frac{\Delta \varepsilon_r}{\varepsilon_{rb}}$ is a linear function of the reflection coefficient and its vice-versa is also true. It may be mentioned again that this approximation for both forward and inverse problems are valid only for *weak* scattering objects, i.e. objects for which $\Delta \varepsilon_r / \varepsilon_{rb} \ll 1$, and $|R(\zeta)| \ll 1$. Hence, the Born approximation method cannot be used to obtain a very accurate *quantitative*

inversion of the permittivity profile unless the contrast between the surrounding medium and the scatterer is very small.

2.3.2 The distorted Born approximation

It was mentioned in the last sub-section that the Born approximation gives a very simple linear relationship between the measured scattering data and the reconstructed permittivity profiles. In the Born approximation, we generally take the first order approximation of the total field and hence it is applicable only for weak scattering objects, i.e. objects for which the permittivity is very close to that of the surrounding medium. In the distorted Born approximation method, which can also be called the second order Born approximation, we try to somewhat relax the criterion of having the permittivity very close to that of the surrounding medium. However, this method can only be applied when some *a priori* information about the scatterer is available. If we incorporate this prior knowledge of the scatterer in defining the total relative permittivity, then (2.62) will be modified as follows

$$\varepsilon_r(x) = \varepsilon_{rb} + \varepsilon_{rp}(x) + \Delta\varepsilon_r(x) \quad (2.75)$$

where $\varepsilon_{rp}(x)$ is the prior knowledge. Now, the value of $\varepsilon_r(x)$ as defined in (2.75) can be substituted in (2.61) to obtain

$$\frac{d^2\Psi}{dx^2} + k_0^2 [\varepsilon_{rb} + \varepsilon_{rp}(x)] \Psi = -k_0^2 \Delta\varepsilon_r(x) \Psi \quad (2.76)$$

The above equation can be solved using Green's function method as outlined in the last section, but the problem is that the Green's function is known only for few sets of profiles corresponding to $\varepsilon_{rp}(x)$. Another possibility is to simplify the overall problem and to consider the priori function as a constant, i.e., $\varepsilon_{rp}(x) = \text{constant}$, say the average of the *a priori* distribution, in which case the Green's function should satisfy the following equation

$$\frac{d^2 g_p(x, x')}{dx^2} + k_p^2 g_p(x, x') = -\delta(x - x') \quad (2.77)$$

where, $k_p^2 = k_0^2 [\varepsilon_{rb} + \varepsilon_{rp}]$ is the wave number taking into account both the background permittivity and *a priori* information. For this constant value of *a priori* information, (2.76) reduces to

$$\frac{d^2\Psi}{dx^2} + k_p^2 \Psi = -k_0^2 \Delta\varepsilon_r(x) \Psi \quad (2.78)$$

As seen clearly, (2.78) is of the same form as (2.63) and hence the method proposed in the previous section can be used to solve this equation to obtain

$$\Psi^{scat}(x) = k_0^2 \int_{-\infty}^{\infty} \Delta\varepsilon_r(x') \Psi(x') g_p(x, x') dx' \quad (2.79)$$

Now, for solution of the forward problem and the corresponding inverse problem, the field inside the integral in (2.79) is approximated by sum of the incident field and the scattered field due to a prior information, i.e.,

$$\Psi^{scat}(x) = k_0^2 \int_{-\infty}^{\infty} \Delta\varepsilon_r(x') \Psi^m(x') g_p(x, x') dx' \quad (2.80)$$

where,

$$\Psi^m(x) = \Psi^{inc} + \Psi_p^{scat} \quad (2.81)$$

and Ψ_p^{scat} is the field scattered from the inhomogeneity described by *a priori* distribution of permittivity ε_{rp} . If we compare (2.80) with (2.67), then we find that both equations have same mathematical form but the field inside the integral in (2.80) also includes the scattering information due to *a priori* knowledge apart from the incident field, whereas in (2.67) this field is simply replaced by the incident field for the forward and inverse solutions. It is mainly because of this slight difference in formulation as compared to the Born approach that the method described in this section is called the *distorted Born* approximation. The inverse solution of (2.80) cannot generally be written in closed form as both terms $\Psi^m(x')$ and $g_p(x, x')$ inside the integral of this equation depend on the prior knowledge. As we are not able to obtain a solution for the inverse problem in a closed form, so generally (2.80) may be used as a forward scattering theory and some iterative method may be used for its inversion. But then, there are many other methods which can give the direct problem formulation in a more accurate way for both weak and strong mediums, so it is not worthwhile to apply iterative techniques to this method. Hence, it can be concluded that the distorted Born method can be used only in some special cases of weak or *transparent* scattering objects, where we want an accuracy of one order more than the simple Born method.

2.3.3 Numerical methods

In previous sections, we described methods which can be used to solve inverse scattering problems in an approximate way. These methods generally do not account for multiple scattering of the electromagnetic field inside a scatterer and are generally applicable for dielectric objects of low contrast. However, in practice these kinds of weak scatterers are not very common, and hence the methods described earlier could be used only under some special circumstances. Generally some numerical methods either in frequency or in time domain are used to solve the inverse scattering problem in more exact way, and in most of the cases they are able to reconstruct the objects with high contrast and very high value of permittivity. But, these methods are computationally quite intense and are often associated with a non-uniqueness and uncertainty of the achieved solution. It may be mentioned here that even the distorted Born method described in the last section may be considered a numerical method, if some iterative algorithm is implemented using this scheme. But since under some conditions, the distorted Born method may give a closed-form solution hence we have not considered them under the category of numerical methods. However the point to be noted here is that it is very difficult to categorize each inverse scattering technique in a very precise way, and some overlapping between different inverse methods might always exist.

The numerical methods depend upon the accuracy of the formulation of direct problem apart from any particular method for inversion. The whole strategy for solving an inverse scattering problem using any numerical method is as follows.

First of all, we try to formulate the direct problem of scattering in the most accurate way. This *direct* or *forward* problem generally relates the parameters like the permittivity profile of the scattering object and the scattering field or the reflection coefficient data. We start with a particular estimate of the scattering object, which is generally considered to be *a priori* information and solve the direct problem using some numerical techniques. It may be mentioned here that nowadays many commercial electromagnetic field simulators are available, which can solve these *direct* problems up to any desired accuracy using a suitable numerical method. For example, CST Microwave studio [89] is a fully featured software for the electromagnetic analysis and design in the high frequency range. This software can be used to solve the direct problem of many types of structures for the dielectric layered media, and it can provide all the four *S*-parameters of these structures over a wide frequency band. The simulated values of the scattering field or the reflection coefficient data generated as a part of the direct problem solution are then compared with measured values. At this stage, a cost function is defined, which represents the difference between simulated and measured values of the reflection coefficient data. Sometimes, the definition of this cost function may include some additional information such as smoothness properties to reduce the uncertainty or ill-posedness of the achieved solution. The inclusion of this information is generally called the *regularization*, and is a widely used technique for the solution of inverse problems. After the proper definition of the cost function, the scattering object is refined in successive steps subject to minimization of this function at each iteration. The whole procedure is repeated unless the required accuracy is achieved. The accuracy of any numerical method for the solution of an inverse problem will mainly depend on the initial guess (*a priori* information), and on the accuracy of the measured data. If the initial guess is not quite far from the actual value and if we are able to carry out the measurement of reflection coefficient data quite accurately, then the reconstruction using numerical methods may be quite accurate. However, as mentioned earlier, numerical methods quite often give rise to a non-unique or unstable solution, which is mostly associated with the non-linearity of the corresponding inverse problem and is most prevalent when the measured data are inaccurate.

As mentioned earlier, the so called exact solution of the inverse scattering problem was first formulated by Gelfand and Levitan, while Marchenko also worked independently at the same time for the development of this method. Hence today this technique is collectively known as Gel'fand-Levitan-Marchenko (GLM) method and the first inverse scattering solution using this method was developed for the solution of Schrödinger equation of the quantum-wave mechanics. However, as the Helmholtz wave equation can in general be re-casted into a Schrödinger equation through a series of transformations, hence the GLM method can, in principle, also be used to solve the electromagnetic inverse scattering problems. For example, we can rewrite the standard Helmholtz equation (2.63) in the following form

$$\frac{d^2\Psi}{dx^2} + k_0^2 (\varepsilon_{rb} + \Delta\varepsilon_r(x)) \Psi = 0 \quad (2.82)$$

Now, if we transform the independent variable x into an optical depth via the Liouville transformation [17]

$$s(x) = \sqrt{\varepsilon_{rb}} \int_{-\infty}^x \left[1 + \frac{\Delta\varepsilon_r(x')}{\varepsilon_{rb}} \right]^{1/2} dx' = \sqrt{\varepsilon_{rb}} \int_{-\infty}^x h(x') dx' \quad (2.83)$$

then (2.82) can be written into this variable s as

$$\frac{d^2\Psi}{ds^2} + \frac{d \ln h}{ds} \frac{d\Psi}{ds} + k_0^2 \Psi = 0 \quad (2.84)$$

In the next step, a new dependent variable is introduced

$$w = \sqrt{h(s)} \psi \quad (2.85)$$

which transforms the original Helmholtz equation into the following Schrödinger equation

$$\frac{d^2w}{ds^2} + (k_0^2 - V(s)) w = 0 \quad (2.86)$$

where $V(s)$ is called the potential function, and is defined as [17]

$$V(s) = \frac{1}{2} \frac{d^2 \ln h}{ds^2} + \frac{1}{4} \left(\frac{d \ln h}{ds} \right)^2 \quad (2.87)$$

Once the basic Helmholtz equation is transformed into the Schrödinger equation given by (2.86), the standard procedure of the *GLM* technique can be used for its solution [17]. The method generally consists of dividing the solution into two parts, one when the scattering potential function is zero and the other when it is non-zero. Let us suppose that the solution corresponding to zero potential of (2.86) is denoted by $w_0(s, k)$. Then the general solution of (2.86) is given by [17]

$$w(s, k) = w_0(s, k) + \int_{-s}^s w_0(y, k) K(s, y) dy \quad (2.88)$$

The above equation is the starting point of the *GLM* analysis. As obvious from this equation, the solutions corresponding to zero and non-zero parts are related linearly by means of an *auxiliary* or *kernel* function $K(s, y)$. The solution corresponding to zero part $w_0(s, k)$ is generally a well-known standard function, so the main task is to calculate the auxiliary function $K(s, y)$. But the problem is that this auxiliary function can be uniquely computed only for certain class of the reflection coefficient functions. The unknown potential is obtained after differentiating this auxiliary function, i.e.,

$$V(s) = 2 \frac{dK(s, s)}{ds} \quad (2.89)$$

which is basically the solution of (2.86). So one of the major criterion for the selection of the auxiliary function is that it should be differentiable. It can be seen from above that once we have obtained the auxiliary function in closed form and if it is differentiable, then the solution of Schrödinger equation (2.86) can be obtained using (2.88) and (2.89). But the problem here is to find the unknown permittivity function as it is related to the equivalent potential function $V(s)$ by a non-linear differential equation as observed from (2.83) and (2.87). Hence even if the *GLM* method gives a unique solution for the quantum mechanics problem, it might

not do so for the electromagnetic case because of the presence of this non-linear differential equation. Another problem with the *GLM* method is that because of the differentiation operation of the auxiliary function, imprecise or inaccurate values of the scattered data may lead to quite inaccurate results. There are some methods such as that proposed by Balanis [34], which try to avoid this differentiation operation. However, these *GLM* type methods do not generally give a solution in the closed form except for some special class of reflection coefficients [17], and hence one is finally forced to look for some iterative numerical methods for a more general solution. But then, for the iterative scheme, we do not have to use the complicated *GLM* method as any standard electromagnetic field simulator can be used for this purpose as mentioned earlier.

2.3.4 The Riccati-equation approach

The Riccati-equation takes its name from the mathematician Riccati, who approximated the first order non-linear differential equation to the second degree, i.e., for the approximation of any function $f(x, y)$

$$\frac{dy}{dx} = f(x, y) \equiv P(x) + Q(x)y + R(x)y^2 + \dots \quad (2.90)$$

he took the nonlinear term y^2 into account. The differential equations of the form (2.90) are called Riccati equations, and they do not have any general solution as they do not fall under the category of any of the classical linear equations. The exact nonlinear Riccati equation to analyze the inhomogeneity of one-dimensional planar structure in terms of the normalized characteristic impedance and the reflection coefficient has already been derived in Section 3.18 of this thesis and is given by (2.43). For a lossless TEM structure, we can assume that the variation in the normalized impedance $\bar{Z}(x)$ is mainly due to an axially varying permittivity profile $\varepsilon_r(x)$ and if this is the case, then the normalized impedance of (2.37) can be expressed as

$$\bar{Z}(x) = \frac{1}{\sqrt{\varepsilon_r(x)}} \quad (2.91)$$

In the actual situation, the phase factor β in (2.43) will also depend linearly on the permittivity profile $\varepsilon_r(x)$. But in the very early stages, β was simply taken to be a constant and the equation (2.43) was linearized after ignoring the Γ^2 term to make it a simple linear equation in terms of $\varepsilon_r(x)$ (after using (2.91)) and the frequency-dependent reflection coefficient Γ . This equation was then inverted to obtain the permittivity profile of inhomogeneous transmission lines in terms of the Fourier transform of the frequency domain reflection coefficient data. But this inversion was valid only for very low-contrast dielectric structures¹ because of ignoring the two factors; i) axial dependence of β , and ii) the Γ^2 term. In the second stage, it was tried to take the $\varepsilon_r(x)$ -dependence of the phase factor β , but the corresponding differential equation was still considered to be linear. This new formulation helped in obtaining the permittivity profiles of somewhat higher contrast, but still the

¹this assumption can in fact be considered as similar to the Born approximation discussed earlier.

dielectric objects of high values of permittivity could not be reconstructed and also the method did not work if the variation in the permittivity was very large.

After few years, the "Renormalization technique" was introduced by some researchers to tackle the nonlinearity of this differential equation in a different way. The overall idea of using this renormalization technique was two fold: the first step involved the coordinate transformation so as to recast the wave equation in terms of an independent variable which effectively accounts for the change in wavelength of the radiation as it passes through the scatterer²; the second step involved solving the linear differential equation, but in terms of an inverse hyperbolic tangent of the reflection coefficient function rather than in terms of the simple reflection coefficient itself. The overall process is called the renormalization because the formula for the reconstruction sums up the series, of which only the first two terms are obtained if the above mentioned steps were not taken into account [59].

In this thesis, we have extended the whole concept of renormalization techniques to solve the one-dimensional non-linear Riccati differential equation in a flexible way. The main idea is to solve the corresponding linear differential equation in terms of an arbitrary function of the reflection coefficient rather than solving it in terms of the reflection coefficient or its inverse hyperbolic tangent function. The exact form of this arbitrary function is determined and optimized by means of an algebraic nonlinear transformation. With the help of our method, the accuracy of the imaging can be increased by simply changing the form of the algebraic transformation. We have also applied this Riccati-equation approach to cylindrical and spherical geometries, which helps to reconstruct the one-dimensional radially-dependent permittivity profiles of those dielectric objects whose boundary coincides with these non-planar coordinate systems.

²For very weak scatterer this variable will be same as the real space variable, but in the case of strong scattering object there will be a big difference.

Chapter 3

The Direct Problem Formulation

It has been mentioned in the last two chapters that the reconstruction of permittivity profiles is basically an inverse scattering process, and that for the solution of an inverse problem, first the corresponding direct problem has to be formulated. It was also briefly described that the accuracy of an inverse problem solution in many cases depends on the validity of the corresponding direct problem formulation. Hence the direct problem formulation plays a very crucial role in the solution of an inverse scattering problem. This chapter deals with the formulation of the direct problem in detail for planar, cylindrical and spherical coordinate systems.

3.1 The planar geometry

First of all, we consider an inhomogeneous half-space medium in a planar coordinate system as shown in Fig. 3.1. The inhomogeneity is considered only in one dimension, i.e. the relative permittivity $\varepsilon_r(x)$ varies only in the direction x in the region $x \geq 0$ starting from ε_{r0} at $x = 0$. It is assumed that the relative permittivity of the background medium is same as that of free space i.e. $\varepsilon_r(x) = 1$ for $x < 0$, and hence there will be a discontinuity at the interface $x = 0$. This lossless one-dimensional medium can equally represent the filling of a transmission line or a waveguide. We will consider here all the cases of illuminations viz. TEM, TE and TM.

3.1.1 TEM illumination

For this case, we assume that a monochromatic plane wave of wave number k_0 is incident normally from the Left hand side at the interface $x = 0$ as shown in Fig. 3.1. Since in real situations we can not have any access to the region $x > 0$ for the measurement, so we formulate the problem in such a way that the reflection coefficient Γ is measured at the point $x = 0$. The inhomogeneous medium shown in Fig. 3.1 can also be approximated by a number of homogeneous regions each of length Δx as shown in Fig. 3.2 provided the number of sections N is quite large, and Δx is sufficiently small so that the permittivity can be considered to be constant in each small region. This approximation is similar to that which was used in the previous chapter to find multiple reflections from inhomogeneous transmission lines. The direct problem is formulated here both for continuous and discontinuous media. For continuous media, the permittivity changes continuously over the region and the formulation is in the form of a nonlinear differential equation relating a very small

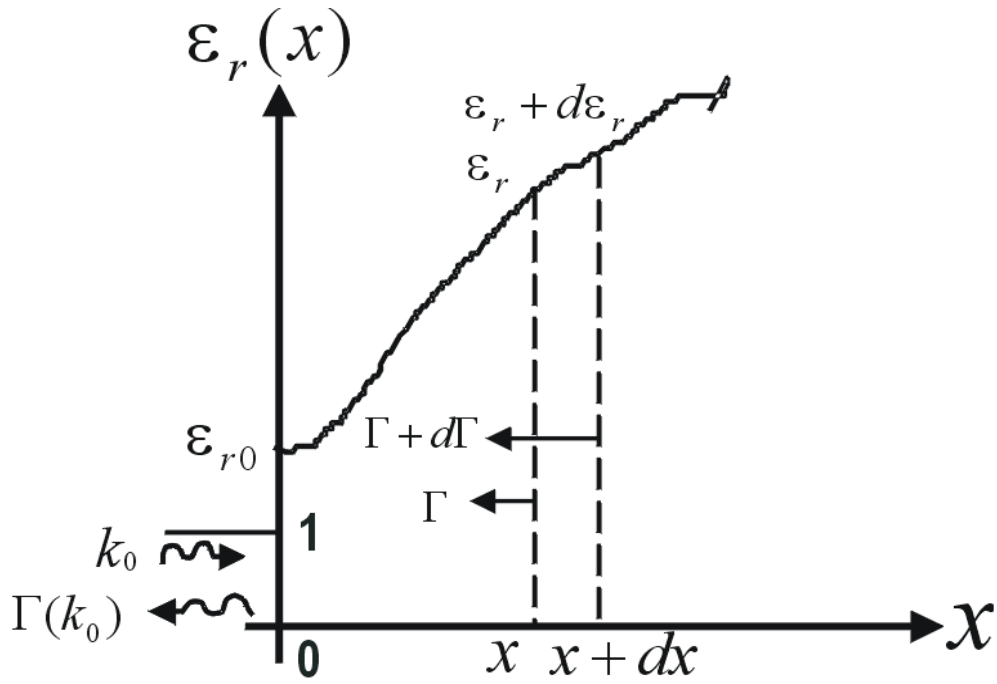


Figure 3.1: The half-space inhomogeneous media

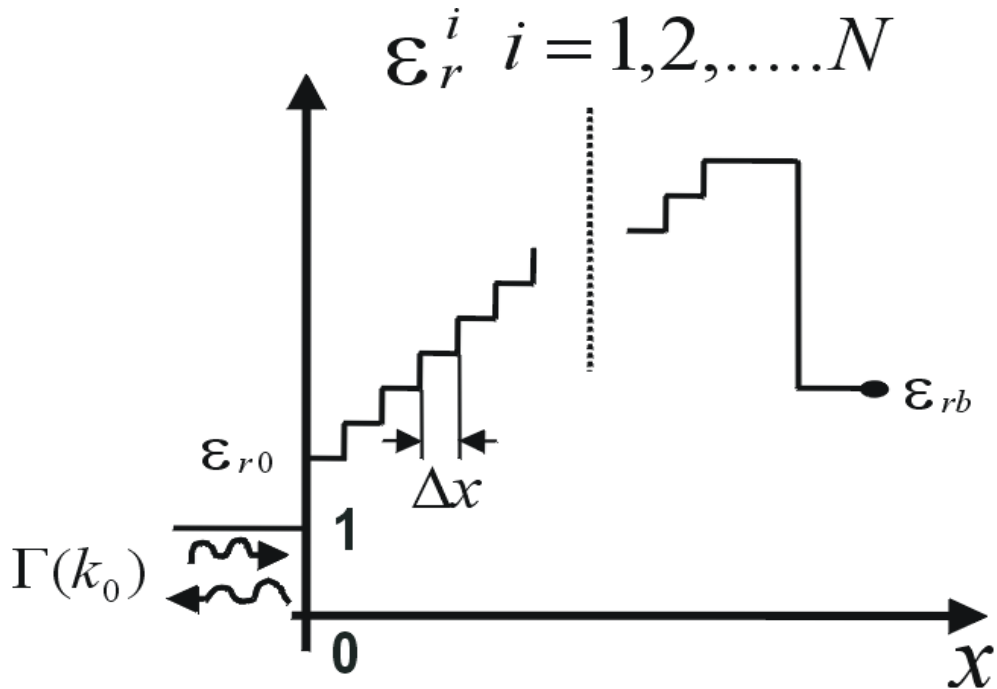


Figure 3.2: The half-space inhomogeneous media approximated by a number of homogeneous layers

change in the permittivity profile to a differential change in the reflection coefficient data. For discontinuous media, the permittivity is assumed to consist of a number of layers and the direct problem formulation is based on the transmission matrix formulation for each layer and then multiplying all these matrices together to obtain the reflection coefficient of the combined structure.

3.1.1.1 The discontinuous structure

For the direct problem formulation of discontinuous structures, we consider the N -layered inhomogeneous media as shown in Fig. 3.2. This N -layered inhomogeneous media can be replaced by $N + 1$ cascaded sections¹ as shown in Fig. 3.3, where each section represents a junction between two layers of different permittivities and a transmission line of length Δx . We assume that each layer i is characterized by a distinct value of relative permittivity ϵ_r^i , and the value of the relative permittivity at the two ends are given by their surface values i.e. $\epsilon_r^1 = \epsilon_{r0}$ and $\epsilon_r^{N+1} = \epsilon_{rb}$ as shown in Fig. 3.2. We also assume that the relative permittivity of the background is same as that of the free space i.e. $\epsilon_r^0 = 1$ at $x = 0$. Our aim here is to calculate

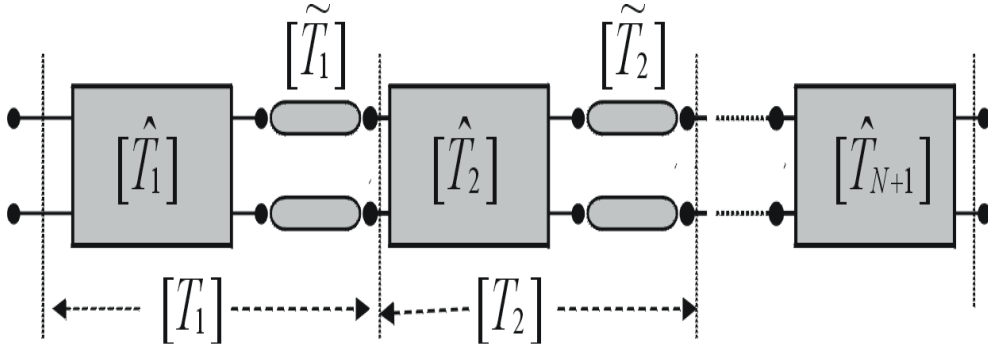


Figure 3.3: The discontinuous media represented by $N+1$ cascaded sections

the scattering parameters or the reflection coefficient of combined sections at the reference position $x = 0$. For this purpose, we represent each layer by a T -matrix, which basically describes all the parameters of input port in terms of the parameters of the output port. The main advantage of this kind of representation is that the $[T]$ matrix of a number of cascaded sections can simply be determined by multiplying the matrices of the individual sections altogether [79]. If we consider any i^{th} section, then its T -matrix is given by [79]

$$[T^i] = [\hat{T}^i] [\tilde{T}^i] = \begin{bmatrix} \hat{T}_{11}^i & \hat{T}_{12}^i \\ \hat{T}_{21}^i & \hat{T}_{22}^i \end{bmatrix} \begin{bmatrix} e^{j\theta^i} & 0 \\ 0 & e^{-j\theta^i} \end{bmatrix} \quad (3.1)$$

where $[\hat{T}^i]$, $i = 1, 2, \dots, N + 1$ is the T matrix of the junction between $(i - 1)^{th}$ and i^{th} layers having permittivities as ϵ_r^{i-1} and ϵ_r^i respectively, and $[\tilde{T}^i]$, $i = 1, 2, \dots, N$ is the T matrix of the i^{th} transmission line of electrical length θ^i , which is given by

$$\theta^i = k_0 \Delta x \sqrt{\epsilon_r^i} \quad (3.2)$$

with k_0 being the free space wave number. For the last section i.e. for $i = N + 1$, $[T^i] = [\hat{T}^i]$ as this section is described only by a junction and there is no transmission line section. Our next task is to calculate the individual elements of the matrix $[\hat{T}^i]$, which basically represents a junction between two layers as shown in Fig. 3.4. The

¹The last $(N + 1)^{th}$ section consists of only a junction between N^{th} layer and the background permittivity ϵ_{rb} as shown in Fig. 3.2.

two layers having different permittivities can also be considered as two transmission lines having different normalized or characteristic impedances as these parameters are inter-related as follows

$$Z = \eta_0 \bar{Z} = \frac{\eta_0}{\sqrt{\epsilon_r}} \Rightarrow \bar{Z} = \frac{1}{\sqrt{\epsilon_r}} \quad (3.3)$$

where $\eta_0 = \omega \mu_0 / k_0 = \sqrt{\mu_0 / \epsilon_0} \simeq 377 \text{ ohms}$ is the intrinsic impedance of the free-space, and \bar{Z} represents the normalized value of the actual characteristic impedance Z . It may be mentioned here that the intrinsic impedance of a medium enters into wave transmission and reflection problems in the same manner as the characteristic impedance of transmission lines [16]. This equivalence of impedances is of great advantage to us because it helps in analyzing the complex inhomogeneous media using the concept of microwave transmission line theory, which is much more simpler than the conventional field theory approach. Meanwhile, the two-port equivalent circuit of the junction connecting two different layers can be drawn as shown in Fig. 3.5, where Z_1 and Z_2 are impedances of two lines connected together and $V_1(I_1)$ and $V_2(I_2)$ represent the voltages(currents) at port one and port two respectively. Now, as the two lines connected together in Fig.3.5 are having different characteristic

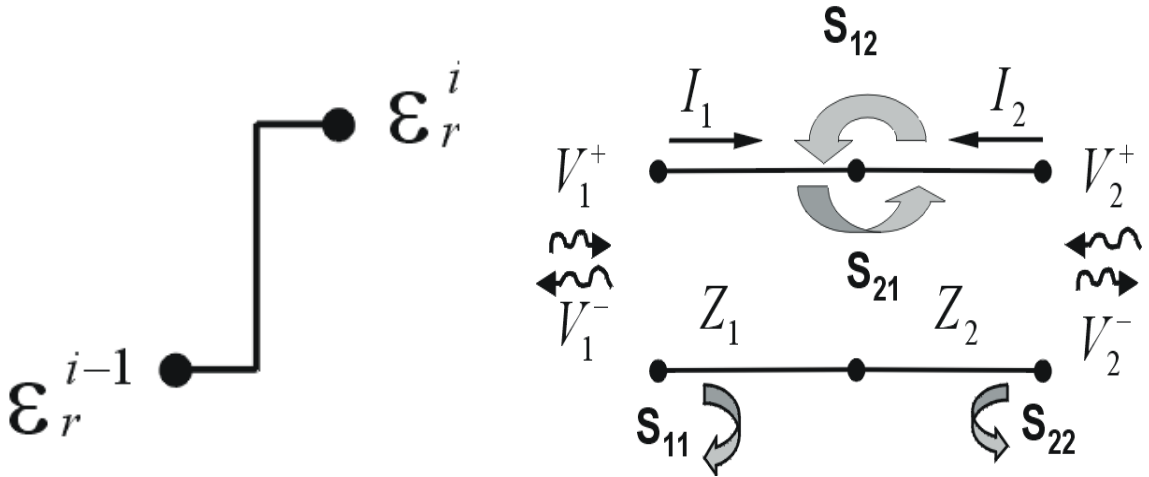


Figure 3.4: A junction between $(i-1)^{th}$ and i^{th} layers

Figure 3.5: The two-port equivalent circuit of a junction combining two lines having different characteristic impedances

impedances, hence we have to define normalized voltages as follows

$$\begin{aligned} \bar{V}_1^+ &= \frac{V_1^+}{\sqrt{Z_1}} & \bar{V}_1^- &= \frac{V_1^-}{\sqrt{Z_1}} \\ \bar{V}_2^+ &= \frac{V_2^+}{\sqrt{Z_2}} & \bar{V}_2^- &= \frac{V_2^-}{\sqrt{Z_2}} \end{aligned} \quad (3.4)$$

where the bar represents the normalized quantity and this normalization is done in order to make the power at each port directly proportional to square of the wave amplitude and not dependent upon the characteristic impedance of the line [58]. The scattering parameters of this two-port network will be given by

$$S_{11} = \left(\frac{\bar{V}_1^-}{\bar{V}_1^+} \right)_{\bar{V}_2^+=0} = \left(\frac{V_1^-}{V_1^+} \right)_{V_2^+=0} = \frac{\bar{Z}_2 - \bar{Z}_1}{\bar{Z}_2 + \bar{Z}_1} = \frac{\sqrt{\varepsilon_r^1} - \sqrt{\varepsilon_r^2}}{\sqrt{\varepsilon_r^1} + \sqrt{\varepsilon_r^2}} \quad (3.5a)$$

$$S_{22} = \left(\frac{\bar{V}_2^-}{\bar{V}_2^+} \right)_{\bar{V}_1^+=0} = \left(\frac{V_2^-}{V_2^+} \right)_{V_1^+=0} = \frac{\bar{Z}_1 - \bar{Z}_2}{\bar{Z}_1 + \bar{Z}_2} = \frac{\sqrt{\varepsilon_r^2} - \sqrt{\varepsilon_r^1}}{\sqrt{\varepsilon_r^1} + \sqrt{\varepsilon_r^2}} = -S_{11} \quad (3.5b)$$

$$\begin{aligned} S_{12} &= \left(\frac{\bar{V}_1^-}{\bar{V}_2^+} \right)_{\bar{V}_1^+=0} = \sqrt{\frac{\bar{Z}_2}{\bar{Z}_1}} \left(\frac{V_1^-}{V_2^+} \right)_{V_1^+=0} = \frac{2\sqrt{\bar{Z}_1\bar{Z}_2}}{\bar{Z}_2 + \bar{Z}_1} \\ &= \frac{2^4\sqrt{\varepsilon_r^1\varepsilon_r^2}}{\sqrt{\varepsilon_r^1} + \sqrt{\varepsilon_r^2}} = \sqrt{1 - (S_{11})^2} \end{aligned} \quad (3.5c)$$

$$\begin{aligned} S_{21} &= \left(\frac{\bar{V}_2^-}{\bar{V}_1^+} \right)_{\bar{V}_2^+=0} = \sqrt{\frac{\bar{Z}_1}{\bar{Z}_2}} \left(\frac{V_2^-}{V_1^+} \right)_{V_2^+=0} = \frac{2\sqrt{\bar{Z}_1\bar{Z}_2}}{\bar{Z}_2 + \bar{Z}_1} \\ &= \frac{2^4\sqrt{\varepsilon_r^1\varepsilon_r^2}}{\sqrt{\varepsilon_r^1} + \sqrt{\varepsilon_r^2}} = S_{12} \end{aligned} \quad (3.5d)$$

where we have made use of (3.3) to define the normalized impedance in terms of the relative permittivity. It may be noted from (3.5c) and (3.5d) that the normalization also helps in obtaining a *symmetrical* $[S]$ matrix, which is otherwise not possible if the voltages are not normalized. The other interesting point to be noted from (3.5) is that all the four S parameters of a junction, connecting two layers of different impedances or difference permittivities, can be defined in terms of S_{11} and phase of S_{22} . Hence the general $[S]$ matrix of a lossless junction combining two layers of difference impedances can be written as

$$[S] = \begin{bmatrix} S_{11} & S_{12} \\ S_{21} & S_{22} \end{bmatrix} = \begin{bmatrix} S_{11} & \sqrt{1 - S_{11}^2} \\ \sqrt{1 - S_{11}^2} & -S_{11} \end{bmatrix} \quad (3.6)$$

The elements of this $[S]$ matrix can be converted to $[T]$ matrix using the following relationship [79]

$$T_{11} = \frac{1}{S_{12}}, \quad T_{12} = -\frac{S_{22}}{S_{12}}, \quad T_{21} = \frac{S_{11}}{S_{12}}, \quad T_{22} = \frac{[S_{12}^2 - S_{11}S_{22}]}{S_{12}} \quad (3.7)$$

Equations (3.5) and (3.7) can be combined to obtain the $[\hat{T}]$ matrix of i^{th} junction shown in Fig. 3.3, which basically connects the $(i-1)^{th}$ and i^{th} layers having relative permittivities ε_r^{i-1} and ε_r^i respectively. The individual elements of this $[\hat{T}^i]$ matrix are given by

$$\hat{T}_{11}^i = \hat{T}_{22}^i = \frac{\sqrt{\varepsilon_r^{i-1}} + \sqrt{\varepsilon_r^i}}{2^4\sqrt{\varepsilon_r^{i-1}\varepsilon_r^i}}, \quad \hat{T}_{12}^i = \hat{T}_{21}^i = \frac{\sqrt{\varepsilon_r^{i-1}} - \sqrt{\varepsilon_r^i}}{2^4\sqrt{\varepsilon_r^{i-1}\varepsilon_r^i}} \quad (3.8)$$

The values given by (3.8) can be substituted in (3.1) to obtain the $[T_i]$ matrix of any individual i^{th} section of Fig. 3.3. The overall $[T]$ matrix of the inhomogeneous media is given by multiplying $[T_i]$ matrices of all the individual sections, i.e.,

$$[T] = \begin{bmatrix} T_{11} & T_{12} \\ T_{21} & T_{22} \end{bmatrix} = \prod_{i=1}^{N+1} [T_i] \quad (3.9)$$

Finally, the $[S]$ matrix of the discontinuous inhomogeneous media is given by

$$[S] = \begin{bmatrix} S_{11} & S_{12} \\ S_{21} & S_{22} \end{bmatrix} = \begin{bmatrix} T_{21}/T_{11} & (T_{11}T_{22} - T_{12}T_{21})/T_{11} \\ 1/T_{11} & -T_{12}/T_{11} \end{bmatrix} \quad (3.10)$$

where individual elements of the $[S]$ matrix are expressed in terms of the elements of (3.9), and the total frequency-dependent reflection coefficient $\Gamma(k_0, x)$ of the discontinuous inhomogeneous dielectric media measured at $(x = 0)$ is given by S_{11} , i.e., $\Gamma(k_0, 0) = S_{11}$.

3.1.1.2 The continuous media

The last sub-section (equations (3.1)- (3.10)) described the direct problem formulation for the discontinuous planar media. In this section, the direct problem is formulated for the planar *continuous* inhomogeneous media. It was briefly mentioned in the last sub-section that any continuous media can be replaced by a number of layers provided each layer is quite thin, and with this approximation Figs. 3.1 and 3.2 can be considered as equivalent to each other. Now, let us consider a small section of the continuous media between points x and $x + dx$, and assume that the total reflection coefficient at these two points are given by Γ and $\Gamma + d\Gamma$ respectively as shown in Fig. 3.1. The permittivity profile changes from $\varepsilon_r(x)$ at x , to $\varepsilon_r(x) + d\varepsilon_r(x)$ at $x + dx$, and this results into the change of normalized impedance from \bar{Z} to $\bar{Z} + d\bar{Z}$. This small section of length dx can be analyzed using the concept of microwave network theory as was done for the discontinuous case, and the equivalent circuit of this small section is given by a transmission line of electrical length $\sqrt{\varepsilon_r(x)}dx$ followed by a 2-port $[\partial S]$ matrix representing the junction between two layers of impedances \bar{Z} to $\bar{Z} + d\bar{Z}$ as shown in Fig. 3.6. To calculate the individual elements of $[\partial S]$ matrix,

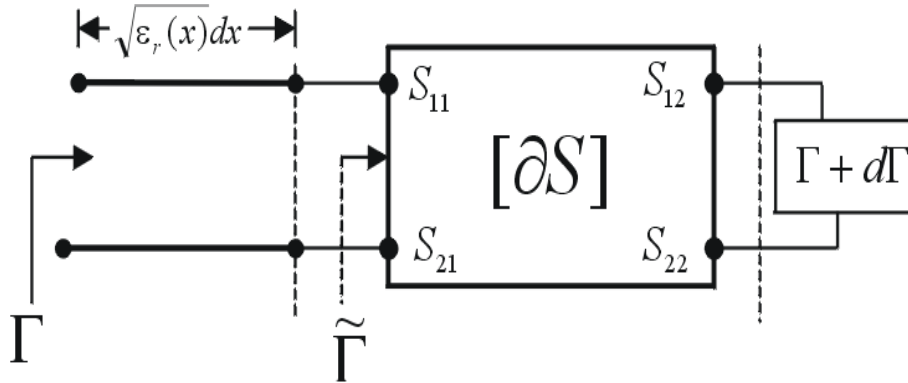


Figure 3.6: The equivalent circuit of a small section of an inhomogeneous medium

we recall from the previous chapter that an incremental change in the normalized impedance $d\bar{Z}$ at the junction will produce a local differential reflection coefficient $d\Gamma_l$ which is basically equal to S_{11} . But the normalized impedance is dependent on the permittivity profile as per equation (3.3), which can be used to obtain the expression for the local differential reflection coefficient in terms of the permittivity profile as follows

$$S_{11} = d\Gamma_l = \frac{\bar{Z} + d\bar{Z} - \bar{Z}}{\bar{Z} + d\bar{Z} + \bar{Z}} \simeq \frac{d\bar{Z}}{2\bar{Z}} = -\frac{\sqrt{\varepsilon_r(x)}}{2} \frac{d\varepsilon_r(x)}{2\varepsilon_r(x)\sqrt{\varepsilon_r(x)}} = -\frac{d\varepsilon_r(x)}{4\varepsilon_r(x)} \quad (3.11)$$

The above approximation holds good if the value of $d\bar{Z}$ is quite small so that all the higher order terms involving $d\bar{Z}$ such as $(d\bar{Z})^2, (d\bar{Z})^3, \dots$ can be neglected. The elements of $[\partial S]$ in Fig. 3.6 as per equation (3.6) in terms of $d\Gamma_l$ is given by

$$[\partial S] = \begin{bmatrix} d\Gamma_l & \sqrt{1 - d\Gamma_l^2} \\ \sqrt{1 - d\Gamma_l^2} & -d\Gamma_l \end{bmatrix} \quad (3.12)$$

where the value of the local differential reflection coefficient $d\Gamma_l$ is given by (3.11). Now, as observed in Fig. 3.6, the output port of the junction defined by $[\partial S]$ matrix is not matched rather it is terminated into an impedance characterized by a reflection coefficient $\Gamma + d\Gamma$. According to the microwave network theory [79], if a circuit or junction is not terminated into its characteristic impedance then this mismatching at the output port will also modify the input reflection coefficient. The actual expression for the input reflection coefficient of a circuit defined by $[S]$ matrix and terminated in a load impedance characterized by the reflection coefficient Γ_L is given by

$$\Gamma_i = S_{11} + \frac{S_{12}S_{21}\Gamma_L}{1 - S_{22}\Gamma_L} \quad (3.13)$$

For our case the $[S]$ matrix is defined by (3.12), the load reflection coefficient Γ_L is given by $\Gamma + d\Gamma$, and the input reflection coefficient is given by the intermediate parameter $\tilde{\Gamma}$ as seen in Fig. 3.6. These values may be substituted in (3.13) to obtain an expression for the intermediate reflection coefficient as

$$\tilde{\Gamma} = d\Gamma_l + \frac{[1 - d\Gamma_l^2](\Gamma + d\Gamma)}{1 + d\Gamma_l(\Gamma + d\Gamma)} \simeq d\Gamma_l + \frac{(\Gamma + d\Gamma)}{1 + \Gamma d\Gamma_l} \quad (3.14)$$

where the higher order infinitesimals such as $d\Gamma_l^2, d\Gamma d\Gamma_l, \dots$ are neglected. This intermediate parameter $\tilde{\Gamma}$ in Fig. 3.6 is separated by an electrical length of $\sqrt{\varepsilon_r(x)}dx$ from the reflection coefficient Γ , and hence $\tilde{\Gamma}$ may be thought of as Γ whose reference plane is shifted inward by this electrical length [58], i.e.,

$$\tilde{\Gamma} = \Gamma e^{2jk_0\sqrt{\varepsilon_r(x)}dx} \simeq \Gamma \left[1 + j2k_0\sqrt{\varepsilon_r(x)}dx \right] \quad (3.15)$$

where the second approximation on the right hand side is obtained by neglecting higher order terms involving dx such as dx^2, dx^3, \dots etc. In the next step, equations (3.14) and (3.15) are equated to obtain

$$\begin{aligned} \Gamma \left[1 + j2k_0\sqrt{\varepsilon_r(x)}dx \right] &= d\Gamma_l + \frac{(\Gamma + d\Gamma)}{1 + \Gamma d\Gamma_l} \\ \Rightarrow \Gamma(1 + \Gamma d\Gamma_l) \left[1 + j2k_0\sqrt{\varepsilon_r(x)}dx \right] &= d\Gamma_l(1 + \Gamma d\Gamma_l) + (\Gamma + d\Gamma) \\ \Rightarrow \Gamma(1 + \Gamma d\Gamma_l) \left[1 + j2k_0\sqrt{\varepsilon_r(x)}dx \right] &= d\Gamma_l(1 + \Gamma d\Gamma_l) + (\Gamma + d\Gamma) \\ \Rightarrow \Gamma + \Gamma^2 d\Gamma_l + (\Gamma + \Gamma^2 d\Gamma_l) \left(j2k_0\sqrt{\varepsilon_r(x)}dx \right) &= d\Gamma_l + \Gamma d\Gamma_l^2 + \Gamma + d\Gamma \end{aligned} \quad (3.16)$$

Now again we neglect the higher order infinitesimals such as $d\Gamma_l^2, d\Gamma_l dx, \dots$ as was done in the derivation of (3.14) and simplify the above equation to obtain

$$\begin{aligned} \Gamma^2 d\Gamma_l + \Gamma \left(j2k_0 \sqrt{\varepsilon_r(x)} dx \right) &= d\Gamma_l + d\Gamma \\ \Rightarrow \frac{d\Gamma}{dx} &= \Gamma j2k_0 \sqrt{\varepsilon_r(x)} - \frac{d\Gamma_l}{dx} (1 - \Gamma^2) \end{aligned} \quad (3.17)$$

The value of $d\Gamma_l$ can be substituted from (3.11) in (3.17) to obtain the following nonlinear Riccati differential equation for one-dimensional planar inhomogeneous media illuminated by a *TEM* plane wave

$$\frac{d\Gamma(k_0, x)}{dx} = \Gamma(k_0, x) j2k_0 \sqrt{\varepsilon_r(x)} + \frac{1}{4\varepsilon_r(x)} \frac{d\varepsilon_r(x)}{dx} [1 - \Gamma^2(k_0, x)] \quad (3.18)$$

where $\Gamma(k_0, x)$ is the frequency-dependent reflection coefficient, and $\varepsilon_r(x)$ represents the unknown one-dimensional permittivity profile of the dielectric media as shown in Fig. 3.1.

3.1.2 TE-mode illumination

For the *TEM* illumination, it was assumed that a monochromatic plane wave of wave number k_0 is incident *normally* at the air-dielectric interface as described in the previous section. Now, we consider a plane wave of wave number k_0 incident from the left hand side (LHS) at *an angle* θ on the air-dielectric interface at $x = 0$ as shown in Fig. 3.7. We will consider only the two cases here for these types of

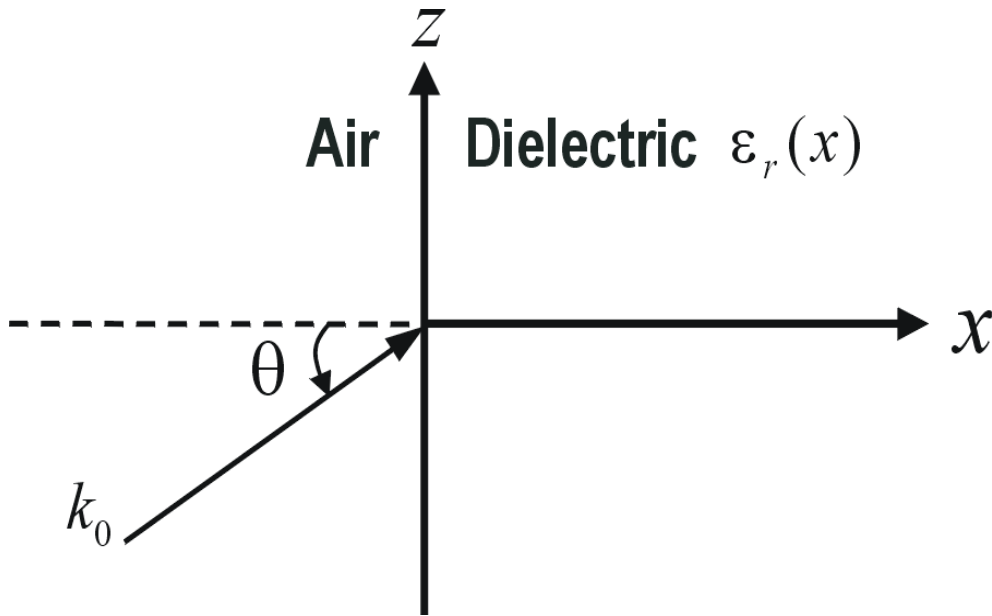


Figure 3.7: Reflection at the air-dielectric interface

inclined illuminations; i) when the electric field of the incident wave is parallel to the interface at $x = 0$ (*TE* case), and ii) when the magnetic field of the incident wave is assumed to be parallel to the interface at $x = 0$ (*TM* -case). A wave of any arbitrary polarization can be considered as a superposition of these two cases [16]. The *TE* case is considered in this section and the *TM* case will be considered in

the next section. For the continuity of tangential electric and magnetic fields over the entire air-dielectric interface in Fig. 3.7, the z variation of the fields in both air and dielectric media should be same, or in other words the z directed propagation constants should be same in air and dielectric, i.e.

$$\beta_z = k_0 \sin \theta \quad (3.19)$$

where β_z is the z directed propagation constant of the dielectric media. Using the above equation, the component of the propagation constant of the dielectric media in the direction of propagation is given by

$$\beta(x) = \sqrt{\beta^2 - \beta_z^2} = k_0 \sqrt{\varepsilon_r(x) - \sin^2 \theta} \quad (3.20)$$

where $\beta = k_0 \sqrt{\varepsilon_r(x)}$ is the *total* propagation constant in the dielectric media. Now for the *TE* case, the electric field of the incident wave is assumed to be parallel to the air-dielectric interface, i.e. there is no component of electric field in the direction of propagation ($E_x = 0$). If we solve Maxwell's equations for this *TE* mode illumination in the planar geometry, then the expression of the characteristic wave impedance² in the direction of propagation is given by [58]

$$Z(x) = \frac{E_y}{H_z} = \frac{\omega \mu_0}{\beta(x)} \quad (3.21)$$

where ω is the angular frequency, and a wave function of the form $e^{-j\beta(x)x}$ is considered for the propagating wave in the x direction. The value of $\beta(x)$ can be substituted from (3.20) into (3.21) to obtain the following expression for the normalized impedance in the dielectric media for a *TE* case

$$\bar{Z}(x) = \frac{Z(x)}{\eta_0} = \frac{\omega \mu_0}{k_0 \sqrt{\varepsilon_r(x) - \sin^2 \theta}} \frac{1}{\eta_0} = \frac{1}{\sqrt{\varepsilon_r(x) - \sin^2 \theta}} \quad (3.22)$$

The direct problem formulation for the discontinuous structure can be formulated on similar lines as was done for the *TEM* case. We will, however, concentrate here on the direct problem formulation for the continuous case which is quite important for the accurate solution of the corresponding inverse problem. For the *TE* illumination, a small section of the continuous dielectric media between points x and $x + dx$ of Fig. 3.1 can be described by a microwave equivalent circuit as shown in Fig. 3.6, which is similar to that of the *TEM* case. However, the electrical length of the small transmission line section in this case will be given by $\sqrt{\varepsilon_r(x) - \sin^2 \theta}$ as shown in Fig. 3.8. The local differential reflection coefficient $S_{11} = d\Gamma_l$ in Fig. 3.8 for the *TE* illumination is given by (3.11), and the value of \bar{Z} is substituted from (3.22), i.e.,

$$\begin{aligned} d\Gamma_l &\simeq \frac{d\bar{Z}}{2\bar{Z}} = -\frac{\sqrt{\varepsilon_r(x) - \sin^2 \theta}}{2} \frac{d\varepsilon_r(x)}{2 [\varepsilon_r(x) - \sin^2 \theta] \sqrt{\varepsilon_r(x) - \sin^2 \theta}} \\ &= -\frac{d\varepsilon_r(x)}{4 [\varepsilon_r(x) - \sin^2 \theta]} \end{aligned} \quad (3.23)$$

²This characteristic impedance of the mode plays the same role in reflection problems as does the characteristic impedance of transmission lines [16].

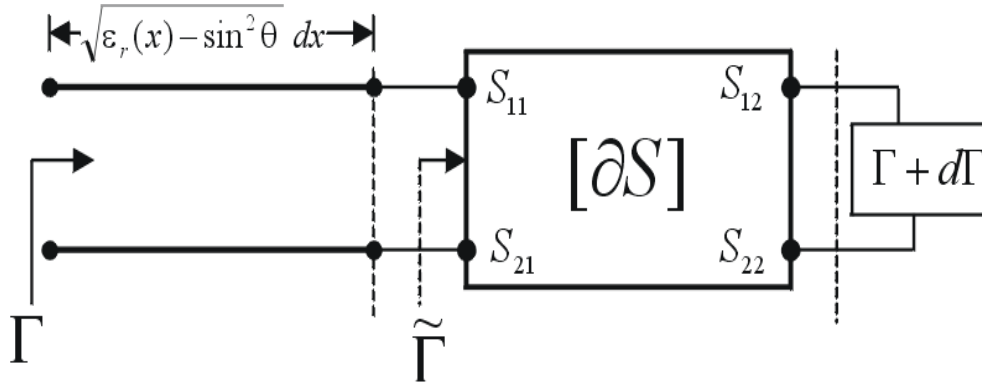


Figure 3.8: Equivalent circuit of a small section of an inhomogeneous medium for TE and TM polarizations

The other elements of ∂S in Fig. 3.8 are given by (3.12) after substituting the value of $d\Gamma_l$ from (3.23). The intermediate parameter $\tilde{\Gamma}$ in Fig. 3.8 is related to the reflection coefficient Γ by

$$\tilde{\Gamma} = \Gamma e^{2jk_0 \sqrt{\epsilon_r(x) - \sin^2 \theta} dx} \simeq \Gamma \left[1 + j2k_0 \sqrt{\epsilon_r(x) - \sin^2 \theta} dx \right] \quad (3.24)$$

where the exponential function is expanded into its Taylor's series and all the higher order terms involving dx are neglected. In the next step, equations (3.24) and (3.14) are combined to obtain the following differential equation in terms of the frequency-dependent reflection coefficient Γ , and the local differential reflection coefficient $d\Gamma_l$

$$\frac{d\Gamma}{dx} = \Gamma j2k_0 \sqrt{\epsilon_r(x) - \sin^2 \theta} - \frac{d\Gamma_l}{dx} [1 - \Gamma^2] \quad (3.25)$$

where again all the higher order infinitesimals are neglected as was done in the TEM case. Finally the value of $d\Gamma_l$ in the above equation is substituted from (3.23) to obtain

$$\begin{aligned} \frac{d\Gamma(k_0, x, \theta)}{dx} = & \Gamma(k_0, x, \theta) j2k_0 \sqrt{\epsilon_r(x) - \sin^2 \theta} \\ & + \frac{1}{4 [\epsilon_r(x) - \sin^2 \theta]} \frac{d\epsilon_r(x)}{dx} [1 - \Gamma^2(k_0, x, \theta)] \end{aligned} \quad (3.26)$$

which is basically the nonlinear Riccati differential equation for one-dimensional planar inhomogeneous media illuminated by a TE plane wave.

3.1.3 TM-mode illumination

The TM -illumination is quite similar to TE case discussed in the last section, where a plane wave of wave number k_0 is considered to be incident from the left hand side at an angle θ on the air-dielectric interface as shown in Fig. 3.7. The component of the propagation constant in the dielectric media along direction x are given by (3.20) for the same reason as explained in the last section. However, in the TM -illumination case, the *magnetic field* of the incident wave is assumed to be parallel to the air-dielectric interface, i.e. there is no component of magnetic field in the direction of

propagation ($H_x = 0$), which is contrary to the TE case where E_x was made equal to zero. If we solve Maxwell's equations for this TM mode illumination in the planar geometry, then the expression for the characteristic wave impedance for these modes in the direction of propagation is given by

$$Z(x) = \frac{E_y}{H_z} = \frac{\beta(x)}{\omega\varepsilon} \quad (3.27)$$

The value of $\beta(x)$ can be substituted from (3.20) into (3.27) to obtain the following expression for the normalized impedance in the dielectric media for the TM case

$$\bar{Z}(x) = \frac{Z(x)}{\eta_0} = \frac{\sqrt{\varepsilon_r(x) - \sin^2 \theta}}{\varepsilon_r(x)} \quad (3.28)$$

For the direct problem formulation in this case, a small section of the continuous dielectric media between points x and $x + dx$ of Fig. 3.1 can be described by a microwave equivalent circuit shown in Fig. 3.8. The electrical length in this case is same as in the TE case. However, the local differential reflection coefficient $S_{11} = d\Gamma_l$ in Fig. 3.8 is given by

$$\begin{aligned} d\Gamma_l &\simeq \frac{d\bar{Z}}{2\bar{Z}} = \frac{\varepsilon_r(x)}{2\sqrt{\varepsilon_r(x) - \sin^2 \theta}} \frac{2\sin^2 \theta - \varepsilon_r(x)}{2\sqrt{\varepsilon_r(x) - \sin^2 \theta} [\varepsilon_r(x)]^2} d\varepsilon_r(x) \\ &= -\frac{[\varepsilon_r(x) - 2\sin^2 \theta]}{4\varepsilon_r(x) [\varepsilon_r(x) - \sin^2 \theta]} d\varepsilon_r(x) \end{aligned} \quad (3.29)$$

where we have made use of (3.23) to express the value of $d\Gamma_l$ in terms of \bar{Z} , and (3.28) is used to substitute the value of \bar{Z} and $d\bar{Z}$. The other elements of ∂S in Fig. 3.8 for TM case are given by (3.12) after substituting the value of $d\Gamma_l$ from (3.29). The intermediate parameter $\tilde{\Gamma}$ in Fig. 3.8 can still be related to the reflection coefficient Γ by (3.24) and this will lead to the differential equation (3.25), wherein the value of $d\Gamma_l$ can be substituted from (3.29) to obtain the following differential equation in terms of frequency-dependent reflection coefficient

$$\begin{aligned} \frac{d\Gamma(k_0, x, \theta)}{dx} &= \Gamma(k_0, x, \theta) j2k_0 \sqrt{\varepsilon_r(x) - \sin^2 \theta} \\ &\quad + \frac{1}{4\varepsilon_r(x)} \frac{d\varepsilon_r(x)}{dx} \frac{[\varepsilon_r(x) - 2\sin^2 \theta]}{[\varepsilon_r(x) - \sin^2 \theta]} [1 - \Gamma^2(k_0, x, \theta)] \end{aligned} \quad (3.30)$$

which is the nonlinear Riccati differential equation for the one-dimensional planar inhomogeneous media illuminated by a TM plane wave. It may be noted here that both differential equations (3.26) and (3.30) corresponding to TE and TM cases reduce to (3.18) of the TEM case, when the angle $\theta = 0$. This seems quite obvious as when the angle θ in Fig. 3.7 is zero, then the situation is equivalent to that of the *normal* wave incidence on the air-dielectric interface.

3.2 The cylindrical geometry

The objects whose boundaries coincide with the cylindrical coordinate system can better be described by considering them in the cylindrical geometry rather than in the planar one. The formulation in the cylindrical coordinate system helps to obtain a better image of the dielectric object, if the antenna used for the transmission and reception are not highly directive. This is, in fact, a practical problem in the field of imaging and remote sensing, as it is very common for the available antenna to have less directivity along one of the lateral directions. If these types of antennas are used to obtain an image of dielectric objects having a curved boundary, then we may lose some detailed information of the object if the analysis is carried out in the Cartesian coordinate system. On the contrary, if we analyze these structures in the cylindrical coordinate system, then the one-dimensional curvature of the object can be locally accounted for and this will provide more accurate image of the object. Hence it can be said that formulation of the problem in the cylindrical coordinate system can compensate for less directivity of the antenna in one of the lateral directions, thus providing an accurate image of dielectric objects under these situations. We focus our attention here on the cylindrical dielectric objects described by the outer radius b , the inner radius ρ_0 , and a one-dimensional radially varying permittivity profile $\varepsilon_r(\rho)$ as shown in Fig. 3.9. The object is located between the conducting plates

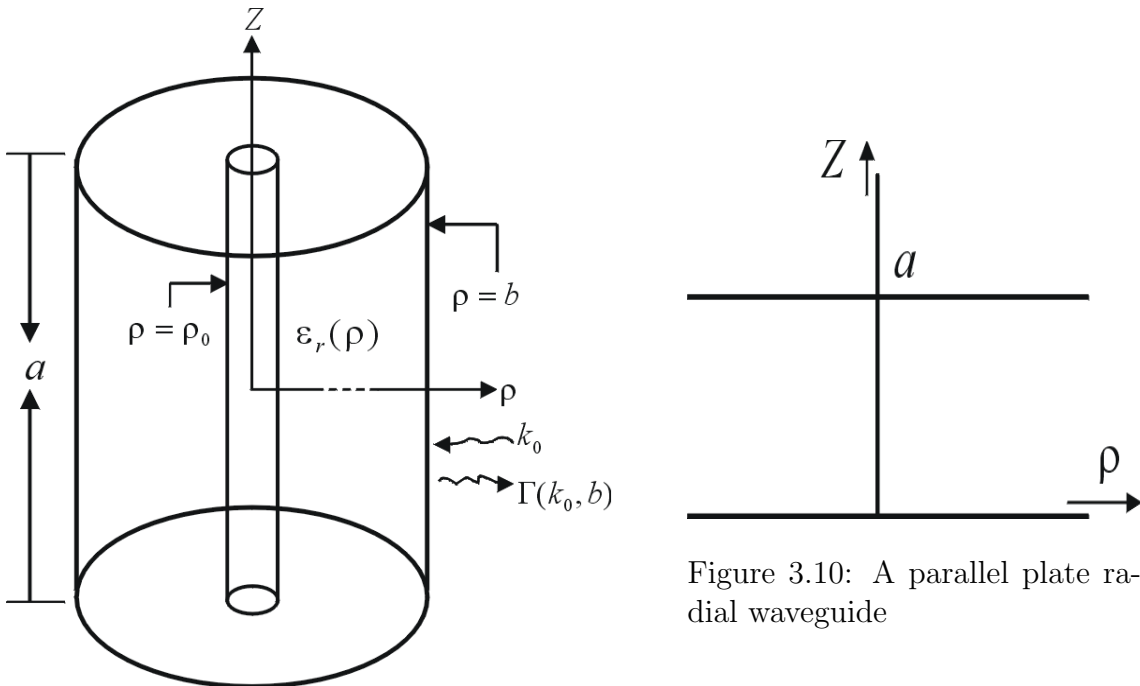


Figure 3.9: The cylindrical dielectric media

at $z = 0$ and $z = a$, and a monochromatic cylindrical wave of wave number k_0 is assumed to be incident from the outer free space ($\rho > b$). The reflection coefficient Γ is measured at outer boundary of the dielectric object i.e., at $\rho = b$. This accounts in fact to the case of outside illuminations of dielectric cylindrical objects and media as, e.g., in the investigation of trees and biological bodies where we do not have any access to inside regions and the only possibility is to measure at the outer boundary of the dielectric object. In the present analysis, the direct problem is formulated

in the cylindrical coordinate system for dielectric objects having one-dimensional inhomogeneity in the radial direction, and illuminated by different lower order and higher order TE and TM modes. It may be mentioned here that the direct problem formulation in the cylindrical coordinate system is quite complicated as compared to that derived in the planar geometry. The main reason for this complexity is the use of *Hankel* functions to express the radially directed travelling waves in the cylindrical geometry, whose properties are more involved than the simple *exponential* functions commonly used to express the travelling waves in the planar coordinate system. We start the whole analysis with the direct problem formulation for lower order illuminations where the equations are somewhat simpler, and later on generalize the overall formulation for any arbitrary order TE_{mn} and TM_{mn} cylindrical mode illuminations.

3.2.1 Radial transmission line approach

First of all, we consider the cylindrical dielectric object illuminated by a lowest order TM mode of wave number k_0 from the outer region ($\rho > b$). The lowest order possible mode in a cylindrical structure supporting radial waves (Fig. 3.10) is the TM_{00} mode. This mode is similar to the TEM mode in planar transmission lines as it does neither have electric field nor magnetic field component in the direction of propagation (radial direction) [16]. It means that for the propagation of waves in the radial direction as shown in Fig. 3.10, this mode can be considered as TEM to ρ and the classical transmission line theory can be used for the analysis in this case. The transmission line approach is clearly more simple and straightforward than the field theory approach, which is quite involved and cumbersome. The radial transmission line approach also helps in formulating the direct problem for layered or discontinuous cylindrical structures, which is in turn an aid to determine the value of permittivity at the air-dielectric interface, as will be shown in the next chapter. The reflection coefficient is measured at the outer radius of the cylindrical body at $\rho = b$, and the inward (towards the z axis) and outward travelling waves are considered as incident and reflected waves respectively.

The wave function for the TM_{00} mode satisfying appropriate boundary conditions for the radial parallel plate geometry shown in Fig. 3.10 is given by [16]

$$\Psi_{00}^{TM} = H_0^{(p)}(k\rho) \quad p = 1 \text{ or } 2 \quad (3.31)$$

where $H_0^{(1)}(k\rho)$ is the Hankel function of the first kind of order zero representing an inward travelling wave, $H_0^{(2)}(k\rho)$ is the Hankel function of the second kind of order zero representing an outward travelling wave, and

$$k = k_0 \sqrt{\varepsilon_r(\rho)} \quad (3.32)$$

is the total propagation constant in the radially varying cylindrical dielectric media. It may be noted from this equation that for the TM_{00} mode in the cylindrical dielectric media, the radial propagation constant is axially and azimuthally independent as there is no variation of the field in z and ϕ directions. The fields TM to z for this mode would be obtained by making the magnetic vector potential z -dependent, i.e.

$$\mathbf{A} = \mathbf{u}_z \Psi = \mathbf{u}_z A_z; \quad \frac{\partial A_z}{\partial z} = 0 \quad (3.33)$$

where Ψ is defined by (3.31). The magnetic field components corresponding to (3.33) for TM_{00} mode in the cylindrical coordinate system is computed from following equation [16]

$$\begin{aligned} \mathbf{H} &= \nabla \times \mathbf{A} \\ \Rightarrow H_\rho \mathbf{u}_\rho + H_\phi \mathbf{u}_\phi + H_z \mathbf{u}_z &= \frac{1}{\rho} \begin{vmatrix} \mathbf{u}_\rho & \rho \mathbf{u}_\phi & \mathbf{u}_z \\ \frac{\partial}{\partial \rho} & 0 & 0 \\ 0 & 0 & A_z \end{vmatrix} = -\mathbf{u}_\phi \frac{\partial \Psi}{\partial \rho} \end{aligned} \quad (3.34)$$

where \mathbf{u}_ρ , \mathbf{u}_ϕ , and \mathbf{u}_z are the unit vectors in ρ , ϕ , and z directions respectively, (3.33) is used to substitute the value of \mathbf{A} , and differentials $\partial/\partial z$, $\partial/\partial \phi$ are made equal to zero because there is no variation in z and ϕ directions for this lowest order mode. The above equation can be simplified to obtain following components

$$H_\rho^- = 0 \qquad H_\rho^+ = 0 \quad (3.35a)$$

$$H_\phi^- = -\frac{\partial \Psi}{\partial \rho} = kH_1^{(1)}(k\rho) \qquad H_\phi^+ = -\frac{\partial \Psi}{\partial \rho} = kH_1^{(2)}(k\rho) \quad (3.35b)$$

$$H_z^- = 0 \qquad H_z^+ = 0 \quad (3.35c)$$

where "−" and "+" superscripts represent inward and outward propagating waves respectively, and the following relationship is used to compute the derivative of Hankel function of order zero [90]

$$\frac{dH_0^{(p)}(z)}{dz} = -H_1^{(p)}(z) \quad p = 1 \text{ or } 2 \quad (3.36)$$

The electric field components for the TM_{00} mode can be computed after expanding one of the Maxwell's curl equations in cylindrical coordinate system and putting H_ρ , H_z components equal to zero as per (3.35), i.e.

$$\begin{aligned} \nabla \times \mathbf{H} &= j\omega\varepsilon\mathbf{E} \\ \Rightarrow \frac{1}{\rho} \begin{vmatrix} \mathbf{u}_\rho & \rho \mathbf{u}_\phi & \mathbf{u}_z \\ \frac{\partial}{\partial \rho} & 0 & 0 \\ 0 & \rho H_\phi & 0 \end{vmatrix} &= \mathbf{u}_z \frac{1}{\rho} \frac{\partial}{\partial \rho}(\rho H_\phi) = j\omega\varepsilon [E_\rho \mathbf{u}_\rho + E_\phi \mathbf{u}_\phi + E_z \mathbf{u}_z] \end{aligned} \quad (3.37)$$

where,

$$\varepsilon = \varepsilon_0 \varepsilon_r(\rho) \quad (3.38)$$

is the total permittivity of the cylindrical inhomogeneous medium. In the next step, different components of the electric field are obtained after substituting the value of H_ϕ from (3.35) in (3.37) to obtain

$$E_\rho^- = 0 \qquad E_\rho^+ = 0 \quad (3.39a)$$

$$E_\phi^- = 0 \qquad E_\phi^+ = 0 \quad (3.39b)$$

$$\begin{aligned}
E_z^- &= \frac{1}{j\omega\varepsilon\rho} \frac{\partial}{\partial\rho} [\rho H_\phi^-] = \frac{1}{j\omega\varepsilon\rho} \frac{\partial}{\partial\rho} [\rho k H_1^{(1)}(k\rho)] = \frac{k^2}{j\omega\varepsilon} H_0^{(1)}(k\rho) \\
E_z^+ &= \frac{1}{j\omega\varepsilon\rho} \frac{\partial}{\partial\rho} [\rho H_\phi^+] = \frac{1}{j\omega\varepsilon\rho} \frac{\partial}{\partial\rho} [\rho k H_1^{(2)}(k\rho)] = \frac{k^2}{j\omega\varepsilon} H_0^{(2)}(k\rho)
\end{aligned} \tag{3.39c}$$

where the following formula is used to compute the derivative of Hankel function of order one [90]

$$\frac{d}{dz} [z H_1^{(p)}(z)] = z H_0^{(p)}(z) \quad p = 1 \text{ or } 2 \tag{3.40}$$

It may be noted from (3.35) and (3.39) that although these equations represent a wave travelling in the ρ direction, but both E_ρ and H_ρ components are zero and hence this particular mode is also called *TEM* to ρ as mentioned earlier. It can also be seen from (3.35) and (3.39) that the only non-zero field components for this mode are E_z and H_ϕ , which for the *inward* travelling waves are given by

$$E_z^- = -j\omega\mu H_0^{(1)}(k\rho) \tag{3.41a}$$

$$H_\phi^- = k H_1^{(1)}(k\rho) \tag{3.41b}$$

Now, considering the *inward* travelling wave in Fig. 3.10, we can define a unique voltage between the plates and a net radially directed current on one of the plates at a given radius ρ

$$V(\rho)^- = a E_z^- = -j a \omega \mu H_0^{(1)}(k\rho) \tag{3.42a}$$

$$I(\rho)^- = 2\pi\rho H_\phi^- = 2\pi\rho k H_1^{(1)}(k\rho) \tag{3.42b}$$

where a is the extent of the cylindrical object in the direction z as shown in Fig. 3.10, and the expressions of the electric and magnetic fields as given by (3.41) are used. The total voltage and current will be obviously given by the sum of both inward and outward travelling waves. But before computing the total voltage and current in this case, let us try to find expressions for the voltage and current derivatives and their corresponding differential equations. Equations (3.42a) and (3.42b) can be differentiated to obtain

$$\frac{dV}{d\rho} = j a \omega \mu k H_1^{(1)}(k\rho) = j\omega \frac{\mu a}{2\pi\rho} I \tag{3.43a}$$

$$\frac{dI}{d\rho} = 2\pi k^2 \rho H_0^{(1)}(k\rho) = j\omega \frac{2\pi\varepsilon\rho}{a} V \tag{3.43b}$$

It may be noted here that in (3.43a) and (3.43b), we have dropped the “-” superscript because these equations are in general valid for both inward and outward travelling waves as well as for total waves. Equations (3.43a) and (3.43b) are quite similar in form as that of simple planar transmission line equations and hence they are called *radial transmission-line equations* [16]. Meanwhile, both of these equations can be differentiated again to separate V from I

$$\frac{d}{d\rho} \left(\rho \frac{dV}{d\rho} \right) = j\omega \frac{\mu a}{2\pi} \frac{dI}{d\rho} = -\omega^2 \mu \varepsilon \rho V \quad (3.44a)$$

$$\frac{d}{d\rho} \left(\frac{1}{\rho} \frac{dI}{d\rho} \right) = j\omega \frac{2\pi\varepsilon}{a} \frac{dV}{d\rho} = \frac{-\omega^2 \mu \varepsilon}{\rho} I \quad (3.44b)$$

where the values of first order derivatives are substituted from (3.43a) and (3.43b). These equations can be further simplified to obtain the second order differential equations in terms of V and I

$$\rho^2 \frac{d^2 V}{d\rho^2} + \rho \frac{dV}{d\rho} + (k\rho)^2 V = 0 \quad (3.45a)$$

$$\rho^2 \frac{d^2 (I/\rho)}{d\rho^2} + \rho \frac{d(I/\rho)}{d\rho} + [(k\rho)^2 - 1] (I/\rho) = 0 \quad (3.45b)$$

If we look carefully at above equations, then we can recognize that (3.45a) is a Bessel equation of order 0 for V , and (3.45b) is a Bessel equation of order 1 for I/ρ . The travelling wave solution of equations (3.45a) and (3.45b) can be written as

$$V(\rho) = V_0^- \frac{H_0^{(1)}(k\rho)}{H_0^{(1)}(kb)} + V_0^+ \frac{H_0^{(2)}(k\rho)}{H_0^{(2)}(kb)} \quad (3.46a)$$

$$I(\rho) = I_0^- \frac{\rho H_1^{(1)}(k\rho)}{b H_1^{(1)}(kb)} + I_0^+ \frac{\rho H_1^{(2)}(k\rho)}{b H_1^{(2)}(kb)} \quad (3.46b)$$

The above two equations represent the *total* voltage and current along a radial transmission line. At this point, it is quite interesting to compare the above two equations with the corresponding equations for the *planar* transmission lines. We have Hankel functions here instead of the exponential functions because the propagation along the radial direction in the cylindrical geometry is expressed in terms of these functions. The presence of a second Hankel function in the denominator of both equations can be explained by the fact that the reference position in this case is taken at the outer boundary $\rho = b$. In case of planar transmission lines, the reference position is generally taken at zero and since the value of the exponential function is unity for the zero argument, nothing appears in the denominator there. The correctness of (3.46a) and (3.46b) can also be tested by the fact that both of these equations satisfy their respective differential equations (3.45a) and (3.45b). Also in (3.46b) the distance ρ is normalized with respect to the outer radius b , so that amplitudes I_0^- and I_0^+ have dimensions of the current. To obtain the expression for the current in terms of the voltage, we combine (3.43a), (3.46a) and (3.46b) to obtain

$$\begin{aligned}
\frac{dV}{d\rho} &= \left(\frac{j\omega \mu a}{2\pi\rho} \right) I(\rho) = -k \left[V_0^- \frac{H_1^{(1)}(k\rho)}{H_0^{(1)}(kb)} + V_0^+ \frac{H_1^{(2)}(k\rho)}{H_0^{(2)}(kb)} \right] \\
\Rightarrow I(\rho) &= \left(\frac{-2\pi\rho k}{j\omega \mu a} \right) \left[V_0^- \frac{H_1^{(1)}(k\rho)}{H_0^{(1)}(kb)} + V_0^+ \frac{H_1^{(2)}(k\rho)}{H_0^{(2)}(kb)} \right] \\
&= \frac{j2\pi}{a} \sqrt{\frac{\varepsilon}{\mu}} \left[V_0^- \frac{bH_1^{(1)}(kb) \rho H_1^{(1)}(k\rho)}{H_0^{(1)}(kb) b H_1^{(1)}(kb)} + V_0^+ \frac{bH_1^{(2)}(kb) \rho H_1^{(2)}(k\rho)}{H_0^{(2)}(kb) b H_1^{(2)}(kb)} \right]
\end{aligned} \tag{3.47}$$

The above equation can be rewritten in the following form

$$I(\rho) = \frac{V_0^-}{Z_0^-} \frac{\rho H_1^{(1)}(k\rho)}{b H_1^{(1)}(kb)} - \frac{V_0^+}{Z_0^+} \frac{\rho H_1^{(2)}(k\rho)}{b H_1^{(2)}(kb)} \tag{3.48}$$

where,

$$Z_0^- = \frac{V_0^-}{I_0^-} = -\frac{j a}{2\pi b} \sqrt{\frac{\mu}{\varepsilon}} \frac{H_0^{(1)}(kb)}{H_1^{(1)}(kb)} \tag{3.49}$$

is the characteristic impedance of the line for the inward travelling waves, and

$$Z_0^+ = -\frac{V_0^+}{I_0^+} = \frac{j a}{2\pi b} \sqrt{\frac{\mu}{\varepsilon}} \frac{H_0^{(2)}(kb)}{H_1^{(2)}(kb)} \tag{3.50}$$

is the characteristic impedance of the line for the outward travelling waves. It may be noted from (3.49) and (3.50) that the characteristic impedance here depends on the reference position $\rho = b$ as well as on the direction of propagation and hence the radial waveguide geometry shown in Fig. 3.10 may be considered to be a *non-uniform* transmission line. Now, for considering the wave reflection in the radial transmission line case, we assume that a lossless radial transmission line is terminated in an arbitrary load impedance Z_L at the reference position $\rho = b$ as shown in Fig. 3.11. The total voltage and current at the load is related by the load

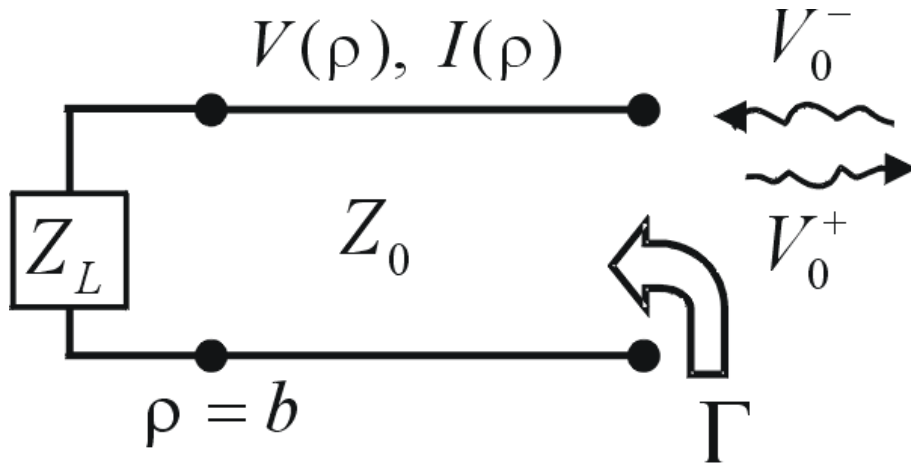


Figure 3.11: Reflection from the radial transmission line

impedance, so at $\rho = b$, we have

$$\begin{aligned}
Z_L &= \frac{V(b)}{I(b)} = \frac{V_0^- + V_0^+}{\frac{V_0^-}{Z_0^-} - \frac{V_0^+}{Z_0^+}} \\
&\Rightarrow \left[\frac{Z_L}{Z_0^-} - 1 \right] V_0^- = \left[\frac{Z_L}{Z_0^+} + 1 \right] V_0^+
\end{aligned} \tag{3.51}$$

where we have made use of (3.46a) and (3.48) to compute the values of $V(b)$ and $I(b)$. From the above equation, the total reflection coefficient Γ may be defined as

$$\Gamma = \frac{V_0^+}{V_0^-} = \frac{Z_0^+}{Z_0^-} \frac{Z_L - Z_0^-}{Z_L + Z_0^+} = \frac{1}{\alpha_r} \frac{Z_L - Z_0^-}{Z_L + Z_0^+} \tag{3.52}$$

where the factor α_r is given by

$$\alpha_r = \frac{Z_0^-}{Z_0^+} \tag{3.53}$$

In the meantime, equations (3.46a) and (3.48) may be rewritten in terms of the above defined factors Γ and α_r

$$V(\rho) = V_0^- \left[\frac{H_0^{(1)}(k\rho)}{H_0^{(1)}(kb)} + \Gamma \frac{H_0^{(2)}(k\rho)}{H_0^{(2)}(kb)} \right] \tag{3.54a}$$

$$I(\rho) = \frac{V_0^-}{Z_0^-} \left[\frac{\rho H_1^{(1)}(k\rho)}{b H_1^{(1)}(kb)} - \alpha_r \Gamma \frac{\rho H_1^{(2)}(k\rho)}{b H_1^{(2)}(kb)} \right] \tag{3.54b}$$

Equations (3.54a) and (3.54b) are the exact expressions for the total voltage and current on a radial transmission line with a reference surface defined at $\rho = b$. Now, to simplify the overall analysis, the Hankel functions in (3.49) and (3.50) can be replaced by their large argument asymptotic expressions as follows

$$\begin{aligned}
Z_0^- &= -\frac{j a}{2\pi b} \sqrt{\frac{\mu}{\varepsilon}} \frac{\sqrt{\frac{2}{j\pi kb}} e^{jkb}}{\sqrt{\frac{2}{j\pi kb}} \frac{1}{j} e^{jkb}} = \frac{a}{2\pi b} \sqrt{\frac{\mu}{\varepsilon}} \\
Z_0^+ &= \frac{j a}{2\pi b} \sqrt{\frac{\mu}{\varepsilon}} \frac{\sqrt{\frac{2j}{\pi kb}} e^{-jkb}}{\sqrt{\frac{2j}{\pi kb}} j e^{-jkb}} = \frac{a}{2\pi b} \sqrt{\frac{\mu}{\varepsilon}}
\end{aligned} \tag{3.55}$$

where following relationships are used for the *large argument approximation* of Hankel functions of order n [16]

$$\begin{aligned}
H_n^{(1)}(x) &\simeq \sqrt{\frac{2}{j\pi x}} j^{-n} e^{jx} \\
H_n^{(2)}(x) &\simeq \sqrt{\frac{2j}{\pi x}} j^n e^{-jx}
\end{aligned} \tag{3.56}$$

The approximations made in (3.55) hold true as long as we are not working very close to the origin. It may be also mentioned here that the Hankel functions are not

defined when their argument becomes zero and have some oscillatory behavior near the origin. Hence this point should be kept in mind while doing analysis for radial structures. Meanwhile as observed from (3.55), the characteristic impedance in both $-\rho$ and $+\rho$ directions become equal when the large argument approximation is used. Hence under these conditions, the expression for the characteristic impedance reduces to

$$Z_0 = \frac{a}{2\pi b} \sqrt{\frac{\mu}{\varepsilon}} = \frac{a}{2\pi b} \eta_0 \bar{Z} \quad (3.57)$$

where,

$$\bar{Z} = \frac{1}{\sqrt{\varepsilon_r(\rho)}} \quad (3.58)$$

is the normalized impedance for the radial cylindrical geometry. It may be mentioned here that for the large argument approximation, the factor α_r in (3.54b) will be unity as obvious from (3.53) and (3.55), and the expression for the reflection coefficient (3.52) is reduced to

$$\Gamma = \frac{Z_L - Z_0}{Z_L + Z_0} \quad (3.59)$$

It is interesting to note that expressions (3.58) and (3.59) become identical to the planar case for the approximation considered here. However, the voltage and current on the line are still given by the exact expressions (3.54a) and (3.54b) with the value of α_r taken as unity. The reflection coefficient in (3.59) is defined as the ratio of the reflected (outgoing) to the incident (incoming) wave at the reference position of the load ($\rho = b$) as shown in Fig. 3.11. However, this quantity can be defined at any arbitrary point ρ on the radial line ($0 < \rho \leq b$) as follows

$$\Gamma(\rho) = \frac{V_0^+}{V_0^-} \left[\frac{H_0^{(2)}(k\rho)}{H_0^{(2)}(kb)} \frac{H_0^{(1)}(kb)}{H_0^{(1)}(k\rho)} \right] = \Gamma(b) \frac{H_0^{(2)}(k\rho) H_0^{(1)}(kb)}{H_0^{(1)}(k\rho) H_0^{(2)}(kb)} \quad (3.60)$$

where we have made use of (3.54a). For considering the one-dimensional radial inhomogeneity in terms of the reflection coefficient for both continuous and discontinuous (stratified) cylindrical media, equations (3.58), (3.59) and (3.60) would be mainly used in this thesis.

3.2.1.1 The stratified media

The cylindrical dielectric inhomogeneous media shown in Fig. 3.9 can be approximated by a number of homogeneous regions each of thickness $\Delta\rho$ as shown in Fig. 3.12 provided that the number of sections N is quite large, and $\Delta\rho$ is sufficiently small so that the permittivity can be considered to be constant in each small region. Now, for the TM_{00} radial mode illumination, this kind of cylindrical media may also be considered as N -cascaded radial transmission lines as shown in Fig. 3.13, and the equivalent 2-port network can be used to represent each layer as shown in Fig. 3.14. The i^{th} 2-port network basically consists of a junction between two homogeneous layers of relative permittivities ε_r^{i-1} and ε_r^i , and a section of radial transmission line of length $\Delta\rho$. Our aim here is to calculate the scattering parameters or the reflection coefficient of combined sections at the reference position $\rho = b$.

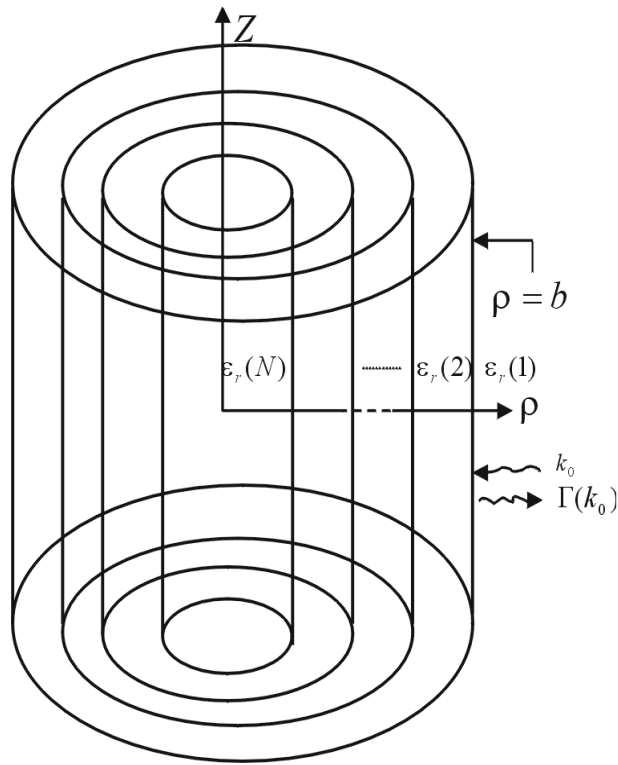


Figure 3.12: The cylindrically stratified media

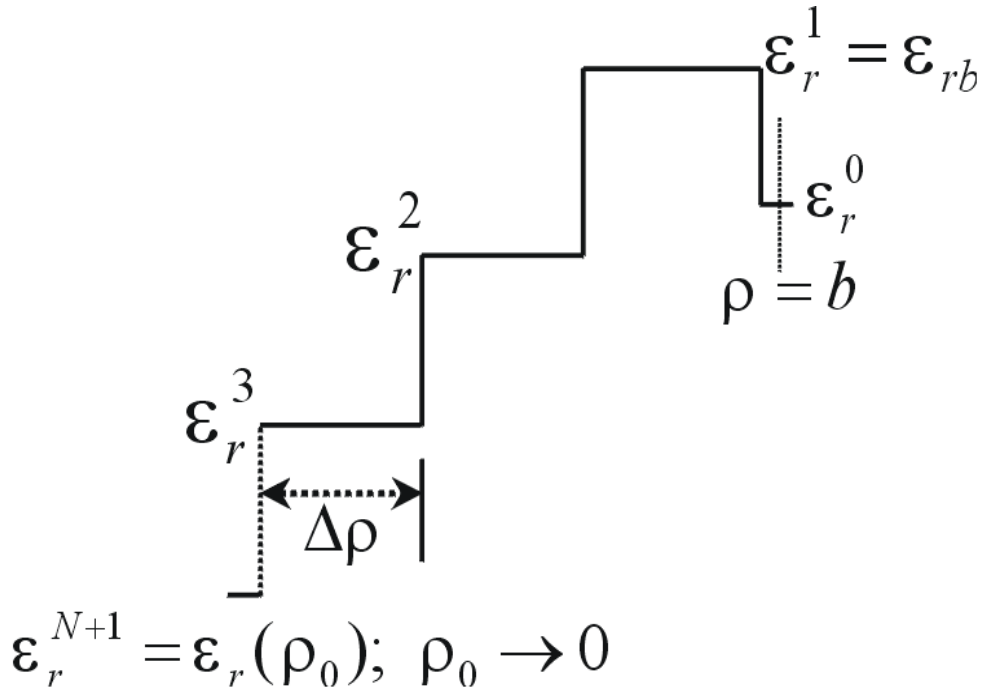


Figure 3.13: N-cascaded radial transmission lines

For this purpose, we represent each layer by a T -matrix so that the T -matrix of the total cylindrical stratified media is simply computed by multiplying the matrices of the individual sections altogether as explained in section 3.1.1.1 for the planar case. The T -matrix of the i^{th} section is given by

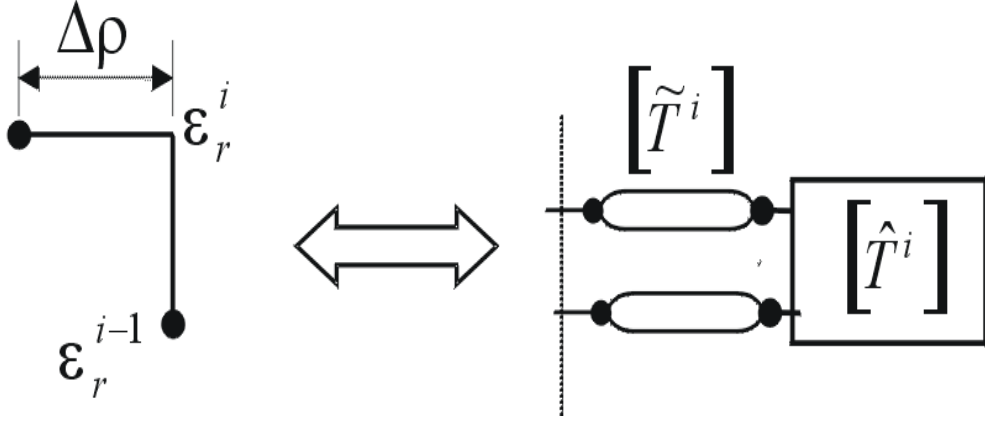


Figure 3.14: The equivalent scattering parameter network for each layer

$$[T^i] = [\hat{T}^i] [\tilde{T}^i] = \begin{bmatrix} \hat{T}_{11}^i & \hat{T}_{12}^i \\ \hat{T}_{21}^i & \hat{T}_{22}^i \end{bmatrix} \begin{bmatrix} \tilde{T}_{11}^i & \tilde{T}_{12}^i \\ \tilde{T}_{21}^i & \tilde{T}_{22}^i \end{bmatrix} \quad (3.61)$$

where $[\hat{T}^i]$, $i = 1, 2, \dots, N + 1$ is the T matrix of the junction between the $(i - 1)^{th}$ and the i^{th} layer having permittivities ε_r^{i-1} and ε_r^i respectively, and $[\tilde{T}^i]$, $i = 1, 2, \dots, N$ is the T matrix of the i^{th} radial transmission line of length $\Delta\rho$. For the last layer i.e. for $i = N + 1$, $[T^i] = [\hat{T}^i]$ as this layer is described only by a junction and there is no transmission line section. As can be seen from (3.58), the expression for the normalized impedance in the radial case (after applying asymptotic approximation) is of the same form as in the planar case. This means that for any i^{th} section, (3.9) and (3.8) can be used to compute the elements of $[\hat{T}^i]$ matrix, i.e.

$$[\hat{T}^i] = \begin{bmatrix} \frac{\sqrt{\varepsilon_r^{i-1}} + \sqrt{\varepsilon_r^i}}{2\sqrt{\varepsilon_r^{i-1}\varepsilon_r^i}} & \frac{\sqrt{\varepsilon_r^{i-1}} - \sqrt{\varepsilon_r^i}}{2\sqrt{\varepsilon_r^{i-1}\varepsilon_r^i}} \\ \frac{\sqrt{\varepsilon_r^{i-1}} - \sqrt{\varepsilon_r^i}}{2\sqrt{\varepsilon_r^{i-1}\varepsilon_r^i}} & \frac{\sqrt{\varepsilon_r^{i-1}} + \sqrt{\varepsilon_r^i}}{2\sqrt{\varepsilon_r^{i-1}\varepsilon_r^i}} \end{bmatrix} \quad (3.62)$$

For the computation of the elements of the second matrix $[\tilde{T}^i]$ in (3.61), we can make use of (3.46a). If we take $i = 1$, i.e. the first section, then the incident and

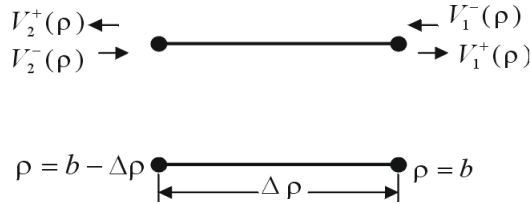
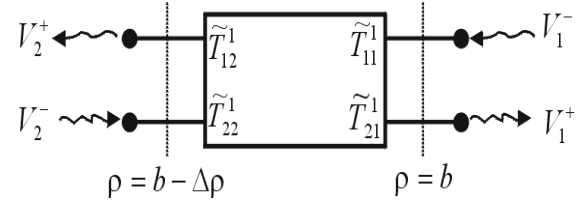


Figure 3.15: A thin layer of the radial transmission line

Figure 3.16: The equivalent $[\tilde{T}]$ network for this thin layer

reflected voltages on the two ports of this small section, as shown in Fig. 3.15 are related as

$$V_2^+(\rho) = V_1^-(\rho) \frac{H_0^{(1)}[k(b - \Delta\rho)]}{H_0^{(1)}[kb]} \quad (3.63a)$$

$$V_2^-(\rho) = V_1^+(\rho) \frac{H_0^{(2)}[k(b - \Delta\rho)]}{H_0^{(2)}[kb]} \quad (3.63b)$$

where the subscripts 1 and 2 represent the input and output ports respectively in Fig. 3.15. Now, this layer of thickness $\Delta\rho$ can be represented by a $[T]$ matrix network as shown in Fig. 3.16, and as per definition of this matrix, (3.63) can be rewritten in the following form

$$\begin{bmatrix} V_1^- \\ V_1^+ \end{bmatrix} = \begin{bmatrix} \frac{H_0^{(1)}[kb]}{H_0^{(1)}[k(b-\Delta\rho)]} & 0 \\ 0 & \frac{H_0^{(2)}[kb]}{H_0^{(2)}[k(b-\Delta\rho)]} \end{bmatrix} \begin{bmatrix} V_2^+ \\ V_2^- \end{bmatrix} = \begin{bmatrix} \tilde{T}_{11}^1 & \tilde{T}_{12}^1 \\ \tilde{T}_{21}^1 & \tilde{T}_{22}^1 \end{bmatrix} \begin{bmatrix} V_2^+ \\ V_2^- \end{bmatrix} \quad (3.64)$$

The above equation can next be generalized for any i^{th} section

$$\begin{bmatrix} \tilde{T}^i \end{bmatrix} = \begin{bmatrix} \tilde{T}_{11}^i & \tilde{T}_{12}^i \\ \tilde{T}_{21}^i & \tilde{T}_{22}^i \end{bmatrix} = \begin{bmatrix} \frac{H_0^{(1)}\{k^i[b-(i-1)\Delta\rho]\}}{H_0^{(1)}[k^i(b-i\Delta\rho)]} & 0 \\ 0 & \frac{H_0^{(2)}\{k^i[b-(i-1)\Delta\rho]\}}{H_0^{(2)}[k^i(b-i\Delta\rho)]} \end{bmatrix} \quad (3.65)$$

where $k^i = k_0\sqrt{\varepsilon_r^i}$ is the wave number for the i^{th} section, and $i = 1, 2, 3, \dots, N+1$. It may be noted that for $i = 1$, the above equation reduces to (3.64), which verifies the validity of the above equation. The value of the above $[\tilde{T}^i]$ matrix along with the $[\hat{T}^i]$ matrix of (3.62) is substituted in (3.61) to obtain the $[T]$ matrix of the i^{th} section. The overall $[T]$ matrix of the cylindrical stratified media shown in Fig. 3.12 is then obtained by multiplying $[T^i]$ matrices of all the individual sections, i.e.

$$[T] = \begin{bmatrix} T_{11} & T_{12} \\ T_{21} & T_{22} \end{bmatrix} = \prod_{i=1}^{N+1} [T^i] \quad (3.66)$$

Finally, the frequency-dependent reflection coefficient of the cylindrically stratified media, measured at the outer radius $\rho = b$ in Fig. 3.12 is computed from the above $[T]$ matrix [79]

$$\Gamma(k_0, b) = T_{21}/T_{11} \quad (3.67)$$

which is the direct problem formulation of the cylindrically layered media, with each layer having a constant value of permittivity as shown in Figs. 3.12 and 3.13.

3.2.1.2 The continuous media

In the previous sub-section, the inhomogeneous cylindrical media was regarded as a stack of homogeneous layers and accordingly an expression was derived for the total reflection coefficient measured at the outer radius of the cylindrical object in terms of the electrical properties of these homogeneous layers. It was also mentioned there that when each homogeneous layer in Fig. 3.12 is sufficiently thin, the discontinuous

media of Fig. 3.12 approaches the cylindrical continuous media of Fig. 3.9, and in this case the length $\Delta\rho$ can be replaced by a differential length $d\rho$. Now, let us consider a small section of the continuous media between points ρ and $\rho - d\rho$ and assume that the total reflection coefficient at these two points are given by $\Gamma(k_0, \rho)$ and $\Gamma(k_0, \rho) - d\Gamma(k_0, \rho)$ respectively as shown in Fig. 3.17. This local change in the reflection coefficient can be attributed to either a change in the permittivity profile from $\varepsilon_r(\rho) - d\varepsilon_r(\rho)$ at $\rho - d\rho$ to $\varepsilon_r(\rho)$ at ρ , or a change in the normalized impedance from $\bar{Z}(\rho) - d\bar{Z}(\rho)$ at $\rho - d\rho$ to $\bar{Z}(\rho)$ at ρ . Meanwhile, this small section of length $d\rho$ can be analyzed using the concept of microwave network theory as discussed in earlier sections, and the equivalent circuit of this thin layer can be given by a transmission line of electrical length $\sqrt{\varepsilon_r(\rho)} d\rho$ followed by a 2-port $[\partial S]$ matrix representing the junction between two layers of impedances $\bar{Z}(\rho) - d\bar{Z}(\rho)$ and $\bar{Z}(\rho)$ as shown in Fig. 3.18. The $[\partial S]$ matrix in Fig. 3.18 basically represents a

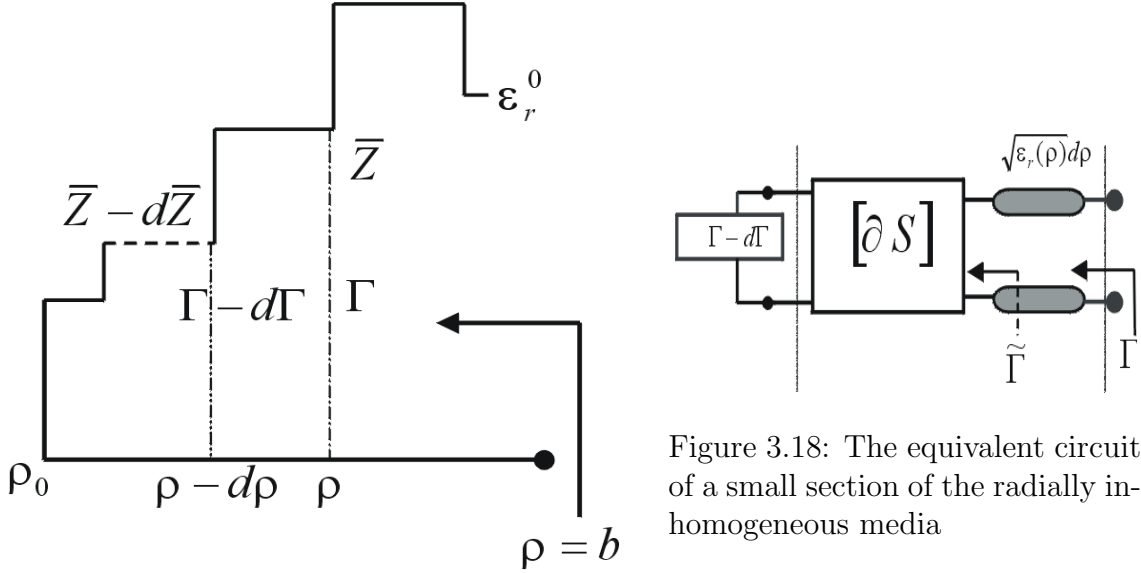


Figure 3.18: The equivalent circuit of a small section of the radially inhomogeneous media

Figure 3.17: The radially inhomogeneous media

lossless two-port junction and it was mentioned in section 3.1.1.1 that for such type of junction, all the four S parameters can be expressed in terms of the parameter S_{11} and the phase of S_{22} as per equation (3.6)

$$[\partial S] = \begin{bmatrix} S_{11} & \sqrt{1 - S_{11}^2} \\ \sqrt{1 - S_{11}^2} & -S_{11} \end{bmatrix} \quad (3.68)$$

The value of the local reflection coefficient S_{11} for this radial transmission line junction in the above equation is computed using (3.59) and (3.58)

$$S_{11} = \frac{(\bar{Z} - d\bar{Z}) - \bar{Z}}{(\bar{Z} - d\bar{Z}) + \bar{Z}} \simeq -\frac{d\bar{Z}}{2\bar{Z}} = \frac{d\varepsilon_r(\rho)}{4\varepsilon_r(\rho)} \quad (3.69)$$

The above approximation holds quite good if the value of $d\bar{Z}$ is reasonably small so that all the higher order terms involving $d\bar{Z}$ such as $(d\bar{Z})^2, (d\bar{Z})^3, \dots$ can be neglected. Now, as observed in Fig. 3.18, the output port of the junction $[\partial S]$ is terminated into an impedance characterized by a reflection coefficient $\Gamma - d\Gamma$. This

situation is similar to Fig. 3.6, and hence equation (3.13) can be used here to obtain an expression for the intermediate reflection coefficient

$$\tilde{\Gamma} = S_{11} + \frac{[1 - S_{11}^2](\Gamma - d\Gamma)}{1 + S_{11}(\Gamma - d\Gamma)} \simeq S_{11} + \frac{(\Gamma - d\Gamma)}{1 + \Gamma S_{11}} \quad (3.70)$$

where the higher order infinitesimals such as $S_{11}^2, d\Gamma S_{11}, \dots$ are neglected. The intermediate parameter $\tilde{\Gamma}$ in Fig. 3.18 may also be related to the reflection coefficient Γ using (3.60)

$$\tilde{\Gamma} = \Gamma \frac{H_0^{(1)}(k\rho) H_0^{(2)}[k(\rho - d\rho)]}{H_0^{(2)}(k\rho) H_0^{(1)}[k(\rho - d\rho)]} \cong \Gamma \left[1 + j \frac{4d\rho}{\pi\rho H_0^{(1)}(k\rho) H_0^{(2)}(k\rho)} \right] \quad (3.71)$$

where the right most term in the above equation is obtained after expanding the Hankel functions of argument $k(\rho - d\rho)$ in terms of its Taylor's series and then neglecting the higher order infinitesimals. In the next step, equations (3.70) and (3.71) are combined together to eliminate the intermediate variable $\tilde{\Gamma}$

$$\begin{aligned} \Gamma \left[1 + j \frac{4d\rho}{\pi\rho H_0^{(1)}(k\rho) H_0^{(2)}(k\rho)} \right] &= S_{11} + \frac{(\Gamma - d\Gamma)}{1 + \Gamma S_{11}} \\ \Rightarrow \Gamma(1 + \Gamma S_{11}) \left[1 + j \frac{4d\rho}{\pi\rho H_0^{(1)}(k\rho) H_0^{(2)}(k\rho)} \right] &= S_{11}(1 + \Gamma S_{11}) + (\Gamma - d\Gamma) \quad (3.72) \\ \Rightarrow \Gamma + \Gamma^2 S_{11} + (\Gamma + \Gamma^2 S_{11}) \frac{j 4d\rho}{\pi\rho H_0^{(1)}(k\rho) H_0^{(2)}(k\rho)} &= S_{11} + \Gamma S_{11}^2 + \Gamma - d\Gamma \end{aligned}$$

If in the above equation, the higher order infinitesimals are neglected, then it will yield

$$\begin{aligned} \Gamma^2 S_{11} + \Gamma \frac{j 4d\rho}{\pi\rho H_0^{(1)}(k\rho) H_0^{(2)}(k\rho)} &= S_{11} - d\Gamma \\ \Rightarrow \frac{d\Gamma}{d\rho} + \Gamma \frac{j 4}{\pi\rho H_0^{(1)}(k\rho) H_0^{(2)}(k\rho)} &= \frac{S_{11}}{d\rho} [1 - \Gamma^2] \quad (3.73) \end{aligned}$$

Finally the value of S_{11} can be substituted from (3.69) in (3.73) to obtain the following nonlinear differential equation relating the frequency dependent reflection coefficient Γ and the one-dimensional radially varying permittivity profile $\varepsilon_r(\rho)$

$$\frac{d\Gamma(k_0, \rho)}{d\rho} + \Gamma(k_0, \rho) \left[\frac{j 4}{\pi\rho H_0^{(1)}(k\rho) H_0^{(2)}(k\rho)} \right] = \frac{1}{4\varepsilon_r(\rho)} \frac{d\varepsilon_r(\rho)}{d\rho} [1 - \Gamma^2(k_0, \rho)] \quad (3.74)$$

which is the required direct problem formulation for the inhomogeneous cylindrical media illuminated by a radial *TEM* mode. The above equation reduces to Riccati equation (3.18) of the planar *TEM* case, except for a change in sign in the term containing $\Gamma(k_0, \rho)$, when the zeroth order Hankel functions are replaced by their

large argument asymptotic expressions. This is to be expected as the cylindrical waves should behave like simple plane waves at large radii, and the change in sign here is attributed to the fact that the direction of propagation of waves here is in the $-\rho$ direction (inward waves). The derivation of the above equation also proves that all the basics of the classical transmission line theory can be applied to analyze the propagation of radial waves in the cylindrical geometry for a TM_{00} cylindrical mode illumination.

3.2.2 Higher order mode illuminations

In the last section, we described the method of the direct problem formulation for the cylindrical geometry using the lowest order TM mode illumination. The main advantage of using the lowest order TM illumination is that it does not have electric or magnetic field in the direction of propagation and hence it is possible to carry out the analysis using the classical transmission line theory. However, the practical antenna arrangements for the illumination (transmitters) or measurement of scattering data (receivers) are generally *not* able to excite or measure a particular lower order mode. Hence it becomes necessary to formulate the problem for any general TE or TM mode, as an arbitrary illuminating or scattered electromagnetic field can be expressed as a superposition of all possible modes due to their completeness property [64].

For example, let us assume that any particular solution of the general Helmholtz equation

$$\nabla^2 \Psi + k^2 \Psi = 0 \quad (3.75)$$

in the cylindrical coordinate system is given by Ψ_n . These solutions are generally called the elementary wave functions, and form a discrete set in a given domain. With each of the wave function Ψ_n , we can associate two vector solutions \mathbf{M}_n and \mathbf{N}_n which are orthogonal to each other. These vectors \mathbf{M}_n and \mathbf{N}_n can be used to represent the electric and magnetic fields, and may be thought of being produced by electric and magnetic vector potentials respectively [16]. The electric vector potential generally gives rise to TE set of modes, while the magnetic vector potential produces TM set of modes. Any general electromagnetic field can then be expressed as a superposition of TE and TM sets of modes. In mathematical form, an arbitrary electric field can be written as [64]

$$\mathbf{E} = \sum_n (a_n \mathbf{M}_n + b_n \mathbf{N}_n) \quad (3.76)$$

where n represents the number of all possible modes which are valid solution of (3.75). It has been proved that each vector \mathbf{M}_n or \mathbf{N}_n corresponding to a particular TE or TM mode is orthogonal to the other valid mode. This orthogonality property can be used to determine the coefficients of expansion in the above equation with the help of equivalent current distribution [64]. To extract the information about a particular TE or TM mode, a multiple illumination / multi-view scenario can be used. For example, let us assume that the first 20 modes contribute significantly to the total field under a particular situation. In this case, we can represent the total electric field of (3.76) in terms of these 20 modes. We can then excite the

object under test with illumination from say, 20 different angles, and the total field (both amplitude and phase) can be measured at a given location in all the cases. These measured values can then be used in accordance with (3.76) to find the actual mode-distribution at a given position. It may be mentioned here that the measured field at each position will be a combination of all possible modes, with each mode having a distinct spatial dependence. Once we are able to determine the specific contribution due to each TE or TM mode, then our proposed technique can be employed for each individual mode.

In this section, we have formulated the direct problem for any arbitrary order TE_{mn} or TM_{mn} illumination. The detailed analysis are carried out for the TE_{mn} mode, while for the TM_{mn} case only the final result will be presented. The wave functions for the TE_{mn} mode satisfying appropriate boundary conditions in Fig. 3.10 are given by [16]

$$\Psi_{mn}^{TE} = (F_z)_{mn} = \sin(k_z z) \cos(n\phi) H_n^{(p)}(k_\rho \rho) \quad p = 1 \text{ or } 2 \quad (3.77)$$

where $m = 1, 2, 3 \dots$, $n = 0, 1, 2 \dots$, $H_n^{(1)}(k_\rho \rho)$ is the Hankel function of the first kind of order n representing an inward travelling wave, $H_n^{(2)}(k_\rho \rho)$ is the Hankel function of the second kind of order n representing an outward travelling wave,

$$k_\rho = \sqrt{k^2 - k_z^2} \quad (3.78)$$

is the radial propagation constant, k is the total propagation constant in the radially varying dielectric media defined by (3.32), and

$$k_z = \frac{m\pi}{a} \quad (3.79)$$

is the propagation constant in the z -direction. It may be mentioned here that for the ϕ -direction, we have considered the $\cos(n\phi)$ variations. However, for a complete set of modes, those with the $\sin(n\phi)$ variations must also be included. But as the analysis is quite similar for both the cases, hence we choose only the former. The electromagnetic fields for the TE_{mn} to z mode are determined after making the electric vector potential F z -directed, i.e.

$$\mathbf{F} = \mathbf{u}_z \Psi_{mn}^{TE} = \mathbf{u}_z F_z \quad (3.80)$$

The electric field components for the TE_{mn} mode in the cylindrical geometry is computed as [91]

$$\begin{aligned} \mathbf{E} &= -\nabla \times \mathbf{F} \\ \Rightarrow E_\rho \mathbf{u}_\rho + E_\phi \mathbf{u}_\phi + E_z \mathbf{u}_z &= -\frac{1}{\rho} \begin{vmatrix} \mathbf{u}_\rho & \rho \mathbf{u}_\phi & \mathbf{u}_z \\ \frac{\partial}{\partial \rho} & \frac{\partial}{\partial \phi} & \frac{\partial}{\partial z} \\ 0 & 0 & F_z \end{vmatrix} = -\mathbf{u}_\rho \frac{1}{\rho} \frac{\partial F_z}{\partial \phi} + \mathbf{u}_\phi \frac{\partial F_z}{\partial \rho} \end{aligned} \quad (3.81)$$

The above equation, along with the value of F_z substituted from (3.77) yields following electric field components

$$\begin{aligned} E_\rho^- &= \frac{n}{\rho} \sin(k_z z) \sin(n\phi) H_n^{(1)}(k_\rho \rho) \\ E_\rho^+ &= \frac{n}{\rho} \sin(k_z z) \sin(n\phi) H_n^{(2)}(k_\rho \rho) \end{aligned} \quad (3.82a)$$

$$E_{\phi}^{-} = k_{\rho} \sin(k_z z) \cos(n\phi) H_n^{(1)'}(k_{\rho}\rho) \quad (3.82b)$$

$$E_{\phi}^{+} = k_{\rho} \sin(k_z z) \cos(n\phi) H_n^{(2)'}(k_{\rho}\rho)$$

$$E_z^{-} = 0 \quad E_z^{+} = 0 \quad (3.82c)$$

where $H_n^{(p)'}(k_{\rho}\rho)$ represents the first derivative of the corresponding Hankel function $H_n^{(p)}(k_{\rho}\rho)$. The magnetic field components for the TE_{mn} mode can be computed by expanding one of the Maxwell's curl equations in the cylindrical coordinate system and neglecting the E_z component as per (3.82), i.e.

$$\begin{aligned} \nabla \times \mathbf{E} &= -j\omega\mu_0\mathbf{H} \\ \Rightarrow \frac{1}{\rho} \begin{vmatrix} \mathbf{u}_{\rho} & \rho\mathbf{u}_{\phi} & \mathbf{u}_z \\ \frac{\partial}{\partial\rho} & \frac{\partial}{\partial\phi} & \frac{\partial}{\partial z} \\ E_{\rho} & \rho E_{\phi} & 0 \end{vmatrix} &= -\mathbf{u}_{\rho} \frac{\partial E_{\phi}}{\partial z} + \mathbf{u}_{\phi} \frac{\partial E_{\rho}}{\partial z} + \mathbf{u}_z \frac{1}{\rho} \left[\frac{\partial}{\partial\rho}(\rho E_{\phi}) - \frac{\partial E_{\rho}}{\partial\phi} \right] \\ &= -j\omega\mu_0 [H_{\rho}\mathbf{u}_{\rho} + H_{\phi}\mathbf{u}_{\phi} + H_z\mathbf{u}_z] \end{aligned} \quad (3.83)$$

The different components of the magnetic field are obtained from the above equation after substituting the value of E_{ϕ} and E_{ρ} from (3.82) in (3.83)

$$H_{\rho}^{-} = \frac{1}{j\omega\mu_0} \frac{\partial E_{\phi}^{-}}{\partial z} = \frac{k_{\rho}k_z}{j\omega\mu_0} \cos(k_z z) \cos(n\phi) H_n^{(1)'}(k_{\rho}\rho) \quad (3.84a)$$

$$H_{\rho}^{+} = \frac{1}{j\omega\mu_0} \frac{\partial E_{\phi}^{+}}{\partial z} = \frac{k_{\rho}k_z}{j\omega\mu_0} \cos(k_z z) \cos(n\phi) H_n^{(2)'}(k_{\rho}\rho)$$

$$H_{\phi}^{-} = -\frac{1}{j\omega\mu_0} \frac{\partial E_{\rho}^{-}}{\partial z} = \frac{-nk_z}{j\omega\mu_0\rho} \cos(k_z z) \sin(n\phi) H_n^{(1)}(k_{\rho}\rho) \quad (3.84b)$$

$$H_{\phi}^{+} = -\frac{1}{j\omega\mu_0} \frac{\partial E_{\rho}^{+}}{\partial z} = \frac{-nk_z}{j\omega\mu_0\rho} \cos(k_z z) \sin(n\phi) H_n^{(2)}(k_{\rho}\rho)$$

$$H_z^{-} = \frac{1}{j\omega\mu_0\rho} \left[\frac{\partial E_{\rho}^{-}}{\partial\phi} - \frac{\partial}{\partial\rho}(\rho E_{\phi}^{-}) \right] = \frac{k_{\rho}^2}{j\omega\mu_0} \sin(k_z z) \cos(n\phi) H_n^{(1)}(k_{\rho}\rho) \quad (3.84c)$$

$$H_z^{+} = \frac{1}{j\omega\mu_0\rho} \left[\frac{\partial E_{\rho}^{+}}{\partial\phi} - \frac{\partial}{\partial\rho}(\rho E_{\phi}^{+}) \right] = \frac{k_{\rho}^2}{j\omega\mu_0} \sin(k_z z) \cos(n\phi) H_n^{(2)}(k_{\rho}\rho)$$

It may be noted from (3.82) and (3.84) that for a general TE_{mn} mode, E_{ρ} and H_{ρ} components are not zero, which is in contrast to the lowest order TM mode where both the electric and magnetic field components were zero in the direction of propagation. After obtaining all field components for the general TE_{mn} mode, our next task is to formulate the direct or forward problem in such a way that the wave incident from the outside ($\rho > b$) travels inside the dielectric object in the radial direction towards the z -axis, and then it gets reflected from different layers of this inhomogeneous object producing a net reflection coefficient at the outer air-dielectric interface at $\rho = b$ as shown in Fig. 3.9. The incident field components are related to the complex conjugate of the corresponding reflected components as follows

$$\begin{aligned} E_{\phi}^{+} &= (E_{\phi}^{-})^* \\ H_z^{+} &= -(H_z^{-})^* \end{aligned} \quad (3.85)$$

where the superscript "*" represents the complex conjugate, and we have made use of the fact that Hankel functions of first and second kinds (of the same order) are complex conjugate to each other. Our basic aim here is to look for a taper solution of the following form

$$H_z = H_z^- + \tilde{\Gamma} H_z^+ = H_z^- - \tilde{\Gamma} (H_z^-)^* \quad (3.86a)$$

$$E_\phi = E_\phi^- + \tilde{\Gamma} E_\phi^+ = E_\phi^- + \tilde{\Gamma} (E_\phi^-)^* \quad (3.86b)$$

where $\tilde{\Gamma}$ is an intermediate reflection coefficient, and we have made use of (3.85). The above two equations (3.86a) and (3.86b) basically mean that the total field is represented as a sum of incident and reflected waves. Now, we try to reformulate (3.86a) and (3.86b) in order to have a form similar to that in the planar case. For this purpose, we define the actual reflection coefficient in terms of $\tilde{\Gamma}$ as

$$\Gamma = -\tilde{\Gamma} \frac{(H_z^-)^*}{H_z^-} \quad (3.87)$$

This value of Γ can be substituted in (3.86) to arrive at

$$H_z = H_z^- \left[1 - \tilde{\Gamma} \frac{(H_z^-)^*}{H_z^-} \right] = H_z^- [1 + \Gamma] \quad (3.88a)$$

$$\begin{aligned} E_\phi &= E_\phi^- \left[1 + \tilde{\Gamma} \frac{(E_\phi^-)^*}{E_\phi^-} \right] = -ZH_z^- \left[1 + \tilde{\Gamma} \left(\frac{-E_\phi^-}{H_z^-} \right)^* \left(\frac{(H_z^-)^*}{H_z^-} \right) \left(\frac{-H_z^-}{E_\phi^-} \right) \right] \\ &= -ZH_z^- \left[1 - \Gamma \frac{Z^*}{Z} \right] = -ZH_z^- [1 - \alpha_c \Gamma] \end{aligned} \quad (3.88b)$$

where,

$$Z = Z_{-\rho}^{TE_{mn}} = -\frac{E_\phi^-}{H_z^-} = -\frac{jk_0\eta_0}{k_\rho} \frac{H_n^{(1)'}(k_\rho\rho)}{H_n^{(1)}(k_\rho\rho)} = \eta_0 \bar{Z} \quad (3.89)$$

is the wave impedance corresponding to radially directed incident waves, with \bar{Z} being the normalized value of the impedance for the TE_{mn} mode, the variable α_c for the cylindrical media is defined as

$$\alpha_c = \frac{Z_{-\rho}^{TE_{mn}^*}}{Z_{-\rho}^{TE_{mn}}} = -\frac{H_{n-1}^{(2)}(k_\rho\rho) - H_{n+1}^{(2)}(k_\rho\rho)}{H_{n-1}^{(1)}(k_\rho\rho) - H_{n+1}^{(1)}(k_\rho\rho)} \frac{H_n^{(1)}(k_\rho\rho)}{H_n^{(2)}(k_\rho\rho)} \quad (3.90)$$

and the following formula is used for the computation of the first derivative of the Hankel function of order n [90]

$$H_n^{(p)'}(z) = \frac{dH_n^{(p)}(z)}{dz} = \frac{1}{2} \left[H_{n-1}^{(p)}(z) - H_{n+1}^{(p)}(z) \right] \quad p = 1 \text{ or } 2 \quad (3.91)$$

It can be observed from (3.88a) and (3.88b) that after the reformulation, these two equations have similar form as in the planar case except for the factor α_c . For

the planar geometry, this factor α_c is basically equal to unity as the impedance or admittance for the propagating waves is generally real. In this thesis, we always try to obtain the total field components in the form given by (3.88a) and (3.88b) for both cylindrical and spherical geometry because of the above mentioned reason. After defining the total field components in (3.88a) and (3.88b), our next task is to obtain the radial derivative of these components and this is achieved after expanding the Maxwell's second curl equation into the cylindrical coordinate system for the TE_{mn} mode

$$\begin{aligned}
\nabla \times \mathbf{H} &= j\omega\varepsilon_0\varepsilon_r(\rho)\mathbf{E} \\
\Rightarrow \frac{1}{\rho} \begin{vmatrix} \mathbf{u}_\rho & \rho\mathbf{u}_\phi & \mathbf{u}_z \\ \frac{\partial}{\partial\rho} & \frac{\partial}{\partial\phi} & \frac{\partial}{\partial z} \\ H_\rho & \rho H_\phi & H_z \end{vmatrix} &= j\omega\varepsilon_0\varepsilon_r(\rho) [E_\rho\mathbf{u}_\rho + E_\phi\mathbf{u}_\phi + E_z\mathbf{u}_z] \\
\Rightarrow \frac{\partial H_z}{\partial\phi} - \frac{\partial}{\partial z}(\rho H_\phi) &= j\omega\varepsilon_0\varepsilon_r(\rho)\rho E_\rho \\
\frac{\partial H_\rho}{\partial z} - \frac{\partial H_z}{\partial\rho} &= j\omega\varepsilon_0\varepsilon_r(\rho)E_\phi \\
\frac{\partial}{\partial\rho}(\rho H_\phi) - \frac{\partial H_\rho}{\partial\phi} &= 0
\end{aligned} \tag{3.92}$$

Our basic aim for solving (3.92) is to obtain an expression for the radial derivative of H_z in terms of E_ϕ . This is achieved using one of the above equations as follows

$$\begin{aligned}
\frac{\partial H_\rho}{\partial z} - \frac{\partial H_z}{\partial\rho} &= j\omega\varepsilon_0\varepsilon_r(\rho)E_\phi \\
\Rightarrow \frac{\partial H_z}{\partial\rho} &= \left[\frac{\omega^2\mu_0\varepsilon_0\varepsilon_r(\rho) - k_z^2}{j\omega\mu_0} \right] E_\phi = \frac{-jk_\rho^2}{\omega\mu_0} E_\phi
\end{aligned} \tag{3.93}$$

where (3.84) and (3.82) are used for expressing the value of $\partial H_\rho/\partial z$ in terms of E_ϕ . The radial derivative of E_ϕ in terms of H_z is obtained using (3.84c)

$$\begin{aligned}
\left[\frac{\partial E_\rho}{\partial\phi} - \frac{\partial}{\partial\rho}(\rho E_\phi) \right] &= j\omega\mu_0\rho H_z \\
\Rightarrow \frac{\partial}{\partial\rho}(\rho E_\phi) &= \frac{\partial E_\rho}{\partial\phi} - j\omega\mu_0\rho H_z = \frac{jn^2\omega\mu_0}{\rho k_\rho^2} H_z - j\omega\mu_0\rho H_z \\
\Rightarrow \frac{\partial}{\partial\rho}(\rho E_\phi) &= j\omega\mu_0\rho \left(\frac{n^2}{\rho^2 k_\rho^2} - 1 \right) H_z
\end{aligned} \tag{3.94}$$

After all these simplifications, equations (3.93) and (3.94) are written together

$$\begin{aligned}
\frac{\partial (H_z)}{\partial\rho} &= \frac{-jk_\rho^2}{k_0\eta_0} (E_\phi) \\
\frac{\partial}{\partial\rho}(\rho E_\phi) &= jk_0\eta_0\rho \left(\frac{n^2}{\rho^2 k_\rho^2} - 1 \right) H_z
\end{aligned} \tag{3.95}$$

At this juncture, it may be useful to give some physical interpretation of equation (3.95). Our aim here is basically to analyze the one-dimensional inhomogeneity in the radial direction, and hence we have considered $\partial/\partial\rho$ derivatives in both of these equations. Also, for the radial propagation of waves, the wave impedance in the ρ -direction should be considered and this involves transverse electric and magnetic field components [58]. The transverse field components, which are possible in the case of TE -illumination are H_z and E_ϕ as seen in (3.95). Meanwhile, the total E_ϕ and H_z fields can be substituted from (3.88) in (3.95) to obtain

$$j \frac{k_\rho^2}{k_0} \bar{Z} (1 - \alpha_c \Gamma) H_z^- = \frac{\partial}{\partial \rho} \left((1 + \Gamma) H_z^- \right) \quad (3.96a)$$

$$jk_0 \rho \left[1 - \frac{n^2}{\rho^2 k_\rho^2} \right] (1 + \Gamma) H_z^- = \frac{\partial}{\partial \rho} \left(\rho \bar{Z} (1 - \alpha_c \Gamma) H_z^- \right) \quad (3.96b)$$

Now, our aim is to solve equations (3.96a) and (3.96b) simultaneously in order to eliminate the common function H_z^- , and this is done using the method proposed in Appendix A, which yields

$$\begin{aligned} & \left\{ j \frac{k_\rho^2}{k_0} \bar{Z} (1 - \alpha_c \Gamma) - \frac{\partial \Gamma}{\partial \rho} \right\} [\rho \bar{Z} (1 - \alpha_c \Gamma)] \\ & = \left\{ jk_0 \rho \left[1 - \frac{n^2}{\rho^2 k_\rho^2} \right] (1 + \Gamma) - \frac{\partial}{\partial \rho} [\rho \bar{Z} (1 - \alpha_c \Gamma)] \right\} (1 + \Gamma) \end{aligned} \quad (3.97)$$

The above equation is simplified and rewritten into the differential equation form as

$$\frac{\partial \Gamma}{\partial \rho} + \frac{1}{(1 + \alpha_c) \rho \bar{Z}} \left\{ \begin{aligned} & \Gamma^2 \left[jk_0 \rho \left(1 - \frac{n^2}{\rho^2 k_\rho^2} - \frac{k_\rho^2}{k_0^2} \alpha_c^2 \bar{Z}^2 \right) + \frac{\partial}{\partial \rho} (\rho \alpha_c \bar{Z}) \right] \\ & + \Gamma \left[2jk_0 \rho \left(1 - \frac{n^2}{\rho^2 k_\rho^2} + \frac{k_\rho^2}{k_0^2} \alpha_c \bar{Z}^2 \right) + \frac{\partial}{\partial \rho} (\rho (\alpha_c - 1) \bar{Z}) \right] \\ & + \left[jk_0 \rho \left(1 - \frac{n^2}{\rho^2 k_\rho^2} - \frac{k_\rho^2}{k_0^2} \bar{Z}^2 \right) - \frac{\partial}{\partial \rho} (\rho \bar{Z}) \right] \end{aligned} \right\} = 0 \quad (3.98)$$

The different terms in (3.98) are computed separately and the values of \bar{Z} and α_c are substituted from (3.89) and (3.90). The terms involving derivatives in the above equation are generally the most complicated ones and after some mathematical manipulation, they are computed as

$$\begin{aligned} \frac{\partial}{\partial \rho} (\rho \bar{Z}) & = jk_0 \rho \left[1 - \frac{H_{n+1}^{(1)}(k_\rho \rho) H_{n-1}^{(1)}(k_\rho \rho)}{(H_n^{(1)}(k_\rho \rho))^2} \right. \\ & \quad \left. + \frac{H_{n+1}^{(1)}(k_\rho \rho) - H_{n-1}^{(1)}(k_\rho \rho)}{2H_n^{(1)}(k_\rho \rho)} \frac{\partial}{\partial \rho} \left(\frac{1}{k_\rho} \right) \right] \end{aligned} \quad (3.99a)$$

$$\begin{aligned} \frac{\partial}{\partial \rho} (\rho \alpha_c \bar{Z}) = -jk_0 \rho \left[1 - \frac{H_{n+1}^{(2)}(k_\rho \rho) H_{n-1}^{(2)}(k_\rho \rho)}{(H_n^{(2)}(k_\rho \rho))^2} \right. \\ \left. + \frac{H_{n+1}^{(2)}(k_\rho \rho) - H_{n-1}^{(2)}(k_\rho \rho)}{2H_n^{(2)}(k_\rho \rho)} \frac{\partial}{\partial \rho} \left(\frac{1}{k_\rho} \right) \right] \end{aligned} \quad (3.99b)$$

where we have made use of (3.91), and the following properties of the Hankel function for simplifications [90]

$$\frac{d}{dz} [z^n H_n^{(p)}(z)] = z^n H_{n-1}^{(p)}(z) \quad p = 1 \quad \text{or} \quad 2 \quad (3.100a)$$

$$\frac{d}{dz} \left[\frac{H_n^{(p)}(z)}{z^n} \right] = -\frac{H_{n+1}^{(p)}(z)}{z^n} \quad p = 1 \quad \text{or} \quad 2 \quad (3.100b)$$

The value of the derivative $\frac{\partial}{\partial \rho} (\rho(\alpha_c - 1)\bar{Z})$ in (3.98) is computed from the difference of (3.99a) and (3.99b). The common factor in (3.98) is computed as

$$(1 + \alpha_c) \rho \bar{Z} = \rho (\bar{Z} + \bar{Z}^*) = \frac{4k_0}{\pi k_\rho^2 H_n^{(1)}(k_\rho \rho) H_n^{(2)}(k_\rho \rho)} \quad (3.101)$$

where the following *Wronskian* formula for the Hankel function of n^{th} order is used [92]

$$\left[H_n^{(2)}(z) H_{n+1}^{(1)}(z) - H_n^{(1)}(z) H_{n+1}^{(2)}(z) \right] = \frac{4}{j\pi z} \quad (3.102)$$

The other terms in (3.98) are computed using a step-by-step approach, and finally all individual terms of this equation are combined along with equations (3.99) and (3.101) to obtain the following non-linear differential equation for the radially varying frequency-dependent reflection coefficient $\Gamma(k_0, \rho)$ due to a TE_{mn} illumination

$$\begin{aligned} \frac{\partial \Gamma}{\partial \rho} + \Gamma \left\{ \frac{4j}{\pi \rho H_n^{(1)}(k_\rho \rho) H_n^{(2)}(k_\rho \rho)} - \frac{j\pi \rho}{8} \frac{\partial k_\rho}{\partial \rho} \right. \\ \left. \left[\begin{array}{l} \left(H_n^{(1)}(k_\rho \rho) H_{n-1}^{(2)}(k_\rho \rho) + H_{n-1}^{(1)}(k_\rho \rho) H_n^{(2)}(k_\rho \rho) \right) \\ - \left(H_n^{(2)}(k_\rho \rho) H_{n+1}^{(1)}(k_\rho \rho) + H_{n+1}^{(2)}(k_\rho \rho) H_n^{(1)}(k_\rho \rho) \right) \end{array} \right] \right\} \\ = \left\{ \frac{j\pi \rho}{4} H_n^{(2)}(k_\rho \rho) \left[H_{n-1}^{(1)}(k_\rho \rho) - \frac{n}{k_\rho \rho} H_n^{(1)}(k_\rho \rho) \right] \frac{\partial k_\rho}{\partial \rho} \right\} [1 - \alpha_c \Gamma^2] \end{aligned} \quad (3.103)$$

It may be observed here that the structural form of (3.103) is quite similar to that of Riccati equation (3.26) of the planar case, and hence (3.103) will be called as the *Riccati-similar* differential equation of the cylindrical geometry due to an arbitrary order TE_{mn} mode illumination. The other point to be noted here is that (3.103) is a non-linear equation in Γ because of the presence of Γ^2 term, and this non-linearity takes into account the effect of multiple reflections from different layers of the cylindrical dielectric inhomogeneous media.

The analysis for an arbitrary order TM_{mn} mode illumination in the cylindrical geometry can be carried out on similar lines as described above for the TE_{mn} mode. The final expression of the *Riccati-similar* non-linear differential equation for the radially varying frequency-dependent reflection coefficient $\Gamma(k_0, \rho)$ due to a TM_{mn} illumination in the cylindrical geometry is given by

$$\begin{aligned} \frac{\partial \Gamma}{\partial \rho} + \Gamma & \left\{ \begin{array}{l} \frac{4j}{\pi \rho H_n^{(1)}(k_\rho \rho) H_n^{(2)}(k_\rho \rho)} + \frac{j\pi \rho k_\rho^2}{8\varepsilon_r(\rho)} \frac{\partial}{\partial \rho} \left(\frac{\varepsilon_r(\rho)}{k_\rho} \right) \\ \left[\begin{array}{l} \left(H_n^{(1)}(k_\rho \rho) H_{n-1}^{(2)}(k_\rho \rho) + H_{n-1}^{(1)}(k_\rho \rho) H_n^{(2)}(k_\rho \rho) \right) \\ - \left(H_n^{(2)}(k_\rho \rho) H_{n+1}^{(1)}(k_\rho \rho) + H_{n+1}^{(2)}(k_\rho \rho) H_n^{(1)}(k_\rho \rho) \right) \end{array} \right] \end{array} \right\} \\ & = - \left\{ \frac{j\pi \rho k_\rho^2}{4\varepsilon_r(\rho)} H_n^{(2)}(k_\rho \rho) \left[H_{n-1}^{(1)}(k_\rho \rho) - \frac{n}{k_\rho \rho} H_n^{(1)}(k_\rho \rho) \right] \frac{\partial}{\partial \rho} \left(\frac{\varepsilon_r(\rho)}{k_\rho} \right) \right\} [1 - \alpha_c \Gamma^2] \end{aligned} \quad (3.104)$$

where $m = 0, 1, 2 \dots$, $n = 0, 1, 2 \dots$, and all other symbols have same meaning as in the TE_{mn} case. The above described formulation for the TE_{mn} and TM_{mn} modes helps in analyzing cylindrical structures having one-dimensional radially varying permittivity profile, for any arbitrary order TE or TM mode illumination. The formulation for any general order TE and TM mode is quite important, as any practical excitation using a typical antenna setup produces a superposition of all possible modes.

3.3 The spherical geometry

The previous two sections of this chapter described the procedure for the direct problem formulation in planar and cylindrical objects. However, many dielectric objects have boundaries coinciding with the spherical coordinate system and these objects can better be described by considering them in the spherical geometry rather than in the planar or cylindrical ones. The formulation in the spherical coordinate system also provides a better image of dielectric objects, when the available antenna is *not* highly directive. This is specially true in cases when the object is having a curved boundary and the antenna is not able to provide a very high localized beam. These kinds of curved structures have been mostly analyzed in the past using a plane-wave approximation, which is true only in those cases where the antenna is highly directive in both the lateral directions. However, under practical situations it is very difficult to obtain such kinds of antennas. Hence it looks more suitable to use the commonly available antennas, which are less directive, and formulate the overall problem in a non-planar coordinate system rather than in a planar one. In the last section, it was mentioned that the cylindrical geometry could take the one-dimensional curvature into account and hence this was suitable for cases where the antenna can provide the highly directive beam in only one direction. Now, suppose the available antennas are less directive in *both* the lateral directions. In this case, it looks more appropriate to analyze the inhomogeneity in the spherical coordinate system as it can take the two-dimensional curvature into account, and hence it can compensate for the antenna's directivity in both the lateral directions. Now, since

the cross-sectional image of the spherical object can be obtained using e.g., a number of antennas or using a multi-view approach, hence the whole problem of imaging reduces to that of reconstructing the depth-dependent part of the inhomogeneity. In this section, we have formulated the direct problem to analyze this depth-dependent inhomogeneity by considering a spherically shaped inhomogeneous dielectric object as shown in Fig. 3.19. The depth-dependent permittivity profile $\varepsilon_r(r)$ of this object changes in the r direction, and the inner radius of the dielectric object is taken as r_0 as shown in this figure. In the limiting case, the radius r_0 approaches zero. However, care is being taken so that this inner radius is never made equal to zero to avoid the singularity of spherical Hankel functions. The typical geometry of the spherical coordinate system is shown in Fig. 3.20. A monochromatic spherical wave of wave number k_0 is assumed to be incident from the outer free space ($r > a$) and the reflection coefficient Γ is measured at outer boundary of the dielectric object i.e., at $r = a$ as shown in Fig. 3.19. The measurement of the reflection coefficient is chosen to be carried out at the outer diameter of the spherical object, because in most of the practical situations e.g. in case of imaging of different vegetation canopies, we do not have any access to the inside regions of the unknown object or media and the only feasibility is to measure at the outer boundary.

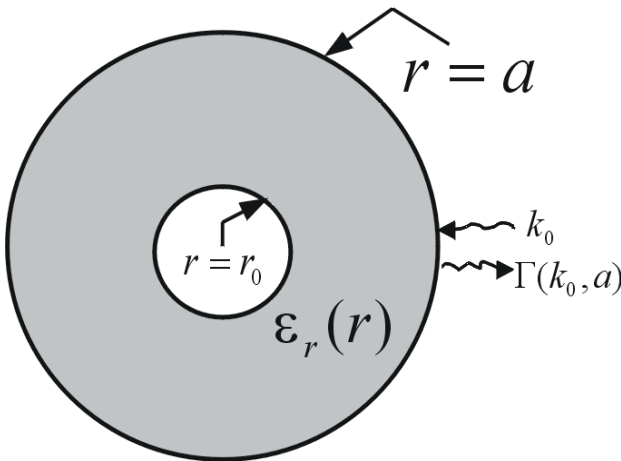


Figure 3.19: The spherical object, whose one-dimensional permittivity profile changes in the r -direction

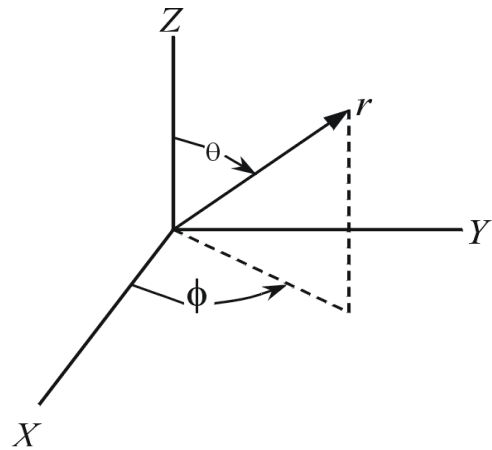


Figure 3.20: The spherical coordinate system

In the present analysis, the direct problem is formulated in the spherical coordinate system for dielectric objects having one-dimensional inhomogeneity in the r -direction, and illuminated by any arbitrary order TE or TM mode. It may be mentioned here that the transmission of waves in the r direction in spherical coordinate system is described by the *spherical Hankel* functions. Since the waves are supposed to be incident from the outer free space and reflection coefficient is measured at the outer radius of the spherical body, hence the *inward* and *outward* travelling waves are considered as *incident* and *reflected* waves respectively for all the cases described here. We will consider here the detailed analysis for any arbitrary order TM_{mn} spherical mode illumination, and equation for the TE_{mn} spherical mode will simply be presented. These equations will be simplified for lower order mode illuminations for both TE and TM cases.

3.3.1 Higher order mode illuminations

It was mentioned in the cylindrical case that any arbitrary electromagnetic field could be represented as a superposition of its TE and TM parts. The same theory applies to the spherical coordinate system, as the general Helmholtz equation given by (3.75) can be formulated in the spherical geometry as well. As already mentioned, it is usually not feasible to excite a particular TE or TM mode using a practical antenna setup. Hence, it becomes necessary to formulate the problem for any arbitrary order TE_{mn} or TM_{mn} mode. An arbitrary electromagnetic field produced by a typical antenna can be decomposed into all possible TE_{mn} and TM_{mn} modes due to the completeness property [64]. The information on the scattering of a certain TE or TM mode can be obtained after illuminating the object from say, multiple directions, and separating the contribution due to each particular mode.

In the spherical coordinate system, an arbitrary field is generally represented in terms of TE to r , and TM to r modes. This is in contrary to the planar and cylindrical coordinate systems, where an arbitrary field is generally represented in terms of TE to z , and TM to z modes. These r mode sets are somewhat simpler in case of spherical geometry, and hence are considered here for further analysis. We will present the full analysis for a TM_{mn} to r case, and for a TE_{mn} to r case only final result would be presented. The wave function used to generate TM_{mn} to r spherical modes, considering *even tesseral harmonics*³, is given by [16]

$$\Psi_{mn}^{TM} = (A_r)_{mn} = P_n^m(\cos \theta) \cos m\phi \hat{H}_n^{(p)}(kr) \quad p = 1 \quad \text{or} \quad 2 \quad (3.105)$$

where, A_r is the r -directed magnetic vector potential, $n = 1, 2, 3, \dots$; $m = 0, 1, 2, \dots, n$; $P_n^m(\cos \theta)$ is the associated Legendre function of the first kind [92],

$$k = k_0 \sqrt{\varepsilon_r(r)} \quad (3.106)$$

is the total propagation constant in the spherical dielectric media, and

$$\hat{H}_n^{(p)}(kr) = kr h_n^{(p)}(kr) \quad p = 1 \quad \text{or} \quad 2 \quad (3.107)$$

is a special type of spherical Hankel function defined by Schelkunoff [93], with $h_n^{(p)}(kr)$ being the standard definition of the spherical Hankel function [92]. For the wave function defined in terms of a magnetic vector potential (3.105), the magnetic field components are computed as [91]

$$\begin{aligned} \mathbf{H} &= \nabla \times \mathbf{A} \\ \Rightarrow H_r \mathbf{u}_r + H_\theta \mathbf{u}_\theta + H_\phi \mathbf{u}_\phi &= \frac{1}{r^2 \sin \theta} \begin{vmatrix} \mathbf{u}_r & r \mathbf{u}_\theta & r \sin \theta \mathbf{u}_\phi \\ \frac{\partial}{\partial r} & \frac{\partial}{\partial \theta} & \frac{\partial}{\partial \phi} \\ A_r & 0 & 0 \end{vmatrix} \\ &= \mathbf{u}_\theta \frac{1}{r \sin \theta} \frac{\partial A_r}{\partial \phi} - \mathbf{u}_\phi \frac{1}{r} \frac{\partial A_r}{\partial \theta} \end{aligned} \quad (3.108)$$

³The functions $P_n^m(\cos \theta) \cos m\phi$ and $P_n^m(\cos \theta) \sin m\phi$ are called even and odd *tesseral harmonics* respectively because of their similarity with sinusoidal functions, and also due to fact that these sets form a complete orthogonal set on the surface of a sphere.

where \mathbf{u}_r , \mathbf{u}_θ , and \mathbf{u}_ϕ are unit vectors in r , θ , and ϕ directions respectively. The above equation is simplified to obtain

$$H_r^- = 0 \quad H_r^+ = 0 \quad (3.109a)$$

$$H_\theta^- = \frac{-m}{r \sin \theta} P_n^m(\cos \theta) \sin m\phi \hat{H}_n^{(1)}(kr) \quad (3.109b)$$

$$H_\theta^+ = \frac{-m}{r \sin \theta} P_n^m(\cos \theta) \sin m\phi \hat{H}_n^{(2)}(kr)$$

$$H_\phi^- = \frac{-1}{r} P_n^{m'}(\cos \theta) \cos m\phi \hat{H}_n^{(1)}(kr) \quad (3.109c)$$

$$H_\phi^+ = \frac{-1}{r} P_n^{m'}(\cos \theta) \cos m\phi \hat{H}_n^{(2)}(kr)$$

where,

$$P_n^{m'}(\cos \theta) = \frac{d}{d\theta} [P_n^m(\cos \theta)] \quad (3.110)$$

represents the first order derivative of $P_n^m(\cos \theta)$. The electric field components for this mode are obtained by expanding one of the Maxwell's curl equations in the spherical coordinate system and making H_r component to zero as per (3.109), i.e.

$$\begin{aligned} \nabla \times \mathbf{H} &= j\omega\varepsilon\mathbf{E} \\ \Rightarrow \mathbf{u}_r \frac{1}{r \sin \theta} \left[\frac{\partial}{\partial \theta} (\sin \theta H_\phi) - \frac{\partial H_\theta}{\partial \phi} \right] - \mathbf{u}_\theta \frac{1}{r} \frac{\partial}{\partial r} (r H_\phi) + \mathbf{u}_\phi \frac{1}{r} \frac{\partial}{\partial r} (r H_\theta) & \quad (3.111) \\ &= j\omega\varepsilon [E_r \mathbf{u}_r + E_\theta \mathbf{u}_\theta + E_\phi \mathbf{u}_\phi] \end{aligned}$$

where $\varepsilon = \varepsilon_0 \varepsilon_r(r)$ is the total permittivity in the spherical dielectric media. The above equations are solved after substituting the value of H_θ and H_ϕ from (3.109) and this yields the following electric field components

$$E_r^- = \frac{1}{j\omega\varepsilon r \sin \theta} \left[\frac{\partial}{\partial \theta} (\sin \theta H_\phi^-) - \frac{\partial H_\theta^-}{\partial \phi} \right] = \frac{1}{j\omega\varepsilon_0 \varepsilon_r(r)} \left[\frac{\partial^2}{\partial r^2} + k^2 \right] A_r^- \quad (3.112a)$$

$$E_r^+ = \frac{1}{j\omega\varepsilon r \sin \theta} \left[\frac{\partial}{\partial \theta} (\sin \theta H_\phi^+) - \frac{\partial H_\theta^+}{\partial \phi} \right] = \frac{1}{j\omega\varepsilon_0 \varepsilon_r(r)} \left[\frac{\partial^2}{\partial r^2} + k^2 \right] A_r^+$$

$$E_\theta^- = \frac{-1}{j\omega\varepsilon r} \frac{\partial}{\partial r} [r H_\phi^-] = \frac{1}{j\omega\varepsilon_0 \varepsilon_r(r) r} P_n^{m'}(\cos \theta) \cos m\phi \hat{H}_n^{(1)'}(kr) \quad (3.112b)$$

$$E_\theta^+ = \frac{-1}{j\omega\varepsilon r} \frac{\partial}{\partial r} [r H_\phi^+] = \frac{1}{j\omega\varepsilon_0 \varepsilon_r(r) r} P_n^{m'}(\cos \theta) \cos m\phi \hat{H}_n^{(2)'}(kr)$$

$$E_\phi^- = \frac{1}{j\omega\varepsilon r} \frac{\partial}{\partial r} [r H_\theta^-] = \frac{-m}{j\omega\varepsilon_0 \varepsilon_r(r) r \sin \theta} P_n^m(\cos \theta) \sin m\phi \hat{H}_n^{(1)'}(kr) \quad (3.112c)$$

$$E_\phi^+ = \frac{1}{j\omega\varepsilon r} \frac{\partial}{\partial r} [r H_\theta^+] = \frac{-m}{j\omega\varepsilon_0 \varepsilon_r(r) r \sin \theta} P_n^m(\cos \theta) \sin m\phi \hat{H}_n^{(2)'}(kr)$$

where

$$\hat{H}_n^{(p)'}(kr) = \frac{d}{dr} [\hat{H}_n^{(p)}(kr)] \quad p = 1 \quad \text{or} \quad 2 \quad (3.113)$$

is the first order derivative of the spherical Hankel function of order n . Equations (3.112b) and (3.112c) directly follow from (3.109). However, for the derivation of (3.112a), we have used the following scalar Helmholtz equation for the r component of the magnetic vector potential in the spherical coordinate system [16]

$$\frac{\partial^2 A_r}{\partial r^2} + \frac{1}{r^2 \sin \theta} \frac{\partial}{\partial \theta} \left(\sin \theta \frac{\partial A_r}{\partial \theta} \right) + \frac{1}{r^2 \sin^2 \theta} \frac{\partial^2 A_r}{\partial \phi^2} + k^2 A_r = 0 \quad (3.114)$$

The second order derivative $\frac{\partial^2 A_r}{\partial r^2}$ in (3.112a) is expressed in terms of the wave function A_r using (B.11) as follows

$$\frac{\partial^2 A_r}{\partial r^2} = k^2 \left[\frac{n(n+1)}{k^2 r^2} - 1 \right] A_r \quad (3.115)$$

The above equation is then substituted in (3.112a) to obtain E_r components

$$\begin{aligned} E_r^- &= \left[\frac{n(n+1)}{j\omega\varepsilon_0\varepsilon_r(r)r^2} \right] P_n^m(\cos\theta) \cos m\phi \hat{H}_n^{(1)}(kr) \\ E_r^+ &= \left[\frac{n(n+1)}{j\omega\varepsilon_0\varepsilon_r(r)r^2} \right] P_n^m(\cos\theta) \cos m\phi \hat{H}_n^{(2)}(kr) \end{aligned} \quad (3.116)$$

After obtaining all field components for this mode, our next task is to formulate the direct or forward problem in such a way that the wave incident from the free space ($r \geq a$) travels inside the dielectric object in the radial direction towards the origin, and then it gets reflected from different layers of this inhomogeneous spherical object producing a net reflection coefficient at the outer air-dielectric interface at $r = a$ as shown in Fig. 3.19. The formulation of the direct problem here will include the effect of *multiple reflections* from different layers of the spherical inhomogeneous media as was the case in planar and cylindrical structures. If we look at equations (3.109) and (3.112), then we can relate the incident field components with the corresponding reflected components as follows

$$\begin{aligned} H_\theta^+ &= (H_\theta^-)^* \\ E_\phi^+ &= -(E_\phi^-)^* \end{aligned} \quad (3.117)$$

It may be noted that our aim here is to analyze the inhomogeneity in the r -direction, and hence we have considered H_θ and E_ϕ components in (3.117), which are used to define the radially directed impedance in the spherical geometry. Now, to consider this radial inhomogeneity using the reflection theory, we define the field components as

$$H_\theta = H_\theta^- + \tilde{\Gamma} H_\theta^+ = H_\theta^- + \tilde{\Gamma} (H_\theta^-)^* \quad (3.118a)$$

$$E_\phi = E_\phi^- + \tilde{\Gamma} E_\phi^+ = E_\phi^- - \tilde{\Gamma} (E_\phi^-)^* \quad (3.118b)$$

where $\tilde{\Gamma}$ is an intermediate reflection coefficient, and we have made use of (3.117). This factor $\tilde{\Gamma}$ is reformulated to have the following form

$$\Gamma = \tilde{\Gamma} \frac{(H_\theta^-)^*}{H_\theta^-} \quad (3.119)$$

This value of Γ can be substituted in (3.118) to arrive at

$$H_\theta = H_\theta^- \left[1 + \tilde{\Gamma} \frac{(H_\theta^-)^*}{H_\theta^-} \right] = H_\theta^- [1 + \Gamma] \quad (3.120a)$$

$$\begin{aligned} E_\phi &= E_\phi^- \left[1 - \tilde{\Gamma} \frac{(E_\phi^-)^*}{E_\phi^-} \right] = Z H_\theta^- \left[1 - \tilde{\Gamma} \frac{(E_\phi^-)^*}{(H_\theta^-)^*} \frac{(H_\theta^-)^*}{H_\theta^-} \frac{H_\theta^-}{E_\phi^-} \right] \\ &= Z H_\theta^- \left[1 - \Gamma \frac{Z^*}{Z} \right] = Z H_\theta^- [1 - \alpha_s \Gamma] \end{aligned} \quad (3.120b)$$

It may be noted here that after the reformulation of the reflection coefficient in (3.119), equations (3.120a) and (3.120b) have the standard form as in the planar and cylindrical cases. The impedance Z for the inward travelling waves in above equations is defined as

$$Z = Z_{-r}^{TM_{mn}} = \frac{E_\phi^-}{H_\theta^-} = -\frac{j\eta_0}{k_0 \varepsilon_r(r)} \frac{\hat{H}_n^{(1)'}(kr)}{\hat{H}_n^{(1)}(kr)} \quad (3.121)$$

where the values of H_θ and E_ϕ are substituted from (3.109) and (3.112), and $\alpha_s = \frac{Z^*}{Z}$. Now, for considering the radial inhomogeneity here, the radial derivatives of E_ϕ and H_θ are needed. The radial derivative of H_θ is defined using (3.112c). For the computation of radial derivative of E_ϕ , the Maxwell's second curl equation $\nabla \times \mathbf{E} = -j\omega\mu_0\mathbf{H}$ has to be expanded into the spherical coordinate system for the TM_{mn} mode, and this gives

$$\left[\frac{\partial}{\partial \theta} (\sin \theta E_\phi) - \frac{\partial E_\theta}{\partial \phi} \right] = 0 \quad (3.122a)$$

$$\left[\frac{\partial}{\partial r} (r E_\phi) - \frac{1}{\sin \theta} \frac{\partial E_r}{\partial \phi} \right] = j\omega\mu_0 r H_\theta \quad (3.122b)$$

$$\left[\frac{\partial E_r}{\partial \theta} - \frac{\partial}{\partial r} (r E_\theta) \right] = j\omega\mu_0 r H_\phi \quad (3.122c)$$

Equation (3.122b) is next solved to compute the radial derivative of E_ϕ in term of H_θ

$$\begin{aligned} \frac{\partial}{\partial r} (r E_\phi) &= j\omega\mu_0 r H_\theta + \frac{1}{\sin \theta} \frac{\partial E_r}{\partial \phi} \\ &= j\omega\mu_0 r H_\theta + \frac{n(n+1)}{j\omega\varepsilon_0\varepsilon_r(r)r} H_\theta = \left[\frac{n(n+1) - k^2 r^2}{j\omega\varepsilon_0\varepsilon_r(r)r} \right] H_\theta \end{aligned} \quad (3.123)$$

where (3.116) is used to compute the ϕ -derivative of E_r . Meanwhile, (3.123) is written together along with (3.112c) in terms of the common variable H_θ^- using (3.120)

$$jk_0 r \varepsilon_r(r) \bar{Z} (1 - \alpha_s \Gamma) [H_\theta^-] = \frac{\partial}{\partial r} [r (1 + \Gamma) H_\theta^-] \quad (3.124a)$$

$$\left[\frac{n(n+1) - k^2 r^2}{jk_0 r \varepsilon_r(r)} \right] (1 + \Gamma) [H_\theta^-] = \frac{\partial}{\partial r} [r \bar{Z} (1 - \alpha_s \Gamma) H_\theta^-] \quad (3.124b)$$

where,

$$\bar{Z} = \frac{Z_{-r}^{TM_{mn}}}{\eta_0} = \frac{-j}{(2n+1) \sqrt{\varepsilon_r(r)}} \left[\frac{(1+n) \hat{H}_{n-1}^{(1)}(kr) - n \hat{H}_{n+1}^{(1)}(kr)}{\hat{H}_n^{(1)}(kr)} \right] \quad (3.125)$$

is the normalized impedance for the TM_{mn} spherical mode, and

$$\alpha_s = \frac{\bar{Z}^*}{\bar{Z}} = - \frac{[(1+n) \hat{H}_{n-1}^{(2)}(kr) - n \hat{H}_{n+1}^{(2)}(kr)] \hat{H}_n^{(1)}(kr)}{[(1+n) \hat{H}_{n-1}^{(1)}(kr) - n \hat{H}_{n+1}^{(1)}(kr)] \hat{H}_n^{(2)}(kr)} \quad (3.126)$$

Our next task is to solve (3.124a) and (3.124b) to eliminate the common variable H_θ^- , and for doing this the method proposed in Appendix A can be used to obtain

$$\begin{aligned} r(1+\Gamma) \left[\frac{n(n+1) - k^2 r^2}{jk_0 r \varepsilon_r(r)} (1+\Gamma) - (1 - \alpha_s \Gamma) \frac{\partial}{\partial r} (r \bar{Z}) + r \bar{Z} \left(\alpha_s \frac{\partial \Gamma}{\partial r} + \Gamma \frac{\partial \alpha_s}{\partial r} \right) \right] \\ + r \bar{Z} (1 - \alpha_s \Gamma) \left[1 + \Gamma + r \frac{\partial \Gamma}{\partial r} - jk_0 r \varepsilon_r(r) \bar{Z} (1 - \alpha_s \Gamma) \right] = 0 \end{aligned} \quad (3.127)$$

The above equation is simplified to combine the terms containing Γ , Γ^2 , and $\partial \Gamma / \partial r$ etc ...

$$\frac{\partial \Gamma}{\partial r} + \frac{1}{(1 + \alpha_s) r \bar{Z}} \left\{ \begin{aligned} & \Gamma^2 \left[\frac{n(n+1) - k^2 r^2}{jk_0 r \varepsilon_r(r)} - jk_0 r \varepsilon_r(r) \alpha_s^2 \bar{Z}^2 + r \frac{\partial}{\partial r} (\alpha_s \bar{Z}) \right] \\ & + \Gamma \left[\frac{2[n(n+1) - k^2 r^2]}{jk_0 r \varepsilon_r(r)} + j2k_0 r \varepsilon_r(r) \alpha_s \bar{Z}^2 \right. \\ & \quad \left. + r \frac{\partial}{\partial r} ((\alpha_s - 1) \bar{Z}) \right] \\ & + \left[\frac{n(n+1) - k^2 r^2}{jk_0 r \varepsilon_r(r)} - jk_0 r \varepsilon_r(r) \bar{Z}^2 - r \frac{\partial \bar{Z}}{\partial r} \right] \end{aligned} \right\} = 0 \quad (3.128)$$

The different terms in (3.128) are computed after substituting the values of \bar{Z} and α_s from (3.125) and (3.126). The derivative $\frac{\partial \bar{Z}}{\partial r}$, after some simplifications, is given by

$$\frac{\partial \bar{Z}}{\partial r} = \frac{-j}{(2n+1)} \left\{ \begin{array}{l} \frac{2n(n+1)(2n+1)}{k_0 r^2 \varepsilon_r(r)} - k_0(2n+1) - k_0 n \frac{\hat{H}_{n+1}^{(1)^2}(kr)}{\hat{H}_n^{(1)^2}(kr)} \\ - k_0(n+1) \frac{\hat{H}_{n-1}^{(1)^2}(kr)}{\hat{H}_n^{(1)^2}(kr)} - \frac{1}{2\varepsilon_r(r) \sqrt{\varepsilon_r(r)}} \frac{d\varepsilon_r(r)}{dr} \\ \cdot \left[\frac{[(1+n)\hat{H}_{n-1}^{(1)}(kr) - n\hat{H}_{n+1}^{(1)}(kr)]}{\hat{H}_n^{(1)}(kr)} \right] \end{array} \right\} \quad (3.129)$$

Similarly the other derivative $\frac{\partial}{\partial r} (\alpha_s \bar{Z})$ in (3.128) can be simplified to give

$$\frac{\partial}{\partial r} (\alpha_s \bar{Z}) = \frac{j}{(2n+1)} \left\{ \begin{array}{l} \frac{2n(n+1)(2n+1)}{k_0 r^2 \varepsilon_r(r)} - k_0(2n+1) - k_0 n \frac{\hat{H}_{n+1}^{(2)^2}(kr)}{\hat{H}_n^{(2)^2}(kr)} \\ - k_0(n+1) \frac{\hat{H}_{n-1}^{(2)^2}(kr)}{\hat{H}_n^{(2)^2}(kr)} - \frac{1}{2\varepsilon_r(r) \sqrt{\varepsilon_r(r)}} \frac{d\varepsilon_r(r)}{dr} \\ \cdot \left[\frac{[(1+n)\hat{H}_{n-1}^{(2)}(kr) - n\hat{H}_{n+1}^{(2)}(kr)]}{\hat{H}_n^{(2)}(kr)} \right] \end{array} \right\} \quad (3.130)$$

The other terms in (3.128) may be computed as

$$jk_0 r \varepsilon_r(r) \bar{Z}^2 = \frac{j 2k_0 r n(n+1)}{(2n+1)^2} \frac{\hat{H}_{n-1}^{(1)}(kr) \hat{H}_{n+1}^{(1)}(kr)}{\hat{H}_n^{(1)^2}(kr)} \quad (3.131a)$$

$$- \frac{jk_0 r}{(2n+1)^2 \hat{H}_n^{(1)^2}(kr)} \left[(n+1)^2 \hat{H}_{n-1}^{(1)^2}(kr) + n^2 \hat{H}_{n+1}^{(1)^2}(kr) \right]$$

$$jk_0 r \varepsilon_r(r) \alpha_s^2 \bar{Z}^2 = \frac{j 2k_0 r \varepsilon_r(r) n(n+1)}{(2n+1)^2} \frac{\hat{H}_{n-1}^{(2)}(kr) \hat{H}_{n+1}^{(2)}(kr)}{\hat{H}_n^{(2)^2}(kr)} \quad (3.131b)$$

$$- \frac{jk_0 r}{(2n+1)^2 \hat{H}_n^{(2)^2}(kr)} \left[(n+1)^2 \hat{H}_{n-1}^{(2)^2}(kr) + n^2 \hat{H}_{n+1}^{(2)^2}(kr) \right]$$

$$\frac{1}{(1+\alpha_s) \bar{Z}} = \frac{\sqrt{\varepsilon_r(r)} \hat{H}_n^{(1)}(kr) \hat{H}_n^{(2)}(kr)}{2} \quad (3.131c)$$

$$j2k_0 r \varepsilon_r(r) \alpha_s \bar{Z}^2 = - \frac{j2n(n+1)}{(2n+1) \sqrt{\varepsilon_r(r)}} \left[\frac{\hat{H}_{n-1}^{(1)}(kr)}{\hat{H}_n^{(1)}(kr)} + \frac{\hat{H}_{n+1}^{(1)}(kr)}{\hat{H}_n^{(1)}(kr)} \right] \quad (3.132)$$

$$+ \frac{j2k_0 r}{(2n+1)} \left[\frac{(n+1)\hat{H}_{n-1}^{(1)}(kr)\hat{H}_{n-1}^{(2)}(kr)}{\hat{H}_n^{(1)}(kr)\hat{H}_n^{(2)}(kr)} + \frac{n\hat{H}_{n+1}^{(1)}(kr)\hat{H}_{n+1}^{(2)}(kr)}{\hat{H}_n^{(1)}(kr)\hat{H}_n^{(2)}(kr)} \right]$$

The derivative $\frac{\partial}{\partial r} ((\alpha_s - 1) \bar{Z})$ in (3.128) can be expressed using (3.129) and (3.130), and finally all individual terms computed above are combined together in (3.128)

to obtain the following nonlinear differential equation for the spherical geometry in terms of a frequency-dependent reflection coefficient $\Gamma(k_0, r)$

$$\begin{aligned} \frac{\partial \Gamma}{\partial r} + \Gamma & \left\{ \frac{j2k_0 \sqrt{\varepsilon_r(r)}}{\hat{H}_n^{(1)}(kr) \hat{H}_n^{(2)}(kr)} - \frac{j}{4\varepsilon_r(r)(2n+1)} \frac{d\varepsilon_r(r)}{dr} \right. \\ & \left. \left[\begin{array}{l} (1+n) \left[\hat{H}_n^{(2)}(kr) \hat{H}_{n-1}^{(1)}(kr) + \hat{H}_n^{(1)}(kr) \hat{H}_{n-1}^{(2)}(kr) \right] \\ -n \left[\hat{H}_n^{(2)}(kr) \hat{H}_{n+1}^{(1)}(kr) + \hat{H}_{n+1}^{(2)}(kr) \hat{H}_n^{(1)}(kr) \right] \end{array} \right] \right\} \\ & = -\frac{j}{4\varepsilon_r(r)} \frac{d\varepsilon_r(r)}{dr} \frac{\hat{H}_n^{(2)}(kr)}{(2n+1)} \left[n\hat{H}_{n+1}^{(1)}(kr) - (n+1)\hat{H}_{n-1}^{(1)}(kr) \right] [1 - \alpha_s \Gamma^2] \end{aligned} \quad (3.133)$$

The above equation is the *Riccati-similar* differential equation due to a TM_{mn} spherical mode illumination, and it provides a direct relationship between the one-dimensional radially varying permittivity profile of spherical dielectric objects, and the frequency-dependent reflection coefficient data measured at the outer air-dielectric boundary.

The analysis for an arbitrary order TE_{mn} mode illumination in the spherical coordinate system can be carried out on similar lines as described above for the TM_{mn} mode. The final expression of the *Riccati-similar* non-linear differential equation for the radially varying frequency-dependent reflection coefficient $\Gamma(k_0, r)$ due to a TE_{mn} illumination in the spherical geometry is given by

$$\begin{aligned} \frac{\partial \Gamma}{\partial r} + \Gamma & \left\{ \frac{j2k_0 \sqrt{\varepsilon_r(r)}}{\hat{H}_n^{(1)}(kr) \hat{H}_n^{(2)}(kr)} + \frac{j}{4\varepsilon_r(r)(2n+1)} \frac{d\varepsilon_r(r)}{dr} \right. \\ & \left. \left[\begin{array}{l} (1+n) \left[\hat{H}_n^{(2)}(kr) \hat{H}_{n-1}^{(1)}(kr) + \hat{H}_n^{(1)}(kr) \hat{H}_{n-1}^{(2)}(kr) \right] \\ -n \left[\hat{H}_n^{(2)}(kr) \hat{H}_{n+1}^{(1)}(kr) + \hat{H}_{n+1}^{(2)}(kr) \hat{H}_n^{(1)}(kr) \right] \end{array} \right] \right\} \\ & = \frac{j}{4\varepsilon_r(r)} \frac{d\varepsilon_r(r)}{dr} \frac{\hat{H}_n^{(2)}(kr)}{(2n+1)} \left[n\hat{H}_{n+1}^{(1)}(kr) - (n+1)\hat{H}_{n-1}^{(1)}(kr) \right] [1 - \alpha_s \Gamma^2] \end{aligned} \quad (3.134)$$

where $n = 0, 1, 2, \dots$. The above described formulation for the TE_{mn} and TM_{mn} modes helps in analyzing cylindrical structures having one-dimensional radially varying permittivity profile, for any arbitrary order TE or TM mode illumination.

3.3.2 Lower order mode illuminations

In the last sub-section, we have formulated the direct problem for spherical dielectric objects illuminated by any arbitrary order TE_{mn} or TM_{mn} mode. As can be seen from equations (3.133) and (3.134), the formulation for any higher order mode is quite complicated in the case of spherical geometry. However, for lower order illuminations these equations reduce to very simple forms. The simplicity is mainly obtained because of the fact that the spherical Hankel functions of lower order can be replaced by the exponential functions. In this section, we obtain specialized forms of (3.133) and (3.134) for lower order modes. The lowest possible TM to r

mode in the spherical geometry is TM_{01} mode and the wave function for this mode, considering *even tesseral harmonics*, is given by [16]

$$\Psi_{01}^{TM} = (A_r)_{01} = \cos \theta \hat{H}_1^{(p)}(kr) \quad p = 1 \quad \text{or} \quad 2 \quad (3.135)$$

where,

$$\hat{H}_1^{(1)}(kr) = -e^{jkr} \left(1 + \frac{j}{kr} \right) \quad (3.136)$$

is the spherical Hankel function of the first kind of order one representing an inward travelling wave, and

$$\hat{H}_1^{(2)}(kr) = -e^{-jkr} \left(1 - \frac{j}{kr} \right) \quad (3.137)$$

is the spherical Hankel function of the second kind of order one representing an outward travelling wave. From (3.135), (3.136) and (3.137), it can be seen that for this lower order illumination the associated Legendre functions are replaced by the simple trigonometric functions, and the spherical Hankel functions are replaced by the exponential functions. It is mainly because of these substitutions that equations for the lower order mode become simpler in form than corresponding equations for the higher order modes. The expression for the normalized impedance and the factor α_s for the TM_{01} to r mode is given by

$$\bar{Z}_{-r}^{TM_{01}} = \frac{1}{\sqrt{\varepsilon_r(r)}} \left[\frac{j}{kr} + \frac{1}{(1 + j/kr)} \right] \quad (3.138)$$

$$\alpha_s^{TM_{01}} = \frac{Z_{-r}^{TM_{01}*}}{Z_{-r}^{TM_{01}}} = \frac{k^3 r^3 - j}{k^3 r^3 + j} \quad (3.139)$$

The simpler forms of (3.138) and (3.139) can be appreciated if we compare these equations with (3.125) and (3.126) of the corresponding higher order mode illuminations. The analysis of this lower order spherical mode illumination using the procedure laid down in the last section will yield (3.128) with $n = 1$. The value of \bar{Z} and α_s can then be substituted from (3.138) and (3.139) into the reduced equation, and this finally leads to

$$\frac{\partial \Gamma}{\partial r} + \Gamma \left[\frac{2jk^3 r^2}{(k^2 r^2 + 1)} + \frac{j}{2k^3 r^3 \varepsilon_r(r)} \frac{d\varepsilon_r(r)}{dr} \right] = -\frac{(j + k^3 r^3)}{4k^3 r^3 \varepsilon_r(r)} \frac{d\varepsilon_r(r)}{dr} [1 - \alpha_s \Gamma^2] \quad (3.140)$$

which is the *Riccati-similar* nonlinear differential equation for the spherical geometry due to a TM_{01} mode illumination.

The analysis for the lower order TE mode illumination can also be carried out in a similar way as described above for the TM case, and this leads to the following nonlinear differential equation in terms of the frequency-dependent reflection coefficient $\Gamma(k_0, r)$ for a TE_{01} to r spherical mode illumination

$$\frac{\partial \Gamma}{\partial r} + \Gamma \left[\frac{2jk^3 r^2}{(k^2 r^2 + 1)} - \frac{j}{2k^3 r^3 \varepsilon_r(r)} \frac{d\varepsilon_r(r)}{dr} \right] = \frac{(j + k^3 r^3)}{4k^3 r^3 \varepsilon_r(r)} \frac{d\varepsilon_r(r)}{dr} [1 - \alpha_s \Gamma^2] \quad (3.141)$$

Chapter 4

The Inverse Solution

The last chapter discussed in detail the direct problem formulation of planar, cylindrical and spherical objects to analyze the one-dimensional inhomogeneity. In this chapter, we will describe in detail the proposed technique to invert those direct problems. It has already been mentioned that the reconstruction of permittivity profiles is basically an inverse process and hence proposing an appropriate algorithm for the inversion of the corresponding direct problem is the most crucial part in the whole reconstruction process. We start this section with a simple planar geometry, and then consequently cylindrical and spherical geometries are considered to obtain a closed-form expression for the depth-dependent permittivity profile in each case.

4.1 The planar geometry

First of all, we take the planar inhomogeneous medium considered in section 3.1, and described by the Fig. 3.1. We assume that the one-dimensional *unknown* permittivity profile is given by $\varepsilon_r(x)$ in the region $x \geq 0$ starting from ε_{r0} at $x = 0$. It is assumed that the relative permittivity of the background medium is same as that of free space i.e. $\varepsilon_r(x) = 1$ for $x < 0$, and hence there will be a discontinuity at the interface $x = 0$. We consider here all cases of illuminations viz. TEM, TE and TM.

4.1.1 TEM illumination

For the *TEM*-case, a monochromatic plane wave of wavenumber k_0 is incident *normally* from the Left hand side at the interface $x = 0$ as shown in Fig. 3.1. The exact Riccati non-linear differential equation for the one-dimensional planar inhomogeneous media illuminated by a *TEM* plane wave has been derived in section 3.1.1 and is given by (3.18). This equation is basically a non-linear one in Γ because of the presence of Γ^2 term and hence it does not have any general analytical solution. However, for the direct problem solution, (3.18) can always be solved *numerically* for a given permittivity profile to obtain the frequency-dependent reflection coefficient data. But as mentioned earlier, the basic aim of our work is to seek a stable *inversion* of (3.18), which is much more complicated process as compared to the direct problem solution. To describe our proposed technique of inversion, the Riccati equation for the TEM case (3.18) is rewritten in the following form

$$\frac{1}{(1-\Gamma^2)} \frac{d\Gamma}{dx} = j2k_0 \sqrt{\varepsilon_r(x)} \frac{\Gamma}{(1-\Gamma^2)} + \frac{1}{4\varepsilon_r(x)} \frac{d\varepsilon_r(x)}{dx} \quad (4.1)$$

In the next step, a *virtual reflection coefficient* $\hat{\Gamma}$ is introduced as the solution of a linearized version of (4.1), which is called the *auxiliary equation*

$$\frac{d\hat{\Gamma}}{dx} = j2k_0 \sqrt{\varepsilon_r(x)} \hat{\Gamma} + \frac{1}{4\varepsilon_r(x)} \frac{d\varepsilon_r(x)}{dx} \quad (4.2)$$

The subtraction of (4.1) from (4.2) gives

$$\left[\frac{d\hat{\Gamma}}{dx} - \frac{1}{(1-\Gamma^2)} \frac{d\Gamma}{dx} \right] = j2k_0 \sqrt{\varepsilon_r(x)} \left[\hat{\Gamma} - \frac{\Gamma}{(1-\Gamma^2)} \right] \quad (4.3)$$

For equation (4.3) to be satisfied for all values of $\sqrt{\varepsilon_r(x)}$, the terms in parenthesis on both sides of this equation should be zero. This can be achieved only if

$$\hat{\Gamma} = \tanh^{-1} \Gamma, \quad \text{and} \quad \hat{\Gamma} = \frac{\Gamma}{(1-\Gamma^2)} \quad (4.4)$$

where we have made use of the following relationship

$$\frac{d}{dx} \tanh^{-1} \Gamma(x) = \frac{1}{1-\Gamma^2(x)} \frac{d\Gamma(x)}{dx} \quad (4.5)$$

Equation (4.4) can not be fulfilled because of the following. Let us expand the inverse hyperbolic tangent function into its Taylor series as shown below, and then try to find out the conditions under which (4.4) may be valid approximately

$$\begin{aligned} \tanh^{-1} \Gamma &= \Gamma + \frac{\Gamma^3}{3} + \frac{\Gamma^5}{5} + \dots \\ \Rightarrow \frac{1-\Gamma^2}{\Gamma} \tanh^{-1} \Gamma &= (1-\Gamma^2) \left(1 + \frac{\Gamma^2}{3} + \frac{\Gamma^4}{5} + \dots \right) \\ &= 1 - \frac{2}{3} \Gamma^2 - \frac{2}{15} \Gamma^4 + \dots \end{aligned} \quad (4.6)$$

The above equation suggests that (4.4) will be *approximately* satisfied only when all the terms starting from its second order on the right hand side of (4.4) are negligible. Form this discussion, it is clear that (4.3) can never be made *exactly* satisfied as the higher order terms involving Γ are not zero under any circumstance. However, this equation can be approximated in two ways. The first approach is to make the virtual reflection coefficient $\hat{\Gamma} = \tanh^{-1} \Gamma$, in which case the left hand side (LHS) of (4.3) would be exactly satisfied but the right hand side (RHS) has to be approximated. The second choice is to make $\hat{\Gamma} = \frac{\Gamma}{(1-\Gamma^2)}$, which will make the RHS of (4.3) exactly zero but in this case the LHS of this equation has to be approximated. In past all the authors who used this method have either taken the first approximation (i.e. $\hat{\Gamma} = \tanh^{-1} \Gamma$) (see e.g. [59]), or have simply neglected the Γ^2 term (e.g. [60], [94]), to solve these kinds of inverse problems. This is obviously biased in one direction. Another possibility could be to consider the second approximation (i.e. $\hat{\Gamma} = \frac{\Gamma}{(1-\Gamma^2)}$), which would be then biased in the other direction.

Our approach for solving the exact nonlinear differential equation (4.1), however, does not involve any approximation at the first instance. We choose the linearized version of (4.1) in terms of a virtual reflection coefficient $\hat{\Gamma}$, and the exact relationship between Γ and $\hat{\Gamma}$ can be found later on depending on our requirement. For example, if we just want a qualitative reconstruction of the image, then we can select a very simple relationship between Γ and $\hat{\Gamma}$. On the other hand, if a very accurate quantitative image of the dielectric object is required, then in that case the virtual reflection coefficient $\hat{\Gamma}$ might be a complicated function of Γ . Hence using our proposed method, we have a choice of selecting the virtual reflection coefficient and the corresponding linear differential equation in a flexible way. We have observed that the following relationship between Γ and $\hat{\Gamma}$ provides a solution, which is very close to optimum

$$\hat{\Gamma} = \frac{1}{2} \left[\tanh^{-1} \Gamma + \frac{\Gamma}{(1 - \Gamma^2)} \right] \quad (4.7)$$

As a matter of fact, we have found that the above choice gives us much better result than previously used approaches for all cases of practical importance, as will be shown in some of the reconstructed examples in the next chapter. The above formula (4.7) works quite well for numerical examples, i.e., cases where the measured reflection coefficient data is given over a frequency band. However, sometimes we are given the reflection coefficient function in an analytical form and our job is to find the equivalent impedance or the permittivity profile. One practical example for this kind of situation is e.g. the conventional filter design, where the reflection coefficient is given as a function of frequency or the wavenumber to define the passband characteristics, and it is required to find the optimum impedance profile corresponding to these passband characteristics [79]. Under these circumstances, it would be quite complicated to use (4.7) because of the presence of a hyperbolic trigonometric function. We have tried to find an alternative form of (4.7) for such cases, and this is given by

$$\hat{\Gamma} = \frac{\Gamma}{(1 - \Gamma^2)} - \frac{1}{3} \Gamma^3 \quad (4.8)$$

The above equation is obtained after substituting the value of hyperbolic tangent function from (4.6) in (4.7)

$$\begin{aligned} \tanh^{-1} \Gamma &\simeq \left(\frac{\Gamma}{(1 - \Gamma^2)} \right) \left(1 - \frac{2}{3} \Gamma^2 \right) \\ \Rightarrow \frac{1}{2} \left[\tanh^{-1} \Gamma + \frac{\Gamma}{(1 - \Gamma^2)} \right] &= \frac{1}{2} \left\{ \frac{\Gamma}{(1 - \Gamma^2)} \left[1 + 1 - \frac{2}{3} \Gamma^2 \right] \right\} \\ &= \frac{\Gamma}{(1 - \Gamma^2)} - \frac{1}{3} \Gamma^3 - \frac{1}{3} \Gamma^5 \dots \end{aligned} \quad (4.9)$$

It may be observed from (4.9) that in deriving (4.8), the higher order terms of Γ starting from Γ^4 are disregarded. However, this has been done just to ease the complexity involved, otherwise we are free to choose as many terms as we want in order to increase the accuracy. It is mainly this flexibility of choosing the algebraic transformation between the measured Γ and virtual $\hat{\Gamma}$, that gives our method an

edge over other available methods for solving inverse problems. So the advantage of the above suggested technique is that we separate the nonlinearity of the exact Riccati equation into a nonlinear algebraic transformation, which relates the actual measurable reflection coefficient Γ and the virtual reflection coefficient $\hat{\Gamma}$. The choice of an algebraic transformation will be generally a compromise between the accuracy required and the complexity involved. The virtual $\hat{\Gamma}$ is not directly measurable, but it renders the differential equation relating the unknown permittivity profile to this virtual reflection coefficient linear (4.2). Our whole process of the reconstruction can be visualized more clearly as in Fig. 4.1. The important thing to be noted here

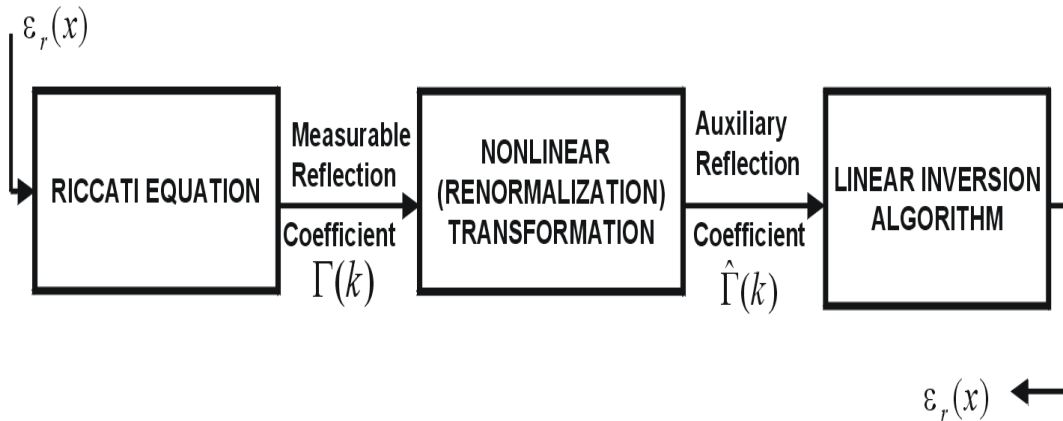


Figure 4.1: Schematic diagram for the direct and inverse problems

is that the proposed technique is based on compensating the difference between the original nonlinear Riccati equation (4.1) and the auxiliary linear one (4.2) via a nonlinear transformation, which in our case is given by (4.7). However, there are no severe constraints on the choice of the virtual reflection coefficient and the related auxiliary linear differential equation. The choice of the auxiliary equation (4.2) in our case after disregarding the quadrature term in (4.1) is just one possibility, and for this choice the required transformation is given by (4.7). Other choices for the selection of a virtual reflection coefficient and the corresponding auxiliary equation are possible as long as an appropriate transformation between the measurable and virtual reflection coefficients can be found.

After obtaining an optimum nonlinear transformation between the actual and the virtual reflection coefficient as discussed above, our next task is to integrate the auxiliary equation (4.2) involving the virtual reflection coefficient $\hat{\Gamma}$. For this purpose, we first consider the case when there is no discontinuity at the at the outer air-dielectric interface, i.e. $\varepsilon_r(0) = 1$ in Fig. 3.1. After obtaining a closed-form solution for this special case, the expression is generalized for any value of permittivity at the outer air-dielectric interface.

4.1.1.1 The special case with a continuity at the air-dielectric interface

For this case, we integrate (4.2) taking $\varepsilon_r(0) = 1$ in Fig. 3.1. The auxiliary equation (4.2) is clearly a linear differential equation, and hence it can be integrated from infinity to a finite point x to have a general solution of the following form [95]

$$\begin{aligned} \hat{\Gamma}(k_0, x) & \exp \left[- \int_{\infty}^x j2k_0 \sqrt{\varepsilon_r(x')} dx' \right] \\ & = \int_{\infty}^x \left\{ \frac{1}{4\varepsilon_r(x')} \frac{d\varepsilon_r(x')}{dx'} \exp \left[- \int_{\infty}^{x'} j2k_0 \sqrt{\varepsilon_r(x'')} dx'' \right] \right\} dx' + C \end{aligned} \quad (4.10)$$

where the constant C is the integration constant to be determined using an appropriate boundary condition, x' and x'' are dummy integration variables. The above equation can be used to analyze the one-dimensional inhomogeneous object of any arbitrary depth, and in the real situation the upper limit ∞ of the integral may be replaced by the approximate extent of the inhomogeneity. Now, let us suppose that the value of the reflection coefficient at infinity is given by Γ_{∞} , and if we use this boundary condition to compute the constant C in the above equation, then (4.10) reduces to

$$\begin{aligned} \hat{\Gamma}(k_0, x) & = \hat{\Gamma}_{\infty} \exp \left[\int_{\infty}^x j2k_0 \sqrt{\varepsilon_r(x')} dx' \right] \\ & + \int_{\infty}^x \left\{ \frac{1}{4\varepsilon_r(x')} \frac{d\varepsilon_r(x')}{dx'} \exp \left[\int_{x'}^x j2k_0 \sqrt{\varepsilon_r(x'')} dx'' \right] \right\} dx' \end{aligned} \quad (4.11)$$

Under the real situations the value of $\hat{\Gamma}_{\infty}$ can be quite often taken as zero. For example, if we are measuring the reflection coefficient of dielectric materials in a waveguide or in a coaxial airline, then we can always put a matched load at the end and this will make $\hat{\Gamma}_{\infty}$ as zero. The same concept can also be applied to the free-space measurements, where the sample is generally placed in an anechoic chamber and the end of the sample matches with the surrounding medium thus producing a net reflection coefficient of zero there. It may be, however, noted that (4.11) can be solved for any arbitrary boundary condition and making $\hat{\Gamma}_{\infty}$ equal to zero is just one of the possibilities. Equation (4.11) for the boundary condition $\hat{\Gamma}_{\infty} = 0$ reduces to

$$\hat{\Gamma}(k_0, x) = \int_{\infty}^x \left\{ \frac{1}{4\varepsilon_r(x')} \frac{d\varepsilon_r(x')}{dx'} \exp \left[\int_{x'}^x j2k_0 \sqrt{\varepsilon_r(x'')} dx'' \right] \right\} dx' \quad (4.12)$$

We are here basically looking for an expression for the frequency-dependent reflection coefficient measured at $x = 0$ in Fig. 3.1, as in real situations we can measure the reflection coefficient data only at the interface, and for this case $\hat{\Gamma}(k_0, 0) = \hat{R}(k_0)$ from (4.12) will be given by

$$\hat{R}(k_0) = - \int_0^{\infty} \left\{ \frac{1}{4\varepsilon_r(x)} \frac{d\varepsilon_r(x)}{dx} \exp \left[-j2k_0 \int_0^x \sqrt{\varepsilon_r(x')} dx' \right] \right\} dx \quad (4.13)$$

It can be easily observed that it is not possible to separate the space and frequency variable explicitly in the above equation because of the presence of $\sqrt{\varepsilon_r(x)}$ term, which is unknown, inside the exponential. For this purpose, we introduce here a virtual space variable

$$l = 2 \int_0^x \sqrt{\varepsilon_r(x')} dx' \quad (4.14)$$

which may be also thought of as the electrical length. This variable l is substituted in (4.13) to obtain

$$\hat{R}(k_0) = - \int_0^\infty \left[\frac{1}{8 \varepsilon_r(x) \sqrt{\varepsilon_r(x)}} \frac{d\varepsilon_r(x)}{dx} \right] \exp[-jk_0 l] dl \quad (4.15)$$

where we have also expressed dx in terms of dl using (4.14). The form of (4.15) now looks quite familiar and it can be compared with the standard Fourier transform equation (2.45) defined in chapter 2. After this comparison, we can recognize that the terms in the parenthesis on the RHS of (4.15) basically represents the inverse Fourier transform of $\Gamma(k_0)$, i.e.,

$$\hat{r}(l) = \mathfrak{F}^{-1} \left[\hat{R}(k_0) \right] = - \frac{1}{8 \varepsilon_r(x) \sqrt{\varepsilon_r(x)}} \frac{d\varepsilon_r(x)}{dx} \quad (4.16)$$

It may be noted here that $\hat{r}(l)$ is usually a causal function and hence its limit starts from zero rather than $-\infty$ in (4.15). The other point to be noted is that the Fourier-transform pair is defined here in the *wavenumber-distance* domain rather than in the conventional frequency-time domain. But this does not make any difference as long as the same convention is used throughout the analysis. Meanwhile, for $l \geq 0$, (4.16) can be rewritten as

$$\hat{r}(l) 2\sqrt{\varepsilon_r(x)} dx = - \frac{1}{4} \frac{d\varepsilon_r(x)}{\varepsilon_r(x)} \quad (4.17)$$

The above equation may be combined with the differential dl taken from (4.14) to obtain

$$d \ln \varepsilon_r(x) = -4 \hat{r}(l) dl \quad (4.18)$$

This equation can be integrated from the starting point $x = 0$ to any arbitrary electrical length l

$$\varepsilon_r(l) = \exp \left[-4 \int_0^l \hat{r}(l') dl' \right] \quad (4.19)$$

where l' is a dummy integration variable corresponding to x' using (4.14). As can be seen from (4.19), this equation gives the value of the permittivity in terms of the electrical length l . To obtain the value of one-dimensional inhomogeneous permittivity profile in terms of the actual depth x , we have to transform the electrical distance l into the real depth x . This transformation is achieved using our proposed numerical algorithm described in the later part of this chapter.

4.1.1.2 The general case with a discontinuity at the air-dielectric interface

In the last section, we discussed a special case when the surface value of the permittivity at the air-dielectric interface was unity, i.e. $\varepsilon_r(0) = 1$. However in most practical cases, there is always a discontinuity at the interface $x = 0$ as shown in Fig. 3.1. To take into account this discontinuity, we have to modify the formula given by (4.19). It was mentioned in section 3.1.1.1 that a discontinuous junction between two layers of different permittivities can be represented by a $[S]$ parameter network given by (3.6). The equivalent $[S]$ parameter network of the discontinuous

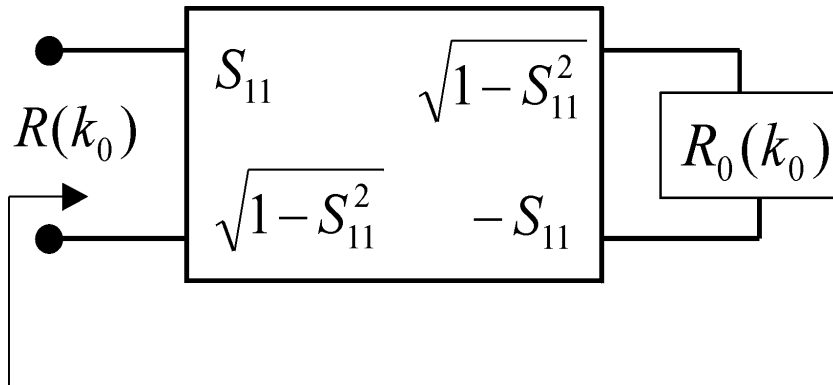


Figure 4.2: The equivalent $[S]$ parameter network of the permittivity discontinuity at the interface

media at $x = 0$ is shown in Fig. 4.2. The value of S_{11} in Fig. 4.2 is given by (3.5a), which for our case reduces to

$$S_{11} = \frac{1 - \sqrt{\epsilon_{r0}}}{1 + \sqrt{\epsilon_{r0}}} \quad (4.20)$$

where we have taken the background medium as air. The parameter $R_0(k_0)$ in Fig. 4.2 now represents the reflection coefficient of the equivalent *continuous* medium after taking the discontinuity at the air-dielectric interface into account as shown in Fig. 4.3. Now using (3.13), we can express the input reflection coefficient $R(k_0)$ in

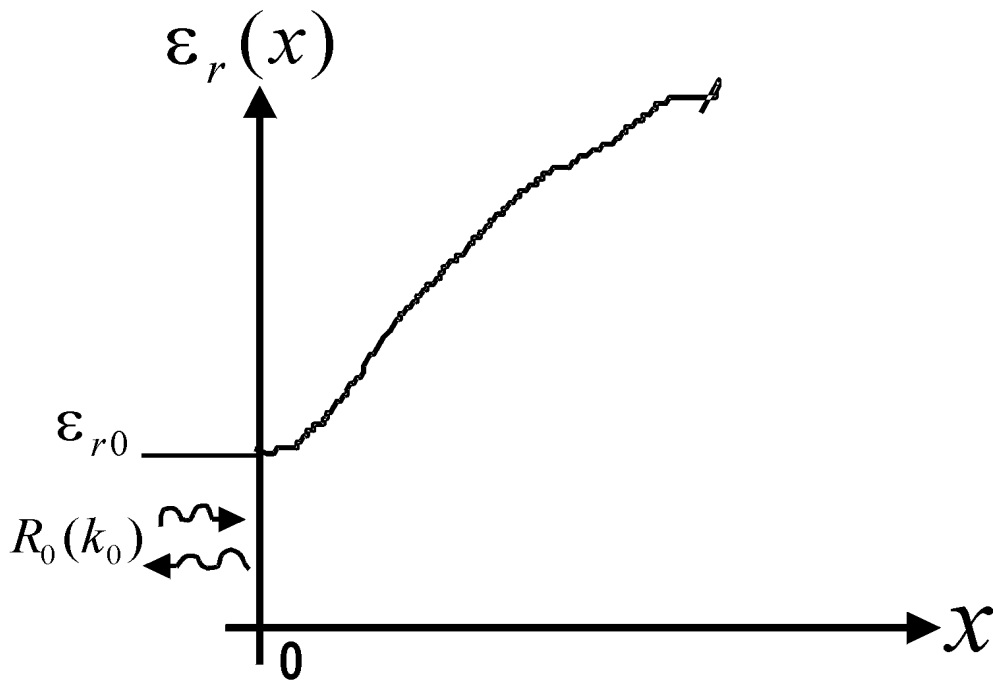


Figure 4.3: The continuous medium after taking the permittivity discontinuity into account

terms of S_{11} and $R_0(k_0)$ of Fig. 4.2

$$R(k_0) = S_{11} + \frac{(1 - S_{11}^2) R_0(k_0)}{1 + S_{11} R_0(k_0)} \quad (4.21)$$

The above equation can be mathematically manipulated to arrive at the following relationship

$$R_0(k_0) = \frac{R(k_0) - S_{11}}{1 - S_{11} R(k_0)} \quad (4.22)$$

where S_{11} is given by (4.20). As $R_0(k_0)$ is the reflection coefficient of an equivalent continuous medium, hence the technique presented in section 4.1.1.1 can now be used for the reconstruction. If $\hat{R}_0(k_0)$ is the virtual reflection coefficient corresponding to the transformed reflection coefficient $R_0(k_0)$, then using (4.17) we can write

$$d \ln \varepsilon_r(x) = -4 \hat{r}_0(l) dl \quad (4.23)$$

where $\hat{r}_0(l)$ is the inverse Fourier transform of $\hat{R}_0(k_0)$. This equation can be integrated for any arbitrary depth x

$$\varepsilon_r(l) = \varepsilon_{r0} \exp \left[-4 \int_0^l \hat{r}_0(l') dl' \right] \quad (4.24)$$

which is the required formula to reconstruct the one-dimensional permittivity profile of a planar half-space medium having a discontinuity at the air-dielectric interface.

It may be noted here that the above equation reconstructs the permittivity profile in terms of the electrical length l , but as l is basically a function of x given by (4.14) hence the profile in (4.24) can be also thought of as a function of the physical depth x . The exact relationship between the electrical length l and the physical depth x is given by a numerical algorithm presented in section 4.1.1.3. Now, corresponding to (4.24), when there is no discontinuity i.e. when $\varepsilon_r(0) = 1$, then this equation reduces to (4.19) as it should be. The overall technique for the reconstruction of one-dimensional permittivity profile can thus be summarized as follows. First we measure the reflection coefficient data $R(k_0)$ (both magnitude and phase) of any dielectric sample or medium over a wide frequency band using a vector network analyzer. The measurement can be carried out either in a transmission line medium or in the free-space. For the measurement in the transmission line medium, the dielectric sample is machined to fit inside a waveguide or a coaxial airline section. The waveguide measurements are simpler because the machining is not very crucial in this case, but the airline setup is preferred in situations where the wide-band data are required. The free-space measurements are totally non-destructive in nature as no machining is required in this case, and the flat sample can directly be placed in front of the antenna. However, the free-space measurements are more prone to errors because of the hostile measuring conditions, and hence special care has to be taken to calibrate the network analyzer in order to obtain a better accuracy. We have carried out the measurement of different dielectric samples both in the transmission line medium and in the free-space, the details about which are given in the next chapter. Here it may just be pointed out that the transmission line measurements are more suitable for the characterization of dielectric materials, while the free-space method looks more appropriate for the imaging applications where the totally *non-destructive* measurements are required. After the measurement of spectral-domain reflection data $R(k_0)$ using any of the methods discussed above, it is transformed to

$R_0(k_0)$ for each frequency using (4.22). The surface value of permittivity ε_{r0} in (4.22) is determined using a separate method described in the next section. The nonlinear transformation given by (4.8) is used to define a virtual reflection coefficient $\hat{R}_0(k_0)$ corresponding to $R_0(k_0)$. Finally the inverse Fourier transform of $\hat{R}_0(k_0)$ is taken to obtain $\hat{r}_0(l)$ and this value is then used in (4.24) to obtain the required permittivity profile as a function of the electrical depth l .

4.1.1.3 Numerical algorithm for transforming the virtual space variable into the actual physical distance

Equations (4.19) and (4.24) both give the expression of the permittivity profile as a function of the virtual space variable l . However, to reconstruct the actual depth-dependent permittivity profile, we have to convert the electrical distance l into the actual depth x . In this section, we present an algorithm for this purpose based on (4.14) and (4.24). Let us define

$$g(l) = \left[-4 \int_0^l \hat{r}_0(l') dl' \right] \quad (4.25)$$

Equation (4.24) then reduces to

$$\varepsilon_r(l) = \varepsilon_{r0} \exp [g(l)] \quad (4.26)$$

Now, under real practical situations, we measure the reflection coefficient data over a wide frequency band and then use some kind of FFT routine to compute its inverse Fourier transform. This means that we will get the discrete values of $\hat{r}_0(l)$ in (4.25) at a constant step size, say Δl . The exact value of Δl will of course depend upon the bandwidth over which the measurements are carried out; greater the bandwidth, higher the resolution in space domain. After having obtained the values of $\hat{r}_0(l)$ at an interval of step-size Δl , we use a simple trapezoidal integration routine to evaluate (4.25) starting from its initial value, $g(0) = 0$ [96]

1. When $x = 0$, $l = 0$ according to (4.14).
2. At $l = l_1 = \Delta l$,

$$g(l_1) = -2\Delta l [\hat{r}_0(0) + \hat{r}_0(\Delta l)]$$

$$\varepsilon_r(l_1) = \varepsilon_{r0} \exp [g(l_1)]$$

But l_1 corresponds to x_1 via (4.14), hence the same trapezoidal integration routine used to evaluate (4.25) can be used to compute (4.14) as well, and this yields

$$x_1 = \frac{\Delta l}{\left[\sqrt{\varepsilon_{r0}} + \sqrt{\varepsilon_r(l_1)} \right]}$$

3. The above equations can be generalized for $l = l_n = n \Delta l$

$$g(l_n) = g(l_{n-1}) - 2\Delta l \{ \hat{r}_0 [(n-1)\Delta l] + \hat{r}_0 [n\Delta l] \} \quad (4.27a)$$

$$\varepsilon_r(l_n) = \varepsilon_{r0} \exp [g(l_n)] \quad (4.27b)$$

$$x_n = x_{n-1} + \frac{\Delta l}{\left[\sqrt{\varepsilon_r(l_{n-1})} + \sqrt{\varepsilon_r(l_n)} \right]} \quad (4.27c)$$

where l_n corresponds to x_n via (4.14). With the help of (4.27a), (4.27b), and (4.27c), the exact permittivity profile $\varepsilon_r(x)$ can be reconstructed as a function of physical distance x in subsequent steps starting from ε_{r0} at $x = 0$.

4.1.1.4 Determination of the permittivity at the air-dielectric interface

From (4.20), (4.22) and (4.24), it is evident that for the evaluation of both $R_0(k_0)$ and $\varepsilon_r(x)$, we need to first determine the surface value of the permittivity at the air-dielectric interface i.e. ε_{r0} or the equivalent reflection coefficient. Here we present two methods, which can be employed for computing these parameters.

The first method is an analytical one and it involves plotting the real and imaginary parts of the reflection coefficient as a function of the wavenumber k_0 . It has been shown in [30] that if we plot the real and imaginary parts of the reflection coefficient data in a complex plane in the high frequency region, then it yields a circle shifted along the real axis. As we can directly measure both the real and imaginary parts of the reflection coefficient data as a function of the wavenumber k_0 using a vector network analyzer, hence both the radius r and the intercept c along the real axis of this circle can be quite accurately determined. The local reflection coefficient due to a discontinuity at the outer air-dielectric interface S_{11} of Fig. 4.2 can be defined in terms of r and c according to [30]

$$S_{11} = \frac{(r^2 - c^2 - 1) + \sqrt{(r^2 - c^2 - 1)^2 - 4c^2}}{2c} \quad (4.28)$$

The permittivity at the outer air-dielectric interface can be written in terms of the above defined S_{11} using (4.20)

$$\varepsilon_{r0} = \left[\frac{1 - S_{11}}{1 + S_{11}} \right]^2 \quad (4.29)$$

As can be seen from (4.28) and (4.29), the surface value of the permittivity ε_{r0} can be determined using these two formulas once we are able to calculate the values of r and c . The main advantage of this method is that it is stable, and is not much sensitive to a change in phase measurements of the reflection coefficient data. These properties are quite significant under some conditions, e.g. for the measurement of the reflection coefficient data in the free-space where it is very difficult to measure the phase quite accurately.

The second method for the reconstruction of permittivity at the air-dielectric interface is based on the behavior of the maximum of modulus of the reflection coefficient data [97]. For a layered media, it can be shown that addition of each layer to the overall permittivity profile results in increasing the maximum of modulus of the reflection coefficient data, and this increase is directly proportional to the step size. It means that different layers of a discontinuous permittivity profile can be reconstructed successively so as to minimize the maximum of modulus of the reflection coefficient data for the remaining region in the frequency band of operation. We use this concept here to determine the surface value of permittivity ε_{r0} . The expression for the reflection coefficient after excluding the air-dielectric interface is given by (4.22)

$$R_0(k_0) = \frac{R(k_0) [1 + \sqrt{\varepsilon_{r0}}] - [1 - \sqrt{\varepsilon_{r0}}]}{[1 + \sqrt{\varepsilon_{r0}}] - R(k_0) [1 - \sqrt{\varepsilon_{r0}}]} \quad (4.30)$$

where we have made use of (4.20) to substitute the value of the local reflection coefficient due to the discontinuity at the interface. The above function is optimized using the criterion

$$\max |R_0(k_0)| \rightarrow \min \quad (4.31)$$

over the given frequency band to obtain the value of ε_{r0} . This algorithm has been implemented using a built-in MATLAB function, and it just takes few seconds to recover the correct value of ε_{r0} provided the reflection coefficient data is given over a wide frequency band. This method of optimization works quite well under most practical situations, and normally gives more accurate result as compared to the previously discussed analytical method because there is no scope of human made error such as the computation of correct values of r and c in (4.28). However, the noise sensitivity of this method is not so good as compared to the corresponding analytical method. It can thus be said that when the measurement is carried out in an unfriendly environment such as free-space, where there is a large scope of error and our aim is to obtain an approximate image of the dielectric object then the analytical method given by (4.28) and (4.29) may be used. However, when the measurement is carried out in a closed medium such as in a waveguide or in a coaxial airline, then the numerical method given by (4.30) and (4.31) are preferable for the quantitative characterization of dielectric materials. Finally, it may be also mentioned here that both the analytical and numerical technique presented in this section can be used to determine quite accurately the relative permittivity of a homogeneous piece of dielectric material.

4.1.2 *TE*-mode illumination

For the *TE* case, a plane wave of wave number k_0 is assumed to be incident from the left hand side (LHS) at an angle θ on the air-dielectric interface as discussed in section 3.1.2. The exact Riccati equation for the *TE* case is given by (3.26), and this equation can be inverted using the same procedure as discussed in the last section for the *TEM* case. However, to take the incidence angle θ into account in (3.26), we define the effective value of permittivity as

$$\tilde{\varepsilon}_r(x) = [\varepsilon_r(x) - \sin^2 \theta] \quad (4.32)$$

An auxiliary equation corresponding to (3.26) in terms of this effective value of permittivity and a virtual reflection coefficient $\hat{\Gamma}(k_0, x, \theta)$ can be written as

$$\frac{d\hat{\Gamma}(k_0, x, \theta)}{dx} = \hat{\Gamma}(k_0, x, \theta) j2k_0 \sqrt{\tilde{\varepsilon}_r(x)} + \frac{1}{4\tilde{\varepsilon}_r(x)} \frac{d\tilde{\varepsilon}_r(x)}{dx} \quad (4.33)$$

which is identical in form to (4.1), except that $\varepsilon_r(x)$ is replaced by $\tilde{\varepsilon}_r(x)$ and the reflection coefficient Γ in this case also depends on the angle θ . The transformation between the actual reflection coefficient $\Gamma(k_0, x, \theta)$ and the virtual one $\hat{\Gamma}(k_0, x, \theta)$ is still defined by (4.7). As the form of (4.33) is the same as (4.1), hence to analyze the one-dimensional inhomogeneity of a dielectric object having a discontinuity at the

air-dielectric interface and illuminated by a TE plane wave, we can modify (4.18) to write into the following form

$$d \ln \tilde{\varepsilon}_r(x) = -4 \hat{r}_0(l, \theta) dl \quad (4.34)$$

where $\hat{r}_0(l, \theta)$ is the inverse Fourier transform of $\hat{R}_0(k_0, \theta) = \hat{\Gamma}_0(k_0, 0, \theta)$. The virtual space variable l in the TE case is related to the physical distance x as

$$l = 2 \int_0^x \sqrt{\tilde{\varepsilon}_r(x')} dx' \quad (4.35)$$

The value of $\hat{\Gamma}_0(k_0, 0, \theta)$ is obtained after integrating (4.33) with an appropriate boundary condition and then evaluating this integral for $x = 0$, as was done in the TEM case. The virtual reflection coefficient $\hat{\Gamma}(k_0, x, \theta)$ is clearly transformed here into $\hat{\Gamma}_0(k_0, x, \theta)$ to take into account the discontinuity at the air-dielectric interface as explained in the previous TEM case. The discontinuity at the interface is modelled by an equivalent microwave network as shown in Fig. 4.2 and 4.3. However, for the TE case, the local reflection coefficient S_{11} in Fig. 4.2 is defined using (3.5a) with the value of \bar{Z} given by (3.22), i.e.

$$S_{11} = \frac{\bar{Z}_2 - \bar{Z}_1}{\bar{Z}_2 + \bar{Z}_1} = \frac{\cos \theta - \sqrt{\varepsilon_{r0} - \sin^2 \theta}}{\cos \theta + \sqrt{\varepsilon_{r0} - \sin^2 \theta}} \quad (4.36)$$

The value of $\hat{\Gamma}_0(k_0, x, \theta)$ in terms of $\hat{\Gamma}(k_0, x, \theta)$ for the TE case is thus obtained using (4.22), with the value of S_{11} given by (4.36). Meanwhile, (4.34) is integrated from the initial point $x = 0$ to any arbitrary point x

$$\varepsilon_r(x) = \sin^2 \theta + [\varepsilon_{r0} - \sin^2 \theta] \exp \left[-4 \int_0^l \hat{r}_0(l') dl' \right] \quad (4.37)$$

which is the required expression for the depth-dependent one-dimensional permittivity profile of a dielectric object illuminated by a TE plane wave. This expression reduces to (4.24) for the angle $\theta = 0$, which also verifies this formulation.

4.1.3 TM -mode illumination

The TM -illumination is quite similar to TE case in the sense that a plane wave of wave number k_0 is also considered here to be incident from the left hand side at an angle θ on the air-dielectric interface as discussed in section 3.1.3. The exact Riccati equation for the TM case, however, is given by (3.30), and an auxiliary equation corresponding to this equation can be written as

$$\frac{d\hat{\Gamma}(k_0, x, \theta)}{dx} = \hat{\Gamma}(k_0, x, \theta) j2k_0 \sqrt{\tilde{\varepsilon}_r(x)} + \frac{1}{4 [\tilde{\varepsilon}_r(x)]} \frac{[\tilde{\varepsilon}_r(x) - \sin^2 \theta]}{[\tilde{\varepsilon}_r(x) + \sin^2 \theta]} \frac{d\tilde{\varepsilon}_r(x)}{dx} \quad (4.38)$$

where $\tilde{\varepsilon}_r(x)$ is the effective value of permittivity, defined by (4.32). The virtual reflection coefficient $\hat{\Gamma}(k_0, x, \theta)$ in the above equation is related with its actual reflection coefficient $\Gamma(k_0, x, \theta)$ using the transformation given by (4.7). Equation (4.38) is integrated in terms of $\hat{\Gamma}(k_0, x, \theta)$ using the same boundary condition as given in the TEM case, and then this integral is evaluated at $x = 0$ to obtain the value of the

reflection coefficient data at the interface, i.e. $\hat{R}_0(k_0, \theta) = \hat{\Gamma}_0(k_0, 0, \theta)$. We consider here the general case with a discontinuity at the air-dielectric interface, and for this purpose the equivalent microwave network shown in Fig. 4.2 and 4.3 will be used. For the *TM* case, the local reflection coefficient S_{11} in Fig. 4.2 is defined using (3.5a) with the value of \bar{Z} given by (3.28), i.e.,

$$S_{11} = \frac{\bar{Z}_2 - \bar{Z}_1}{\bar{Z}_2 + \bar{Z}_1} = \frac{\sqrt{\varepsilon_{r0} - \sin^2 \theta} - \varepsilon_{r0} \cos \theta}{\sqrt{\varepsilon_{r0} - \sin^2 \theta} + \varepsilon_{r0} \cos \theta} \quad (4.39)$$

After recovering the value of S_{11} by (4.39), the virtual reflection coefficient $\hat{R}(k_0, \theta)$ is transformed to $\hat{R}_0(k_0, \theta)$ using the bilinear transform (4.22) to take into account the surface discontinuity. Once we have determined the value of this frequency-domain virtual reflection coefficient $\hat{R}_0(k_0, \theta)$, then we can directly write its equivalent expression in the virtual-space domain with the help of (4.15), (4.16) and (4.38)

$$\hat{r}_0(l, \theta) = \mathfrak{S}^{-1} \left[\hat{R}_0(k_0, \theta) \right] = -\frac{1}{8 \tilde{\varepsilon}_r(x) \sqrt{\tilde{\varepsilon}_r(x)}} \frac{[\tilde{\varepsilon}_r(x) - \sin^2 \theta]}{[\tilde{\varepsilon}_r(x) + \sin^2 \theta]} \frac{d\tilde{\varepsilon}_r(x)}{dx} \quad (4.40)$$

where l is still defined by (4.35), and $\hat{r}_0(l, \theta)$ is the inverse Fourier transform of $\hat{R}_0(k_0, \theta)$. The above equation can be integrated from the initial point $x = 0$ to any arbitrary point x

$$\frac{[\varepsilon_r(x)]^2}{\varepsilon_r(x) - \sin^2 \theta} = \frac{[\varepsilon_{r0}]^2}{[\varepsilon_{r0} - \sin^2 \theta]} \exp \left[-4 \int_0^l \hat{r}_0(l') dl' \right] \quad (4.41)$$

If we compare the above equation with (4.37) and (4.24), then clearly its form looks complicated as compared to the corresponding *TEM* and *TE* cases. However, the above equation can be simplified using the fact that the value of $\varepsilon_r(x)$ is greater than unity, and that the value of $\sin \theta$ always lies between 0 and 1. Keeping this information in mind, the left hand side of (4.41) can be rewritten as

$$\frac{[\varepsilon_r(x)]^2}{\varepsilon_r(x) - \sin^2 \theta} = \varepsilon_r(x) \left[1 + \frac{\sin^2 \theta}{\varepsilon_r(x)} + \dots \right] \simeq [\varepsilon_r(x) + \sin^2 \theta] \quad (4.42)$$

The above equation can now be substituted in (4.41) to obtain

$$\varepsilon_r(x) = -\sin^2 \theta + \frac{[\varepsilon_{r0}]^2}{[\varepsilon_{r0} - \sin^2 \theta]} \exp \left[-4 \int_0^l \hat{r}_0(l') dl' \right] \quad (4.43)$$

which is the required expression for the one-dimensional permittivity profile of a dielectric object illuminated by a *TM* plane wave. This expression also reduces to the *TEM* case of (4.24), if the angle θ in the above expression becomes zero, which also verifies the validity of (4.43).

4.2 The *RDE* technique applied to non-planar structures

In the last section, the nonlinear Riccati-differential-equation (*RDE*) derived in section 3.1 was inverted to obtain an expression in a closed-form for the one-dimensional

permittivity profile in terms of an inverse Fourier transform of the spectral domain reflection coefficient data. This analytical approach, generally called the Riccati-differential-equation (*RDE*) technique, works quite well in the *Cartesian coordinate system* and it normally leads to a unique reconstruction of permittivity profiles with moderate contrasts. However, to the best of our knowledge, these kinds of analytical approaches are not available in literature for *cylindrical or spherical coordinate systems*. In this thesis, one of our main aims is to generalize this RDE technique so that it can be applied to non-planar (e.g. cylindrical or spherical) structures as well. This is achieved by relaxing the function form of the transform kernel¹. Any pair of adjoint kernels satisfying certain completeness properties over the spatial and spectral (or temporal) range of interest, can be used to construct a direct and an inverse transformation in a flexible fashion which suits itself to any coordinate system [63]. These transformations can then be used to reconstruct spatially dependent permittivity profiles by making use of time or frequency dependent scattering data. The resolution of the reconstruction can be made arbitrary by controlling the spectral range over which the scattering data are measured. We start this section with revisiting the Fourier-transform approach used in the Cartesian coordinate system, which helps in extracting the basic concepts on which the proposed approach depends. In the next step, these concepts are generalized by relaxing the kernel form of the Fourier direct and inverse transforms giving rise to a new kind of integral transform, which can be used in both Cartesian and other coordinate systems.

4.2.1 Generalization of the one dimensional Fourier transform technique

For the one-dimensional planar half-space medium shown in Fig. 3.1, the nonlinear differential equation was derived in section 3.1 for the reflection coefficient considering both normal and oblique incidences. In this section, we try to make the overall situation more general by considering a one-dimensional permittivity profile as a part of the half-space medium ($x \geq 0$) shown in Fig. 4.4, where the inhomogeneity is assumed to extend from $x = x_1$ to $x = x_2$ only with jumps at both ends. This half-space is supposed to be illuminated with a monochromatic plane wave of angular frequency ω from the left hand side ($x < 0$). For normal and both oblique incidences (parallel and perpendicular polarizations), a spatially dependent reflection coefficient $\Gamma(x)$ can be defined, which satisfies the following nonlinear Riccati differential equation

$$\frac{d\Gamma}{dx} + j \left(\frac{\omega}{c} \right) f[\varepsilon_r(x)] \Gamma(x) + [1 - \Gamma^2(x)] g[\varepsilon_r(x)] = 0 \quad (4.44)$$

where the wave-number k_0 of section 4.1 is replaced here with the angular frequency ω ($k_0 = \omega/c$), f and g are functions of the unknown permittivity profile $\varepsilon_r(x)$, and g vanishes identically for $x < x_1$ and $x > x_2$ ². By comparing the above equation with (3.18), (3.26) and (3.30) of the planar case, it is obvious that (4.44) is quite general in nature satisfying both normal and inclined illuminations. It has

¹which is basically an exponential function in case of the Fourier transform.

²The reason being that this function g is generally proportional to the derivative $\frac{d\varepsilon_r(x)}{dx}$, which reduces to zero when there is no change in the permittivity any more.

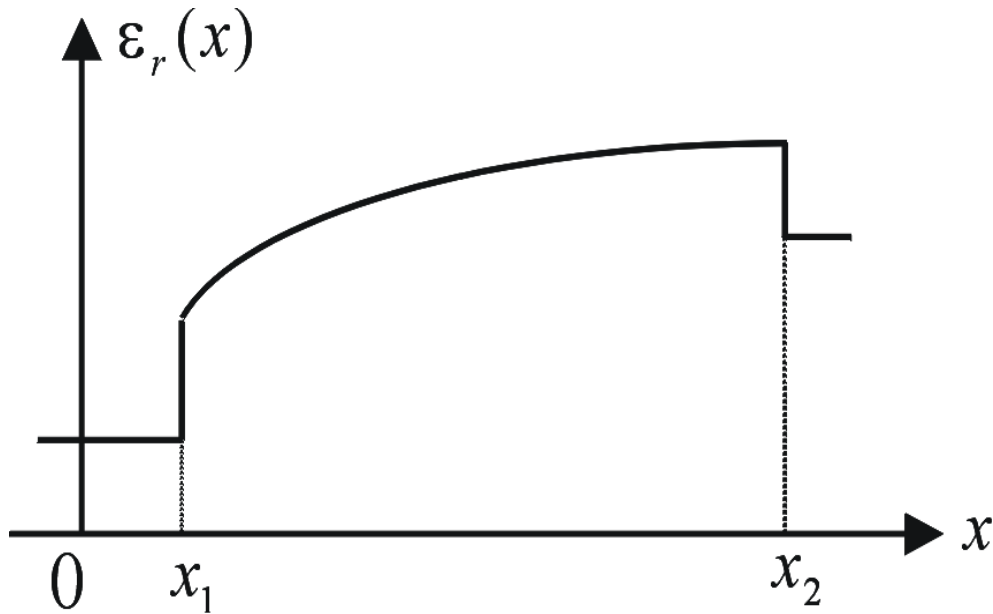


Figure 4.4: A general one-dimensional permittivity profile considered in a Cartesian coordinate system

been shown in section 4.1 that a nonlinear differential equation such as (4.44) can be linearized, if we transform $\Gamma(x)$ into a new variable $\hat{\Gamma}(x)$ through a nonlinear transformation

$$\hat{\Gamma} = N [\Gamma(x)] \quad (4.45)$$

where $\hat{\Gamma}(x)$ is the solution of the following linear differential equation

$$\frac{d\hat{\Gamma}}{dx} + j \left(\frac{\omega}{c} \right) f [\varepsilon_r(x)] \hat{\Gamma}(x) + g [\varepsilon_r(x)] = 0 \quad (4.46)$$

Equation (4.46) can be readily solved using the method explained in section 4.1.1.1 to arrive at

$$\hat{\Gamma}(\omega, x) = \int_t^{t_2} G [\varepsilon_r(t')] \exp(j\omega t') dt' \quad (4.47)$$

where,

$$t(x) = \frac{1}{c} \int_{x_1}^x f [\varepsilon_r(x')] dx' \quad ; \quad t_2 = t(x_2) \quad (4.48)$$

is an intermediate dummy time variable equivalent to the dummy space variable explained in section 4.1.1.1, and

$$G [\varepsilon_r(t)] \equiv c g [\varepsilon_r(x)] \quad (4.49)$$

Now, let $R(\omega)$ and $\hat{R}(\omega)$ be the values of $\Gamma(\omega, x)$ and $\hat{\Gamma}(\omega, x)$ at $x = x_1$ respectively. As already mentioned, $g [\varepsilon_r(x)]$ vanishes identically for $x < x_1$ and $x > x_2$, hence the integration involved in $\hat{R}(\omega)$ can be relaxed to

$$\begin{aligned}\hat{R}(\omega) &= \int_{t_1}^{t_2} G[\varepsilon_r(t')] \exp(j\omega t') dt' \\ &= \int_{-\infty}^{\infty} G[\varepsilon_r(t')] \exp(j\omega t') dt'\end{aligned}\quad (4.50)$$

The permittivity profile function can then be obtained via an inverse Fourier transform of $\hat{R}(k_0)$, i.e.

$$G[\varepsilon_r(t)] = \frac{1}{2\pi} \int_{-\infty}^{\infty} \hat{R}(\omega) \exp(-j\omega t) d\omega \quad (4.51)$$

where $\hat{R}(\omega)$ is related to the measurable reflection coefficient $R(\omega)$ via the nonlinear transformation (4.45). The exact permittivity profile $\varepsilon_r(x)$ can, of course, be easily obtained from this function $G[\varepsilon_r(t)]$ using some kind of numerical algorithm as proposed in section 4.1.1.3.

In order to be able to generalize the above presented technique of reconstructing $\varepsilon_r(x)$ via an inverse Fourier transform of $\hat{R}(\omega)$, we need to consider this procedure with some more details. Let us first distinguish between the original profile function $G_1(t') \equiv G[\varepsilon_r(t')]$ appearing in (4.50), and the reconstructed one $G_2(t) \equiv G[\varepsilon_r(t)]$ appearing in (4.51), i.e. we define

$$\hat{R}(\omega) = \int_{t_1}^{t_2} G_1(t') \exp(j\omega t') dt' \quad (4.52a)$$

$$G_2(t) = \frac{1}{2\pi} \int_{-\infty}^{\infty} \hat{R}(\omega) \exp(-j\omega t) d\omega \quad (4.52b)$$

If we insert (4.52a) into (4.52b), then it will express $G_2(t)$ in terms of $G_1(t)$ as a convolution, i.e.

$$G_2(t) = \int_{t_1}^{t_2} G_1(t') \left[\frac{1}{2\pi} \int_{-\infty}^{\infty} \exp(-j\omega t) \exp(j\omega t') d\omega \right] dt' \quad (4.53)$$

From the above equation, it can be concluded that $G_1(t)$ and $G_2(t)$ are identical because

$$\left[\frac{1}{2\pi} \int_{-\infty}^{\infty} \exp[-j\omega(t-t')] \right] = \delta(t-t') \quad (4.54)$$

and this delta function is used to sample the permittivity function $G_1(t')$ at $t = t'$.

After analyzing the Fourier-transform technique in detail, let us now try to replace the Fourier kernels $\frac{1}{2\pi} \exp(-j\omega t)$ and $\exp(j\omega t')$ with some other generalized functions $K(\omega, t)$ and $\tilde{K}(\omega, t')$, respectively, and the infinite integral in (4.54) is replaced with a finite (band-limited) one. This means that instead of (4.52a), $\hat{R}(\omega)$ is now related to the original permittivity profile function $G_1(t)$ by

$$\hat{R}(\omega) = \int_{t_1}^{t_2} G_1(t') \tilde{K}(\omega, t') dt' \quad (4.55)$$

and instead of (4.52b), $G_2(t)$ is reconstructed from $\hat{R}(\omega)$ according to

$$G_2(t) = \int_{\omega_1}^{\omega_2} \hat{R}(\omega) K(\omega, t) d\omega \quad (4.56)$$

With these modifications, $G_2(t)$ will then be related to $G_1(t)$ by

$$G_2(t) = \int_{t_1}^{t_2} G_1(t') D(t, t') dt' \quad (4.57)$$

where,

$$D(t, t') = \int_{\omega_1}^{\omega_2} K(\omega, t) \tilde{K}(\omega, t') d\omega \quad (4.58)$$

If we compare (4.58) with (4.54), then it is observed that the ideal functional form of $D(t, t')$ is given by a delta function $\delta(t - t')$, which can now be relaxed to other more practical and flexible forms by properly choosing $K(\omega, t)$ and $\tilde{K}(\omega, t')$. All what we need for the reconstruction is a pulse-shaped functional form like that shown in Fig. 4.5 with a maximum at \hat{t} and pulse width τ , which can be moved between t_1 and t_2 by changing t ³. This will allow the reconstruction with a resolution corresponding to the pulse width τ as can be further explained with reference to Fig. 4.6. As a

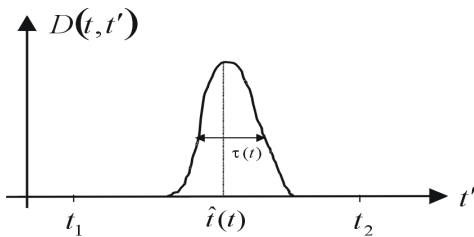


Figure 4.5: A typical shape of the pulse-like function occupying a narrow region between the specified limits

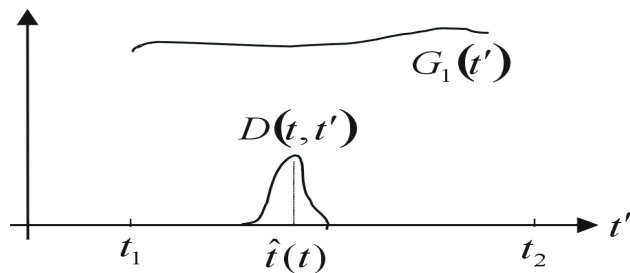


Figure 4.6: The reconstructed permittivity profile function with the moving pulse

matter of fact, both the height and width of this pulse will strongly depend upon the full bandwidth over which the measurements are carried out, and generally greater the bandwidth, higher the resolution. If we look at (4.57), then it basically tells us that $G_2(t)$ is the integral of the product of $G_1(t')$ and $D(t, t')$ with respect to t' . But if we assume that $D(t, t')$ is a pulse-like function as shown in Fig. 4.5, then $G_2(t)$ will be proportional to the average of $G_1(t')$ around $\hat{t}(t)$ over the narrow occupation τ of $D(t, t')$. Consequently, $G_2(t)$ may be considered as the reconstruction of $G_1(t')$ in an average sense. If the original function $G_1(t')$ does not change appreciably within the narrow occupation τ , $G_2(t)$ will be then a good approximation of $G_1(t')$. However, if this is not the case, then one may lose the fine details of G_1 through this averaging process.

The above mentioned features of $D(t, t')$ are general ones. Other concrete features must however be discussed in order to judge on the quality of the reconstruction. The first important feature is the movability of $D(t, t')$ as a function of t' by

³It may be noted here that \hat{t} is always a function of t because the position of the maxima must move over the whole range between t_1 and t_2 , but in some cases the pulse width τ may also change with t due to some distortion in the pulse-shape when we move from one end to another.

using t as a moving parameter. In order to be able to reconstruct the profile over the range $[t_1, t_2]$, we must be able to let the peak of the pulse $\hat{t}(t)$ change between t_1 and t_2 by changing t . The second feature is the distortion (or spreading out) which may occur to $D(t, t')$ as it moves from t_1 to t_2 . Hence care must be taken to minimize this distortion in order to have approximately the same reconstruction resolution over the whole range $[t_1, t_2]$. Any pulse-shaped function of the form $D(t, t') = d(t' - t)$ will provide us with a complete coverage of the range $[t_1, t_2]$ with the same resolution, because such a function can move along the t' axis without much distortion in its shape as we change the variable t .

4.2.2 Extending the validity of the analysis to a general one-dimensional case

In order to be able to reconstruct the one-dimensional permittivity profile in other coordinate systems, e.g. cylindrical, spherical or even specially designed coordinate systems, we may follow the same guiding lines as in the Cartesian case discussed in the previous sub-section. The step-by-step approach for the reconstruction of the permittivity profile of a general one-dimensional case can be described as follows.

1. Write down the non-linear differential equation describing a scattering parameter (e.g. a properly defined reflection coefficient Γ) in terms of the unknown (looked for) permittivity profile.
2. Look for an auxiliary quantity $\hat{\Gamma}$ which satisfies a linearized version of the above mentioned differential equation and is related to the original (measurable) reflection coefficient Γ via a non-linear transformation.
3. Transform the linear differential equation for $\hat{\Gamma}$ in order to arrive at an integration of the form

$$\hat{\Gamma}(\omega, x) = \int_{t(x)}^{t_2} G[\varepsilon_r(x')] \tilde{K}(\omega, t') dt' \quad (4.59)$$

where $t(x)$ is a functional of $\varepsilon_r(x)$, and $t_2 = t(x_2)$.

4. After measuring the reflection coefficient $R(\omega) = \Gamma(\omega, x_1)$, we convert these measurements to frequency-dependent auxiliary data $\hat{R}(\omega) = \hat{\Gamma}(\omega, x_1)$ over the range $[\omega_1, \omega_2]$ by making use of the already determined nonlinear transformation between Γ and $\hat{\Gamma}$.
5. For the function $\tilde{K}(\omega, t')$ appearing in (4.59), look for a corresponding function $K(\omega, t)$, which produces the sampling function $D(t, t')$ given by

$$D(t, t') = \int_{\omega_1}^{\omega_2} K(\omega, t) \tilde{K}(\omega, t') d\omega \quad (4.60)$$

with the properties described before.

6. In terms of the already determined $\hat{R}(\omega)$, construct a transformation $g(t)$ according to

$$g(t) = \int_{\omega_1}^{\omega_2} \hat{R}(\omega) K(\omega, t) d\omega \quad (4.61)$$

7. The transformation $g(t)$ is then a fair reconstruction of $G[\varepsilon_r(x)]$ within the framework of the analysis given before, i.e.

$$\begin{aligned} g(t) &= \int_{t_1}^{t_2} G(t') D(t, t') dt' \\ &\cong G[\hat{t}(t)] \int_{t_1}^{t_2} D(t, t') dt' = G[\hat{t}(t)] d[\hat{t}(t)] \end{aligned} \quad (4.62)$$

At this end we would like to give following remarks about the two kernels described above, which should be taken into consideration before applying the proposed technique to practical problems.

1. The kernel of the inverse transformation $K(\omega, t)$ can be flexibly chosen. However, it must satisfy the orthogonality and completeness properties and generally its choice will determine the functional form of $D(t, t')$. In this thesis, we have always taken some standard integral transforms such as a Fourier transform or a Hankel transform whose orthogonality and completeness properties are well proved in the literature. Furthermore, the frequency range over which the inverse transformation is integrated, is equal to that of the measurement range of the spectral data, namely $\omega_1 \leq \omega \leq \omega_2$. This last characteristic can be systemized by considering $K(\omega, t)$ being multiplied by a pulse function $u(\omega - \omega_1) - u(\omega - \omega_2)$.
2. The kernel of the direct transformation $\tilde{K}(\omega, t')$ is determined according to the type of differential equation describing $\hat{\Gamma}(\omega, x)$, we arrived at. To check the correctness of this kernel, it should be substituted in (4.60) along with $K(\omega, t)$ and the shape of the functional $D(t, t')$ should be considered along with its properties. If this functional is having a pulse-shaped form and satisfies the properties mentioned in section 4.2.1, then our proposed technique can be applied in that particular case.

4.3 The cylindrical geometry

The direct problem formulation of cylindrical dielectric objects with different lower and higher order TE and TM illuminations was discussed in detail in section 3.2. In this section, the inversion procedure is described for the dielectric objects defined by Fig. 3.9, and our main aim is to find an expression in closed-form for the one-dimensional radially varying permittivity profile $\varepsilon_r(\rho)$ of these objects in terms of an integral transform of the reflection coefficient data. It will be assumed that the measurement of the reflection coefficient data is carried out on the outer radius of the object, i.e. at $\rho = b$ in Fig. 3.9, as mentioned in the last chapter. It was mentioned in section 3.2 that because of the presence of Hankel functions in cylindrical coordinate

system the formulation is quite complicated as compared to the planar case, and hence it is to be expected that the inverse solution for the cylindrical objects would also be quite involved. As was the case in the direct problem formulation, we start with a radial transmission line mode illumination, where the analysis is somewhat simpler. In the next part, more general expressions valid for any arbitrary order TE and TM cylindrical mode illumination will be derived.

4.3.1 Radial transmission line approach

Firstly we consider the dielectric object illuminated by a lowest order TM_{00} mode, in which case the classical transmission line approach can be used to analyze the one-dimensional inhomogeneity as described in section 3.2.1. The non-linear differential equation for the radial mode illumination has been derived in section 3.2.1, and is given by (3.74). This equation is similar in form as the corresponding equation (3.18) of the planar TEM case, except that in 3.2.1 the exponential function of the Cartesian case are replaced by the Hankel functions. Hence our general theory of reconstruction described in section 4.2 can be used here for the inversion. To apply this theory, first of all we write an auxiliary linear differential equation corresponding to (3.74) in terms of the virtual reflection coefficient $\hat{\Gamma}(k_0, \rho)$

$$\frac{d\hat{\Gamma}(k_0, \rho)}{d\rho} + \hat{\Gamma}(k_0, \rho) \left[\frac{j 4}{\pi \rho H_0^{(1)}(k\rho)H_0^{(2)}(k\rho)} \right] = \frac{1}{4\varepsilon_r(\rho)} \frac{d\varepsilon_r(\rho)}{d\rho} \quad (4.63)$$

The relationship between Γ and $\hat{\Gamma}$ is defined using a nonlinear transformation given in (4.7). The above differential equation can be integrated from an inner radius $\rho = \rho_0$ of the cylindrical dielectric object shown in Fig. 3.9 to an arbitrary radius ρ to obtain the general solution of the following form

$$\begin{aligned} & \hat{\Gamma}(k_0, \rho) \exp \left[\int_{\rho_0}^{\rho} \frac{j 4}{\pi \rho' H_0^{(1)}(k\rho')H_0^{(2)}(k\rho')} d\rho' \right] \\ &= \int_{\rho_0}^{\rho} \left\{ \frac{1}{4\varepsilon_r(\rho')} \frac{d\varepsilon_r(\rho')}{d\rho'} \exp \left[\int_{\rho}^{\rho'} \frac{j 4}{\pi \rho'' H_0^{(1)}(k\rho'')H_0^{(2)}(k\rho'')} d\rho'' \right] \right\} d\rho' + C \end{aligned} \quad (4.64)$$

where the constant C is the integration constant, which can be determined when the boundary conditions are specified, and ρ' and ρ'' are dummy integration variables. The inner radius $\rho = \rho_0$ may be taken to approach zero under some situations but it cannot be put *exactly* equal to zero as the Hankel functions are infinite for zero argument. However, when it is necessary to determine its value near origin, then the Hankel functions may be replaced by their small argument asymptotic expressions and the total integral may be computed analytically in a very small region near the origin. Meanwhile, supposing that the value of the reflection coefficient at the inner radius is $\Gamma(\rho_0)$, the constant C in the above equation can be determined and in that case (4.64) will reduce to

$$\hat{\Gamma}(k_0, \rho) = \hat{\Gamma}(\rho_0) \exp \left[- \int_{\rho_0}^{\rho} \frac{j 4}{\pi \rho' H_0^{(1)}(k\rho')H_0^{(2)}(k\rho')} d\rho' \right]$$

$$+ \int_{\rho_0}^{\rho} \left\{ \frac{1}{4\varepsilon_r(\rho')} \frac{d\varepsilon_r(\rho')}{d\rho'} \exp \left[\int_{\rho}^{\rho'} \frac{j 4}{\pi \rho'' H_0^{(1)}(k\rho'') H_0^{(2)}(k\rho'')} d\rho'' \right] \right\} d\rho' \quad (4.65)$$

For the further evaluation of this integral, we assume here that the value of the reflection coefficient at the inner radius of the object is zero, i.e. $\Gamma(\rho_0) = 0$. This boundary condition can be satisfied when e.g., the cylindrical structure under test becomes heavily lossy (*dielectric loss*) for $\rho < \rho_0$, and hence all the input power gets absorbed at the radius $\Gamma(\rho_0)$ making the reflection coefficient to be zero at this point. It may be, however, pointed out that the overall formulation derived here can also be made valid for other boundary conditions with only few modifications. After applying the boundary condition $\Gamma(\rho_0) \equiv \hat{\Gamma}(\rho_0) = 0$, (4.65) can be evaluated at the outer boundary of the dielectric object $\rho = b$, i.e.,

$$\begin{aligned} \hat{R}(k_0) &= \hat{\Gamma}(k_0, b) \\ &= \int_{\rho_0}^b \left\{ \frac{1}{4\varepsilon_r(\rho')} \frac{d\varepsilon_r(\rho')}{d\rho'} \exp \left[\int_b^{\rho'} \frac{j 4}{\pi \rho'' H_0^{(1)}(k\rho'') H_0^{(2)}(k\rho'')} d\rho'' \right] \right\} d\rho' \quad (4.66) \end{aligned}$$

It may be mentioned here that when there is a discontinuity at the interface $\rho = b$, then we have to modify the actual measured reflection coefficient $\Gamma(k_0, b)$ of (4.66) before proceeding further as discussed in section 4.1.1.2 for the planar case. The discontinuity at the junction of the radial transmission lines of different permittivities can be modelled by a two-port $[S]$ parameter network as discussed in section 3.2.1.1 and going by this convention, the reflection coefficient $R(k_0) = \Gamma(k_0, b)$ can be transformed to $R_0(k_0)$ of an equivalent continuous media using (4.22)

$$R_0(k_0) = \frac{R(k_0) - S_{11}}{1 - S_{11} R(k_0)} \quad (4.67)$$

The value of S_{11} in our case is given by

$$S_{11} = \frac{1 - \sqrt{\varepsilon_r(b)}}{1 + \sqrt{\varepsilon_r(b)}} \quad (4.68)$$

where $\varepsilon_r(b)$ is the surface value of the permittivity as discussed earlier. The two equations given above can be understood quite well with the help of Fig. 4.2 and 4.3. It may be noted here that generally in all practical cases, a discontinuity at the surface exists and hence the procedure described in section 4.1.1.2 for the planar case should always be followed for non-planar structures also. Once we have obtained an expression for $R_0(k_0)$ representing a continuous medium, we can obtain its corresponding virtual component $\hat{R}_0(k_0)$ using the transformation (4.7) and in this case $\hat{R}(k_0)$ of (4.66) will simply be replaced by $\hat{R}_0(k_0)$ without changing any other parameter. Now, for a proper solution of (4.66) we introduce a *virtual time variable* t according to

$$\begin{aligned} t = \frac{\rho}{c} \sqrt{\varepsilon_r(\rho)}, \quad &\Rightarrow dt = \frac{1}{c} \sqrt{\varepsilon_r(\rho)} \left[1 + \frac{\rho}{2\varepsilon_r(\rho)} \frac{d\varepsilon_r(\rho)}{d\rho} \right] d\rho \\ &\cong \frac{1}{c} \sqrt{\varepsilon_r(\rho)} d\rho \end{aligned} \quad (4.69)$$

The above approximation holds good as long as the relative change in the permittivity profile $d\varepsilon_r(\rho)/d\rho$ is not too large with respect to the actual value of the permittivity $\varepsilon_r(\rho)$. This approximation is in fact quite general. We may recall from the last chapter that also in the case of planar cartesian media, the differential change in the absolute permittivity profile was assumed to be moderate. The virtual time variable t given by (4.69) is similar to the virtual space variable introduced earlier in section 4.1.1.1 for the Cartesian case. The variable t and its derivative given by (4.69) can then be substituted in (4.66) to obtain

$$\hat{R}_0(\omega) = \int_{t_b}^{t_0} \left\{ \frac{c}{4\tilde{\varepsilon}_r(\rho)\sqrt{\tilde{\varepsilon}_r(\rho)}} \frac{d\tilde{\varepsilon}_r(\rho)}{d\rho} * \exp \left[\int_{t_b}^{t'} \frac{4j}{\pi t'' H_0^{(1)}(\omega t'') H_n^{(0)}(\omega t'')} dt'' \right] \right\} dt' \quad (4.70)$$

where,

$$t_b = \frac{b}{c} \sqrt{\varepsilon_r(b)}, \quad \text{and} \quad t_0 = \frac{\rho_0}{c} \sqrt{\varepsilon_r(\rho_0)} \quad (4.71)$$

are the values of t at both ends. The inner integral in the above equation can be computed using the formula given by (C.4), which reduces to

$$\int_{t_b}^{t'} \frac{4j}{\pi t'' H_0^{(1)}(\omega t'') H_0^{(2)}(\omega t'')} dt'' = \ln \left[\frac{H_0^{(1)}(\omega t') H_0^{(2)}(\omega t_b)}{H_0^{(2)}(\omega t') H_0^{(1)}(\omega t_b)} \right] \quad (4.72)$$

The value of the above integral can be substituted in (4.70) yielding

$$\hat{R}_0(\omega) = \int_{t_b}^{t_0} \left\{ \left[\frac{c}{4\varepsilon_r(\rho') \sqrt{\varepsilon_r(\rho')}} \frac{d\varepsilon_r(\rho')}{d\rho'} \right] \frac{H_0^{(1)}(\omega t') H_0^{(2)}(\omega t_b)}{H_0^{(2)}(\omega t') H_0^{(1)}(\omega t_b)} \right\} dt' \quad (4.73)$$

The above equation can now be written in the following form in order to apply the general theory of reconstruction described in section 4.2.2

$$\hat{R}_0(\omega) = \int_{t_b}^{t_0} G(t') \tilde{K}(\omega, t') dt' \quad (4.74)$$

where,

$$G(t') \equiv c g[\varepsilon_r(\rho')] = \left[\frac{c}{4\varepsilon_r(\rho') \sqrt{\varepsilon_r(\rho')}} \frac{d\varepsilon_r(\rho')}{d\rho'} \right] \quad (4.75)$$

is the time-domain equivalent of the permittivity function $g[\varepsilon_r(\rho')]$, and

$$\tilde{K}(\omega, t') = \frac{H_0^{(1)}(\omega t') H_0^{(2)}(\omega t_b)}{H_0^{(2)}(\omega t') H_0^{(1)}(\omega t_b)} \quad (4.76)$$

is the kernel of the frequency domain reflection coefficient $\hat{R}_0(\omega)$. As clearly seen, it is a function of spectral and spatial variables ω and t' only, with no dependence on the variable $\varepsilon_r(\rho)$. The main aim of writing (4.73) in the form given by (4.74) is to be able to use the general one-dimensional integral transform technique given in section 4.2.2 for the reconstruction of $\varepsilon_r(\rho)$. As clearly mentioned there, after

obtaining the kernel $\tilde{K}(\omega, t')$ given by (4.76), we have to look for the corresponding function $K(\omega, t)$ which produces a sampling function given by

$$D(t, t') = \int_0^{\hat{\omega}} K(\omega, t) \tilde{K}(\omega, t') d\omega \quad (4.77)$$

This function should satisfy certain properties as described in section 4.2.1, which we have to verify. But before doing that, we have to also choose a particular kernel $K(\omega, t)$, which suits our needs here. One obvious choice for this is the truncated Hankel transform of order zero, which looks quite natural in the cylindrical coordinate system and whose completeness and orthogonal properties are also well established [80]. Using this Hankel transform, the spectral-domain reflection coefficient of (4.74) is transformed to the spatial domain

$$\hat{r}_0(t) = \int_0^{\hat{\omega}} \hat{R}_0(\omega) K(\omega, t) d\omega = \int_0^{\hat{\omega}} \hat{R}_0(\omega) J_0(\omega t) \omega d\omega \quad (4.78)$$

where J_0 is the Bessel function of order zero, and $\hat{\omega}$ is the highest frequency at which the reflection coefficient data is measured. Meanwhile, the value of \tilde{K} and K can be substituted from (4.76) and (4.78) into (4.77) to obtain an exact expression for the sampling function

$$D(t, t') = \int_0^{\hat{\omega}} \left\{ \frac{\omega H_1^{(1)}(\omega t') H_0^{(2)}(\omega t_b) J_0(\omega t)}{H_0^{(2)}(\omega t') H_1^{(1)}(\omega t_b)} \right\} d\omega \quad (4.79)$$

The ideal form of $D(t, t')$ should clearly be a delta function $\delta(t - t')$, which can be used to sample the permittivity function $G[t]$ according to

$$\hat{r}_0(t) = \int_{t_b}^{t_0} G(t') D(t, t') dt' \quad (4.80)$$

where, (4.74) and (4.77) are substituted in (4.78) to arrive at the above equation. But under practical situations, the form of this function can be relaxed to other pulse-shaped functions as described in section 4.2.1 provided it satisfies certain criteria. To check those criteria, let us study the shape of this function and try to examine its properties in detail. We have plotted the function $D(t, t')$ versus the electrical length $L' = t' * c = \rho' \sqrt{\varepsilon_r(\rho')}$ for different values of the sampling variable $L \equiv (t * c)$ in Figs. 4.7 to 4.9.

It may be clearly noted here that in all these figures, *the physical distance ρ is expressed in cm*, while the permittivity profile $\varepsilon_r(\rho)$ is a dimensionless quantity. We have considered about 800 points in the frequency range from 50MHz to 40GHz in these figures, and the outer radius of the cylindrical dielectric object is taken as 10 cm with the value of the relative permittivity $\varepsilon_r(b) = 4$. However, it may be mentioned here that in these plots the actual parameter is the electrical length $L \equiv \rho \sqrt{\varepsilon_r(\rho)}$, and hence these plots may be valid for other combinations of radii and $\varepsilon_r(\rho)$ as well provided that the product of these two variables remains the same. This, in fact, also shows the flexibility of our reconstruction procedure as we do not have to compute and plot the sampling function $D(t, t')$ every time, and also we do not need any *a-priori* information about the unknown permittivity profile to plot this function. It can be observed from Figs. 4.7 to 4.9 that the sampling function

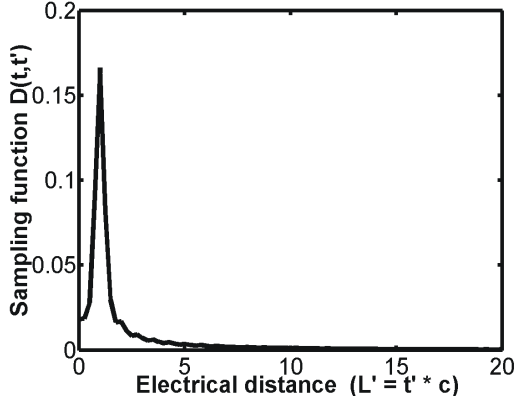


Figure 4.7: The plot of the sampling function for $L \equiv c * t = 38$

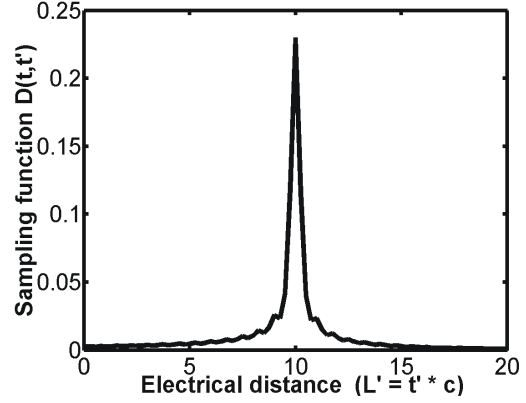


Figure 4.8: The plot of the sampling function for $L \equiv c * t = 20.0$

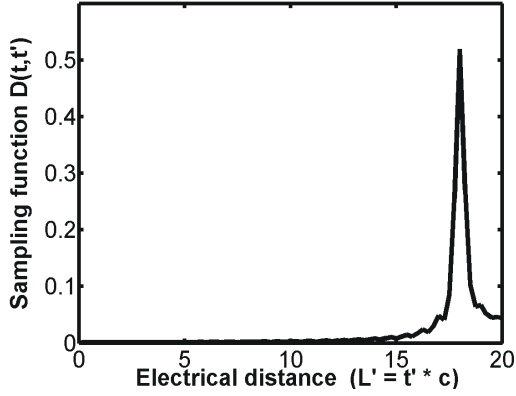


Figure 4.9: The plot of the sampling function for $L \equiv c * t = 4.0$

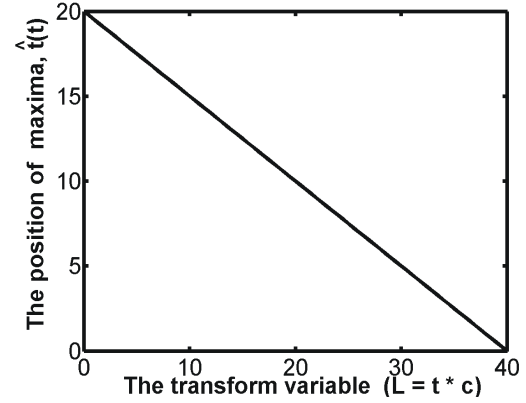


Figure 4.10: The variation of sampling function maxima $L' = \hat{L}(L) \equiv \hat{t}(t)$ with the transformed variable $L \equiv c * t$

$D(t, t')$ of (4.101) has always a pulse shape with a maximum value at $t' = \hat{t}(t)$. The position of this maximum $\hat{t}(t)$ varies with the moving parameter $L \equiv c * t$. To find the exact relationship between the position of the maximum \hat{t} and the transform variables $t = L/c$, we compute (4.79) for a number of values of t and plot them as shown in Fig. 4.10. As observed from this figure, there is a linear relationship between the position of the maxima and the transform variable t . Its mathematical form can be written as

$$t' = \hat{t} = t_b - (0.5 * t) \quad (4.81)$$

which is the required formula to find the position of exact maxima in terms of the sampling variable t , with the value of t_b given by (4.71). The above equation can be verified from Figs. 4.7-4.9, where it can be seen that the position of maxima $\hat{t}(t)$ in all these figures satisfies (4.81) with $t_b = 20/c$. It may be mentioned here that in Figs. 4.7-4.9, we have chosen the optimum value of all the parameters such as bandwidth, frequency-step etc., and hence our reconstruction theory seems to be working fine. However, in real situations, we have to first optimize all these values before applying our proposed theory of reconstruction. To find these optimized

values, it is very important to study the effect of all the parameters on the image reconstruction and to find their limiting values in each case. Here, we try to analyze the effect of these parameter on the reconstructed image both from the qualitative and quantitative point of view. First of all, we study the effect of bandwidth of the spectral domain reflection coefficient data on the reconstruction. In Fig. 4.11, we have plotted the sampling function for different values of the sampling parameter L when the bandwidth of the reflection data varies from $50MHz$ to $10GHz$ keeping all the other parameters same as in Fig. 4.7-4.9. After comparing this plot with previous figures (4.7-4.9), it can be said that the width of the sampling function increases with a decrease in the spectral bandwidth. This point can be further clarified from

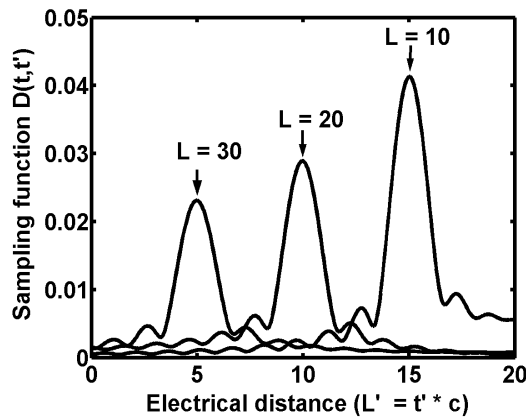


Figure 4.11: The plot of the sampling function using a frequency band from $50MHz$ to $10GHz$

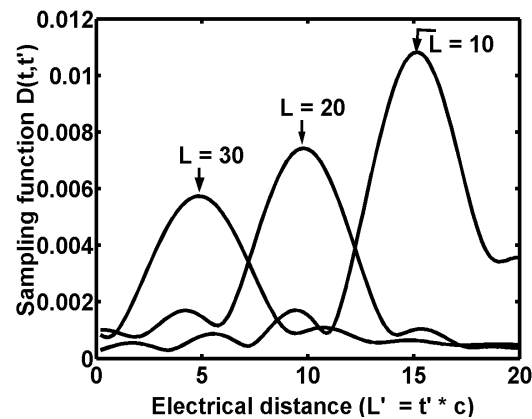


Figure 4.12: The plot of the sampling function using a frequency band from $50MHz$ to $4GHz$

Fig. 4.12, where the bandwidth is decreased to $4GHz$ keeping all other parameters to be same, and as clearly seen, the decrease in bandwidth results into further widening of the sampling function. Now, we may recall from section 4.2 that the actual image is reconstructed assuming that the original function does not change appreciably within the narrow occupancy of the sampling pulse. This assumption is valid as long as the width of the sampling function is very less. But when the pulse becomes too wide, then we may lose the fine details of the object specially if it is a rapidly varying function. The other point to be noted here is that the resolution of the image in the spatial domain is inversely proportional to width of the sampling function. This is due to the fact that in a given space-band now less number of samples can be accommodated with each sample occupying a large portion of the available space. Now as the width of this pulse-function is dependent on the bandwidth, hence the resolution of the image can be increased by increasing the bandwidth of the spectral domain measured data which is in agreement with our statement given in section 4.2. One very important factor for our proposed reconstruction theory to work is the *movability* of the sampling function as mentioned earlier. It may be noted from Figs. 4.11 and 4.12 that the movability property of the sampling function is still satisfied because $D(t, t')$ moves from one end to another with L as the moving parameter. The shape of the function is also approximately intact during this process. Hence, in both of these cases the object can still be in principle reconstructed except for the fact that the resolution of the image will be less and the deviation between the actual and the reconstructed function might be high. But,

if the bandwidth of the measured spectral reflection data is further reduced, then a situation might occur where the proposed theory of reconstruction completely fails *per se*. This can be visualized in Fig. 4.13, where the bandwidth is reduced to $1GHz$ keeping other parameters same as in previous figures. It can be seen from this plot

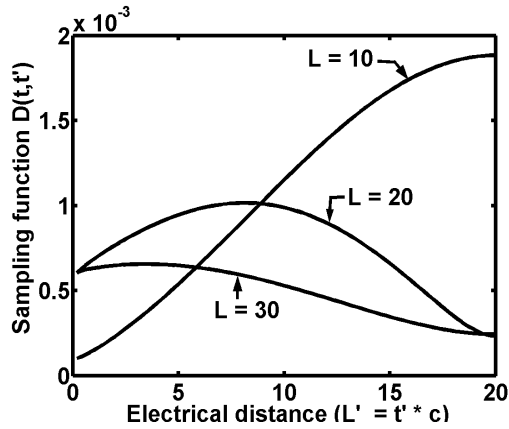


Figure 4.13: The plot of the sampling function using a frequency band from $50MHz$ to $1GHz$

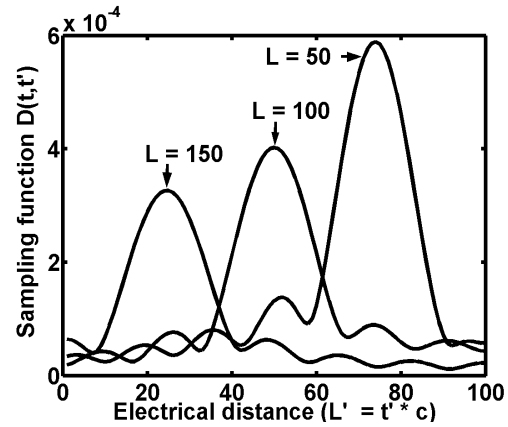


Figure 4.14: The plot of the sampling function using a frequency band from $50MHz$ to $1GHz$ with a different range of L'

that the shape of the sampling function is completely distorted and its movability property is also not well satisfied when the bandwidth of spectral data is reduced to such an extent. However, one interesting point to be noted is that the reflection coefficient data measured in the same frequency band can be used quite accurately for the image reconstruction, if the electrical dimension of the object is high. This can be seen in Fig. 4.14, where the bandwidth is same as in the previous plot but the electrical dimension of the object is high. The shape of the sampling function now looks sensible, and the function is also movable with the change in parameter L without much distortion. Hence our reconstruction theory can now be applied. From the above discussion, it can be concluded that the bandwidth is a very critical parameter and its optimum value should be well determined for a given problem before applying our reconstruction theory.

The other parameter, which is also sometimes important is the frequency step over which the scattering data are measured. Generally, this step-size should not be made too high otherwise it may lead to a false image under some situations. The situation can be better understood from Figs. 4.15 and 4.16. Both of these figures represent object of the same electrical dimension and the measurement of reflection coefficient data is also carried out over the same frequency band. However, in Fig. 4.15 a step-size of $500MHz$ is selected, while in Fig. 4.16 the step-size is reduced to $200MHz$. It basically means that in the former, less number of data points are selected in a given frequency band as compared to later. It can be clearly observed that Fig. 4.16 shows a sampling function as expected, while in the other plot we get two peaks which is totally undesirable and may lead to a false image detection. The presence of two peaks for an increased step-size can be explained by the fact that generally in the frequency domain technique, the largest possible depth of reconstruction is decided by the frequency step [97]. In other words, when the frequency-step of the spectral domain is substantially increased, then the

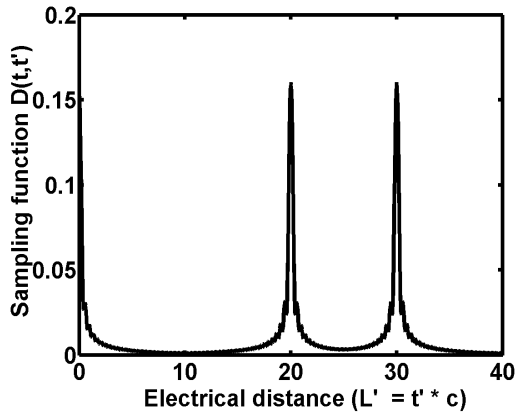


Figure 4.15: The plot of the sampling function using a frequency band from $50MHz$ to $40GHz$ with a step-size of $500MHz$

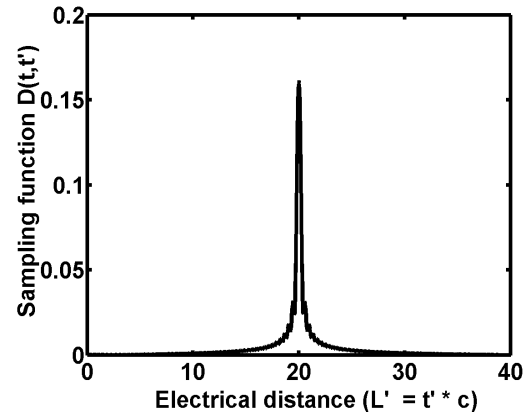


Figure 4.16: The plot of the sampling function using a frequency band from $50MHz$ to $40GHz$ with a step-size of $200MHz$

effective spatial dimension of the object which can be accurately reconstructed will be reduced. This can be explained with the help of Fig. 4.15, where if we divide the whole region into two parts then one peak will be observed in each each region and hence our proposed theory can then be applied quite accurately in each of these regions. The problem of false or ambiguous image can, however, be avoided if always measure the spectral data at a large number of points in a given frequency band.

From the above discussion, it follows that if we choose the optimized values of all the parameters then the sampling function $D(t, t')$ can be used to sample the permittivity function $G[\varepsilon_r(\rho')]$ of (4.80) at $t' = \hat{t}$ according to

$$G(t) = \frac{\hat{r}_0[t(\hat{t})]}{\int_{t_b}^{t_0} D(t(\hat{t}), t') dt'} \quad (4.82)$$

where $t(\hat{t})$ is the inverse function of $\hat{t}(t)$ and it should be computed according to (4.81). It may be noted here that the maximum value of $D(t, t')$ in Figs. 4.11-4.15 varies with the variable $t \equiv L$ as well as with the change in spectral bandwidth. This occurs mainly due to the change in the value of the Bessel function J_0 in (4.79). However, from (4.78) it can be seen that any change in t or in spectral bandwidth also produces a corresponding change in $\hat{r}_0(t)$. This change in $\hat{r}_0(t)$ compensates for the change in the magnitude of the sampling function $D(t, t')$, and hence this does not have any significant effect on the permittivity function $G(t)$ as per (4.82). Once we have computed the sampled values of $G(t)$ using (4.82), we can make use of (4.75) and (4.69) to obtain

$$4G(t') dt' = \frac{d\varepsilon_r(\rho)}{\varepsilon_r(\rho)} \quad (4.83)$$

The above equation can be integrated from the boundary value t_b to any arbitrary value t to obtain the required formula for the one-dimensional radially varying permittivity profile

$$\varepsilon_r(t) = \varepsilon_r(b) * \exp \left[4 \int_{t_b}^t G(\xi) d\xi \right] \quad (4.84)$$

The above equation applied for the cylindrical geometry may be compared to the corresponding equation (4.24) of the planar case. It is quite interesting to note the similarity in their *basic form* despite the lot of complexity involved in deriving the analytical relationship (4.84).

The permittivity profile given as a function of the variable t in (4.84) can be converted to the actual radial distance using a numerical algorithm based on (4.69) and (4.84). The overall procedure is quite similar as proposed in section 4.1.1.3 for the planar case, hence we present here only basic formulas for finding the radial distance ρ successively from the virtual time variable t . We assume that the sampled values $G(t)$ of (4.82) are available at a time-step of $\Delta t = t_n - t_{n-1}$ for $n = 1, 2, \dots, N$ and let us also assume

$$f(t) = \left[4 \int_{t_b}^t G(\xi) d\xi \right] \quad (4.85)$$

With the help of equations (4.85), (4.69), and (4.84), we can write

$$f(t_n) = -2\Delta t [G(t_{n-1}) + G(t_n)] \quad (4.86a)$$

$$\varepsilon_r(t_n) = \varepsilon_r(b) * \exp[f(t_n)] \quad (4.86b)$$

$$\rho_n = \rho_{n-1} - \frac{2\Delta t c}{\left[\sqrt{\varepsilon_r(t_{n-1})} + \sqrt{\varepsilon_r(t_n)} \right]} \quad (4.86c)$$

where t_n corresponds to ρ_n via (4.69). The exact permittivity profile $\varepsilon_r(\rho)$ can be reconstructed as a function of radial distance ρ in subsequent steps starting from $\varepsilon_r(b)$ at $\rho = b$ using (4.86a), (4.86b) and (4.86c).

From (4.68) and (4.84), it is seen that for the evaluation of both $R_0(k_0)$ and $\varepsilon_r(\rho)$, we have to first determine the surface value of the permittivity at the air-dielectric interface i.e. $\varepsilon_r(b)$. We have presented a numerical technique for reconstructing the surface value of permittivity in planar structures in section 4.1.1.4. The same procedure can be extended to determine the surface value of permittivity in radial geometry as well. Hence the reflection coefficient of the cylindrical inhomogeneous region shown in Fig. 3.9 and 3.10, after excluding the first air-dielectric interface at $\rho = b$ can be written using (4.67) and (4.68) as

$$R_1(k_0) = \frac{[R(k_0) + 1] \sqrt{\varepsilon_r(b)} + [R(k_0) - 1]}{[R(k_0) + 1] \sqrt{\varepsilon_r(b)} - [R(k_0) - 1]} \quad (4.87)$$

As explained in detail in section 4.1.1.4, the above function is optimized using the criterion

$$\max |R_1(k_0)| \rightarrow \min \quad (4.88)$$

over the given frequency band to obtain the value of $\varepsilon_r(b)$. This algorithm has been implemented using a built-in MATLAB function, and it gives the reasonably accurate value of the permittivity at the air-dielectric interface provided the reflection coefficient data is measured over a wide frequency band.

4.3.2 Higher order mode illuminations

In the last section, we discussed in detail the procedure of reconstructing a cylindrical dielectric object illuminated by a radial transmission line (TM_{00}) mode. However,

as mentioned earlier in section 3.2.2, it is not always possible to excite a particular lower order mode using practical antenna arrangements. But, an arbitrary electromagnetic field can be decomposed into a number of TE and TM modes. Hence it becomes necessary to obtain a solution which works for any arbitrary order TE or TM mode illumination. This section describes in detail the process of inversion for any arbitrary order TE_{mn} -mode illumination. As the analysis for the TM_{mn} -mode is quite similar, hence only the final expressions for the higher order TM_{mn} -mode illuminations are presented. The corresponding *Riccati-similar* non-linear differential equation of the cylindrical geometry due to a higher order TE_{mn} illumination is given by (3.103). Putting $\alpha = 1$, this equation can be rewritten in the following form to make use of our proposed renormalization technique discussed in section 4.1

$$\begin{aligned} \frac{1}{[1 - \Gamma^2]} \frac{\partial \Gamma}{\partial \rho} + \frac{\Gamma}{[1 - \Gamma^2]} \left\{ \begin{aligned} & \frac{4j}{\pi \rho H_n^{(1)}(k_\rho \rho) H_n^{(2)}(k_\rho \rho)} - \frac{j\pi \rho}{8} \frac{\partial k_\rho}{\partial \rho} \\ & \left[\begin{aligned} & \left(H_n^{(1)}(k_\rho \rho) H_{n-1}^{(2)}(k_\rho \rho) + H_{n-1}^{(1)}(k_\rho \rho) H_n^{(2)}(k_\rho \rho) \right) \\ & - \left(H_n^{(2)}(k_\rho \rho) H_{n+1}^{(1)}(k_\rho \rho) + H_{n+1}^{(2)}(k_\rho \rho) H_n^{(1)}(k_\rho \rho) \right) \end{aligned} \right] \end{aligned} \right\} \\ = \left\{ \frac{j\pi \rho}{4} H_n^{(2)}(k_\rho \rho) \left[H_{n-1}^{(1)}(k_\rho \rho) - \frac{n}{k_\rho \rho} H_n^{(1)}(k_\rho \rho) \right] \frac{\partial k_\rho}{\partial \rho} \right\} \end{aligned} \quad (4.89)$$

The selection $\alpha = 1$ is, in fact, valid for regions away from the origin in Fig. 3.9 as α in (3.90) approaches unity when the Hankel functions are replaced by their large asymptotic equivalents. As a matter of fact, even for cases when the argument of Hankel functions in (3.90) is small and the exact value of alpha is not unity, multiplying a very small number like Γ^2 with a unity or a number close to 1 does not make much difference provided that $|\alpha| \leq 1$. Once we have justified the substitution of α by unity in (4.89), we can compare this equation with the corresponding equation (4.1) of the planar case. It is interesting to observe that both equations are structurally similar in form from the the point of view of the presence of Γ , Γ^2 term, although (4.89) looks quite complicated because of the involvement of different Hankel functions. However, the complicity of (4.89) does not deter us from applying the same renormalizaiton technique used earlier to solve (4.1) of the planar case. Hence using the same convention as in the planar case of section 4.1 to solve (4.89), we may define an auxiliary linear equation in terms of a virtual reflection coefficient $\hat{\Gamma}(k_\rho, \rho)$ corresponding to (4.89). An appropriate linearized version of (4.89) in terms of $\hat{\Gamma}(\rho)$ can be written as

$$\begin{aligned} \frac{\partial \hat{\Gamma}}{\partial \rho} + \hat{\Gamma} \left\{ \begin{aligned} & \frac{4j}{\pi \rho H_n^{(1)}(k_\rho \rho) H_n^{(2)}(k_\rho \rho)} - \frac{j\pi \rho}{8} \frac{\partial k_\rho}{\partial \rho} \\ & \left[\begin{aligned} & \left(H_n^{(1)}(k_\rho \rho) H_{n-1}^{(2)}(k_\rho \rho) + H_{n-1}^{(1)}(k_\rho \rho) H_n^{(2)}(k_\rho \rho) \right) \\ & - \left(H_n^{(2)}(k_\rho \rho) H_{n+1}^{(1)}(k_\rho \rho) + H_{n+1}^{(2)}(k_\rho \rho) H_n^{(1)}(k_\rho \rho) \right) \end{aligned} \right] \end{aligned} \right\} \\ = \left\{ \frac{j\pi \rho}{4} H_n^{(2)}(k_\rho \rho) \left[H_{n-1}^{(1)}(k_\rho \rho) - \frac{n}{k_\rho \rho} H_n^{(1)}(k_\rho \rho) \right] \frac{\partial k_\rho}{\partial \rho} \right\} \end{aligned} \quad (4.90)$$

where k_ρ is the radial propagation constant defined by (3.78), and it can be rewritten for the general TE_{mn} illumination as

$$k_\rho = \sqrt{k_0^2 \varepsilon_r(\rho) - \left(\frac{m\pi}{a}\right)^2} \quad (4.91)$$

To proceed further, we note that in (4.90) if we replace Hankel functions by their large argument asymptotic approximations then the second term involving $\hat{\Gamma}$ will be zero and this equation reduces to

$$\begin{aligned} \frac{\partial \hat{\Gamma}}{\partial \rho} + \hat{\Gamma} \left[\frac{4j}{\pi \rho H_n^{(1)}(k_\rho \rho) H_n^{(2)}(k_\rho \rho)} \right] \\ = \left\{ \frac{j\pi\rho}{4} H_n^{(2)}(k_\rho \rho) \left[H_{n-1}^{(1)}(k_\rho \rho) - \frac{n}{k_\rho \rho} H_n^{(1)}(k_\rho \rho) \right] \frac{\partial k_\rho}{\partial \rho} \right\} \end{aligned} \quad (4.92)$$

It may be noted here that under situations when the Hankel functions can not be replaced by their large argument asymptotic expressions, the virtual reflection coefficient $\hat{\Gamma}$ satisfying the linear differential equation (4.92) can be redefined in order to minimize the difference between this equation and its corresponding nonlinear version (4.89). This flexibility of choosing the form of transformation between Γ and $\hat{\Gamma}$ is, in fact, the main advantage of our proposed method as it eases the complexity involved in obtaining the required solution without compromising on the accuracy. Meanwhile, the differential equation (4.92) can be integrated from the inner radius $\rho = \rho_0$ to an arbitrary radius ρ assuming $\Gamma(k_0, \rho_0) = 0$ as explained in the last section. The evaluation of this integral at the outer radius of the cylindrical dielectric object is given by $\hat{R}(k_0) = \hat{\Gamma}(k_0, b)$

$$\hat{R}(k_0) = \int_{\rho_0}^b \left\{ \frac{j\pi\rho'}{4} H_n^{(2)}(k_{\rho'}\rho') \left[H_{n-1}^{(1)}(k_{\rho'}\rho') - \frac{n}{k_{\rho'}\rho'} H_n^{(1)}(k_{\rho'}\rho') \right] \frac{\partial k_{\rho'}}{\partial \rho'} \right\} \exp \left[\int_b^{\rho'} \frac{4j}{\pi\rho'' H_n^{(1)}(k_{\rho''}\rho'') H_n^{(2)}(k_{\rho''}\rho'')} d\rho'' \right] d\rho' \quad (4.93)$$

As evident from (4.91), the radial propagation constant for the higher order cylindrical mode illuminations also depends on the z -direction, and because of this dependence it is difficult to separate the spectral variable k_0 from the spatial variable function $\varepsilon_r(\rho)$ in an explicit way. However, in order to apply our proposed technique, all terms containing $\varepsilon_r(\rho)$ have to be explicitly defined and separated. To achieve this goal, let us try to rewrite (4.91) in the following form

$$\begin{aligned} k_\rho &= k_0 \sqrt{\varepsilon_r(\rho) - \left(\frac{m\pi}{ak_0}\right)^2} = k_0 \sqrt{\varepsilon_r(\rho) - \left(\frac{m}{2\bar{a}k_0}\right)^2} \\ &= k_0 \sqrt{\varepsilon_r(\rho) - \delta^2} = k_0 \sqrt{\tilde{\varepsilon}_r(\rho)} \end{aligned} \quad (4.94)$$

where

$$\delta = \frac{m}{2\bar{a}k_0} \quad (4.95)$$

is an intermediate parameter,

$$\tilde{\varepsilon}_r(\rho) = \varepsilon_r(\rho) - \delta^2 \quad (4.96)$$

will be called the *effective* value of radially varying permittivity profile, $\bar{a} = \frac{a}{\rho_0}$ is the normalized length of the cylindrical object, and $\bar{k}_0 = \frac{k_0 \rho_0}{2\pi}$ is the normalized value of the free-space wavenumber. It may be observed from (4.95) and (4.96) that the constant δ , and hence $\tilde{\varepsilon}_r(\rho)$, still depends on the spectral variable \bar{k}_0 . For a systematic solution of the inverse problem, these parameters should be frequency independent, which is not generally true and this necessitates introducing some simplifying assumptions. One possibility may be to substitute the average value of \bar{k}_0 in (4.95) to compute δ over which the scattering data measurements are carried out. It has been observed, however, that the overall reconstruction process is much sensitive to the lower value of \bar{k}_0 . As a matter of fact, the reconstruction is quite good, if the value of \bar{k}_0 in (4.95) is taken as three to four times of the lowest value of the wavenumber⁴ at which the actual measurement is carried out. Once we have selected the value of \bar{k}_0 in (4.95) according to the above described criterion, the effective permittivity $\tilde{\varepsilon}_r(\rho)$ in (4.96) may be considered to be frequency-independent and in this case, (4.93) reduces to

$$\hat{R}_0(k_0) = \int_b^{\rho_0} \left\{ \frac{j\pi\rho'k_0}{8\sqrt{\tilde{\varepsilon}_r(\rho')}} \frac{d\tilde{\varepsilon}_r(\rho')}{d\rho'} H_n^{(2)} \left[k_0\rho' \sqrt{\tilde{\varepsilon}_r(\rho')} \right] \begin{bmatrix} \frac{nH_n^{(1)} \left[k_0\rho' \sqrt{\tilde{\varepsilon}_r(\rho')} \right]}{k_0\rho' \sqrt{\tilde{\varepsilon}_r(\rho')}} \\ -H_{n-1}^{(1)} \left[k_0\rho' \sqrt{\tilde{\varepsilon}_r(\rho')} \right] \end{bmatrix} \right. \\ \left. \cdot \exp \left[\int_b^{\rho'} \frac{4j}{\pi\rho'' H_n^{(1)} \left[k_0\rho'' \sqrt{\tilde{\varepsilon}_r(\rho'')} \right] H_n^{(2)} \left[k_0\rho'' \sqrt{\tilde{\varepsilon}_r(\rho'')} \right]} d\rho'' \right] \right\} d\rho' \quad (4.97)$$

where we have modified the reflection coefficient data to $\hat{R}_0(k_0)$ in order to take into account the discontinuity at the air-dielectric interface, and this modified reflection data is related to $\hat{R}(k_0)$ of (4.93) by equations (4.67) and (4.68). Now, for the proper solution of (4.97), we can introduce a *virtual time variable* $t = \frac{\rho}{c} \sqrt{\tilde{\varepsilon}_r(\rho)}$ as described in the last section, and this leads to

$$\hat{R}_0(\omega) = \int_{t_b}^{t_0} \left\{ \begin{bmatrix} \frac{\pi c}{8\tilde{\varepsilon}_r(\rho') \sqrt{\tilde{\varepsilon}_r(\rho')}} \frac{d\tilde{\varepsilon}_r(\rho')}{d\rho'} \end{bmatrix} j \frac{H_n^{(2)}(\omega t_b)}{H_n^{(1)}(\omega t_b)} H_n^{(1)}(\omega t') \right\} dt' \\ * \left[n H_n^{(1)}(\omega t') - \omega t' H_{n-1}^{(1)}(\omega t') \right] \quad (4.98) \\ \equiv \int_{t_b}^{t_0} G(t') \tilde{K}(\omega, t') dt'$$

where, the inner integral in (4.97) has been computed using the formula given by (C.4). The spectral domain function $\hat{R}_0(\omega)$ defined by (4.98) can be converted to its equivalent time-domain by using the Hankel transform of the n^{th} order, i.e.,

⁴It has been of course assumed here that the lowest value of \bar{k}_0 is never made equal to zero as the Hankel functions are not defined for zero argument.

$$\hat{r}_0(t) = \int_0^{\hat{\omega}} \hat{R}_0(\omega) K(\omega, t) d\omega = \int_0^{\hat{\omega}} \hat{R}_0(\omega) J_n(\omega t) \omega d\omega \quad (4.99)$$

where J_n is the Bessel function of order n . The value of $\hat{R}_0(\omega)$ can be substituted from (4.98) into the above equation, which yields

$$\hat{r}_0(t) = \int_{t_b}^{t_0} G(t') D(t, t') dt' \quad (4.100)$$

where the order of integration is interchanged, and

$$\begin{aligned} D(t, t') &= \int_0^{\hat{\omega}} K(\omega, t) \tilde{K}(\omega, t') d\omega \\ &= \int_0^{\hat{\omega}} \left\{ \frac{j\omega J_n(\omega t) H_n^{(2)}(\omega t_b) H_n^{(1)}(\omega t')}{H_n^{(1)}(\omega t_b)} \left[n H_n^{(1)}(\omega t') - \omega t' H_{n-1}^{(1)}(\omega t') \right] \right\} d\omega \end{aligned} \quad (4.101)$$

is the sampling function, whose actual shape and behavior is still to be ascertained. To plot this sampling function for different values of t , we define the normalized values of the frequency, and virtual time variable in terms of the inner radius ρ_0 of the cylindrical dielectric object shown in Fig. 3.9, i.e.,

$$\bar{t} = \bar{\rho} \sqrt{\tilde{\epsilon}_r(\rho)} = \frac{\rho}{\rho_0} \sqrt{\tilde{\epsilon}_r(\rho)} \quad (4.102a)$$

$$\bar{\omega} = \bar{k}_0 = \frac{k_0 \rho_0}{2\pi} = \frac{\omega \rho_0}{2\pi c} \quad (4.102b)$$

$$\Rightarrow \bar{\omega} \bar{t} = \frac{\omega}{2\pi} \frac{\rho \sqrt{\tilde{\epsilon}_r(\rho)}}{c} = \frac{\omega t}{2\pi} \quad (4.102c)$$

Now, let us assume (just as an illustrating example) that the inhomogeneity of the cylindrical dielectric object varies between the inner radius ρ_0 and $2\rho_0$ i.e., the normalized radial distance $\bar{\rho}$ of (4.102) varies between 1 and 2. Hence the normalized quantity \bar{t} as per (4.102a) should vary between $2 * \sqrt{\tilde{\epsilon}_r(b)}$ and 1^5 . For any typical permittivity profile $\tilde{\epsilon}_r(\rho)$ in the inhomogeneous region, let us assume that the wavelength is changed from ∞ to one-tenth of the inner radius of the object under consideration. After assigning all these values, we compute and plot $D(t, t')$ of (4.101) for different values of sampling variable t as shown in Figs. 4.17-4.20 assuming a TE_{11} mode illumination. It can be clearly seen from these figures that the sampling function in all cases is well behaved. However as mentioned earlier, in all these figures the wavelength is changed from ∞ to one-tenth of the inner radius of the object under consideration, which is basically equivalent to a very wide-bandwidth. These values are in fact optimum ones. If we decrease the bandwidth of the spectral domain data, then the pulse-width of these sampling functions increases as shown in Fig. 4.21 and hence the resolution of the reconstructed image will be less. The effect of bandwidth on the reconstructed image can better be described with the help of Fig. 4.22, where we have used the reflection coefficient data of different bandwidths. In this figure, the sampling function is plotted for $\bar{t} = 3.0$ using three

⁵In the real situation, this normalized quantity \bar{t} varies between $2 * \sqrt{\tilde{\epsilon}_r(b)}$ and $1 * \sqrt{\tilde{\epsilon}_r(\rho_0)}$, but since the value of the relative permittivity at the inner radius $\tilde{\epsilon}_r(\rho_0)$ may not be known in advance, hence this value is taken as unity to avoid any ambiguity.

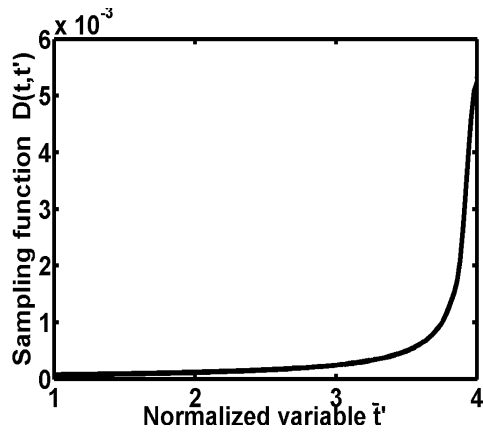


Figure 4.17: The plot of the sampling function for $\bar{t} = 0$

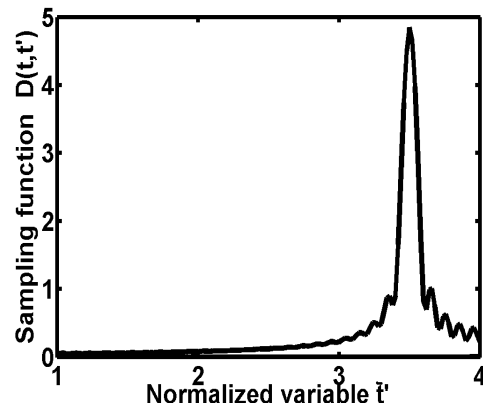


Figure 4.18: The plot of the sampling function for $\bar{t} = 1.0$

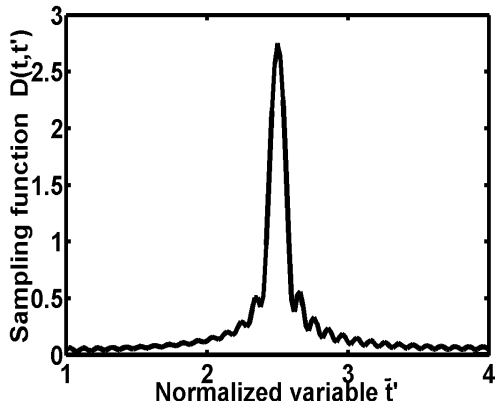


Figure 4.19: The plot of the sampling function for $\bar{t} = 3.0$

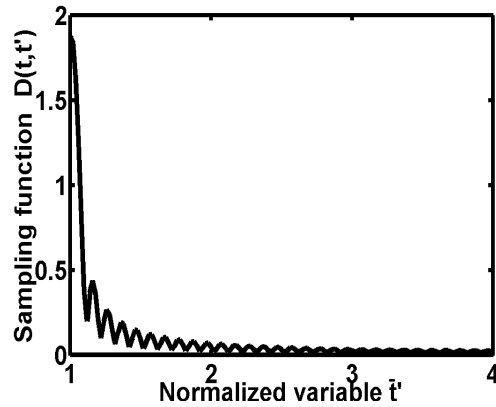


Figure 4.20: The plot of the sampling function for $\bar{t} = 6.0$

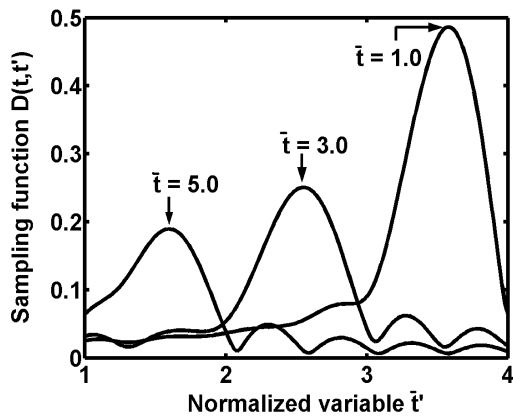


Figure 4.21: The plot of the sampling function for $\bar{k}_0 = 0.02 : 0.02 : 1.0$

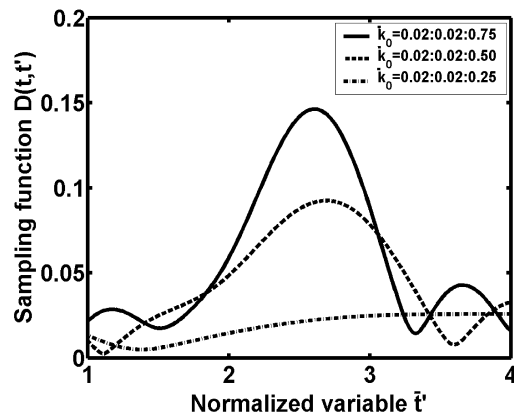


Figure 4.22: The plot of the sampling function at $\bar{t} = 3.0$ for spectral data of different bandwidths

different ranges of reflection coefficient data. It can be seen from this figure that as the bandwidth decreases, the pulse gets wider and wider. Finally, a stage is reached where the sampling function is totally distorted and the original function cannot be recovered from the reflection data if the bandwidth is so low. It may be, however,

mentioned here that the lowest limit of the bandwidth which can be used to recover the unknown function will generally depend upon the electrical dimension of the object and hence it should be determined in advance for a particular problem before applying our technique. In Fig. 4.23, we have plotted the sampling function for a

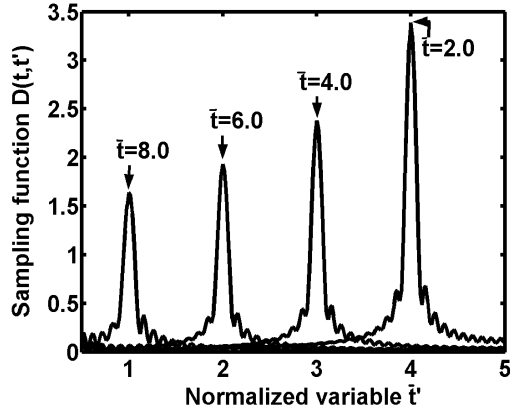


Figure 4.23: The plot of the sampling function for a TE case

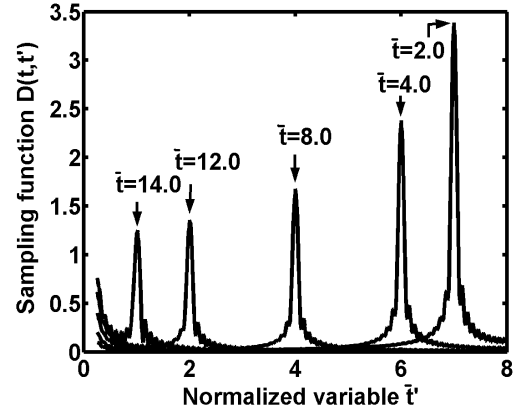


Figure 4.24: The plot of the sampling function for a TM case

TE case using different values of the moving parameter \bar{t} and Fig. 4.24 represents a TM case. In both of these figures, the wavelength is changed from ∞ to one-fifth of the inner radius of the object under consideration. It can be seen from these figures that even at this bandwidth, the shape of the sampling function is very close to a practical delta function and hence it can be very conveniently used to sample the permittivity function. In Fig. 4.25, we have considered a higher order

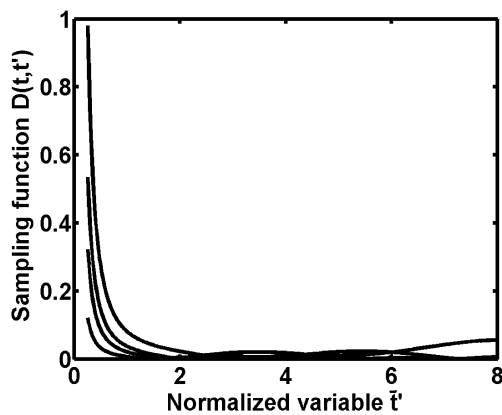


Figure 4.25: The plot of the sampling function for different values of \bar{t}

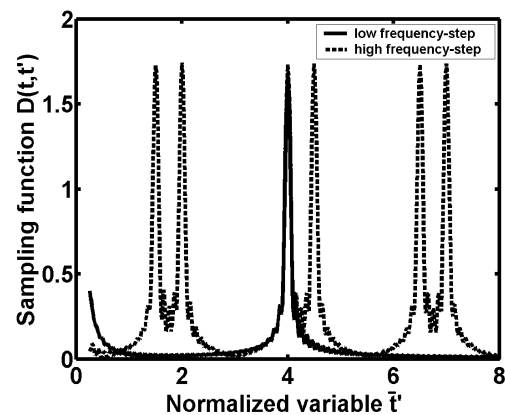


Figure 4.26: The plot of the sampling function for a TM case with different frequency steps

TM illumination to see the effect of bandwidth on the movability property of the sampling function. The bandwidth in this plot is taken as quite low (equivalent to $\bar{k}_0 = 0.02 : 0.02 : 0.250$) for all the cases. It can be observed from this plot that when the bandwidth is very low then the sampling function does not move with the parameter \bar{t} , and hence this function cannot be used for the sampling any more. It was mentioned in the last section that the step-size of the spectral data can also

have adverse effect on the image especially if its value gets too high. This can also be observed in Fig. 4.26, where we have plotted the sampling function for a higher order TM case with two different frequency steps. The solid curve in this plot corresponds to the same step-size as in Fig. 4.24 for $\bar{t} = 8.0$, while the dashed curve represents the sampling function for same \bar{t} and bandwidth but with a higher value of the step-size. As observed from this figure, a number of peaks are now available in the same band which is obviously undesirable and should be avoided under all practical considerations. It may be mentioned here that in all the plots the variable t and t' always represent normalized values unless specified otherwise.

After having optimized all parameters such as the bandwidth and the step-size, we can see from Figs. 4.17-4.24 that the position of maxima $\hat{t}(t)$ of the sampling function always changes with the moving parameter t . In Fig. 4.27 we have plotted the position of this maxima as a function of the transformed variable t , and this curve follows (4.81) with $t_b = 6/c$. From this curve, it can be said that one required feature of the sampling function, which is the *movability* as described in section 4.2.1 is satisfied by (4.101). The other important feature, which should be satisfied by the sampling function, is the minimum distortion (or spreading out) as we move over the desired band of interest. This effect can be visually seen from Fig. 4.17-4.24, where it is observed that the shape of the sampling function $D(t, t')$ is almost constant as it moves from one end of the region to the other end. To have some idea about the distortion in quantitative term, we plot the $3 - dB$ pulse width⁶ of the sampling function corresponding to Fig. 4.17-4.20 versus the transform variable t as shown in Fig. 4.28. It can be seen from this figure that the width of sampling pulse

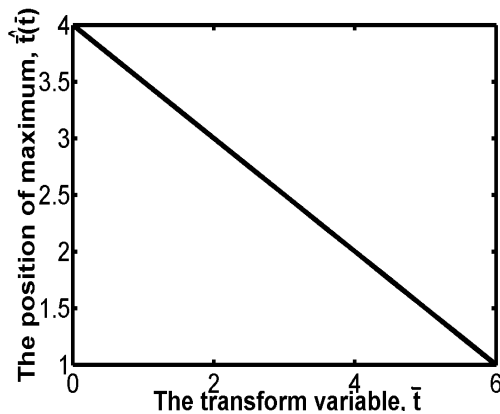


Figure 4.27: The variation of sampling function maxima with the transformed variable t

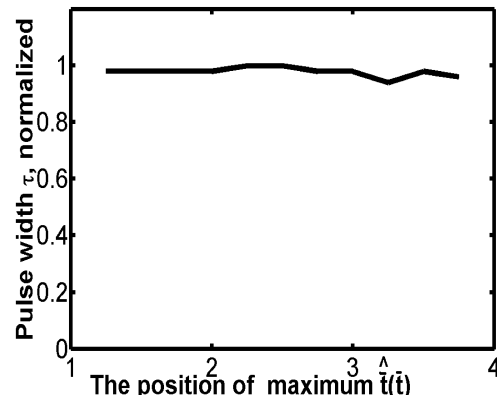


Figure 4.28: The $3dB$ pulse-width of the sampling function v/s the position of its maximum

remains almost constant, while the position of the maximum changes from one end to another.

From the above discussion, it can be concluded that the sampling function $D(t, t')$ defined by (4.101) is pulse-shaped which is movable along the t' axis without much distortion, and hence it can be used to sample the permittivity function $G[t']$ of (4.100) over the whole range with the same resolution. Once we have determined

⁶the width of the sampling function when the amplitude has fallen to $3dB$ of its maximum value.

the sampled values of $G(t)$, we can make use of (4.69) and (4.98) to obtain the required formula for the reconstruction due to a TE_{mn} illumination

$$\varepsilon_r(t) = \delta^2 + [\varepsilon_r(b) - \delta^2] * \exp \left[\frac{8}{\pi} \int_{t_b}^t G(\xi) d\xi \right] \quad (4.103)$$

The permittivity profile given by the above formula in terms of variable t can be converted to the radial distance ρ using an algorithm based on (4.86) with some modifications.

The analysis for the TM_{mn} illumination can be carried out on similar lines as given above for the general TE_{mn} case. The form of the sampling function for the higher order TM case is same as given by (4.101) except for a change of sign. The final closed-form expression of the radially varying permittivity profile due to a TM_{mn} illumination is given by

$$\varepsilon_r(t) = -\delta^2 + \frac{[\varepsilon_r(b)]^2}{[\varepsilon_r(b) - \delta^2]} * \exp \left[\frac{8}{\pi} \int_{t_b}^t G(\xi) d\xi \right] \quad (4.104)$$

4.4 The spherical geometry

After describing the inversion procedure for planar and cylindrical objects in the last two sections, we present here the technique to invert the radially varying one-dimensional permittivity profiles of spherical dielectric objects shown in Fig. 3.19. As mentioned in section 3.3, a monochromatic spherical wave of wave number k_0 is assumed to be incident from the outer free space ($r > a$) and the reflection coefficient Γ is measured at outer boundary of the dielectric object i.e., at $r = a$ as shown in Fig. 3.19. Our basic aim in this section will be to derive closed-form expressions for the one-dimensional radially varying permittivity profile $\varepsilon_r(r)$ of spherical objects in terms of an appropriate integral transform of the reflection coefficient data measured at $r = a$, due to lower and higher order TE and TM illuminations. As was the case in the direct problem formulation, we consider here the detailed analysis for any arbitrary order TM_{mn} and TE_{mn} spherical mode illuminations.

It was mentioned in section 3.3.1 that an arbitrary field in the spherical coordinate system can be decomposed in terms of TE to r and TM to r modes. It is very important to formulate the problem for any arbitrary order TE and TM modes as it is not always possible to excite a particular order mode. In this section, we describe the general procedure of inverse solution due to *higher order* spherical TM_{mn} mode illuminations. As the overall procedure for the spherical TE_{mn} -mode illuminations is quite similar to that of the spherical TM_{mn} case, hence the details will be given only for one case. The *Riccati-similar* non-linear differential equation in the spherical coordinate system due to a higher order TM_{mn} illumination is given by (3.133) as derived in section 3.3.1. This equation can be rewritten, after substituting the value of α by its asymptotic value (unity), in the following form to make use of our proposed reconstruction technique

$$\begin{aligned}
& \frac{1}{[1-\Gamma^2]} \frac{\partial \Gamma}{\partial r} + \frac{\Gamma}{[1-\Gamma^2]} \left\{ \frac{j2k_0\sqrt{\varepsilon_r(r)}}{\hat{H}_n^{(1)}(kr)\hat{H}_n^{(2)}(kr)} + \frac{j}{4\varepsilon_r(r)(2n+1)} \frac{d\varepsilon_r(r)}{dr} \right. \\
& \left. \left[\begin{array}{l} (1+n) \left[\hat{H}_n^{(2)}(kr)\hat{H}_{n-1}^{(1)}(kr) + \hat{H}_n^{(1)}(kr)\hat{H}_{n-1}^{(2)}(kr) \right] \\ -n \left[\hat{H}_n^{(2)}(kr)\hat{H}_{n+1}^{(1)}(kr) + \hat{H}_{n+1}^{(2)}(kr)\hat{H}_n^{(1)}(kr) \right] \end{array} \right] \right\} \\
& = -\frac{j}{4\varepsilon_r(r)} \frac{d\varepsilon_r(r)}{dr} \frac{\hat{H}_n^{(2)}(kr)}{(2n+1)} \left[n\hat{H}_{n+1}^{(1)}(kr) - (n+1)\hat{H}_{n-1}^{(1)}(kr) \right] \quad (4.105)
\end{aligned}$$

An auxiliary *linear* differential equation corresponding to (4.105), and describing a virtual reflection coefficient $\hat{\Gamma}$ can be written as

$$\begin{aligned}
& \frac{\partial \hat{\Gamma}}{\partial r} + \hat{\Gamma} \left\{ \frac{j2k_0\sqrt{\varepsilon_r(r)}}{\hat{H}_n^{(1)}(kr)\hat{H}_n^{(2)}(kr)} - \frac{j}{4\varepsilon_r(r)(2n+1)} \frac{d\varepsilon_r(r)}{dr} \right. \\
& \left. \left[\begin{array}{l} (1+n) \left[\hat{H}_n^{(2)}(kr)\hat{H}_{n-1}^{(1)}(kr) + \hat{H}_n^{(1)}(kr)\hat{H}_{n-1}^{(2)}(kr) \right] \\ -n \left[\hat{H}_n^{(2)}(kr)\hat{H}_{n+1}^{(1)}(kr) + \hat{H}_{n+1}^{(2)}(kr)\hat{H}_n^{(1)}(kr) \right] \end{array} \right] \right\} \\
& = -\frac{j}{4\varepsilon_r(r)} \frac{d\varepsilon_r(r)}{dr} \frac{\hat{H}_n^{(2)}(kr)}{(2n+1)} \left[n\hat{H}_{n+1}^{(1)}(kr) - (n+1)\hat{H}_{n-1}^{(1)}(kr) \right] \quad (4.106)
\end{aligned}$$

The relationship between the actual measurable reflection coefficient Γ of (4.105) and the virtual $\hat{\Gamma}$ of (4.106) can be obtained using an optimized nonlinear transformation (4.7) as explained in previous sections. Now, the second term involving $\hat{\Gamma}$ on the left hand side of (4.106) reduces to zero if we replace spherical Hankel functions by their large argument asymptotic approximations. Hence, the actual differential equation for the spherical TM_{mn} case will reduce to

$$\frac{\partial \hat{\Gamma}}{\partial r} + \hat{\Gamma} \left[\frac{j2k_0\sqrt{\varepsilon_r(r)}}{\hat{H}_n^{(1)}(kr)\hat{H}_n^{(2)}(kr)} \right] = -\frac{j}{4\varepsilon_r(r)} \frac{d\varepsilon_r(r)}{dr} \frac{\hat{H}_n^{(2)}(kr)}{(2n+1)} \left[\begin{array}{l} n\hat{H}_{n+1}^{(1)}(kr) \\ - (n+1)\hat{H}_{n-1}^{(1)}(kr) \end{array} \right] \quad (4.107)$$

It may be noted here that even under situations when the spherical Hankel functions can not be replaced by their large argument asymptotic expressions, the virtual reflection coefficient $\hat{\Gamma}$ satisfying the linear differential equation (4.107) can be redefined in order to minimize the difference between this equation and its corresponding nonlinear version (4.105) as explained in the previous section for the cylindrical case. The above equation can be integrated from the inner radius $r = r_0$ of the spherical dielectric object shown in Fig. 3.19 to an arbitrary radius r using the boundary condition $\Gamma(k_0, r_0) = 0$

$$\hat{\Gamma}(k_0, r) = \int_{r_0}^r \left\{ -\frac{j}{4\varepsilon_r(r')} \frac{d\varepsilon_r(r')}{dr'} \left[n\hat{H}_{n+1}^{(1)}(k'r') - (n+1)\hat{H}_{n-1}^{(1)}(k'r') \right] \right. \\
\left. \frac{\hat{H}_n^{(2)}(k'r')}{(2n+1)} * \exp \left[\int_r^{r'} \left[\frac{j2k_0\sqrt{\varepsilon_r(r'')}}{\hat{H}_n^{(1)}(k''r'')\hat{H}_n^{(2)}(k''r'')} \right] dr'' \right] \right\} dr' \quad (4.108)$$

This integral is evaluated at the outer radius yielding

$$\hat{R}_0(k_0) = \hat{\Gamma}(k_0, a) = \int_{r_0}^a \left\{ \begin{array}{l} -\frac{j}{4\varepsilon_r(r')} \frac{d\varepsilon_r(r')}{dr'} \left[n\hat{H}_{n+1}^{(1)}(k'r') - (n+1)\hat{H}_{n-1}^{(1)}(k'r') \right] \\ \frac{\hat{H}_n^{(2)}(k'r')}{(2n+1)} * \exp \left[\int_a^{r'} \frac{j2k_0\sqrt{\varepsilon_r(r'')}}{\hat{H}_n^{(1)}(k''r'')\hat{H}_n^{(2)}(k''r'')} dr'' \right] \end{array} \right\} dr' \quad (4.109)$$

where we have modified the reflection coefficient data to $\hat{R}_0(k_0)$ in order to take into account the discontinuity at the air-dielectric interface, and this modified reflection data is related to $\hat{R}(k_0)$ corresponding to (4.108) by equations (4.67) and (4.68). In the next step, a variable transformation is introduced for the proper solution of (4.109), as was done in cylindrical geometries, and for this purpose the *virtual time variable* t is now defined as

$$t = \frac{r}{c} \sqrt{\varepsilon_r(r)}, \quad \Rightarrow dt \cong \frac{1}{c} \sqrt{\varepsilon_r(r)} dr \quad (4.110)$$

which holds reasonably good for moderate values of $d\varepsilon_r(r)/dr$. If we substitute (4.110) in (4.109), then it yields

$$\hat{R}_0(\omega) = \int_{t_0}^{t_a} \left\{ \begin{array}{l} -\frac{jc}{4\varepsilon_r(r')\sqrt{\varepsilon_r(r')}} \frac{d\varepsilon_r(r')}{dr'} \left[n\hat{H}_{n+1}^{(1)}(\omega t') - (n+1)\hat{H}_{n-1}^{(1)}(\omega t') \right] \\ \frac{\hat{H}_n^{(2)}(\omega t')}{(2n+1)} * \exp \left[\int_{t_a}^{t'} \frac{j2\omega}{\hat{H}_n^{(1)}(\omega t'')\hat{H}_n^{(2)}(\omega t'')} dt'' \right] \end{array} \right\} dt' \quad (4.111)$$

The inner integral in (4.111) can be evaluated using (C.9), which reduced to

$$\exp \left[\int_{t_a}^{t'} \frac{j2\omega}{\hat{H}_n^{(1)}(\omega t'')\hat{H}_n^{(2)}(\omega t'')} dt'' \right] = \frac{\hat{H}_n^{(1)}(\omega t')\hat{H}_n^{(2)}(\omega t_a)}{\hat{H}_n^{(2)}(\omega t')\hat{H}_n^{(1)}(\omega t_a)} \quad (4.112)$$

The value of the above integral can be substituted into (4.111), which yields

$$\hat{R}_0(\omega) = \int_{t_a}^{t_0} \left\{ \begin{array}{l} \left[\frac{c}{4\varepsilon_r(r')\sqrt{\varepsilon_r(r')}} \frac{d\varepsilon_r(r')}{dr'} \right] \frac{j\hat{H}_n^{(2)}(\omega t_a)\hat{H}_n^{(1)}(\omega t')}{\hat{H}_n^{(1)}(\omega t_a)(2n+1)} \\ * \left[n\hat{H}_{n+1}^{(1)}(\omega t') - (n+1)\hat{H}_{n-1}^{(1)}(\omega t') \right] \end{array} \right\} dt' \quad (4.113)$$

The above equation can now be written in our standard form in order to apply the general theory of reconstruction described in section 4.2.2

$$\hat{R}_0(\omega) = \int_{t_a}^{t_0} G(t') \tilde{K}(\omega, t') dt' \quad (4.114)$$

where,

$$G(t') \equiv cg[\tilde{\varepsilon}_r(\rho')] = \left[\frac{c}{4\varepsilon_r(r')\sqrt{\varepsilon_r(r')}} \frac{d\varepsilon_r(r')}{dr'} \right] \quad (4.115)$$

is an explicit function of $\varepsilon_r(r')$, and

$$\tilde{K}(\omega, t') = \frac{j \hat{H}_n^{(2)}(\omega t_a)}{\hat{H}_n^{(1)}(\omega t_a)} \frac{\hat{H}_n^{(1)}(\omega t')}{(2n+1)} * \left[n \hat{H}_{n+1}^{(1)}(\omega t') - (n+1) \hat{H}_{n-1}^{(1)}(\omega t') \right] \quad (4.116)$$

is the kernel of the spectral domain integral $\hat{R}(\omega)$. Our next task is to look for an appropriate transform or kernel in order to convert the spectral domain function $\hat{R}(\omega)$ into its *equivalent time-domain*. In this thesis, we have proposed a special kind of *spherical Fourier-Bessel transform* which looks more suitable to account for the one-dimensional radial variation in the spherical coordinate system. The actual expressions for this transform has been derived in appendix D. Making use of this transform we obtain

$$\hat{r}_0(t) \equiv \int_0^{\hat{\omega}} \hat{R}_0(\omega) K(\omega, t) d\omega = \int_0^{\hat{\omega}} \hat{R}_0(\omega) j_0(\omega t) \omega^2 d\omega \quad (4.117)$$

where $j_0(\omega t)$ is the spherical bessel function of order zero [91], and $\hat{R}(\omega)$ is defined using (4.113). The above equation can be combined with (4.113), and (4.114) to obtain

$$\hat{r}_0(t) = \int_{t_a}^{t_0} G(t') D(t, t') dt' \quad (4.118)$$

where $G(t')$ is defined using (4.115), and

$$\begin{aligned} D(t, t') &\equiv \int_0^{\hat{\omega}} K(\omega, t) \tilde{K}(\omega, t') d\omega \\ &= \int_0^{\hat{\omega}} \left\{ \frac{j \hat{H}_n^{(2)}(\omega t_a)}{\hat{H}_n^{(1)}(\omega t_a)} \frac{\hat{H}_n^{(1)}(\omega t')}{(2n+1)} \left[n \hat{H}_{n+1}^{(1)}(\omega t') - (n+1) \hat{H}_{n-1}^{(1)}(\omega t') \right] j_0(\omega t) \omega^2 \right\} d\omega \end{aligned} \quad (4.119)$$

is the sampling function for the TM_{mn} spherical mode, whose actual shape and behavior has to be determined before proceeding further. To study the behavior of this function $D(t, t')$, the frequency and time variables are normalized using (4.102) with ρ and $\tilde{\varepsilon}_r(\rho)$ replaced by r and $\varepsilon_r(r)$ respectively. In Fig. 4.29, we have plotted this sampling function for a lower order TM mode using a wide-band spectral data (the wavelength varying from ∞ to one-fifth of the inner radius of the object under consideration, which is equivalent to $0 \leq \bar{k}_0 \leq 5.0$). At this bandwidth, the function can clearly seen to be of narrow width which is also movable with the sampling parameter \bar{t} . The same function is plotted in Fig. 4.30 using the spectral data of somewhat lower band ($0 \leq \bar{k}_0 \leq 0.75$). The function is still pulse-shaped but it is now spread-out due to lowering of the bandwidth. But if the bandwidth is further reduced (say, $0 \leq \bar{k}_0 \leq 0.25$), then the shape of this function is totally distorted as shown in Fig. 4.31. The function in this figure also does not move any longer with the change in parameter \bar{t} . Hence at this stage, this function can not be used to sample the unknown function. In Fig. 4.32, we have plotted the sampling function for an object of higher electrical size using the TM_{02} illumination. The bandwidth

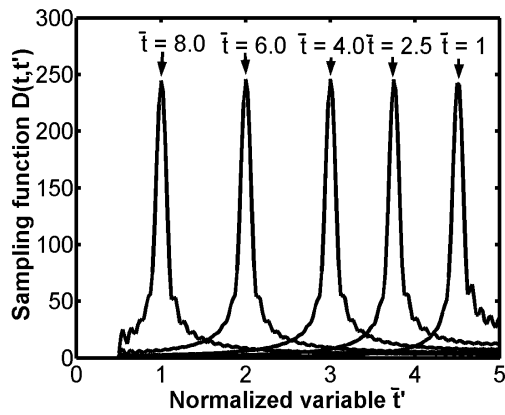


Figure 4.29: The plot of the sampling function for different values of \bar{t} using a wide-band spectral data

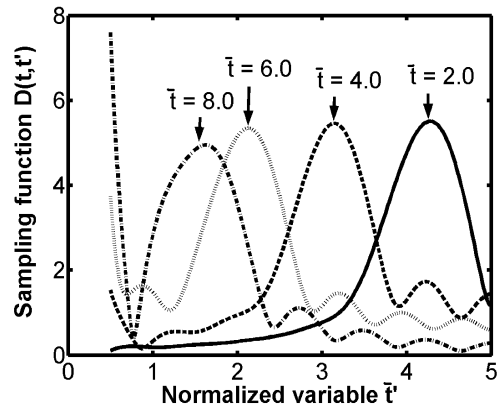


Figure 4.30: The plot of the sampling function using the spectral data of low bandwidth

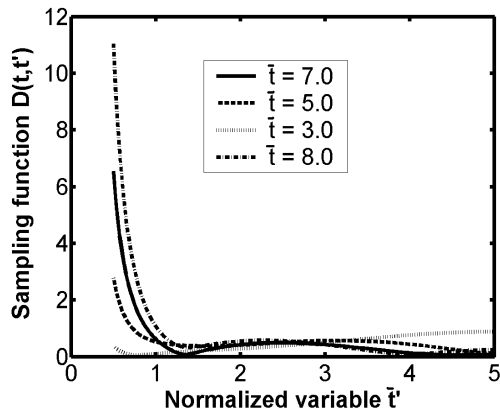


Figure 4.31: The plot of the sampling function when the spectral bandwidth becomes very low

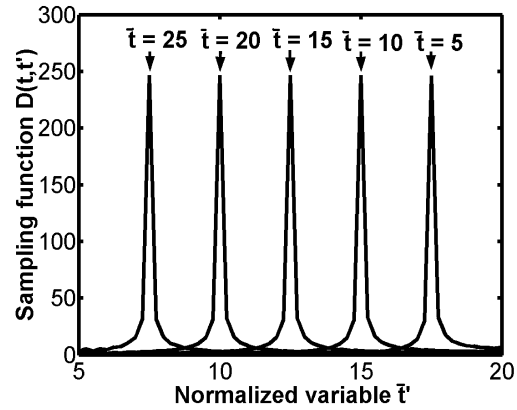


Figure 4.32: The plot of the sampling function for $\bar{k}_0 = 0.01 : 0.01 : 5.0$

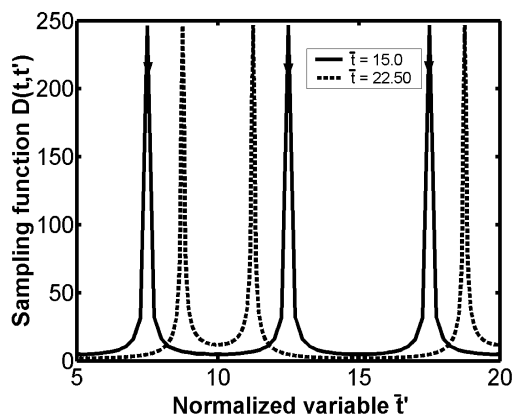


Figure 4.33: The plot of the sampling function using a larger step-size

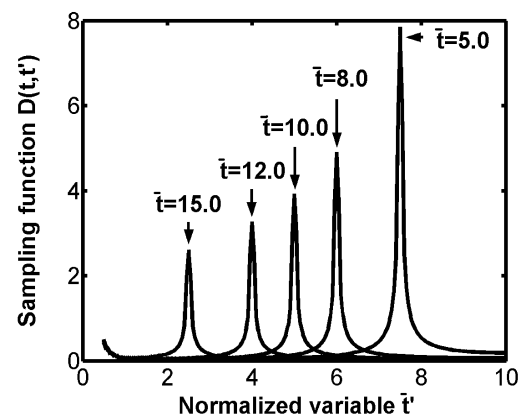


Figure 4.34: The plot of the sampling function for a TE_{01} mode

for this case is same as considered in Fig. 4.29. To see the effect of the step-size in the spherical case, we have plotted the sampling function for two different values of

the transform variable \bar{t} in Fig. 4.33. It can be seen from this plot that an increase in the *step-size* might lead to a false determination of the target as now many peaks are present in the given spatial range. After considering different *TM* cases, we have plotted the shape of this sampling function for *TE* cases as well. Figs. 4.34 and 4.35 show the sampling function using a lower order *TE* illumination for two

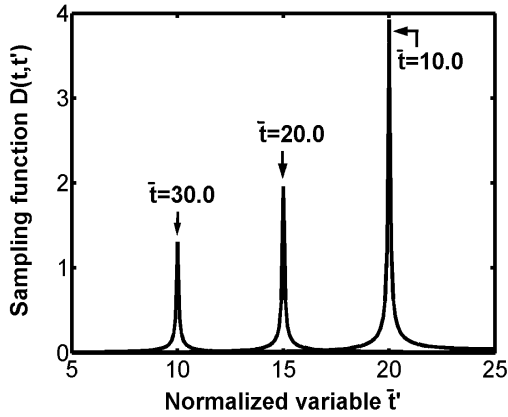


Figure 4.35: The plot of the sampling function for a TE_{01} mode

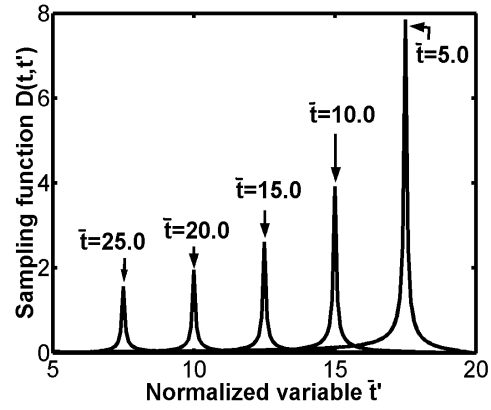


Figure 4.36: The plot of the sampling function for a TE_{02} mode

objects of different electrical sizes. In Fig. 4.36, we have considered a higher order *TE* illumination. The spectral data of wide frequency band are utilized in these cases, and it can be observed from these figures that even for a *TE* case the shape of the sampling function is very close to a delta function and its movability property is also satisfied. However, if the bandwidth of the spectral data is reduced then

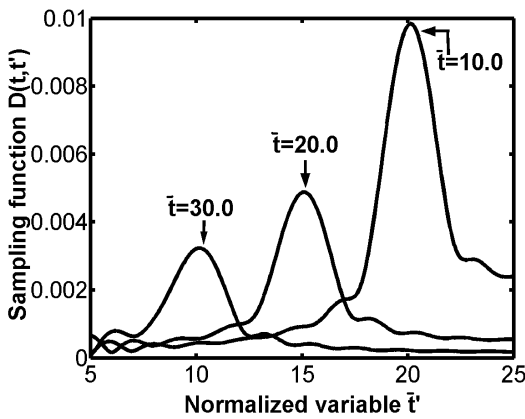


Figure 4.37: The plot of the sampling function for a higher order *TE* illumination with low bandwidth

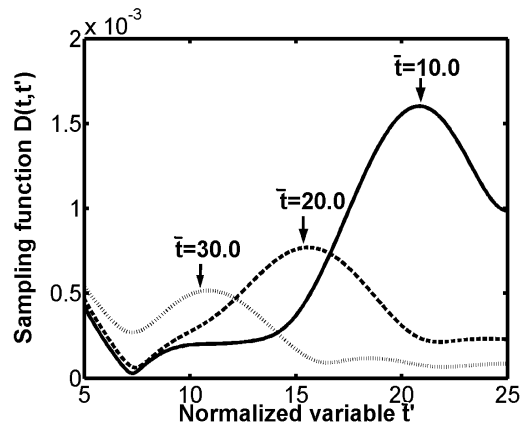


Figure 4.38: The plot of the sampling function for a higher order *TE* illumination with a very low bandwidth

these pulses get distorted as observed from Fig. 4.37 and 4.38. The position of the maximum of sampling function $\hat{t}(\bar{t})$ is related linearly with the sampling parameter \bar{t} as shown in Fig. 4.39. This situation is similar as was the case in the cylindrical geometry, and this curve fits (4.81) with the value of $\bar{t}_b = 25.0$. In Fig. 4.40, we have plotted the 3-dB pulse-width of the sampling function versus the position of its maximum. It can be seen from this figure that the pulse-width remains almost

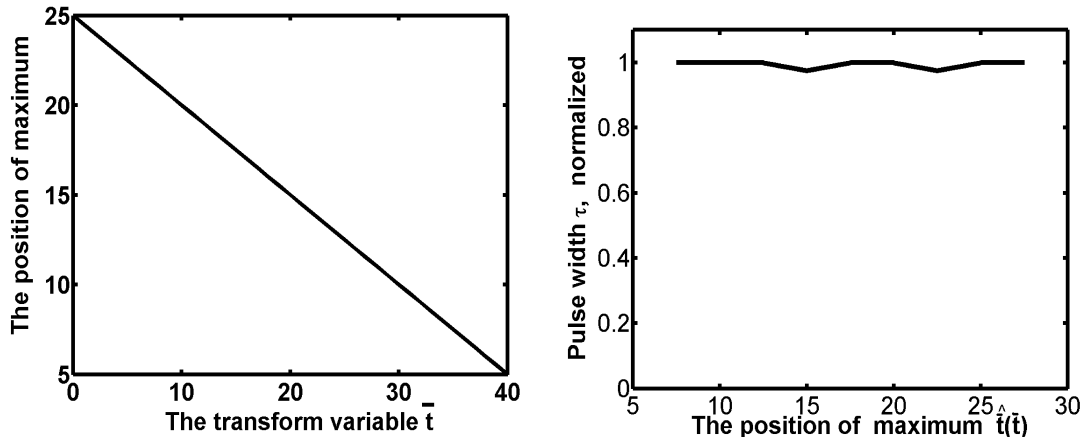


Figure 4.39: The variation of the sampling function maxima with the transformed variable \bar{t} Figure 4.40: The $3dB$ pulse-width of the sampling function v/s the position of its maximum

constant as we move over the whole range of the electrical distance t' , which basically guarantees the shape of the function in quantitative term. Once we have determined the basic shape and characteristics of the sampling function $D(t, t')$ as given above, it can be used to sample the function $G(t')$ of (4.118) according to

$$G(t) = \frac{\hat{r}_0 [t(\hat{t})]}{\int_{t_a}^{t_0} D(t(\hat{t}), t') dt'} \quad (4.120)$$

After determining the sampled values of $G(t)$ as per (4.120), we can make use of (4.115) and (4.110) to obtain

$$4 G(t') dt' = \frac{d\varepsilon_r(r)}{\varepsilon_r(r)} \quad (4.121)$$

which can be integrated from the boundary value t_a to any arbitrary value t to obtain the required formula for the one-dimensional radially varying permittivity profile of spherical objects illuminated by a TM_{mn} mode

$$\varepsilon_r(t) = \varepsilon_r(a) * \exp \left[4 \int_{t_a}^t G(\xi) d\xi \right] \quad (4.122)$$

The intermediate variable t of the above equation is transformed into the radial distance r using a numerical algorithm similar to described in section 4.1.1.3.

It may be mentioned here that the radial propagation constant k in the spherical geometry is independent of the axial or azimuthal direction even for higher order modes. Hence the basic form of (4.122) remains the same for higher order TE_{mn} modes as well as for lower order TE and TM spherical modes. However, the form of the sampling function (4.119) will be different for each mode. Hence, before using the expression given by (4.122) for the reconstruction, it is necessary to have a look at the shape of the sampling function for the particular mode. However, the overall method of reconstruction for any spherical mode is exactly similar as described above for the TM_{mn} case.

Chapter 5

Reconstructed Examples

The basic theory and all the details about our proposed technique to reconstruct the one-dimensional permittivity profiles of planar and non-planar dielectric objects have been discussed in the previous chapters. In this chapter, we have reconstructed different kinds of permittivity profiles in planar, cylindrical and spherical coordinate systems to validate the proposed technique. Firstly, we have considered simulated examples, where the reflection coefficient data have been synthetically generated for a given permittivity profile by either solving numerically the exact non-linear differential equations or by using the $[T]$ matrix method described in chapter 3. This is followed by the experimental examples, where the reflection coefficient data of many known dielectric samples have been measured over a wide frequency band both in transmission lines and in the free-space. The dielectric samples of different permittivities have been stacked together in different combinations in order to obtain a *multi-layer* structure, and accordingly the reflection coefficient data of this multi-layer dielectric media have also been measured. Both in case of simulated and experimental examples, the permittivity profile is reconstructed from the reflection coefficient data using the proposed inverse algorithm, and is then compared with the actual profile.

5.1 Simulated results

First of all, we consider here the planar dielectric objects having the one-dimensional depth-dependent permittivity variation. Afterwards, the cylindrical and spherical dielectric objects, whose relative permittivity changes in the radial direction, are considered.

5.1.1 Planar geometry

We start this section with an analytical example, whose reflection coefficient is given by the following single pole expression

$$\Gamma(k_0) = \frac{1}{(1 + j2k)} \quad (5.1)$$

where $k = k_0\sqrt{\varepsilon_r(x)}$, and the relaxation distance λ has been chosen equal to 2.0. To reconstruct the permittivity profile corresponding to above expression of the

reflection coefficient, we first try to ascertain whether the permittivity is continuous at the air-dielectric interface. From the above equation, it is obvious that $\lim_{k_0 \rightarrow \infty} \Gamma(k_0) = 0$. This means that in the high frequency region, plotting the real and imaginary parts of this reflection coefficient in the complex plane yields a point $r = 0, c = 0$, where r and c are defined in the same way as in section 4.1.1.4. If we substitute these values in (4.28), then we have

$$\begin{aligned}
 S_{11} &= \lim_{\substack{c \rightarrow 0 \\ (r=0)}} \frac{(r^2 - c^2 - 1) + \sqrt{(r^2 - c^2 - 1)^2 - 4c^2}}{2c} \\
 &= \lim_{c \rightarrow 0} \frac{(-c^2 - 1) + \sqrt{(-c^2 - 1)^2 - 4c^2}}{2c} \\
 &= \lim_{c \rightarrow 0} \frac{(-c^2 - 1) + (-c^2 + 1)}{2c} \\
 &= 0
 \end{aligned} \tag{5.2}$$

Hence in the limiting case the value of S_{11} reduces to zero. If we substitute this value in (4.20), then the value of the permittivity at the air-dielectric interface is computed as unity. The virtual reflection coefficient $\hat{\Gamma}(k_0)$ corresponding to the above $\Gamma(k_0)$ can be derived using (4.8) and is given by

$$\hat{\Gamma}(k_0) = \frac{1}{4jk(jk+1)} + \frac{1}{2(jk+1)} - \frac{1}{24(jk+1/2)^3} \tag{5.3}$$

The inverse Fourier transform of the above equation yields [63]

$$\hat{r}(l) = \frac{1}{4} (1 + e^{-l}) - \frac{1}{48} l^2 e^{-l/2} \tag{5.4}$$

where $l = x \sqrt{\varepsilon_r(x)}$ is the normalized electrical length, with x being normalized in terms of λ . The expression for the permittivity profile in terms of l can now be derived using (5.4) and (4.19)

$$\varepsilon_r(l) = \exp \left\{ -1 [1 + l - e^{-l}] + \frac{1}{12} \left[e^{-l/2} (-2l^2 - 8l - 16) + 16 \right] \right\} \tag{5.5}$$

The electrical length l is converted to the physical distance x using the numerical algorithm proposed in section 4.1.1.3. The permittivity profile $\varepsilon_r(x)$ corresponding to the reflection coefficient (5.1) is finally plotted as a function of the normalized distance x using (5.5) and (4.27) as shown in Fig. 5.1. In this figure, the exact permittivity profile corresponding to (5.1) is also plotted, which is basically given by [94]

$$\varepsilon_r(x) = (1 + 3x)^{-4/3} \tag{5.6}$$

For the comparison of our method with previous ones, we have also plotted the permittivity profile reconstructed by Cui *et.al.* [94] in this graph. It can be clearly seen from this curve that the reconstructed permittivity profile using our method

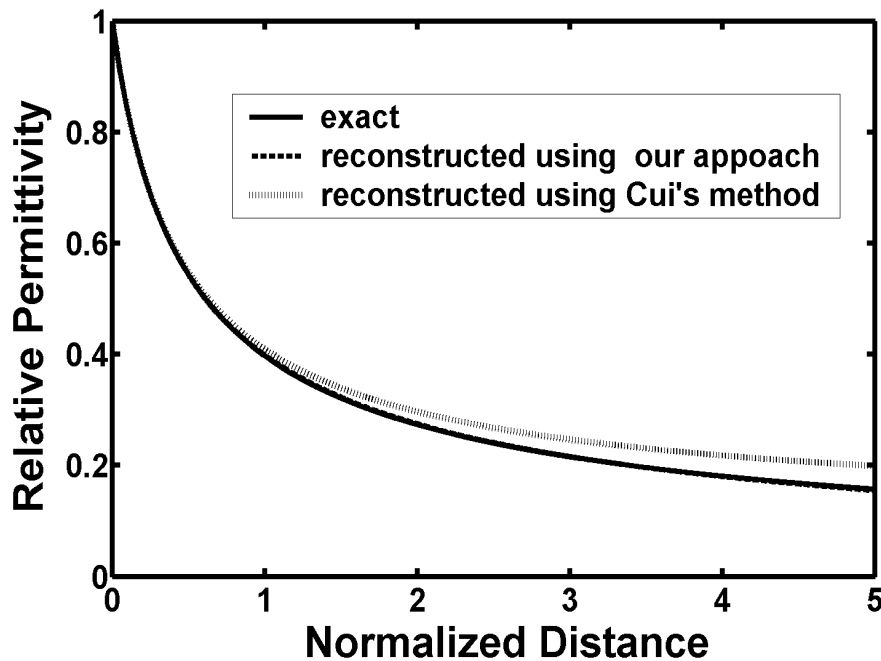


Figure 5.1: Exact and reconstructed permittivity profiles for an analytical case

is very close to the actual one and is definitely much better than using e.g., the previously proposed method *Cui* [94].

After considering the analytical example as described above, we consider here a number of numerical examples for the validation of our technique. In all these examples, we synthetically generate the actual reflection coefficient data after solving the exact nonlinear Riccati differential equation (3.18) using *MATLAB* for a given permittivity profile. These data are then used to reconstruct the permittivity profile using the proposed technique. The numerical examples are more versatile in nature than analytical ones as we can consider many kinds of permittivity profiles using this method and comparison of the reconstructed profile with the actual one gives an idea about the applicability of the proposed method of reconstruction. Firstly, a linearly varying permittivity profile with a very high contrast (4 : 1), which is continuous at the air-dielectric interface i.e. $\varepsilon_{r0} = 1$ is considered as shown in Fig. 5.2. This figure shows the plots of exact and reconstructed permittivity profiles using our method (4.7) (*present*), using $\hat{\Gamma} = \Gamma / (1 - \Gamma^2)$ (*approach_1*), and using $\hat{\Gamma} = \tanh^{-1} \Gamma$ (*approach_2*). It can be seen from this figure that the *approach_1* reconstructs the permittivity profile which is always higher than its exact value. On the other hand if we use the *approach_2*, then the reconstructed values of the permittivity profile are lower than actual. However, if we use our method then there is much better agreement between the exact and the reconstruction permittivity profile than using e.g. the two approaches described above. As a matter of fact, the proximity between the exact and reconstructed permittivity profile using our approach is so high that sometimes it is difficult to distinguish between them as can be further seen in Figs. 5.3 to 5.6. Fig. 5.3 shows a linearly varying permittivity profile with a positive slope and a discontinuity at the outer air-dielectric interface. The good agreement between the actual and the reconstructed permittivity profile can be observed from this figure. In Fig. 5.4, another linearly varying profile with a

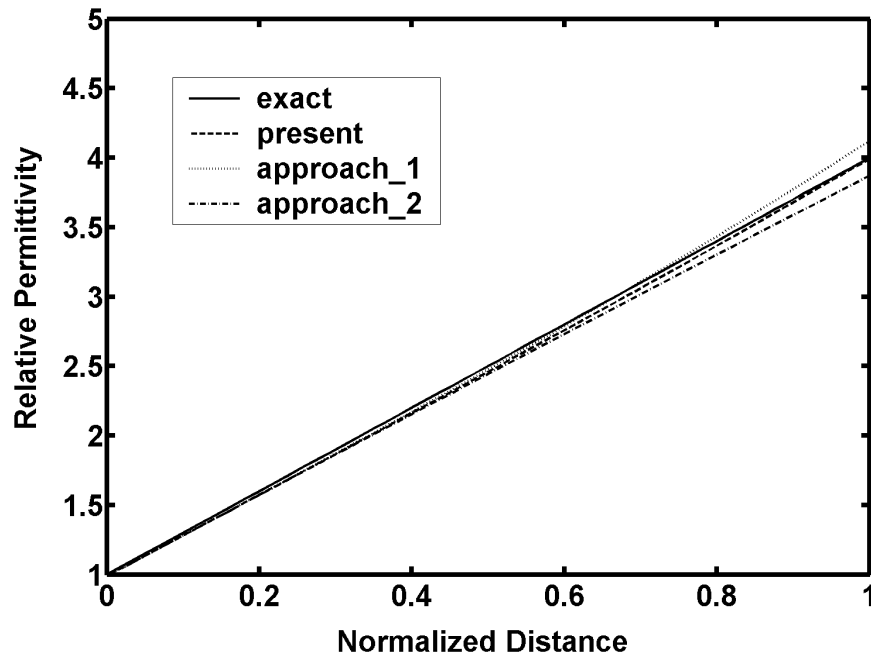


Figure 5.2: Exact and reconstructed permittivity profiles using different approaches

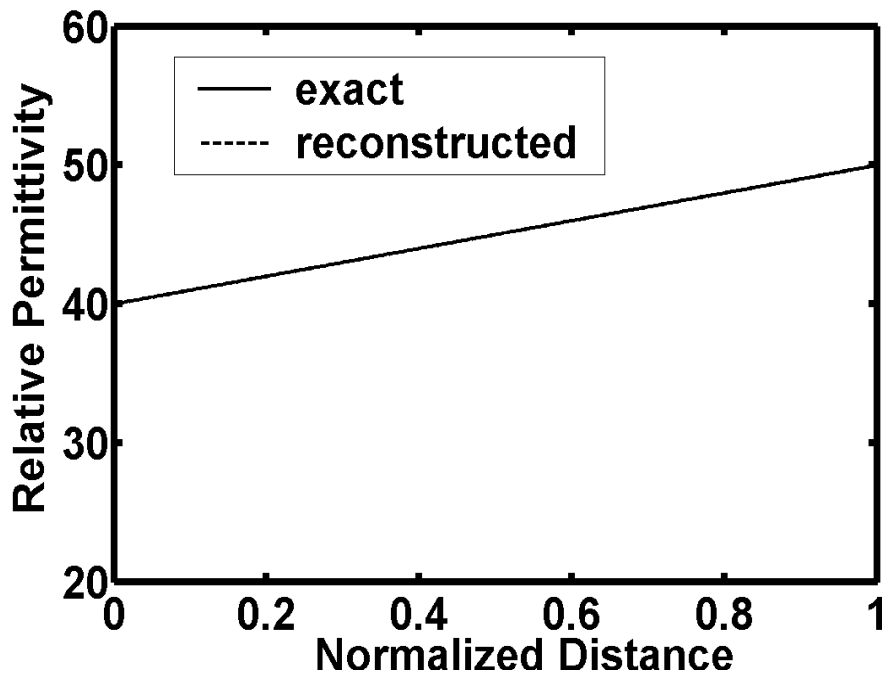


Figure 5.3: Exact and reconstructed permittivity profiles for a linear case

very high value of relative permittivity and a negative slope is reconstructed. It can be seen that our method is able to give a reasonably good result even for scattering objects whose relative permittivity approaches 100. For both of these cases, the formula given by (4.24) is used for the reconstruction. After considering the linearly varying profiles, two nonlinearly varying permittivity profiles are considered for the reconstruction as shown in Figs. 5.5 and 5.6. In Fig. 5.5 we have considered a

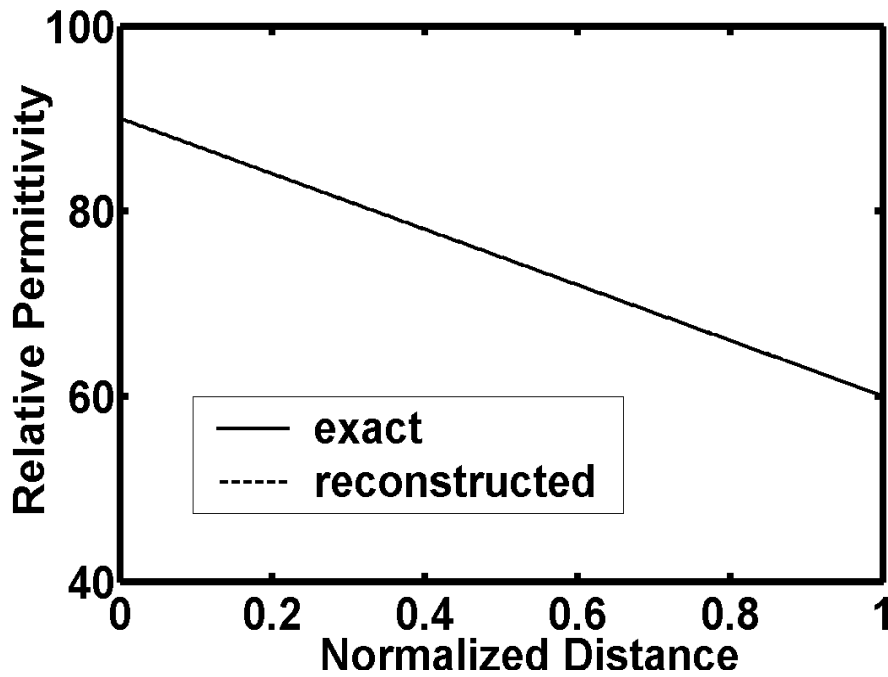


Figure 5.4: Exact and reconstructed permittivity profiles for a very high value of permittivity

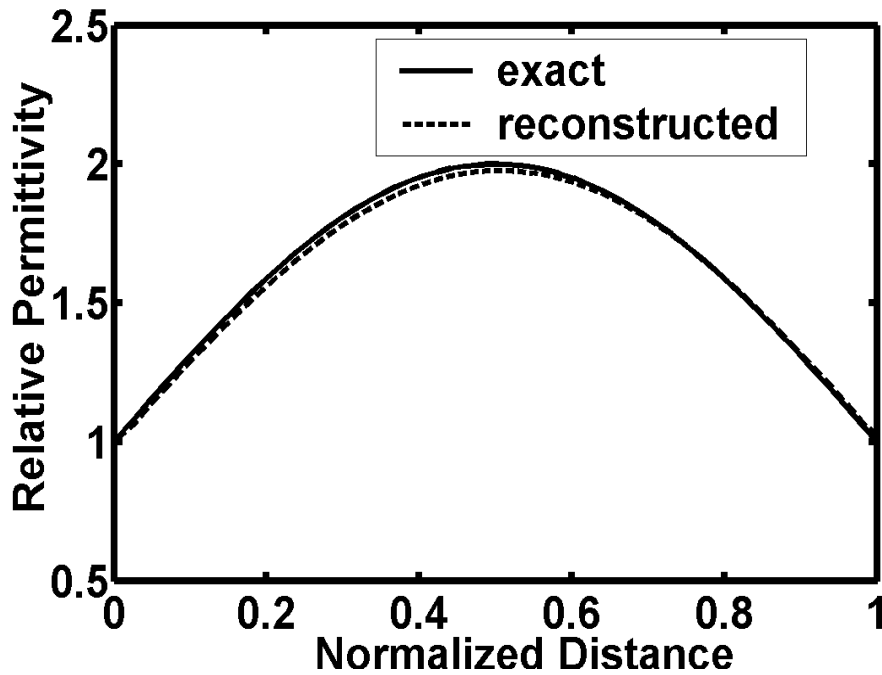


Figure 5.5: Exact and reconstructed permittivity profiles for a nonlinear case

sinusoidal variation, while Fig. 5.5 represents a *cosine* variation. It can be seen from these two curves that our method works quite well even for non-linear cases, where the rate of change of permittivity is very high. It may be noted that in all numerical examples presented here, around 100 reflection coefficient data points covering the spectral range from infinity to one-tenth of the maximum depth of

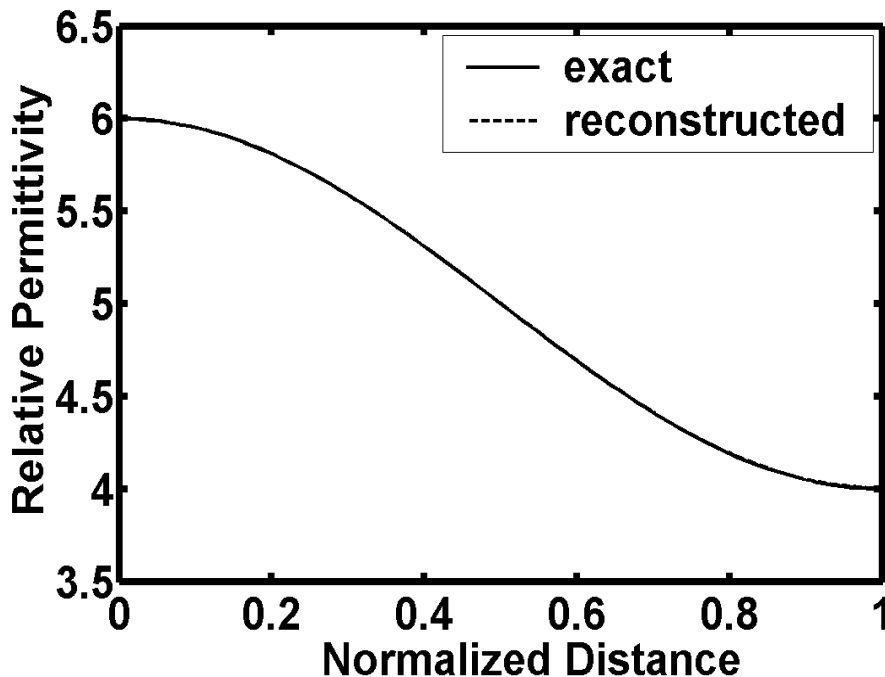


Figure 5.6: Exact and reconstructed permittivity profiles for a nonlinear case with a discontinuity at the air-dielectric interface

reconstruction have been used in conjunction with our technique. The distance in all plots (Fig. 5.2- 5.6) is *normalized* with respect to the maximum depth over which the permittivity profile is to be determined. The error between the exact and reconstructed permittivity profile in the above examples is less than 1% in all cases. After reconstructing the continuous permittivity profiles, we consider some *layered* (discontinuous) profiles which occur more frequently in nature. The reflection coefficient data for these kinds of layered permittivity profiles cannot be generated by solving the Riccati equation, as the derivative of the permittivity profile cannot be explicitly defined for these cases. The technique presented in section 3.1.1.1 is used to simulate the reflection coefficient data for these kinds of discontinuous permittivity profiles. We first consider the *two-layer* and *three-layer* dielectric media as shown in Figs. 5.7 and 5.8, where both the actual and reconstructed permittivity profiles are shown. The reflection coefficient data for these two cases lie in the range from 50 MHz to 40 GHz with a step-size of 50 MHz. In Figs. 5.9 and 5.10, we have reconstructed the permittivity profile of multi-layered media having a quite high value of permittivity with larger contrast. The reflection coefficient data used for these two cases lie in the range of 5 MHz to 10 GHz with a step of 5 MHz. It can be seen from Figs. 5.7 to 5.10 that even for layered (discontinuous) media, there is very good agreement between the exact and reconstructed permittivity profiles using our method. This is, in fact, one of the major advantages of our method because many other methods which have been presented in the past fail to reconstruct rapidly varying or *step-like* permittivity profiles very accurately. As a matter of fact, even the numerical methods which are normally used to reconstruct high contrast dielectric objects incorporate some kinds of *smoothness* criterion for a stable convergence, and hence these methods have problem in determining very sharp steps [7]. It may be mentioned here that

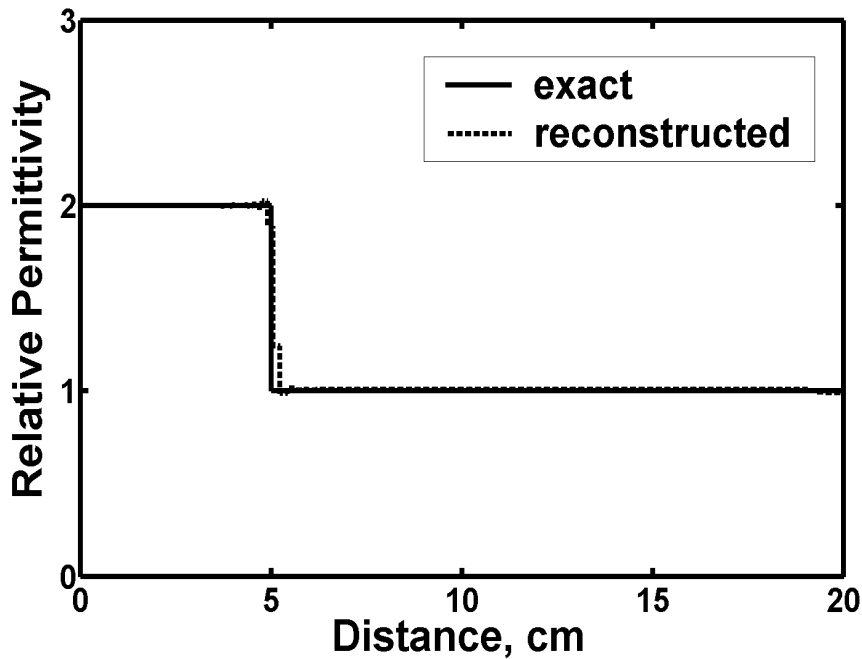


Figure 5.7: Exact and reconstructed permittivity profiles for the dielectric media with two layers

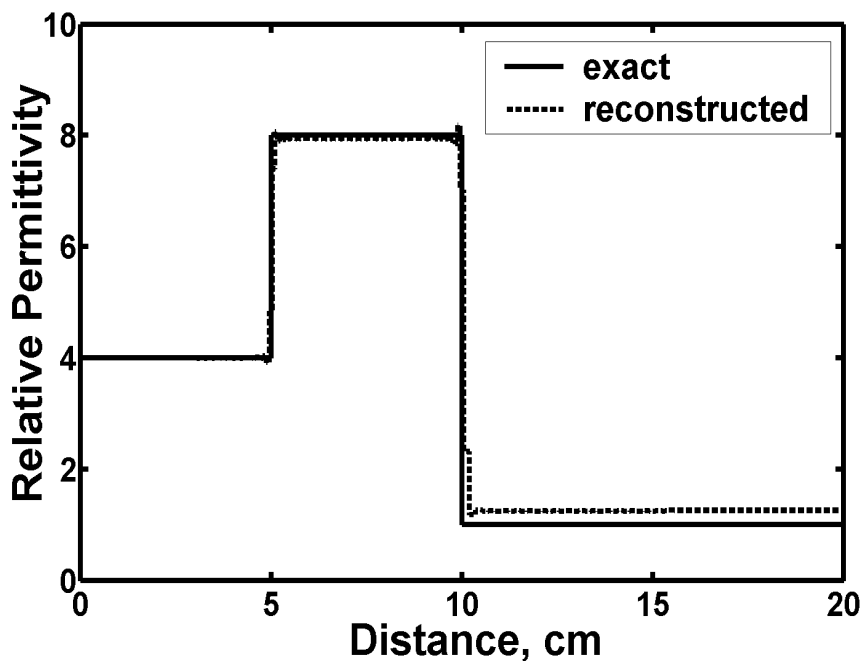


Figure 5.8: Exact and reconstructed permittivity profiles for the dielectric media with three layers

it is very common to observe some kind of overshoots at the discontinuity if some *FFT* and *IFFT* routines are used. This can also be seen in Figs. 5.7 to 5.10, if we look carefully at these graphs. This kind of overshoot effect is generally observed in all the layered structures, which occurs mainly due to limited bandwidth and

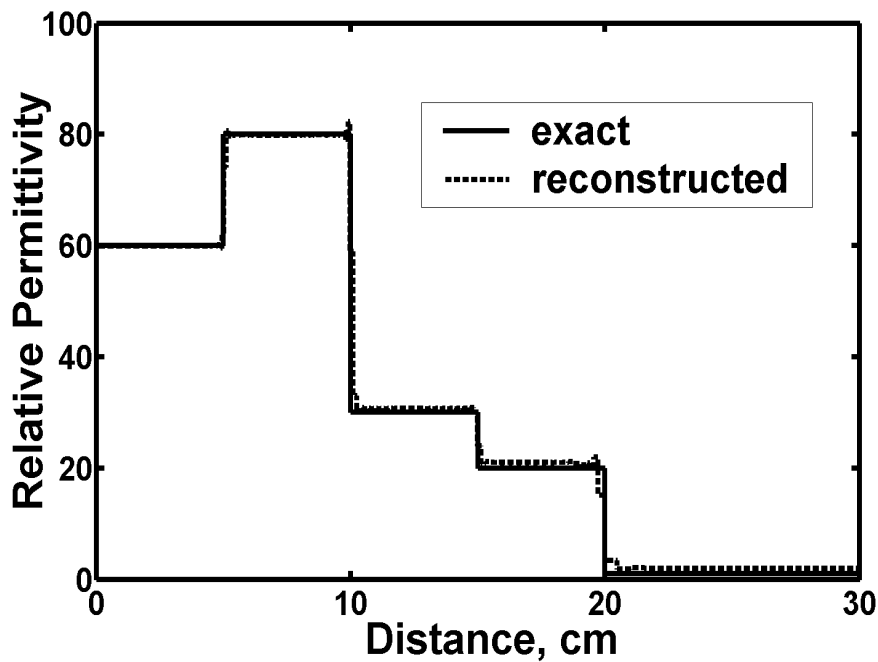


Figure 5.9: Exact and reconstructed permittivity profiles for the dielectric multi-layered media with high contrast

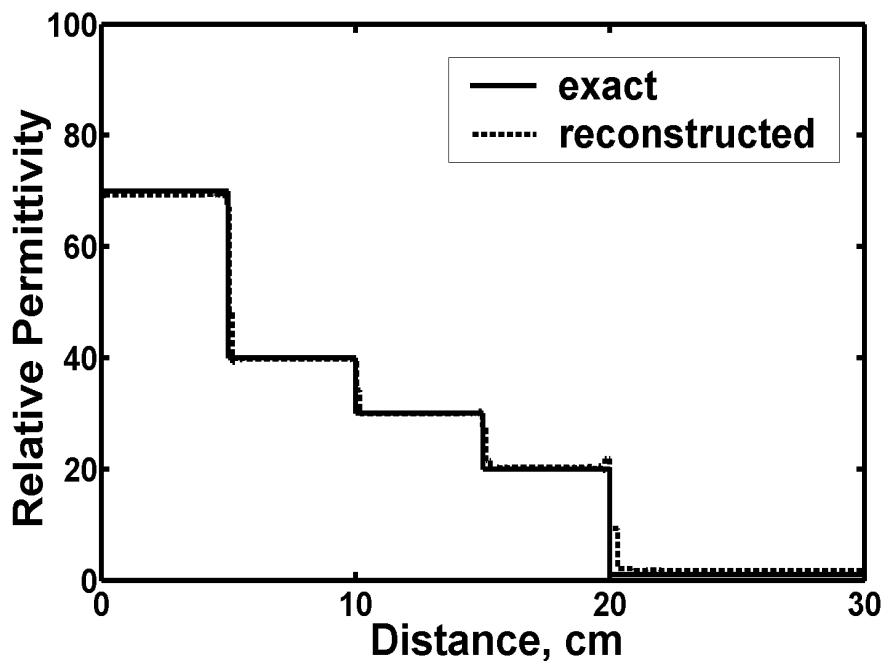


Figure 5.10: Exact and reconstructed permittivity profiles for the dielectric multi-layered media with quite high value of permittivity

large step-size. It is a general rule that the resolution of the reconstructed profile is directly proportional to the bandwidth over which the reflection coefficient data have been measured. The maximum depth which can be accurately reconstructed depends on the other hand on the minimum step-size.

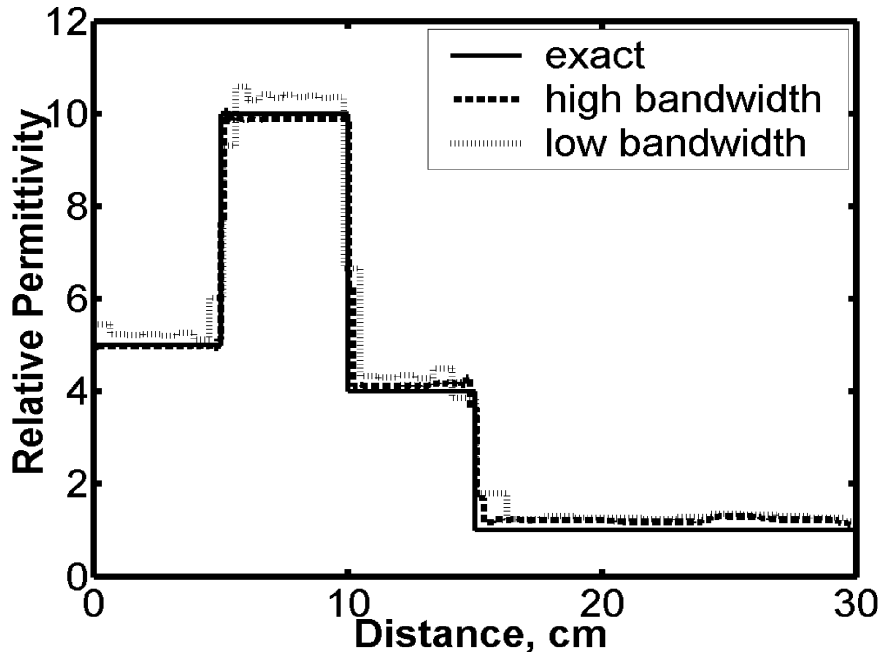


Figure 5.11: Exact and reconstructed permittivity profiles with different bandwidths

In our method, the permittivity profile is first reconstructed in terms of the virtual space variable l which is proportional to the permittivity profile as per (4.14). As the relative value of the permittivity is always assumed to be greater than unity, hence the resolution in the real space domain will always be more than in the virtual space domain. This is also one of the reasons for a very good match between the actual and the reconstructed permittivity profiles in Figs. 5.7 to 5.10, where we cannot even observe the bumps at the edges due to very high resolution. However, even in our case when the bandwidth of the reflection coefficient data becomes very low, then the distortion is observed in the reconstructed profile, specially some bumps are present at the edges. This can be seen in Fig. 5.11, where the permittivity profile is reconstructed for two values of spectral bandwidths. The dashed curve in this figure represents the reconstructed profile corresponding to a spectral bandwidth of 20 GHz, while the dotted curve corresponds to 5 GHz bandwidth. The discrepancy between the exact and the reconstructed values can be clearly observed in this figure, when the bandwidth is decreased from 20 GHz to 5 GHz keeping the same frequency-step. The concept of virtual space (time) variable or the electrical length also affects the physical depth which can be reconstructed with a reasonable amount of accuracy. The electrical length will be generally higher for objects having large value of permittivity. This means that objects having high values of permittivity may require somewhat lower values of the step-size in the frequency domain. The effect of this step-size can be further explained with the help of Fig. 5.12, where *reconstructed:1* represents the determined permittivity profile using the step-size of 10 MHz while *reconstructed:2* is the profile obtained if a step-size of 40 MHz is used for a fixed bandwidth of 20 GHz. It can be clearly seen from these curves that decreasing the step-size from 40 MHz to 10 MHz (for the same bandwidth) significantly increases the accuracy of the overall reconstruction. But as the range of the relative permittivity may not always be known in advance, hence it is always advisable to

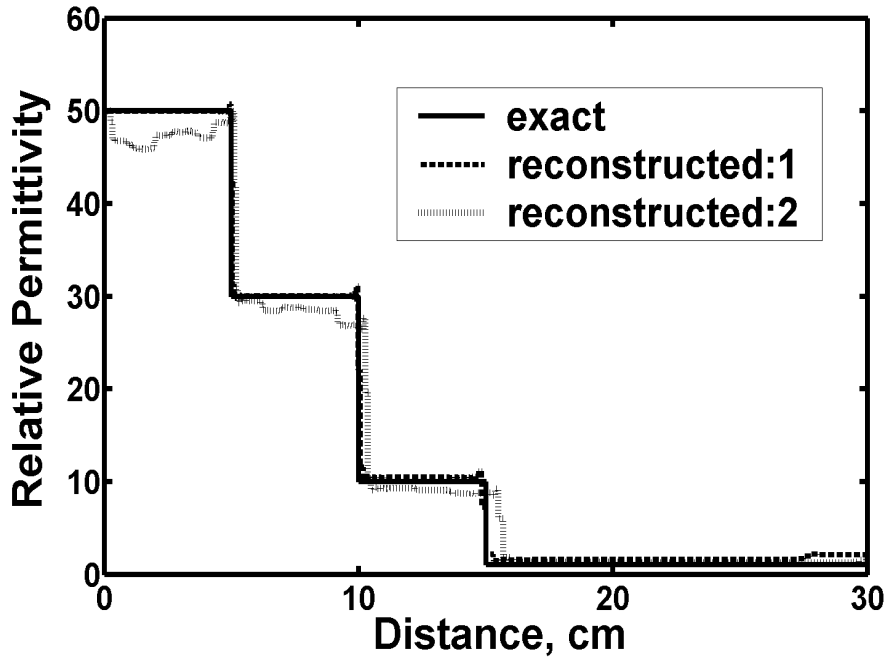


Figure 5.12: Exact and reconstructed permittivity profiles for the dielectric layered media using two different values of frequency steps

to take larger number of measurement data points of the reflection coefficient in the given frequency band. It may finally be mentioned that in all the examples discussed here, the permittivity at the air-dielectric interface has been first determined using the numerical method presented in section 4.1.1.4. The one-dimensional permittivity profile in terms of the electrical length has then been reconstructed starting from this initial value using (4.24). The electrical length has been transformed into the actual physical depth using the algorithm presented in section 4.1.1.3.

5.1.2 Cylindrical geometry

In this section, a number of radially varying permittivity profiles of cylindrical objects for both TE and TM illuminations are considered to show the validity of our technique in the case of cylindrical geometry. Firstly we consider a TM_{00} illumination, and reconstruct a linearly varying permittivity profile with a continuity at the outer air-dielectric interface ($\epsilon_r(0) = 1$) using two different approaches as shown in Fig. 5.13. In this figure, we have not used any coordinate transformation such as given by (4.69). To separate the spectral and spatial variables, we have, however, approximated the actual wavenumber k of (3.32) in two ways. The first approach (approach_1) in this figure assumes the wavenumber k to be equal to the free-space value k_0 multiplied by the square root of the average value of the permittivity at two ends. In the second approach, (approach_2) the value of k is simply taken to be equal to k_0 . It can be seen from this graph that the reconstruction using the first approach is better and resembles closely the exact permittivity profile as compared to the second one. This behavior of reconstructed profiles looks quite logical as the first approach provides an accuracy of one order more as compared to the second method. After ascertaining the fact that the first approach works better, two more

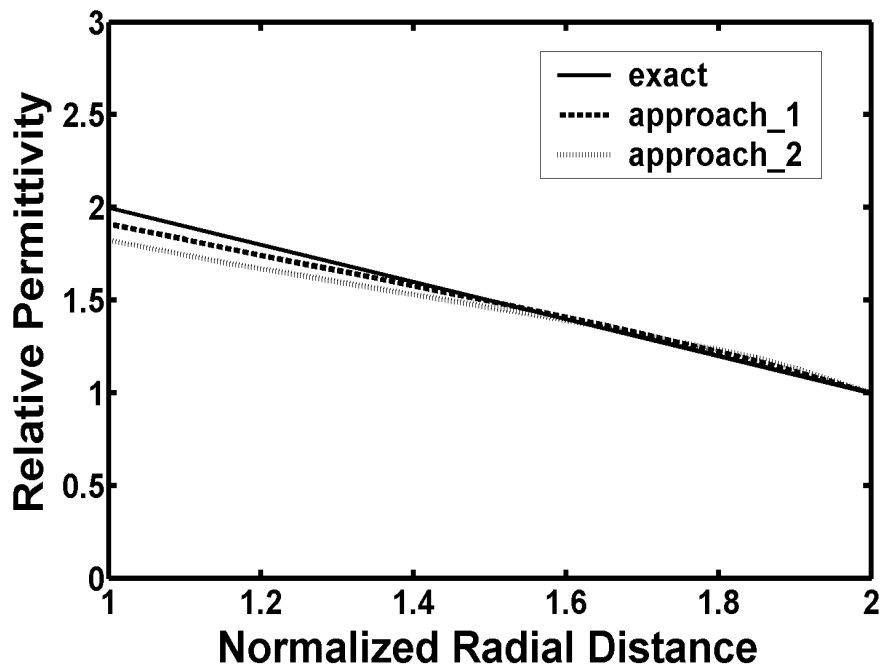


Figure 5.13: Exact and reconstructed permittivity profiles using two approaches in the cylindrical geometry

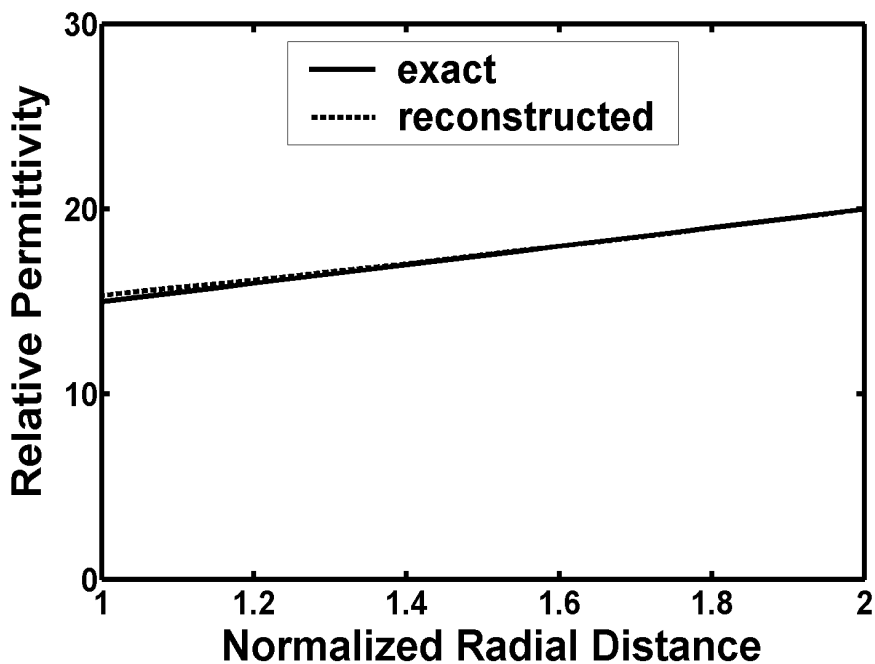


Figure 5.14: Exact and reconstructed permittivity profiles with a discontinuity at the air-dielectric interface

examples have been considered as shown in Figs. 5.14 and 5.15 using this approach. As can be clearly seen from these two figures, the radially varying permittivity profiles with moderate contrasts can be accurately reconstructed as well. However, there are two problems with this approach. The first problem is that we have to know the permittivity values at both ends of the object in advance. The permittivity

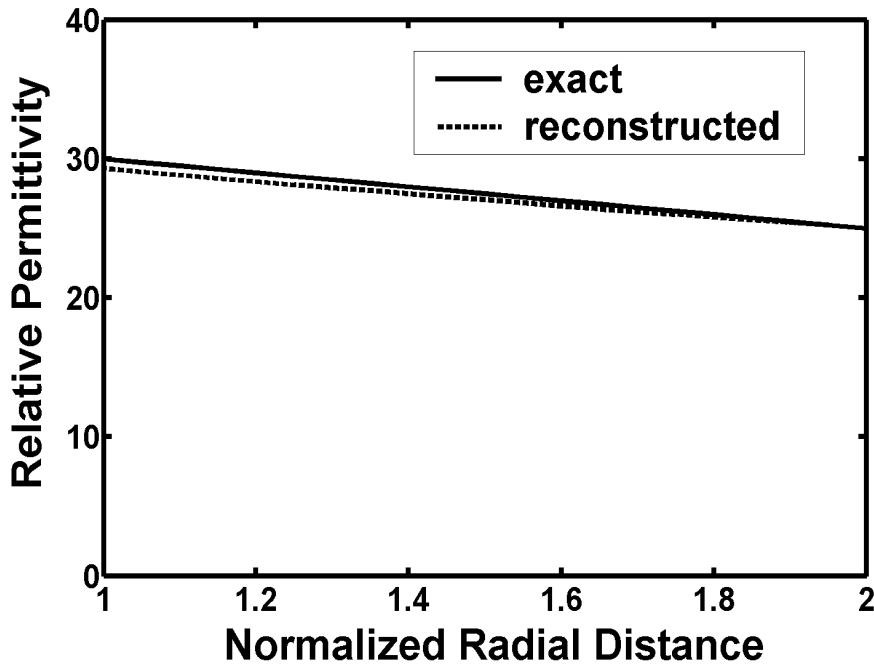


Figure 5.15: Exact and reconstructed permittivity profiles using a lower order TM illumination

at the outer end (air-dielectric boundary) may be determined using methods given in section 4.3.1, but knowing the value of the permittivity at the other end of the object might be difficult under practical situations. The second problem is that the method might not give an accurate reconstruction if the contrast in permittivity at the two ends of the object is very high.

To solve the above mentioned problem, a coordinate transformation is introduced, and accordingly an intermediate virtual time variable t has been defined as described in section 4.3.1. After the introduction of this virtual time variable, we do not require any approximation of the wavenumber k at the first instance. The reason is that the variable t can take into account the permittivity profile, and actual reconstruction can be carried out in terms of this intermediate variable t without having any knowledge of the permittivity value at two ends in advance. The permittivity profile in terms of the physical depth can then be reconstructed using our numerical algorithm described in section 4.3.2. As a matter of fact, this coordinate transformation also helps in separating the spectral and spatial variables more accurately for the solution of inverse problem as explained in sections 4.3.1 and 4.3.2. As we do not require any approximation of k , hence the permittivity profiles of quite high values with moderate contrasts can be reconstructed as well. This can be seen in the following examples, where we have used (4.103) and (4.104) to reconstruct the permittivity profile in terms of t , and then the numerical algorithm (4.86) has been used to convert this intermediate variable into the physical distance. First we consider the higher order TE mode illumination to reconstruct the permittivity profiles of cylindrical objects having quite high values of permittivity as shown in Figs. 5.16 and 5.17. From these two figures, it can be observed that the reconstructed profiles are in very close agreement with their exact values even when the relative permittivity value is as high as 100. It may be mentioned here that for higher order

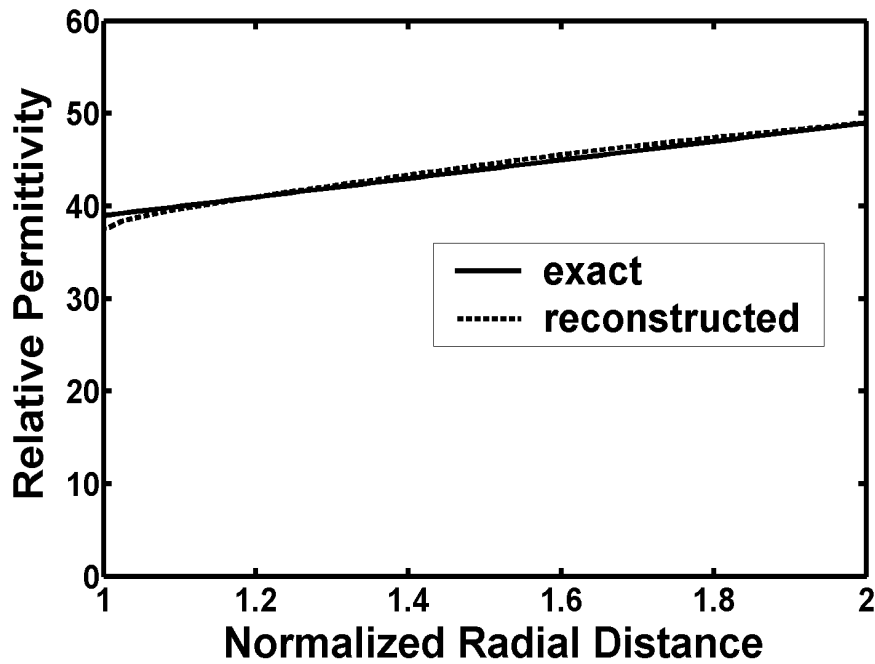


Figure 5.16: Exact and reconstructed permittivity profiles using a higher order TE illumination

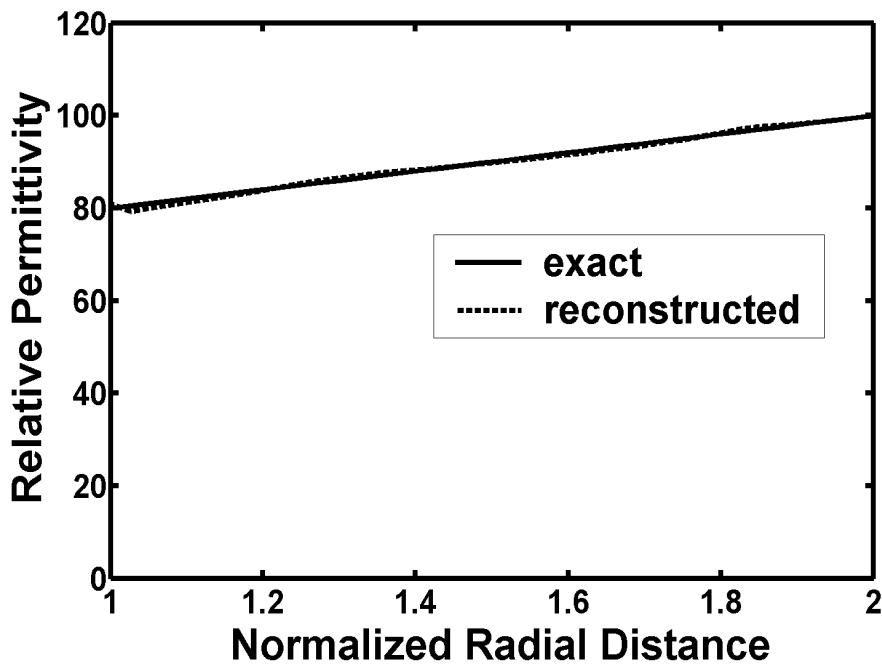


Figure 5.17: Exact and reconstructed permittivity profiles for for a quite high value of permittivity (TE mode)

modes, the formulas for reconstruction are quite complicated because of the dependence of radial propagation constant on the axial length as seen in (4.91). However, after comparing (4.103) of the TE case with the corresponding equation (4.104) of the TM case, it is observed that the reconstruction using a higher order TE illu-

mination is somewhat simpler than that of a higher order TM illumination. The expression for the TM illumination is more involved because the impedance in this case is dependent in more complicated way on the radial propagation constant and the permittivity profile [16]. Hence under situations when the length of the object can not be considered to be infinite and the axial dependence of the radial propagation constant cannot be avoided, it is preferable to use a TE rather than a TM illumination because of its simpler expression. Another parameter, which is also sometimes very critical for the reconstruction of the *finite length* cylindrical object is the lowest value of the free-space wavenumber k_0 over which the measurements are carried out. Ideally this value should be zero (see e.g. (4.100)). However, since the Hankel functions are infinite when their arguments approach zero, so we normally skip this point and start from any finite value close to zero. Another possibility is to replace the Hankel functions by their small argument asymptotic expressions and to compute the corresponding equations analytically near the zero argument region. The selection of the lowest value of this free space wave number normally depends on two factors. When the starting value of k_0 is taken as very low then it might give some ambiguous value of the effective radially varying permittivity profile $\tilde{\varepsilon}_r(\rho)$. This is because of the fact that to make the effective permittivity profile $\tilde{\varepsilon}_r(\rho)$ frequency-independent, the value of \bar{k}_0 in (4.95) is taken as three to four times of the lowest value of the free-space wavenumber as mentioned in section 4.3.2. But when the lowest value of \bar{k}_0 is chosen as very small, then it might make the value of the intermediate parameter δ of (4.96) large as compared to the exact permittivity profile $\varepsilon_r(\rho)$ resulting in ambiguity. On the other hand, if we take this value to be quite high, then the reconstruction may not be accurate, as our inverse algorithm is quite sensitive to the lower values of \bar{k}_0 as discussed earlier. Thus, a trade off has to be made in order to optimize this lower value of \bar{k}_0 . In all the examples considered here for higher order TE and TM cylindrical mode illuminations, the lowest value of \bar{k}_0 is taken in the range of 0.1 – 0.2. The length of all cylindrical objects is taken as ten times the inner radius of the object, i.e. $\bar{a} = 10$ in (4.95).

After considering the higher order TE illumination, we try to reconstruct some profiles using higher order TM illuminations. Firstly we take a simple case of linearly varying permittivity profile as shown in Fig. 5.18, where the axial dependence of the radial propagation constant is taken into account. The agreement between the reconstructed and the exact permittivity profile is certainly quite good for this case as obvious from the figure. Similarly, Fig. 5.19 shows a permittivity profile considering a higher order TM illumination for a *nonlinear* case. As evident from this plot, the agreement between the original and reconstructed profiles is not as good as it was for the linear case. This is because of the fact that the spatial derivative of the relative permittivity is reasonably high in this case. However, the agreement between the exact and the reconstructed profiles is still acceptable provided that the absolute value of the relative permittivity is also reasonably high. This is obvious from Fig. 5.20, where again a higher order TM illumination has been used but the agreement between the exact and the reconstructed permittivity profile in this case is better than e.g. in Fig. 5.19. This phenomenon may be explained with the help of (4.69), where it is seen that when the absolute value of the relative permittivity is high as compared to its spatial derivative, then the factor $\left[\frac{1}{\varepsilon_r(\rho)} \frac{d\varepsilon_r(\rho)}{d\rho} \right]$ becomes reasonably small as compared to unity and hence it

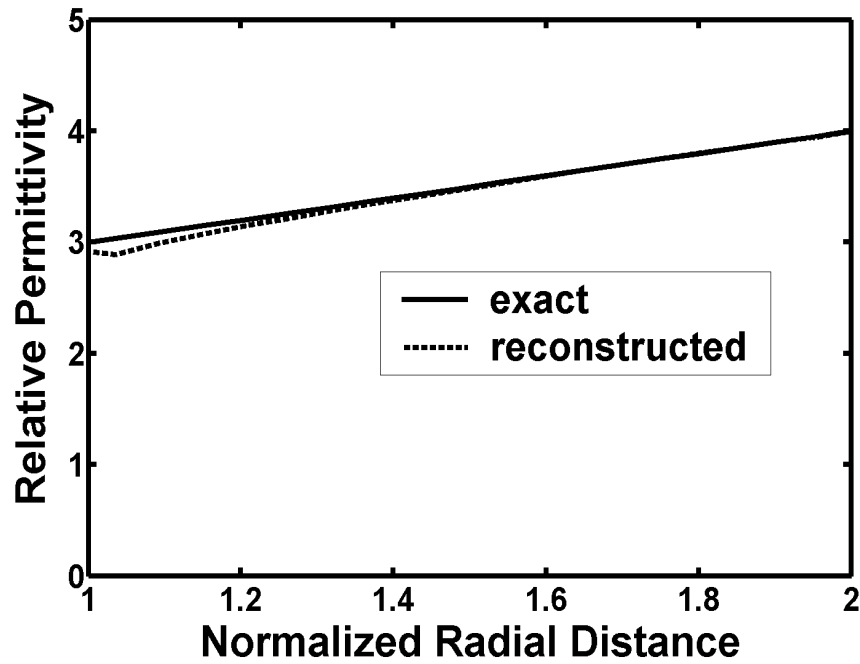


Figure 5.18: Exact and reconstructed permittivity profiles for the linear case (TM mode)

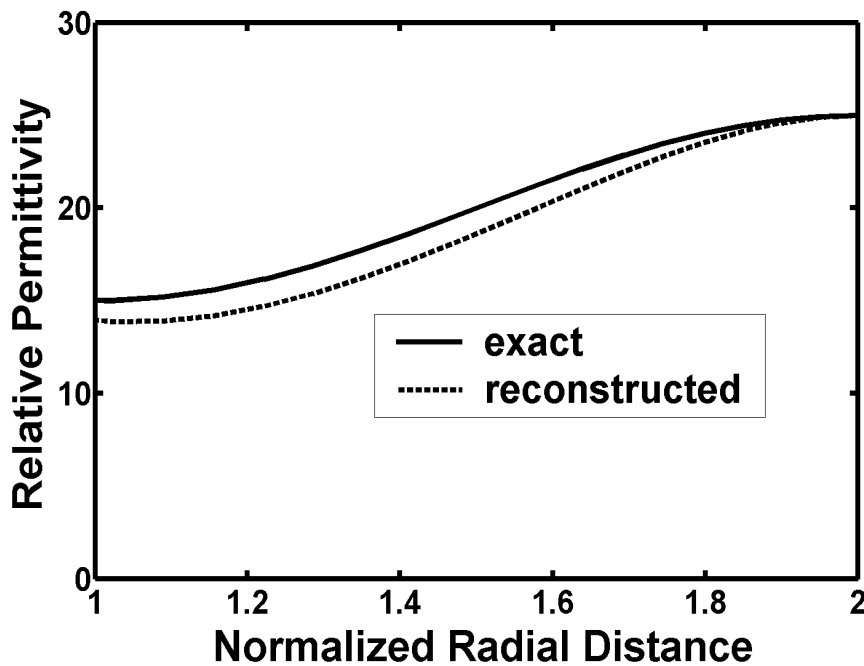


Figure 5.19: Exact and reconstructed permittivity profiles for the nonlinear case (TM mode)

can be safely neglected. It may be noted here that the reflection coefficients data are supposed to be measured at the outer radius ($\bar{\rho} = b/\rho_0 = 2$), and hence the reconstruction process in all the plots always starts from the outer air-dielectric boundary making the reconstructed profile more deviated from the exact one as one

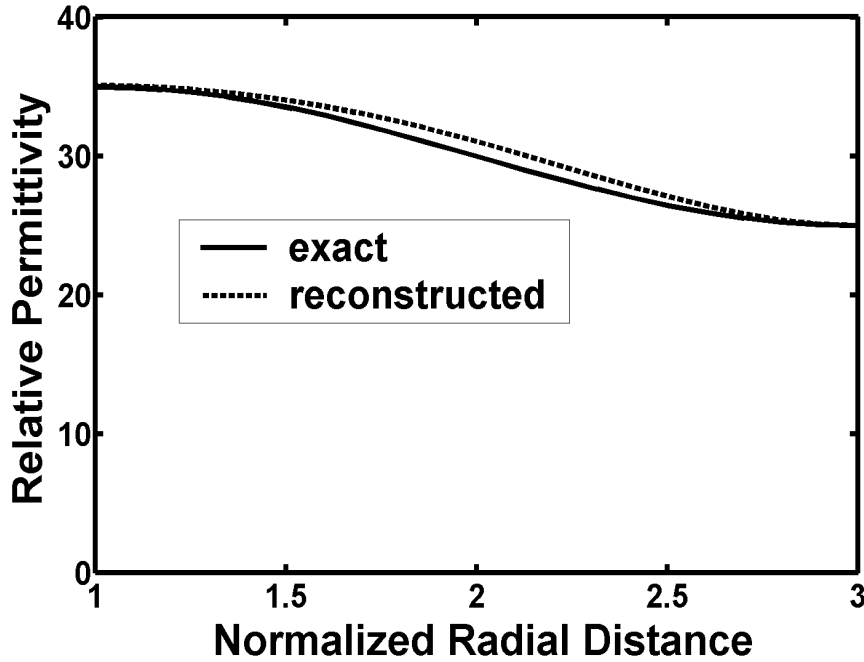


Figure 5.20: Exact and reconstructed permittivity profiles for the nonlinear case with a reasonably high value of permittivity (*TM* mode)

moves towards the inner radius ($\bar{\rho} = 1$).

In all the above considered examples, error- and noise-free scattering data have been synthetically produced by solving the nonlinear Riccati-similar differential equations for known permittivity profiles using MATLAB. However, usually the measurement data may have some inherent noise in it due to many factors and hence it becomes necessary to study the effect of noise on the overall reconstruction. This is done by adding few percent random error to the calculated reflection coefficient data, i.e.,

$$\Gamma(k_0)(\text{new}) = \Gamma(k_0) + \{[(RAND - 0.5) * 0.01p] + j * [(RAND - 0.5) * 0.01p]\} \quad (5.7)$$

where $\Gamma(k_0)$ is the simulated reflection coefficient, $RAND$ is a uniformly distributed random number satisfying $0 \leq RAND \leq 1$, and p is the percentage error. The random error is added to the simulated spectral domain reflection coefficient data at each frequency. As the random error is added to both the real and imaginary parts of the reflection coefficient data as per (5.7), hence the noise is introduced in both the amplitude and phase of the simulated data. The reconstructed permittivity profile using the noisy scattering data for a higher order *TM* mode is shown in Fig. 5.21 along with its exact profile. As observed from this example, even with 2% random noise in the scattering data, there is a very good match between the exact and reconstructed profiles. It may be mentioned here that in Figs. 5.13 to 5.21, around 100 to 150 data points covering the spectral wavelength range from infinity down to one fifth of the inner diameter of the cylindrical object have been used for the reconstruction of the radially-varying permittivity profile. The radial distance in all these plots is normalized with respect to the inner radius of the cylindrical object under consideration as given by (4.102). To see the effect of noise on the permittivity

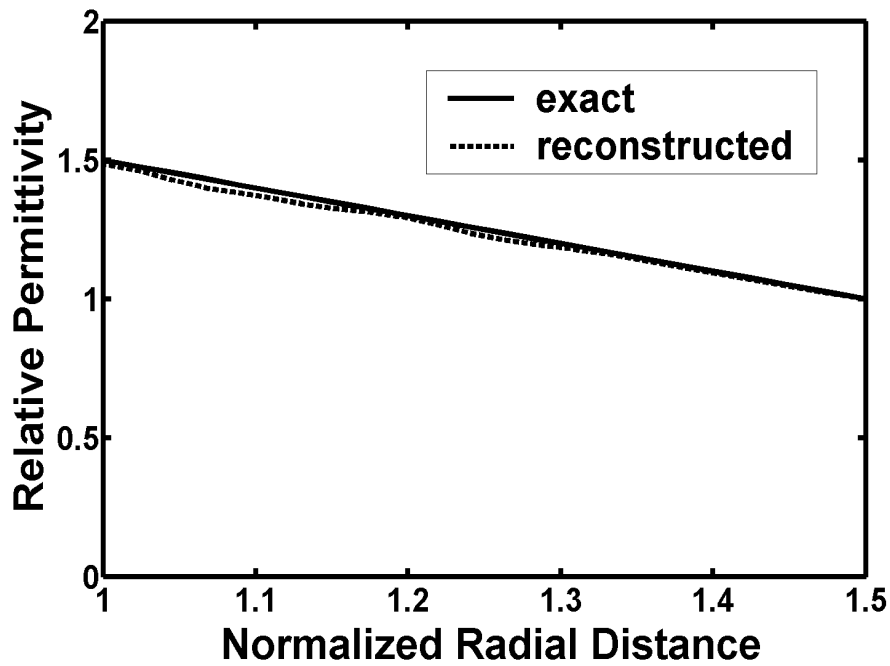


Figure 5.21: Exact and reconstructed permittivity profiles with 2% random noise

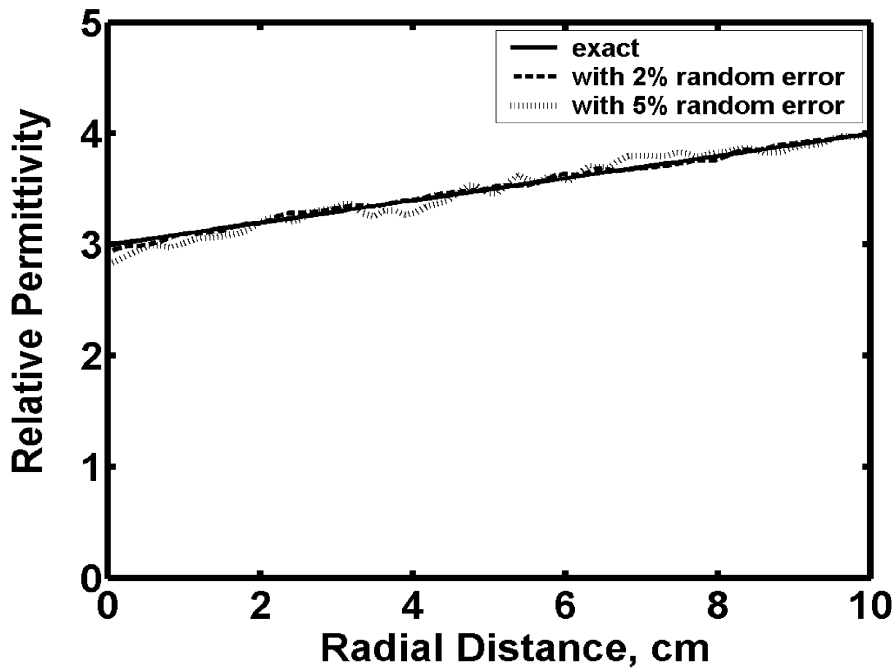


Figure 5.22: Exact and reconstructed permittivity profiles with different noise levels

reconstruction, we consider here few more examples. For this purpose, We make use of the radial transmission line mode described in section 4.3.1. Fig. 5.22 shows the exact and reconstructed permittivity profiles with 2% and 5% added random noise. It can be observed from this figure that with 2% added noise, the matching between the reconstructed and exact profile is so good that it is even difficult to distinguish between them. Even when the error in the simulated data is increased

to 5%, the reconstructed profile is within affordable limit. Figs. 5.23 and 5.24 show

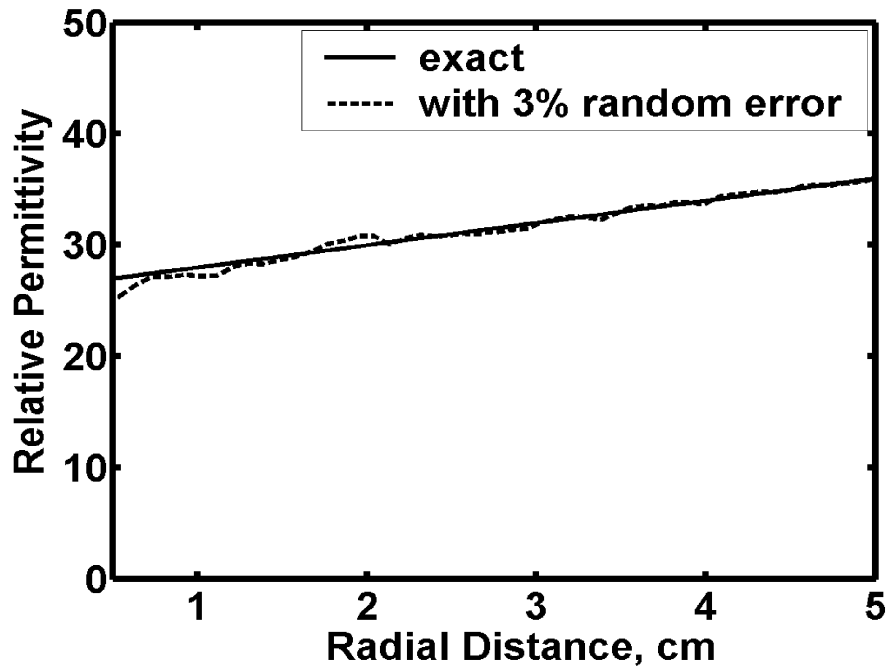


Figure 5.23: Exact and reconstructed permittivity profiles with 3% random error

the effect of noise for somewhat higher values of permittivity profiles. In Fig. 5.23

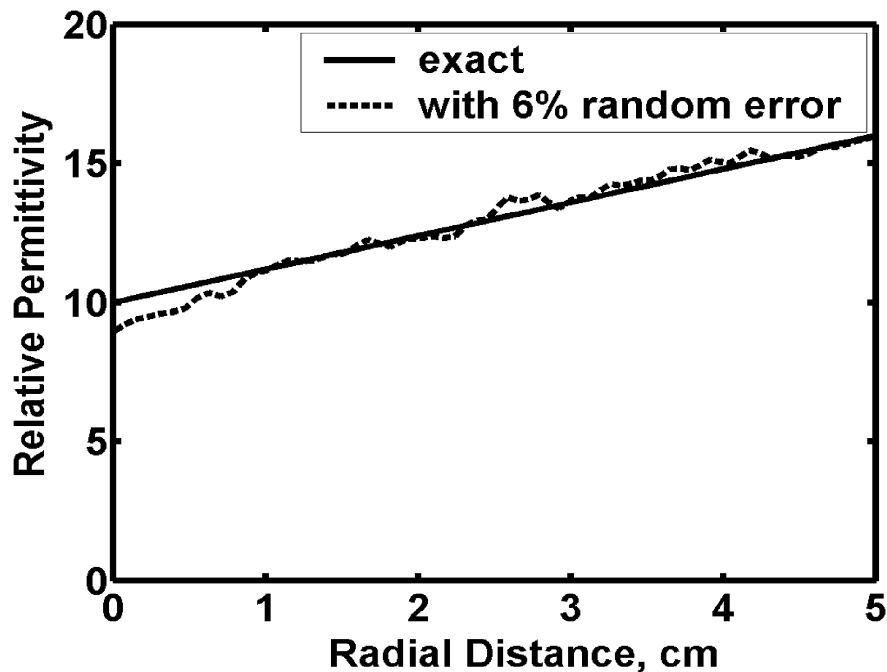


Figure 5.24: Exact and reconstructed permittivity profiles with 6% random error

we have added 3% noise to the simulated reflection coefficient data, while Fig. 5.24 shows the reconstructed permittivity profile with 6% added noise. In Figs. 5.22 to 5.24, we have considered 1000 reflection coefficient data points starting from 20

MHz to 20 GHz, and the dashed line in all these plots represents the reconstructed permittivity profile from the noisy scattering data. It may be noted here that

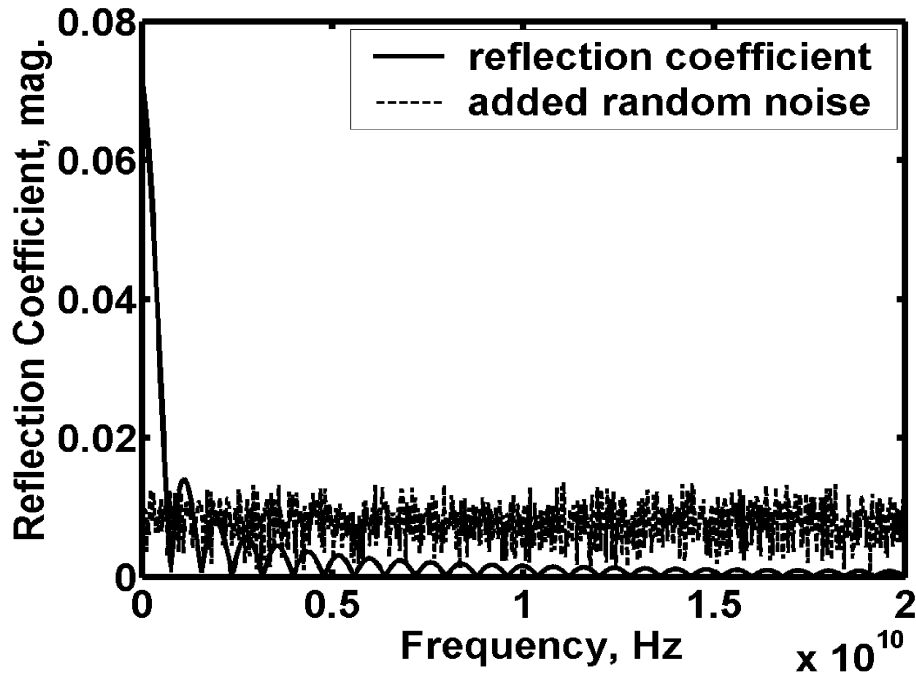


Figure 5.25: The magnitude of reflection coefficient data along with the added noise when we add the random error to the reflection coefficient data as per (5.7), then sometimes the level of the added noise becomes quite significant as compared to the actual scattering data. This can be seen in Figs. 5.25 and 5.26, where we have

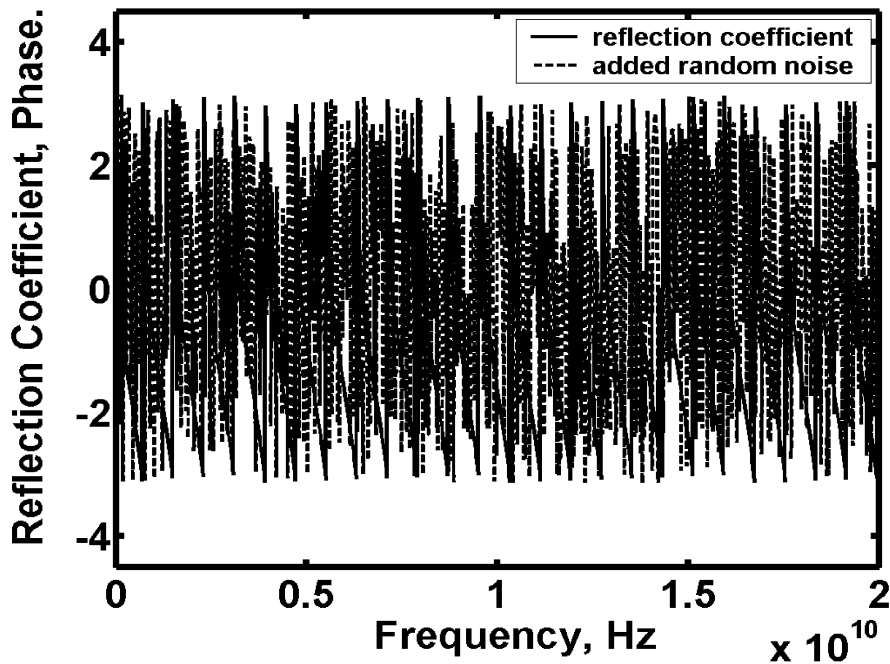


Figure 5.26: The phase of the reflection coefficient data along with the added noise plotted the amplitude and phase of the reflection coefficient data along with the

added noise level which basically corresponds to Fig. 5.24. It can be observed from Fig. 5.25 that at higher frequencies, the magnitude of the reflection coefficient data is small and hence the added noise of 6% becomes quite significant. But as observed in Fig. 5.24, the difference between the exact and the reconstructed profile is less than 5% even when the noise level becomes quite significant. Hence it can be said that our method is not much sensitive to the addition of noise in the measured scattering data. It is worthy noting here that the inverse problems are generally very ill-posed and so they are quite sensitive to the measuring data. Sometimes even a small change in the measuring data may result in very large deviation in the reconstructed parameter specially when some numerical methods are used for the inverse solution. The ruggedness and insensitivity to noise of the input measuring data is also one of the main advantages of our method.

After considering a number of continuous permittivity profiles for the cylindrical geometry using both TE and TM illuminations as given above, we try to reconstruct few *layered* permittivity profiles. For these cases also the radial transmission line approach described in section 4.3.1 is used.

It has already been mentioned previously that the radial transmission line approach helps in simulating the reflection coefficient data for discontinuous or layered permittivity profiles, which is otherwise not possible using the so called Riccati-equation approach. Figs. 5.27 and 5.28 show the exact and reconstructed permit-

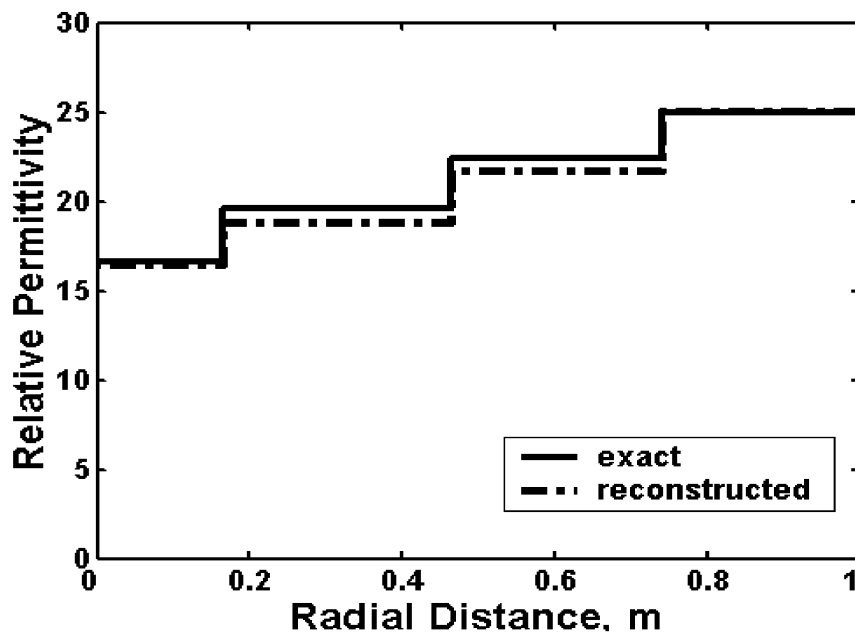


Figure 5.27: Exact and reconstructed permittivity profiles for the layered cylindrical media

tivity for a step-like radial profile with a discontinuity at the outer air-dielectric interface ($\rho = b$). As mentioned earlier, the reconstructed process starts from the outer radius ($\rho = b$) of the cylindrical object and different layers are reconstructed in subsequent steps as we move towards the origin. The value of the permittivity at the air-dielectric interface $\epsilon_r(b)$ for these two examples is first determined using (4.87) and (4.88), and the exact permittivity profile as a function of the radial distance

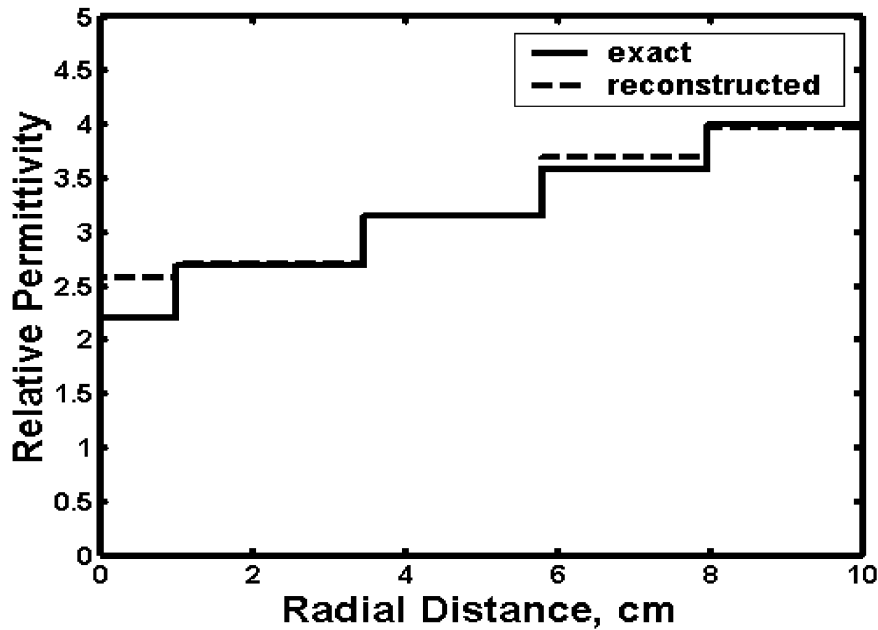


Figure 5.28: Exact and reconstructed permittivity profiles for the layered cylindrical media

is reconstructed starting from $\varepsilon_r(b)$ using (4.84) and (4.86). It can be seen from both curves that the reconstructed permittivity layers resemble very closely to the exact ones near the outer radius, but they deviate from the original values as we go very near to the origin. This is to be expected as every inverse method has some maximum depth over which the permittivity profile can be reconstructed quite accurately and after some distance, the results start deteriorating. This is because the information gained becomes weaker and weaker as we go away from the boundary, where actual measurements are carried out. The other reason for this deviation here is probably also the behavior of Hankel functions near the origin. We have tried to compute the Hankel functions numerically near the origin by substituting a very small value as its argument, but even then the behavior of these functions cannot be guaranteed when its argument becomes very small. It may be mentioned here that the Hankel functions can also be replaced by their low asymptotic expressions for computing this integral analytically near the origin. For both examples, the reflection coefficient data in the range from 50 MHz to 15 GHz with a step 50 MHz have been used. These data were generated using the direct method proposed in section 3.2.1.1. It may be also mentioned here that in Fig. 5.27 the value of the relative permittivity is more, and hence the resolution of the reconstructed profile for this case in the real space domain will be high as compared to Fig. 5.28 when the reflection coefficient data over the same frequency range are used in both the cases. It is mainly due to this high resolution that the resemblance between the exact and the reconstructed permittivity profile is better in Fig. 5.27 than in Fig. 5.28.

5.1.3 Spherical geometry

In this section, we reconstruct the one-dimensional radially-varying permittivity profiles of *spherical* objects using methods described in sections 3.3 and 4.4. Firstly, we consider the permittivity profile reconstruction using lower order *TE* and *TM* illuminations. Fig. 5.29 shows the exact and the reconstructed profiles for a spher-

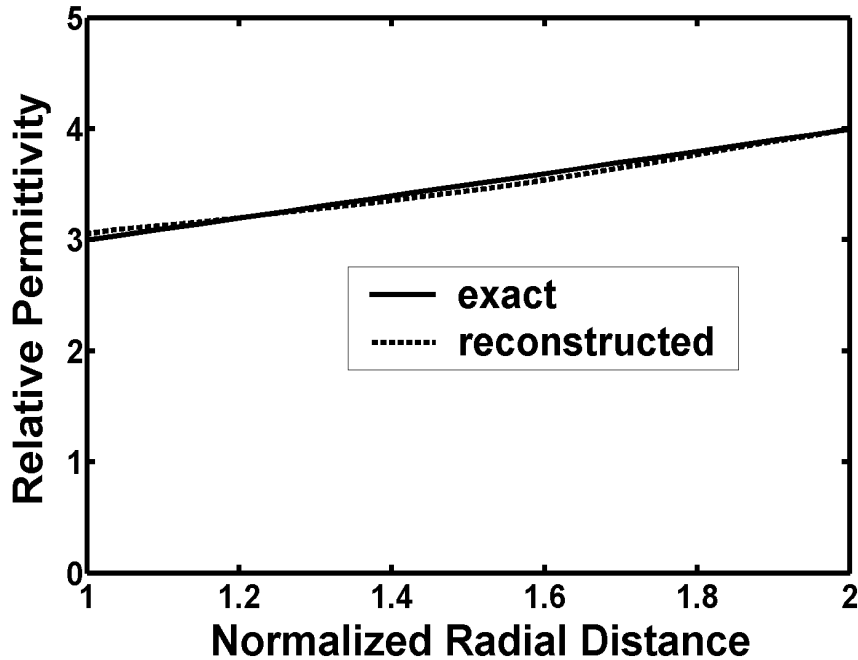


Figure 5.29: Exact and reconstructed permittivity profiles for the spherical TM_{01} case

ical object having low permittivity value, while in Fig. 5.30, we have reconstructed a profile for reasonably high value of relative permittivity by making use of a TM_{01} illumination. It can be seen from these two plots that for the lower order *TM* illumination, the reconstructed profile matches well with the exact profile for both low and high values of permittivity. For these two cases, the reflections coefficient data have been generated after solving the nonlinear differential equation (3.140) numerically. These simulated reflection coefficient data have then been used in the algorithm presented in section 4.4 to reconstruct the unknown permittivity profile. Fig. 5.31 shows the exact and reconstructed permittivity profile using a spherical TE_{01} illumination. The reflection coefficient data for this case is generated by solving (3.141). From this figure, it can be seen that even for very high dielectric contrast our method works quite well and a good agreement between the exact and the reconstructed permittivity is achieved.

Next, we reconstruct some permittivity profile using higher order illuminations. In Fig. 5.32 we have reconstructed a permittivity profile using a TE_{11} illumination, while Fig. 5.33 shows the exact and reconstructed permittivity profiles for a TE_{12} illumination. The accuracy of the reconstructed permittivity profiles in both cases show that our method can be used to reconstruct the permittivity profile for any arbitrary order illumination provided that we are able to measure the scattering data for the particular mode with sufficient accuracy. The suitability of a method

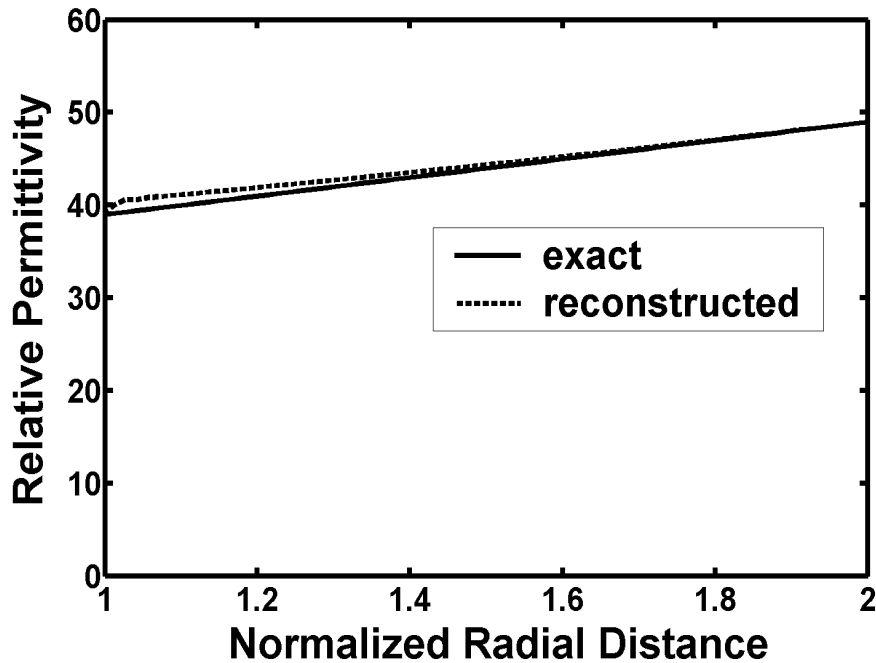


Figure 5.30: Exact and reconstructed permittivity profiles for the spherical TM_{01} case

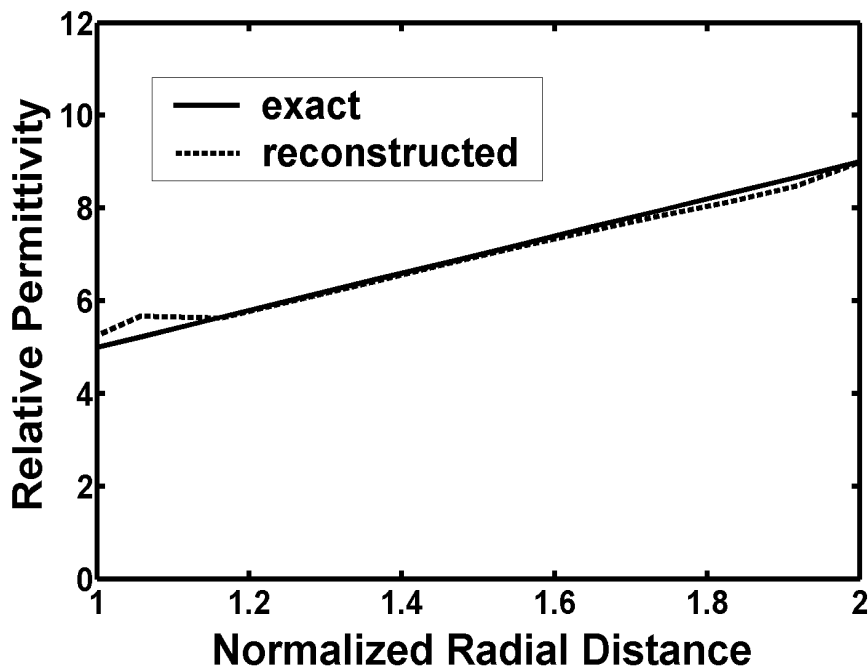


Figure 5.31: Exact and reconstructed permittivity profiles for the spherical TE_{01} case

for any arbitrary order illumination is definitely advantageous in many situations as a general electromagnetic field produced by an antenna setup is a combination of all possible modes. It is, however, in principle possible to separate the information corresponding to each mode due to the orthogonal properties exhibited by them [64]. We have also observed that sometimes it is advantageous to illuminate the dielectric

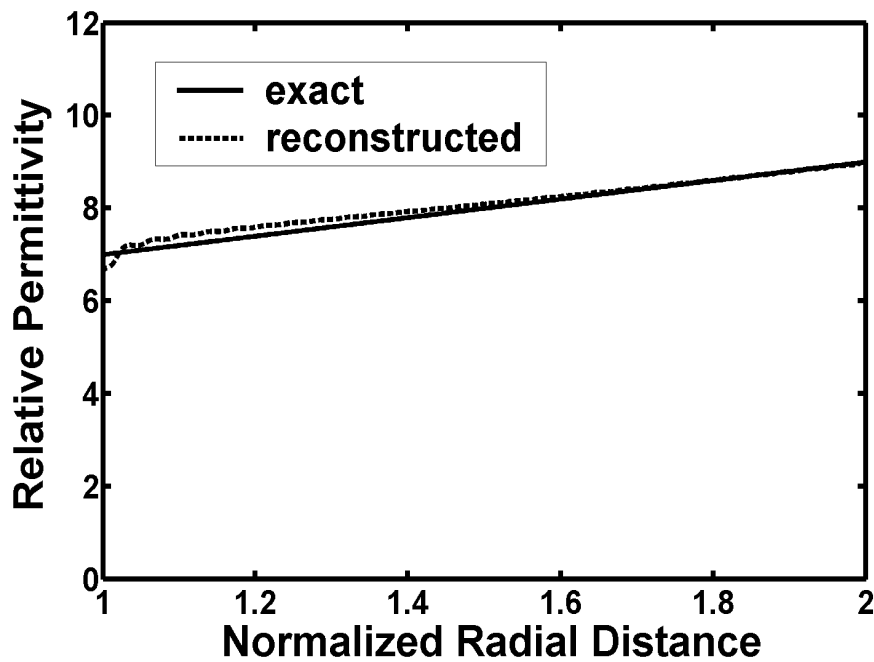


Figure 5.32: Exact and reconstructed permittivity profiles for the spherical TE_{11} case

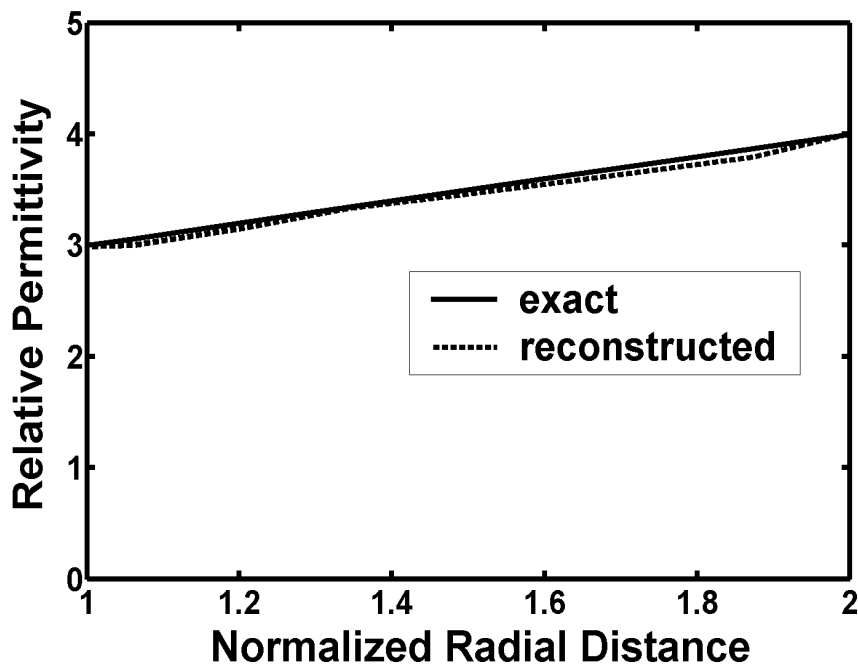


Figure 5.33: Exact and reconstructed permittivity profiles for the spherical TE_{12} case

object with different modes and then take average of the individual reconstructions. This is evident from Fig. 5.34, which shows the exact and reconstructed radially-varying permittivity profiles of the cylindrical dielectric object using a TE_{m1} and TE_{m2} illuminations. In this figure, we have also plotted the reconstructed permittivity profile using the average of these two illuminations and it can be seen that

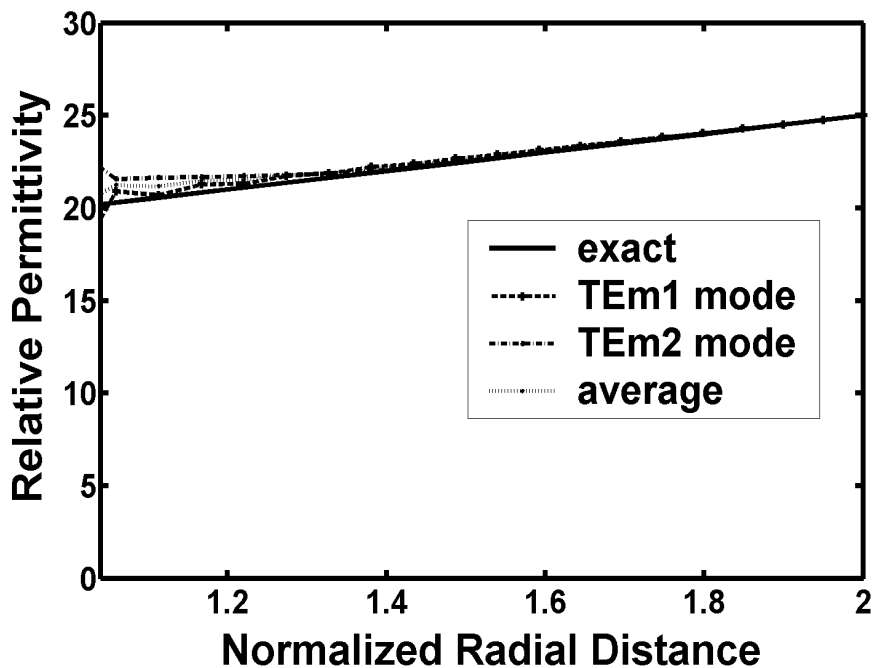


Figure 5.34: Exact and reconstructed permittivity profiles for the spherical TE case with different mode illuminations

the averaging process helps in obtaining a better accuracy. This behavior can be explained by the fact that waves of different order modes might have different noise behavior producing the deviation above and below the exact profile, and hence the averaging process might help in neutralizing the error up to some extent. The other point to be noted here is that the radial propagation constant in the spherical geometry does not depend on the θ or ϕ -direction even for higher order modes.

After considering higher order TE cases, we reconstruct few permittivity profiles using higher order TM mode illumination. Fig. 5.35 shows a reconstructed permittivity profile using a TM_{11} mode for a moderate contrast, while Fig. 5.36 shows a reconstructed permittivity profile using a TM_{12} mode for a dielectric object of higher contrast. Both of these figures also show the exact permittivity profiles for comparison. It can be seen that there is a reasonably good agreement between the exact and reconstructed profiles for both low and high contrast dielectric objects. In Fig. 5.37, we have reconstructed a nonlinearly varying permittivity profile using a TM_{11} illumination. It can be seen from this curve that although the agreement between the exact and reconstructed permittivity profiles in this case is not as good as it was in the linear case, but the reconstructed data are still lying within 3 – 4% of the exact values.

It may be mentioned here that in Figs. 5.29 to 5.37, the reflection coefficient data used for the reconstruction represent *error-* and *noise-free* values, which have been generated by solving numerically the corresponding nonlinear differential equations derived in section 3. However, in real situations, the actual measurement data may have some inherent noise in it, and to study the effect of noise on the overall reconstruction, we have added 1% and 2% random noise to the simulated reflection coefficient data. The noise is added to both the amplitude and phase of the uncorrupted reflection coefficient data as per (5.7), and the reconstructed profile from this

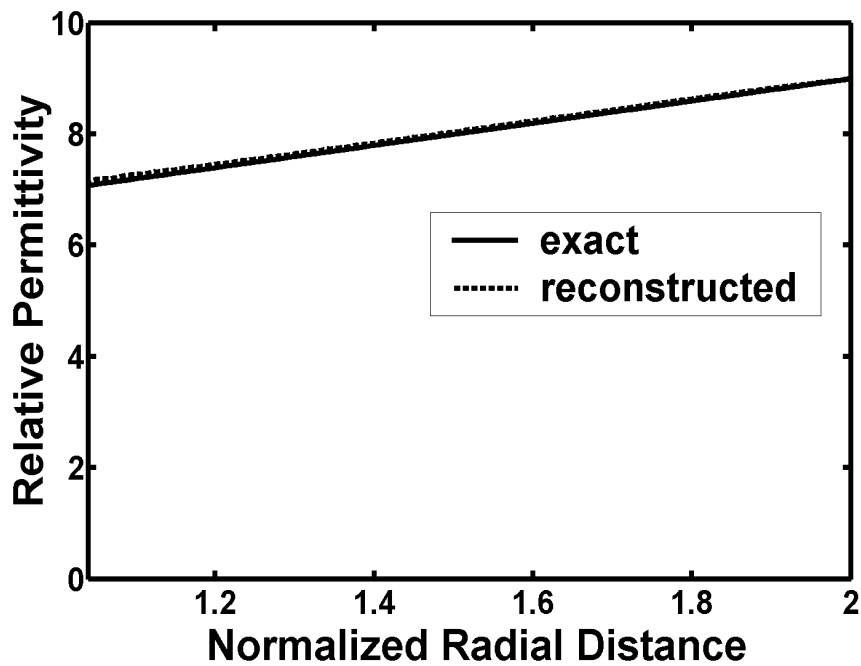


Figure 5.35: Exact and reconstructed permittivity profiles for the spherical TM_{11} case

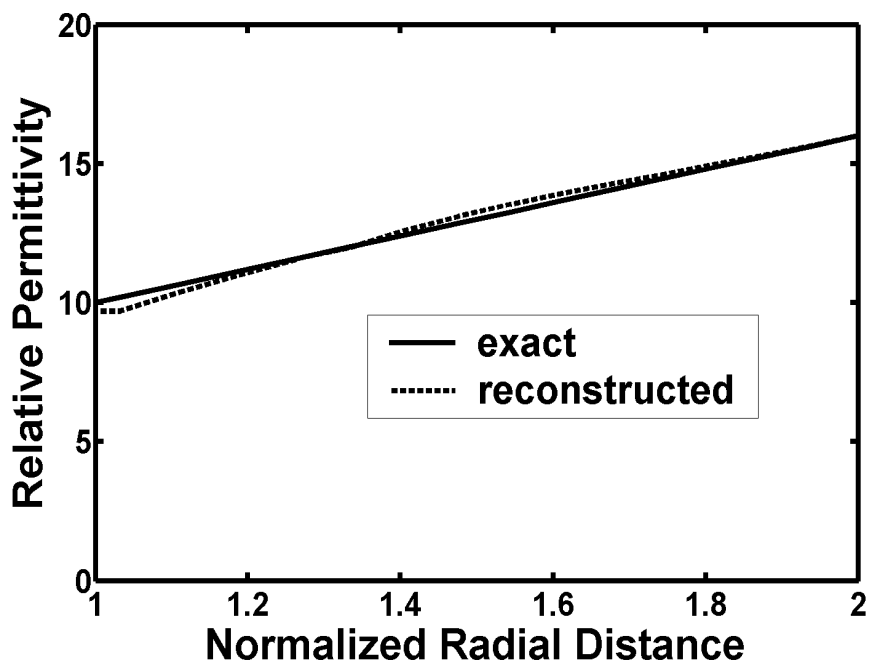


Figure 5.36: Exact and reconstructed permittivity profiles for the spherical TM_{12} case

noisy data is shown Fig. 5.38. It can be seen from this curve that although the added noise affects the reconstructed permittivity profile, but this deviation in the output parameter is proportional to the error in the input scattering data thus producing a stable inversion. It may be noted here that the percentage error added to the uncorrupted data in Fig. 5.38 is independent of the magnitude of exact scattering

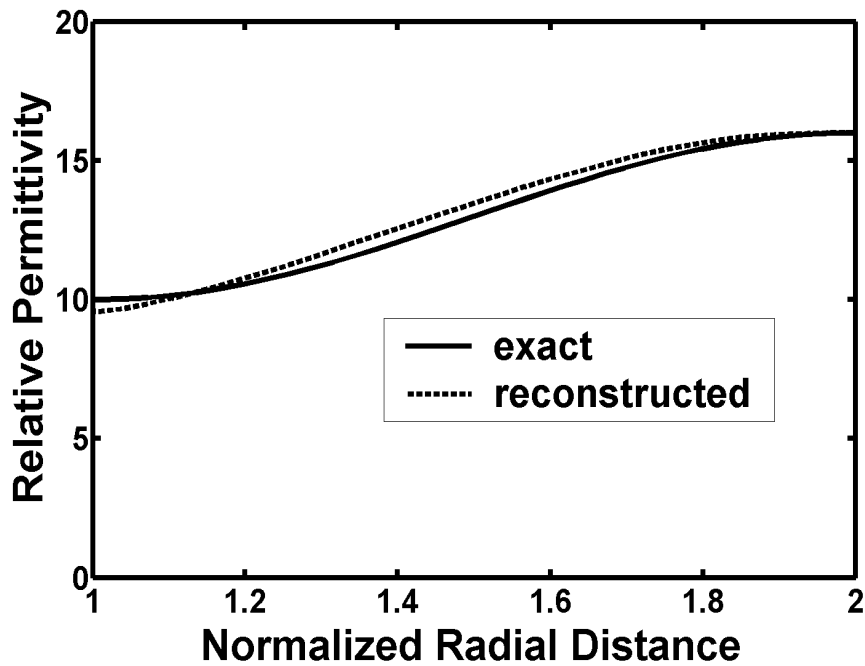


Figure 5.37: Exact and reconstructed (*non-linear*) permittivity profiles for the spherical TM_{11} case

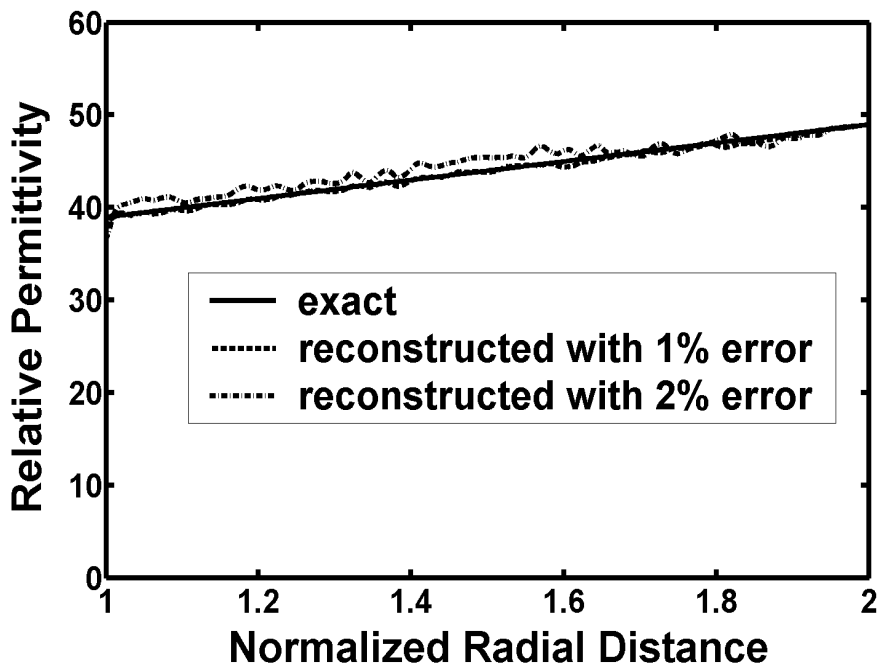


Figure 5.38: Exact and reconstructed permittivity profiles from the noisy scattering data for the spherical TM_{11} case

data. This means that when the magnitude of the scattering data is low, then even 2 – 3% error added to the uncorrupted data as per (5.7) might be quite significant. To see the effect of noise, which is in *proportion* to the magnitude of the exact scattering data, we have added here one more plot as shown in Fig. 5.39. In this figure,

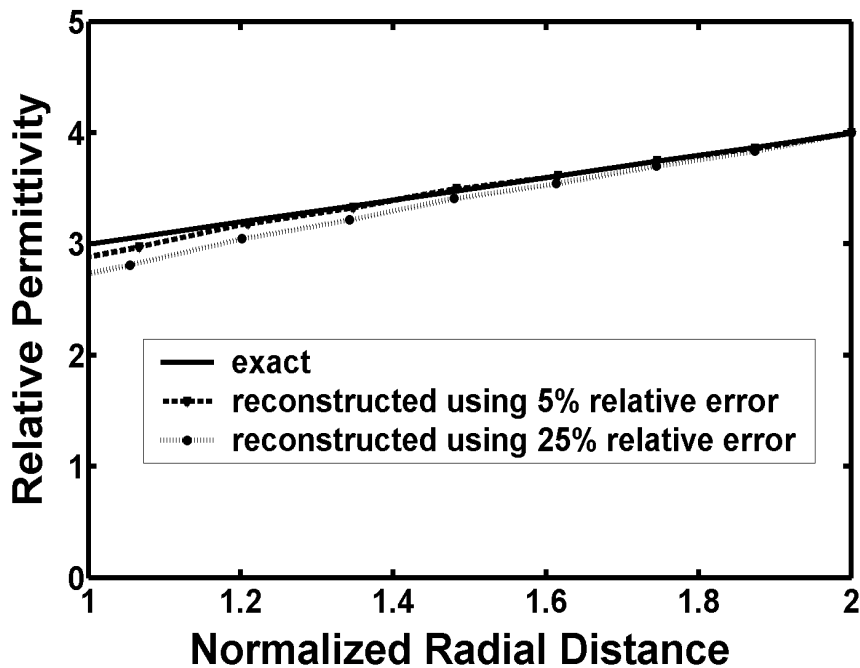


Figure 5.39: Exact and reconstructed permittivity profiles for the spherical TE_{11} case with 5% and 25% *relative* error in the scattering data

a maximum *relative* error of up to 25% of the scattering data is added to the exact simulated values over the whole frequency band. It can be clearly observed from this curve that even for such a high level of noise, the reconstruction permittivity profile is within the prescribed limit. The *stability* of the proposed technique to solve the inverse scattering problem with even high percentage of noise in the measuring data is the main advantage of our method as compared to the numerical iterative routines, which are generally associated with *ill-posedness* and where sometimes even a small drift in the input data might produce a large change in the output parameter.

5.2 Experimental results

In this section, we reconstruct a number of permittivity profiles from the measured reflection coefficient data. At microwave frequencies, the reflection coefficient data are generally measured using a vector network analyzer (VNA). Any modern VNA can make measurements of complex reflection coefficients or S -parameters over a wide frequency band on 2-port microwave networks. The analyzer applies a signal that is transmitted through the test device, or reflected from its input, and then compares it with the incident signal generated by the swept RF source. The signals are then applied to a receiver for measurement, signal processing and display [98]. One very important aspect of making measurements using a VNA is its calibration or error-correction procedure. Components of the measurement setup, such as interconnecting cables and adapters, introduce variations in the measured magnitude and phase that can mask the actual response of the device under test (DUT). The calibration is an accuracy enhancement procedure that removes the systematic errors (repeatable measurement variations) in the test setup. The analyzer measures

known standard devices e.g. a short, open or a matched load, and uses the results of these measurements to characterize the system. The number of standards required may depend upon the particular situation. The one-port measurement, for example, normally requires three known standards, while full two-port measurement may require four or more standards. At present, the methods available in the literature for the measurement of reflection coefficient or S parameters of dielectric materials using *VNA* can be broadly classified into two main groups

1. The transmission line measurements, which mainly involve placing the material under test (MUT) either in the coaxial airline or in a waveguide; and
2. Free-space measurements.

The first group of methods are generally more common because in this case a small sample of MUT can be machined and directly placed inside the transmission line media in which the electromagnetic energy is confined and well defined. The other main reason for the popularity of these group of methods is the availability of accurate calibration standards, which helps making the measurements of S parameters with sufficient accuracy. In this group, the waveguide methods are normally used under situations where the scattering data over a narrow band (e.g. X-band or Ku band) are sufficient. However as mentioned in previous chapters, to determine the inhomogeneous one-dimensional permittivity profiles using our technique, the reflection coefficient data over a wide frequency band are generally required. Hence we have used the coaxial airline technique, where the sample is machined in the form of a cylinder, and is fitted inside the coaxial transmission line in order to measure the reflection coefficient data over a wide frequency range (dc to 18 GHz).

The main advantage of the second group of method (free-space technique) is that it is totally non-destructive and non-contacting. Hence the free-space measurement techniques can work even under hostile environments. It may be mentioned here that although in the transmission line measurements, the MUT is not destroyed during measurement, it must be however machined to fit precisely into the waveguide or the coaxial line. We have measured the reflection coefficient data of different dielectric samples in the coaxial airline as well as in free-space, and have used these measured data to reconstruct the permittivity profile. Here, first we take up the coaxial airline measurements for the reconstruction, and then later on free-space techniques are considered.

5.2.1 Coaxial airline measurements

In this case, coaxial airlines are basically used as sample holders. The small samples of the dielectric MUT are machined precisely to fill the cross-section of 20 cm coaxial airline manufactured by Maury Microwave Corporation as shown in Fig. 5.40. The measurement setup using this coaxial airline and the vector network analyzer is shown in Fig. 5.41. The two ports of the airline are connected to the vector network analyzer. The full two-port calibration is achieved using Open-Short-Match-Thru method. In this method, the open, short and matched load are first connected to each port and measured. Next, a through connection is achieved by connecting both the ports of the network analyzer together without connecting the device-under-test (DUT) and its characteristics are measured. Finally, the characteristics



Figure 5.40: The 20 cm coaxial airline manufactured by Maury Microwave Corporation

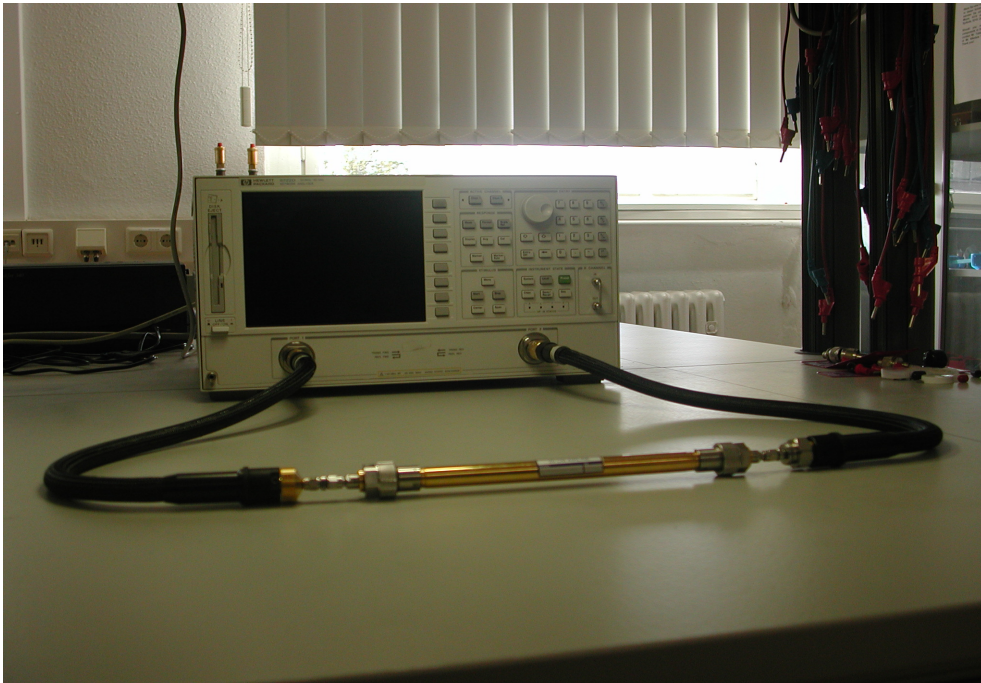


Figure 5.41: The measurement setup using the coaxial airline and the vector network analyzer

of all these four standards are used in the 12-error term model to measure the four S parameters of DUT quite accurately under real situations. The only problem with these airline measurements is that material should be machined quite precisely to fit inside the cross-section, and any air-gaps should be avoided as they can sometimes affect the results quite significantly. The reflection coefficient data in our case have

been measured from 40 MHz to 18 GHz with a step of 40 MHz using the Rohde & Schwarz *ZVR* vector network analyzer. We have taken three different lossless dielectric samples, whose relative permittivity is known and is almost constant over the measured frequency range. These materials are machined quite precisely in the form of coaxial cylinders so that they can be fitted inside the airline with minimum air-gap.

Our basic aim here is to reconstruct the *depth-dependent* permittivity profile of multi-layered dielectric media. It means that both thickness and the permittivity values of different dielectric layers are determined from the measurement of reflection coefficient data using the proposed technique. First we take the teflon

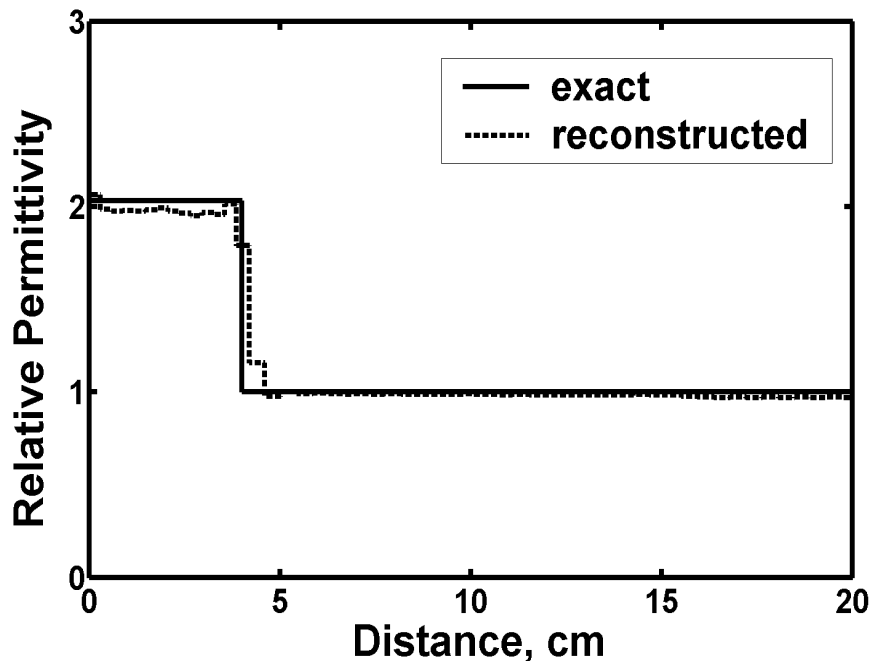


Figure 5.42: Exact and reconstructed permittivity profiles of two-layer dielectric media (teflon-Air) from the measured reflection coefficient data in a coaxial airline

and PVC samples individually, representing two-layer dielectric media (*dielectric-air*), and make use of our algorithm to reconstruct the relative permittivity and the thickness of each layer from the measured reflection coefficient data. The exact and reconstructed permittivity profile for these two samples are shown in Figs. 5.42 and 5.43 respectively, where it can be seen that overall reconstruction is reasonably good except at the interface between two layers which is because of a limited bandwidth. It may be noted here that the distance in all the plots here basically represents the *thickness* of each dielectric layer. Fig. 5.44 shows the reconstructed permittivity profile for the third dielectric sample, whose relative permittivity is also known in advance. It can be observed from figure 5.44 that the agreement between the exact and the reconstructed permittivity profile is not as good in this case as the earlier two examples. The reason for the discrepancy is mainly due to the fragile nature of this dielectric material, which is somewhat difficult to machine accurately and hence some air-gaps are unavoidable. It may be noted from these three figures that our method is able to determine both the relative permittivity and the thickness of individual dielectric samples quite accurately from the reflection coefficient

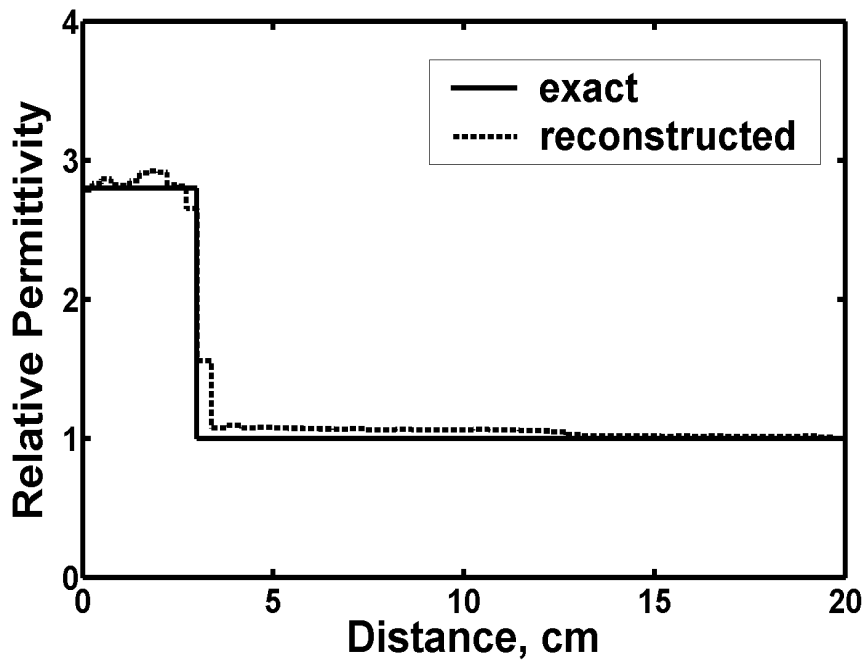


Figure 5.43: Exact and reconstructed permittivity profiles of two-layer dielectric media (PVC-Air) from the measured reflection coefficient data in a coaxial airline

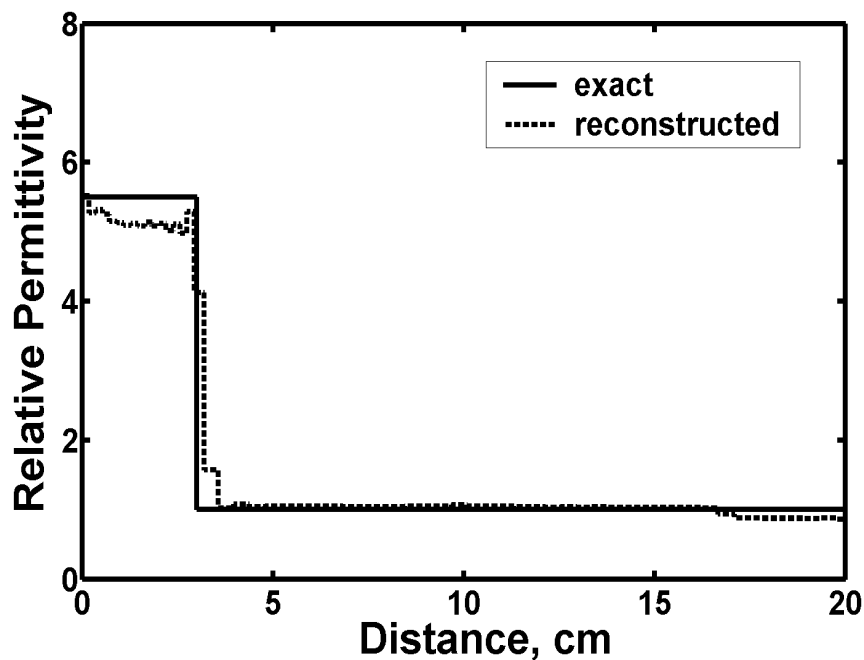


Figure 5.44: Exact and reconstructed permittivity profiles of a two-layer dielectric media from the measured reflection coefficient data in a coaxial airline

measurement data. After measuring the dielectric materials individually, we place these materials together in different combinations in the airline to see the effect of *multi-layer* inhomogeneity on our method. Firstly, we put teflon and PVC samples together in the airline and reconstruct the permittivity profile of this combination

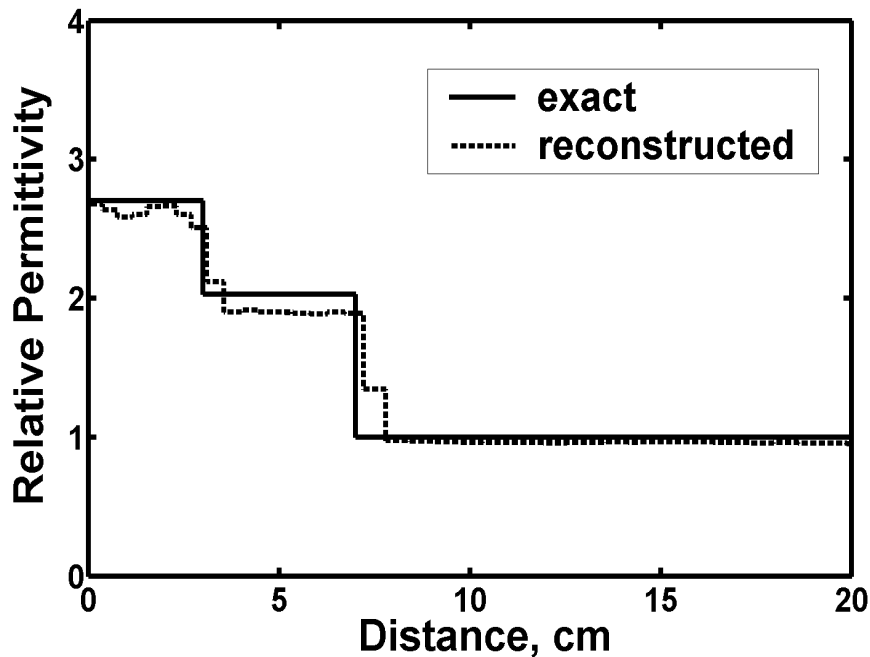


Figure 5.45: Exact and reconstructed permittivity profiles of three-layer dielectric media from the measured reflection coefficient data in the coaxial airline

using our method. The reconstructed permittivity profile along with its exact value is shown in Fig. 5.45 and as seen from this figure, the deviation is more in this multi-layer media as compared to the individual layers shown in previous figures. This deviation can be attributed to the placement of different layers in the airline and also their alignment with respect to each other. The length of the airline is 20 cm while the total length of samples in this case comes out to be only 7 cm. Hence the samples can not be fixed very accurately on both the ends, and due to this reason there might be some air-gaps between different samples in the axial direction which contributes to the error in measurements. Figs. 5.46 and 5.47 show two more examples of three-layer dielectric media with different combinations. From these two curves, it can be established that profiles of both ascending and descending values can be reconstructed without any major difference in the overall result. After considering two-layer and three-layer dielectric media, we consider multi-layer permittivity profiles as shown in Figs. 5.48 and 5.49. For these two cases, we have taken different samples of all three dielectric materials and placed them together in the airline. In Fig. 5.48 the three samples are arranged in descending order with respect to their permittivity values, while Fig. 5.49 represents the three-layer profile in arbitrary order. It is seen from these two figures that even for the multi-layered dielectric media, different permittivity layers can be reconstructed with a reasonable amount of accuracy and this accuracy can be increased by minimizing the air-gap in both axial and circumferential direction. It may be mentioned here that in Figs. 5.42- 5.49, the error between the exact and the reconstructed permittivity values is around 2 to 3 %.

After measuring the reflection coefficient data in the frequency domain using the VNA, we also used the time-domain reflectometer Agilent 54754A Differential *TDR* model to measure the reflection coefficient data in the coaxial airline. The advantage

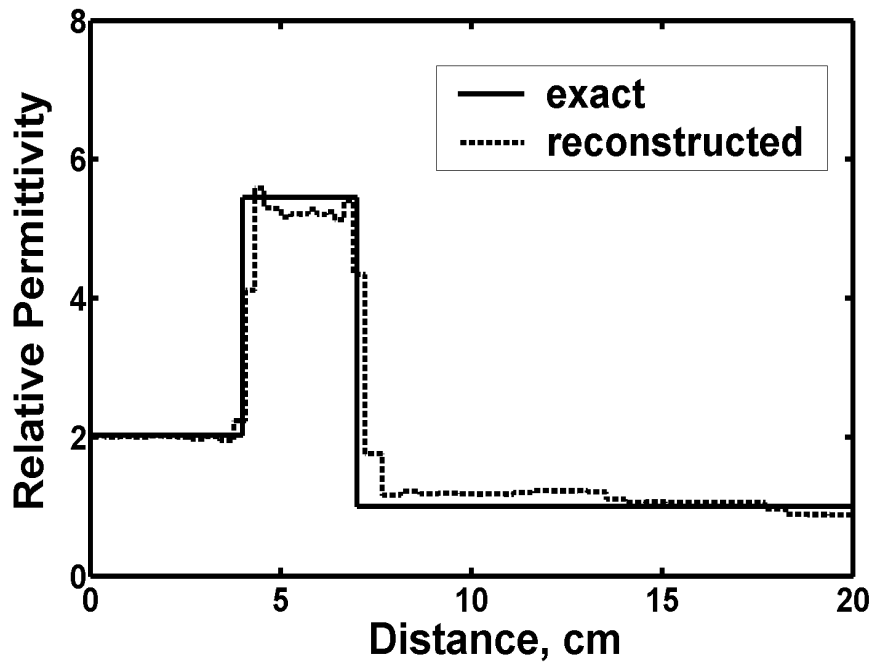


Figure 5.46: Exact and reconstructed permittivity profiles of three-layer dielectric media from the measured reflection coefficient data in the coaxial airline

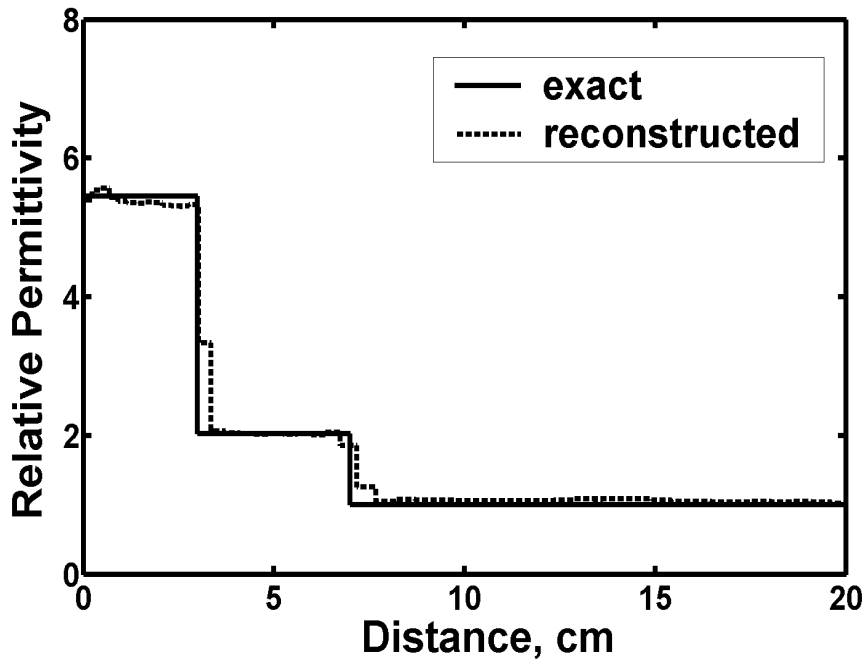


Figure 5.47: Exact and reconstructed permittivity profiles of three-layer dielectric media from the measured reflection coefficient data in the coaxial airline

of *TDR* measurement is that the relative permittivity of the dielectric material can be determined in a straight forward manner by simply reading the electrical length Δx from the instrument and dividing this length by the physical depth d of the

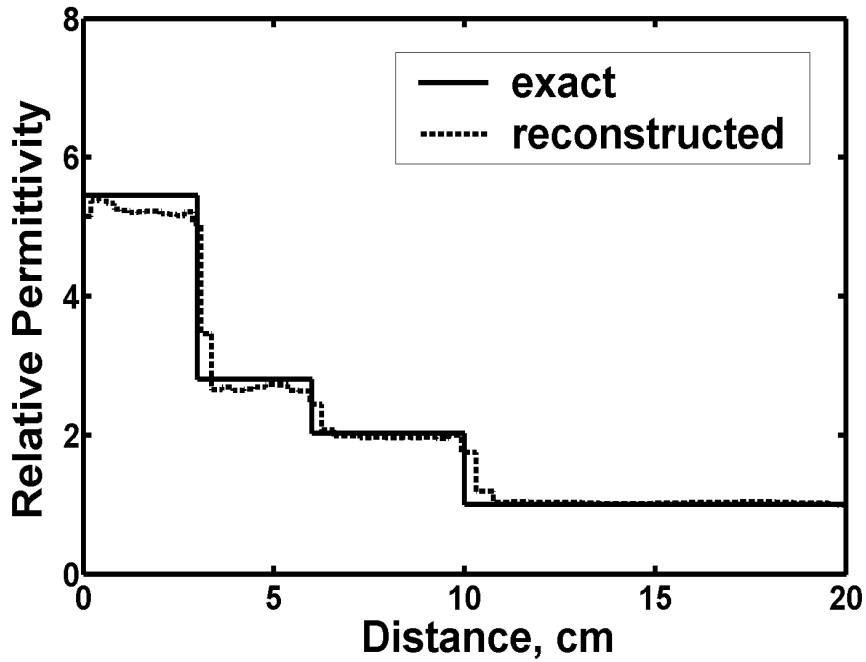


Figure 5.48: Exact and reconstructed permittivity profiles of multi-layer dielectric media from the measured reflection coefficient data in the coaxial airline

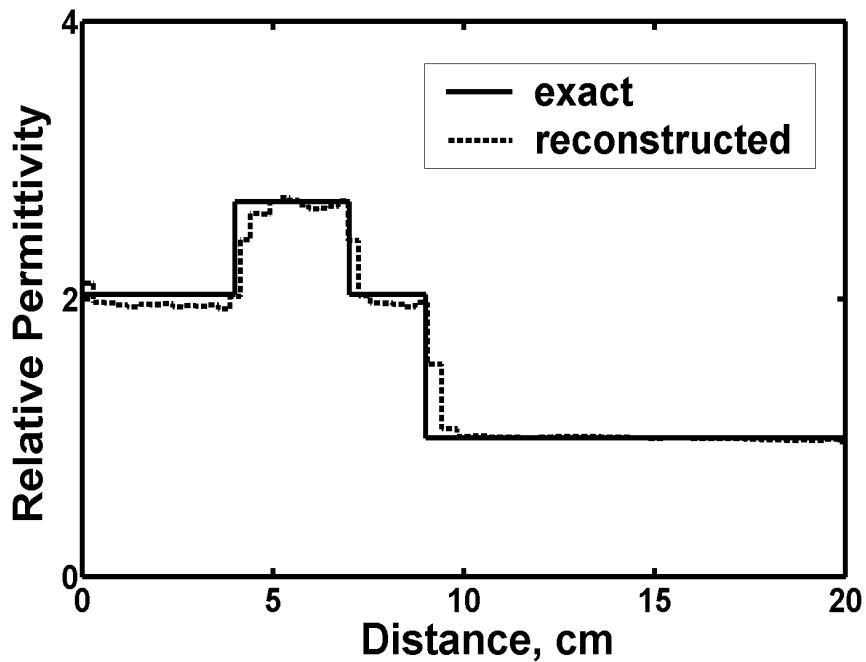
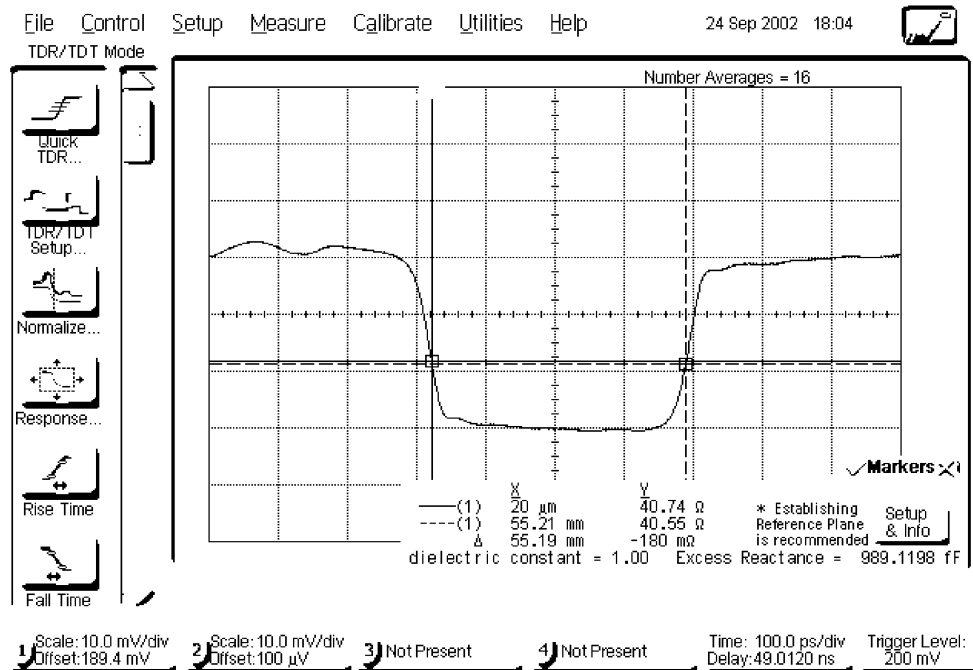
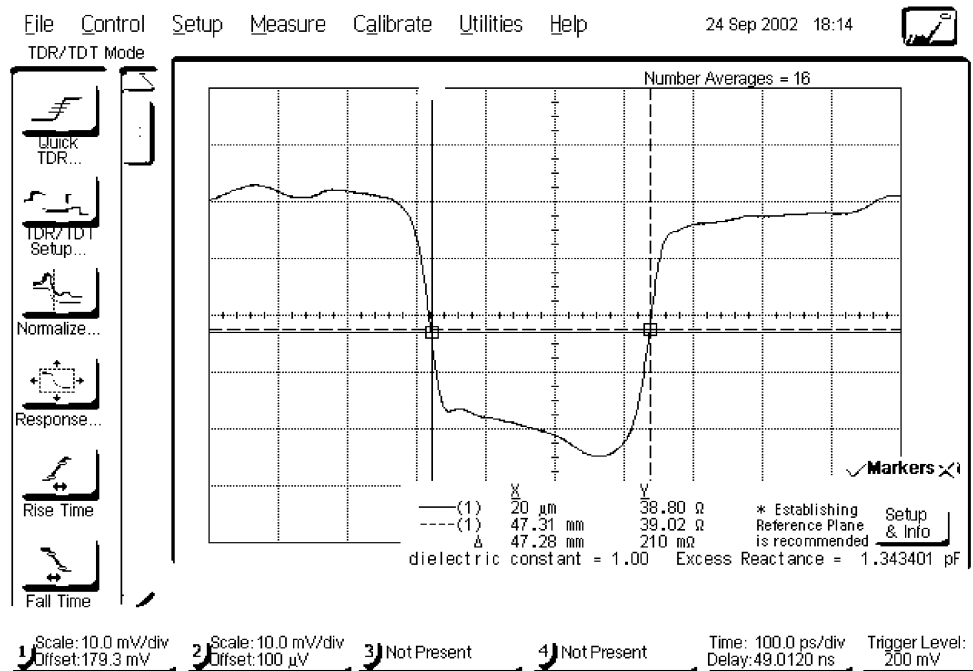


Figure 5.49: Exact and reconstructed permittivity profiles of multi-layer dielectric media from the measured reflection coefficient data in the coaxial airline

object, i.e.

$$\varepsilon_r = \left[\frac{\Delta x}{d} \right]^2 \quad (5.8)$$

The value of Δx can be directly read from the TDR as can be seen in Figs. 5.50

Figure 5.50: The *TDR* measurement of a single-layer dielectric materialFigure 5.51: The *TDR* measurement of a single-layer dielectric material

to 5.52 and this value is substituted in (5.8) to determine the relative permittivity of the particular dielectric material. It may be mentioned here that Figs. 5.50 to 5.52 represent the direct output of the *TDR*, and hence the resolution in these figures is not very good. Meanwhile, the reconstructed relative permittivity of these three samples are plotted in Fig. 5.53 along with their respective actual values and the typical accuracy for all the three cases is about 2 – 3%. It may be,

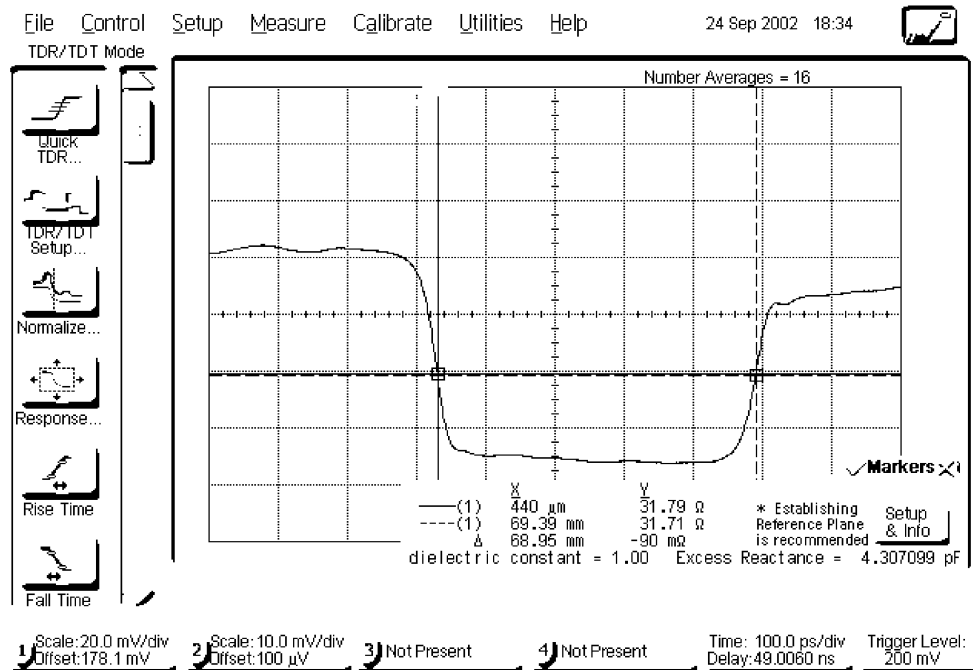


Figure 5.52: The *TDR* measurement of a single-layer dielectric material

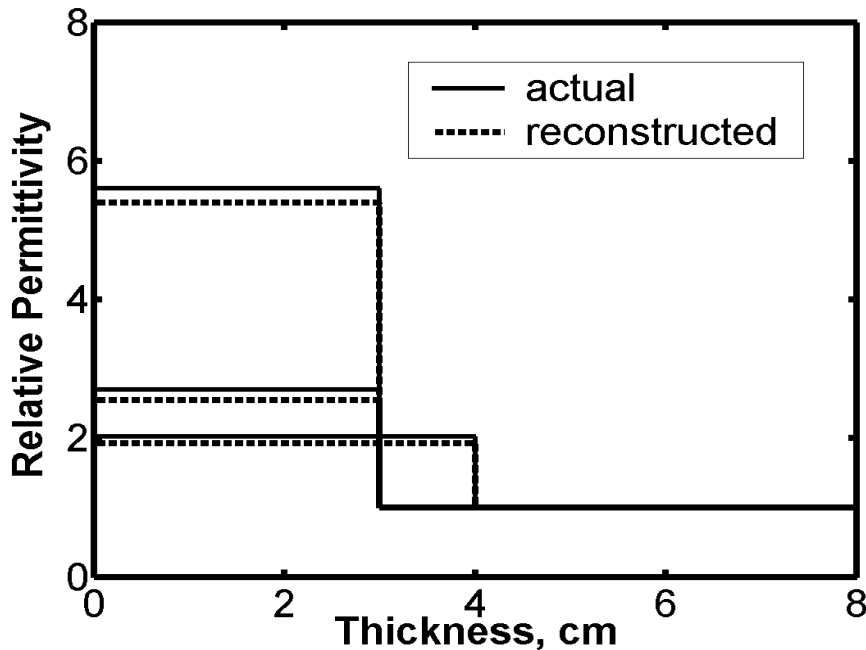


Figure 5.53: Actual and reconstructed relative permittivities of three samples from the *TDR* measurements

however, mentioned here that the *TDR* method can only determine the relative permittivity of single layer material provided its length d is accurately known. For multi-layer media, the inhomogeneity can be seen in time domain to have some idea in the qualitative term, but the method as such is not suitable for determining the quantitative values of permittivity of different layers very accurately as this approach does *not* take into account the effect of multiple reflections.

5.2.2 Free-space measurements

In the free-space measurement technique, large flat samples of the material under test (MUT) are placed in an anechoic chamber, either in front of the antenna or between a pair of antennas for the reflection and transmission measurements respectively. As no machining is required in this case, hence this method is suitable for materials which are fragile in nature and cannot be machined precisely. The sample of MUT is not contained in any fixture here, hence the error from possible air-gaps is not a concern. The free-space measurements can be carried out in extremely high temperatures or other hostile environments, and because of the use of large planar sheets in this case, this method is compatible for characterization of materials used e.g., in radar applications. The free-space method also looks more suitable for the imaging and remote sensing applications, where the containment of the object under test inside any transmission media is not feasible. However, one of the main problems in using a free-space technique is the introduction of various errors in measurements, and the requirement of special calibration considerations to overcome these errors. The inaccuracies in free-space measurements are due to two main sources of errors:

1. The diffraction effects at the edges of the material specimen/sample;
2. The multiple reflection between the antenna aperture and the sample surface.

The amount of error present depends on the measurement configuration employed, which can be classified into two categories: near field focussed system and far field system. The near field systems use the spot-focusing lens antennas, which produce a localized beam at the sample surface to minimize the diffraction effects from the sample and the calibration standards. However, this method is limited by the depth of focus of the antenna and only very thin samples can be used for this setup [99]. The other problem with this method is the requirement of special type of spot-focussing antennas which are not commonly available. These antennas are custom-made having two-equal plano-convex lenses mounted back to back in a conical horn antenna. One plano-convex lens gives an electromagnetic plane wave and the other plano-convex lens focuses the electromagnetic radiation at the focus. These antennas have characteristics such that the electromagnetic fields in the neighborhood of focal plane can be assumed to be a plane wave in character.

In the far field measurement systems, the samples are placed in the far field of the antenna's radiation pattern. This configuration obviously increases the amount of perimeter diffraction, but it is still the most common way of measuring the free space reflection coefficient at microwave frequencies [100]. The popularity of this method is probably due to its simple setup, its applicability to thicker samples, and no need for special types of lens antennas. The edge-diffraction effect in this case can be minimized by making the transverse dimensions of the sample much larger than the antenna aperture. The effects of multiple reflection can be eliminated by a special type of signal processing technique known as *time-domain gating*, which is available in most of the modern network analyzers. The time-domain gating is implemented by converting the frequency-domain reflection coefficient data into time-domain by taking its inverse Fourier transform. The gating is then applied over the main path of the reflection data, which is equivalent to applying a low-pass filtering in

the spatial domain. The basic idea here is that the multiple reflected signals can be differentiated in the spatial-domain as they will arrive at different time intervals. We can then choose the portion of the signal, which has travelled through the main path and separate it out from the other unwanted portions. These gated time-domain data are converted to the frequency-domain by taking the Fourier transform. The gating procedure can also be implemented manually if this facility is not available in the network analyzer, by making use of standard *FFT* (Fast Fourier transform) and *IFFT* routines. We have used the far field system for the measurement of reflection coefficient data of different dielectric samples in the free-space. As we are only interested in the reflection coefficient or S_{11} , hence the standard one-port calibration (short-offset short-matched load) involving three standards is employed [100]. The matched load in this case is achieved by an empty room, as the propagating free space wave will meet the free space at the sample reference plane producing a net reflection coefficient of zero at this position. Hence this situation becomes equivalent to the placement of an absorbing plate at the reference plane. The accuracy of the measurement will, of course, depend upon the reflectivity characteristic of the absorber material placed in the anechoic chamber. The second standard (short) in the free-space is a metallic plate placed at the reference position, which produces a net reflection coefficient of -1 . The transverse dimension of this plate is taken to be equal to that of the actual sample to avoid any shadow effects under the actual measuring condition. For obtaining the third standard, this conducting plate is shifted by an offset length d to produce a reflection coefficient given by $e^{j\pi(1+4d/\lambda_0)}$. It is preferable to choose this distance d equal to the quarter wavelength ($d = \lambda_0/4$), where λ_0 is the free-space wavelength corresponding to the middle frequency over which the reflection coefficient data are measured. The whole idea of choosing d this way is to simulate an *open* condition producing a net reflection coefficient of $+1$ at the reference plane. It may be mentioned here that the positioning of the reference plane is very critical in the free-space measurement system and this has specially a big influence on the phase measurements. Hence a special care must be taken to accurately position the metallic calibration plate and the sample. For our measurement, the one-port calibration kit for coaxial line of the vector network analyzer has been modified by defining standards as described above. The sample was placed in the far field of the antenna, where the electromagnetic fields can be assumed to be a plane wave in character. The setup for measuring the reflection coefficient data is shown in Fig. 5.54. The one-port of the vector network analyzer is connected to the Horn antenna through a cable and a coaxial-to-waveguide adapter. The measurements have been carried out in X and Ku bands using two different pyramidal Horn antennas. The front view of the measurement setup using the Wiltron 37347 A vector network analyzer, the coax-to-waveguide adapter and a Horn antenna is shown in Fig. 5.55. The inside view of the setup having a horn and the dielectric sample (all in the anechoic chamber) is shown in Fig. 5.56. For placing such a large sample inside the anechoic chamber, we have fabricated a mechanical stand shown in Fig. 5.57. This stand includes a mechanism to accurately position the metallic plate and the dielectric sample. The reference position for placing the calibration standards and the sample is chosen around one meter away from the aperture of antenna to satisfy the far-field condition in both X and Ku bands. We have used the metallic plate of 1 square meter for the calibration, and the samples were also taken of the same transverse dimension to avoid any ambiguity. This

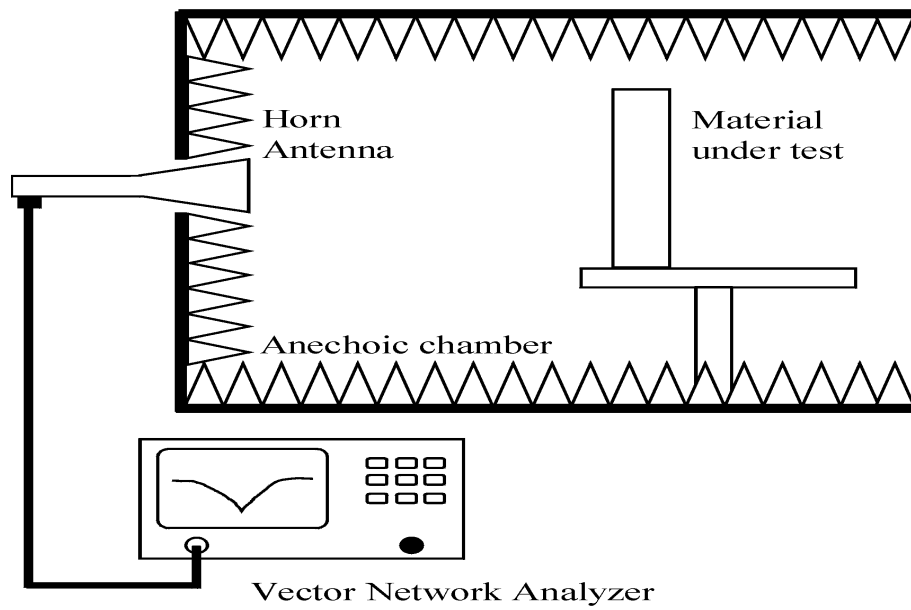


Figure 5.54: Schematic diagram of the measurement system



Figure 5.55: Actual measurement setup from the front

transverse dimension of 1 square meter is quite large as compared to the maximum horn aperture¹, and hence the edge-diffraction effects are minimized.

The offset lengths for the *X*-band and *Ku*-band measurements were taken as 5 cm and 4 cm respectively, which are approximately equal to one-quarter wavelengths at the mid-frequency in their respective frequency bands.

¹The highest aperture of the *X* band pyramidal Horn being used in our setup is 109 mm.

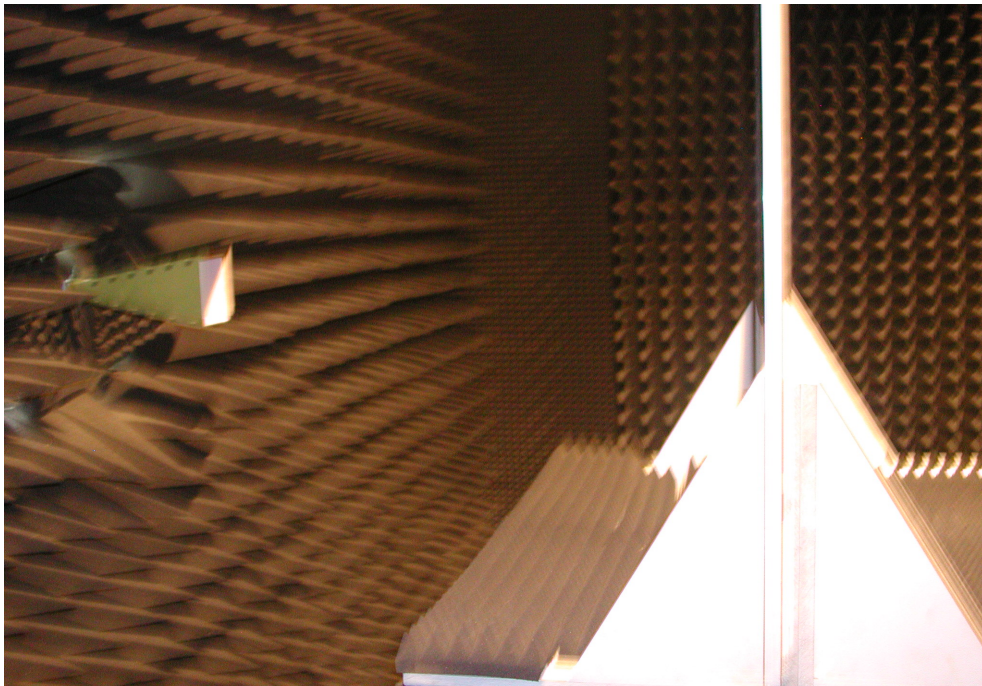


Figure 5.56: The measurement setup inside the anechoic chamber

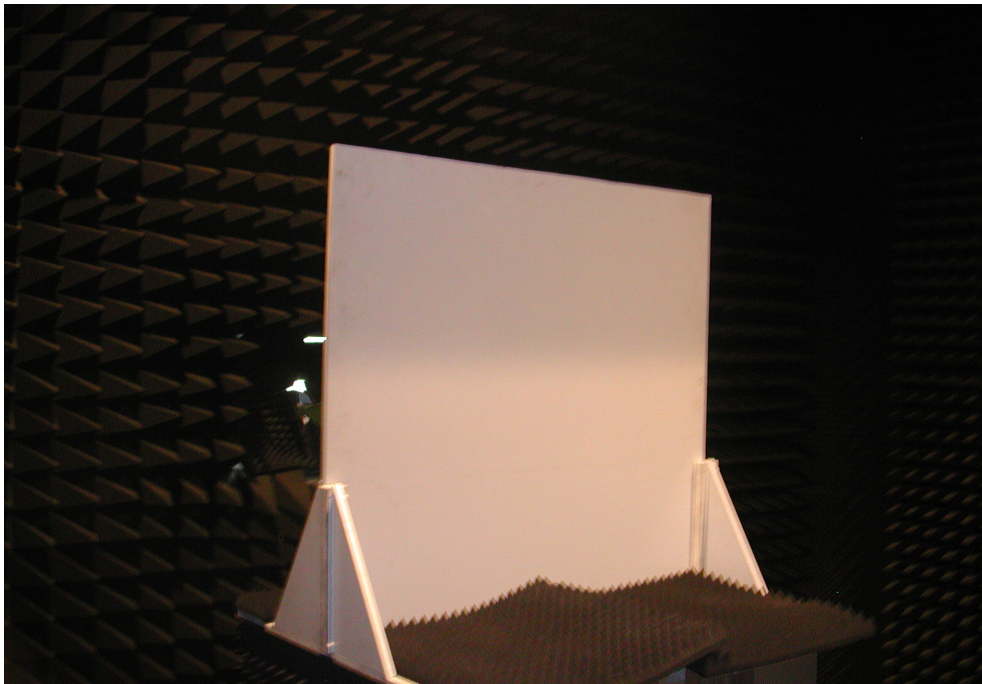


Figure 5.57: The mechanical stand with the dielectric sample

To test the accuracy of our measurement setup, the metallic plate (short) was placed at the reference position after the calibration was done. The characteristics obtained for this short for the X -band are shown in Figs. 5.58 and 5.59. It can be seen from both figures that the magnitude and phase of the measured reflection coefficient in X band are $0.0 \pm 0.4 \text{ dB}$ and $\pm 180.0 \pm 2^\circ$ respectively. The characteristics of the short in the Ku -band also show the same behavior. The magnitude of the

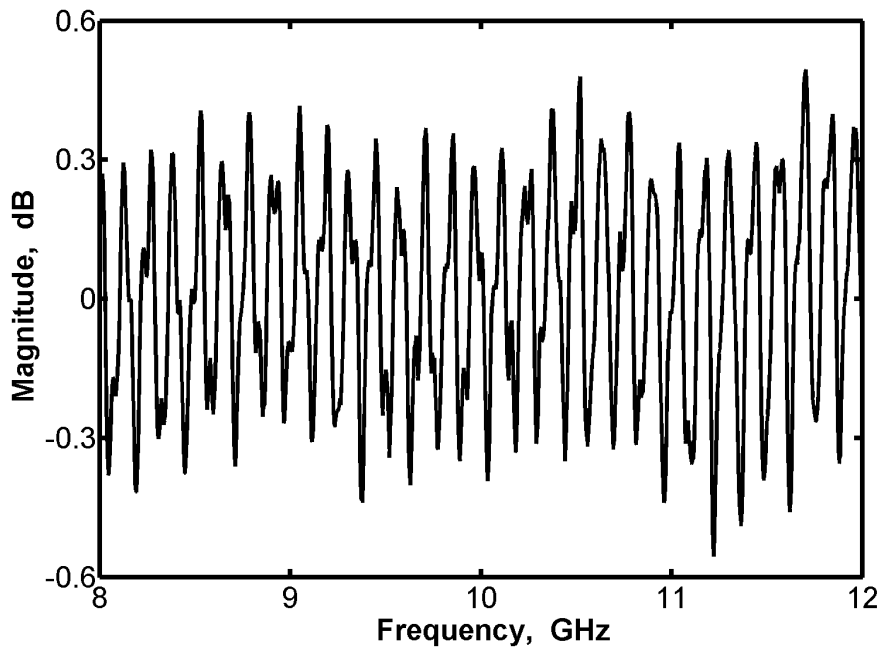


Figure 5.58: The magnitude of the reflection coefficient for the metallic plate placed at the reference point for X band

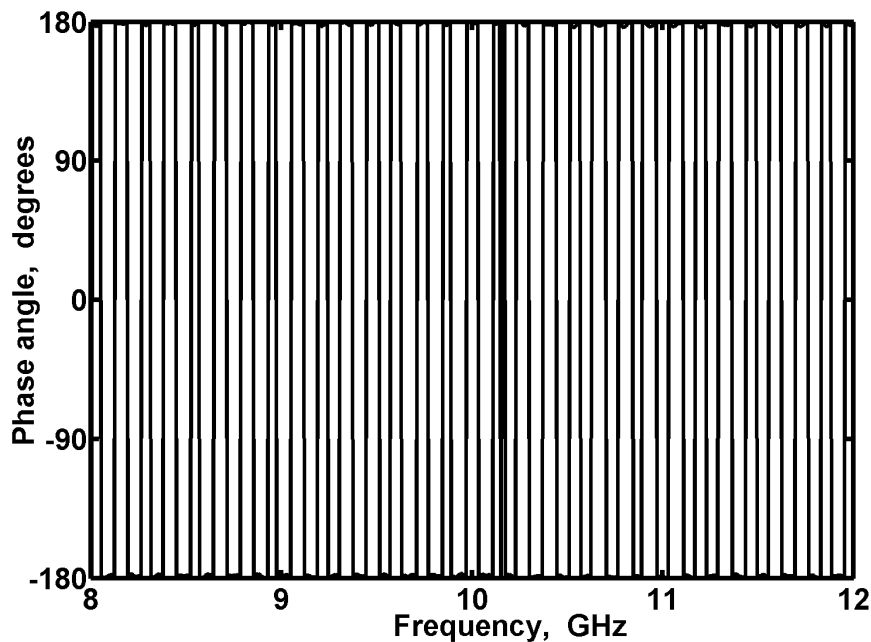


Figure 5.59: The phase of the reflection coefficient for the metallic plate placed at the reference point for X band

reflection coefficient for an empty room after calibration is less than -50 dB in both the frequency bands. After verifying the calibration procedure, the dielectric samples were measured. Because of the problem in obtaining the dielectric pieces of larger transverse dimension, we could obtain only two samples of teflon and PVC each of 1 square meter cross-section and about 1.5 cm thick. The samples were

taken of the same transverse dimension as that of the metallic calibration plate in order to have the same condition. The time-domain gating of the VNA was applied in order to avoid any multiple reflections and to remove ripples from the measured reflection data. To see the effect of time-domain gating, we have plotted

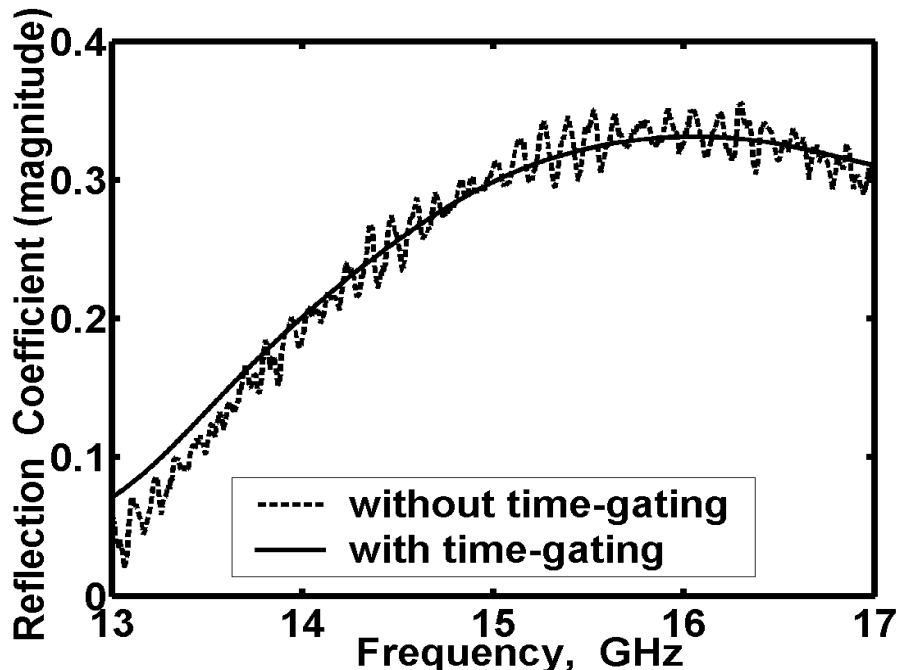


Figure 5.60: The magnitude of the reflection coefficient of the teflon sample in Ku band with and without time-gating

the magnitude of the reflection coefficient data of teflon sample in Ku band with and without the time-domain gating as shown in Fig. 5.60. The ripples can clearly be seen in the raw data with no gating, which disappear after the application of time-domain gating. The reflection coefficient in the time-domain as seen on VNA is plotted in Fig. 5.61, where many side lobes occurring due to multiple reflections can be observed. To remove the effect of these multiple reflections, the gating is applied in the time-domain along the main path and then the Fourier transform is taken to obtain the frequency-domain reflection coefficient data with time-gating. Figs. 5.62 and 5.63 show the magnitude and phase of the reflection coefficient data of PVC sample measured in X band with time-domain gating. It can be observed from these two figures that the free-space calibration technique along with the applied time-domain gating is able to measure the reflection data with minimum ripples. Finally, we have reconstructed the relative permittivity of both teflon and PVC samples from the measured frequency-domain reflection coefficient data using our proposed algorithm as shown in Figs. 5.64 and 5.65. In both of these examples, first the analytical method presented in section 4.1.1.4 has been used to determine the value of permittivity at the air-dielectric interface, and then the formulas derived in section 4.1.1.2 and 4.1.1.3 have been used to reconstruct the permittivity profile starting from this initial value. Since in both of these cases, we have only one layer of dielectric material hence our aim is basically to determine the thickness and ϵ_r of these materials. But as can be seen from these figures, the reconstructed permittivity profile (both the value of the relative permittivity and the thickness of the material)

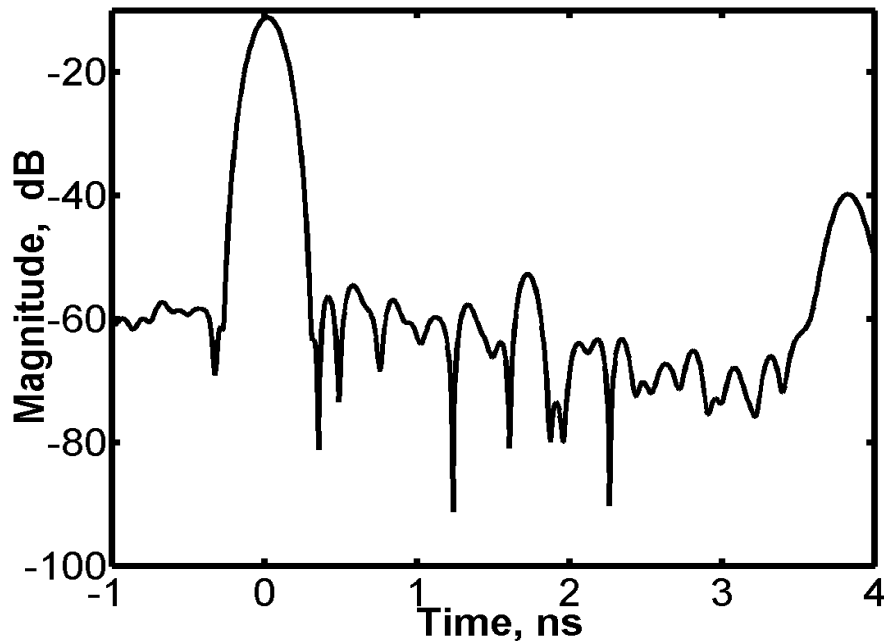


Figure 5.61: The reflection coefficient data of the teflon for *Ku* band in time-domain

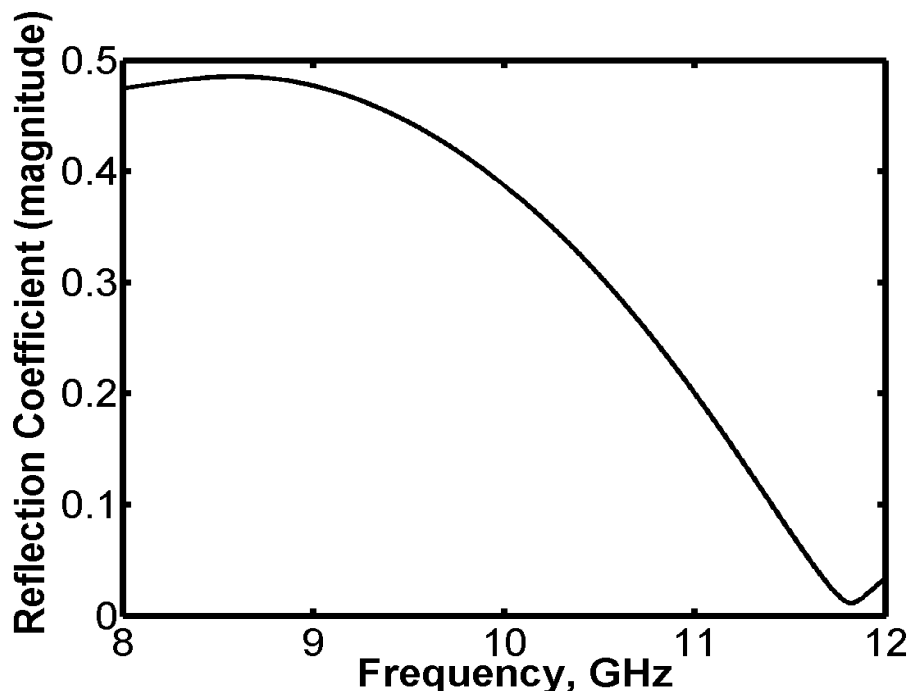


Figure 5.62: The magnitude of the reflection coefficient data of PVC sample in *X* band with time-gating

is not as good (typical accuracy in this case is 5%) as it was e.g. in the airline case. The reason for this discrepancy is two-fold. The first reason is that the positioning of calibration standards and the material sample is quite problematic in free-space measurements. We have observed that sometimes even an error of the order of one-tenth of a millimeter can make a big difference specially on the phase measurements.

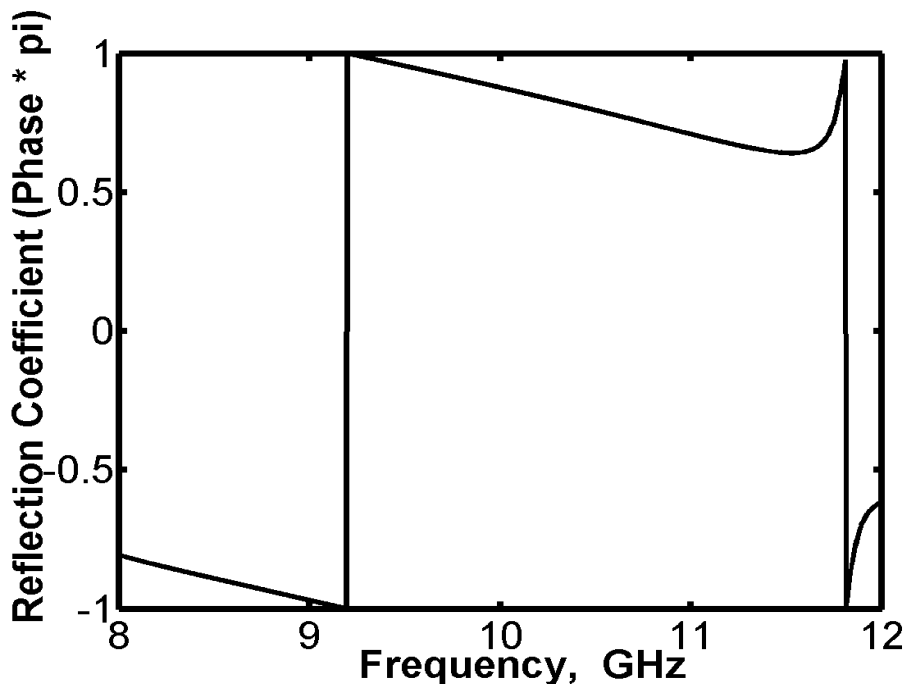


Figure 5.63: The phase of the reflection coefficient data of PVC sample in X band with time-gating

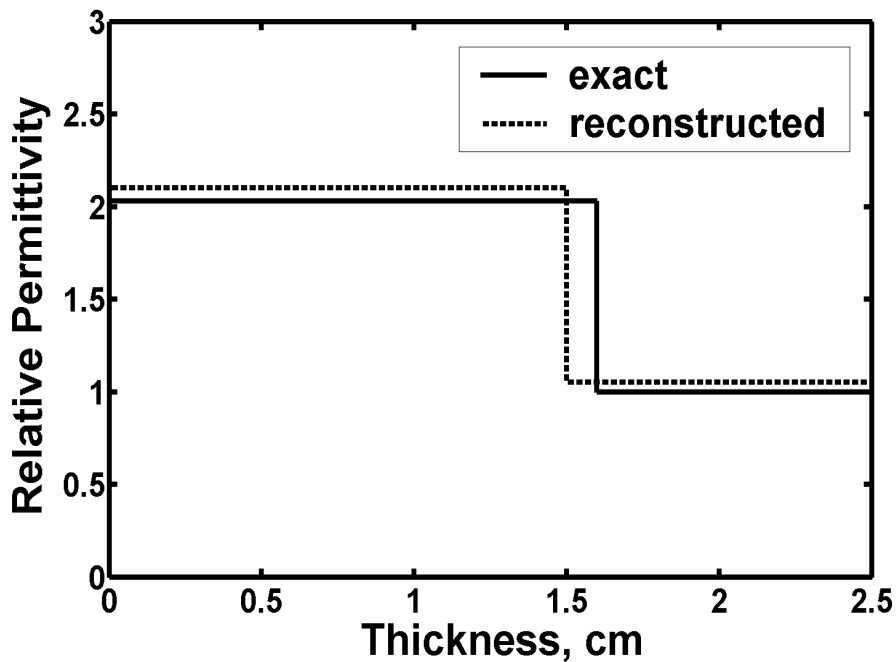


Figure 5.64: The reconstructed permittivity profile of the teflon sample from the reflection data measured in free-space

We have used the offset-short method for the calibration. In this case it is difficult to define precisely the offset length. In addition, accurately placing the short and sample at the specified position using our manual method has also been a problem. The metallic plates and samples are also quite big in the transverse dimension and

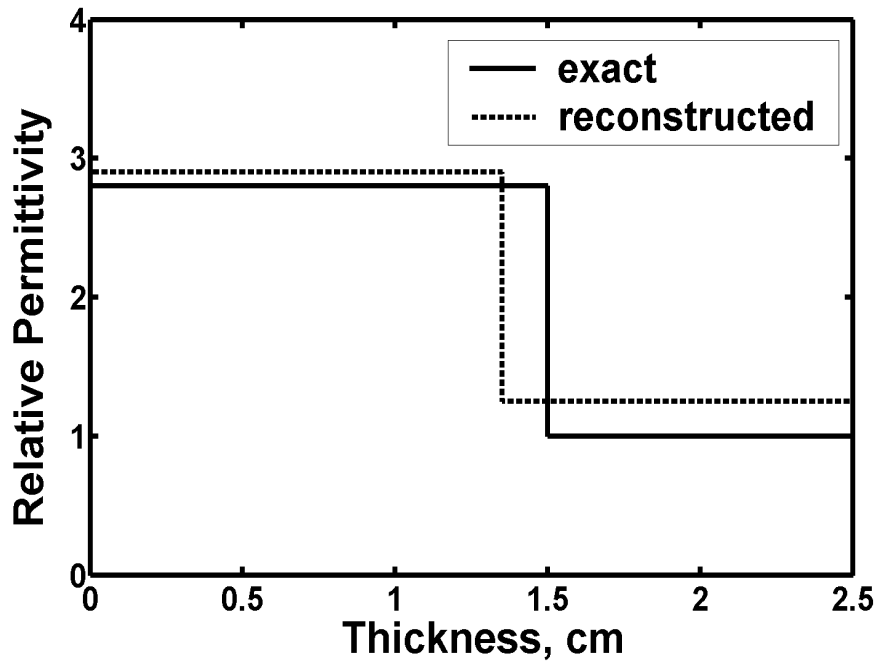


Figure 5.65: The relative permittivity of the PVC sample reconstructed from the measured reflection data in free-space

hence sometimes it might be difficult to maintain their position exactly in one plane unless some precaution is taken to hold them tightly at the reference plane. This problem of positioning can probably be solved up to much extent by making the whole setup automatic and controlling the reference position of the standards and the sample by means of a servomotor. The second reason for the high amount of error in the free-space case as compared to the coaxial airline is due to the limited bandwidth available in former. We have used the Horn antenna for the measurement and as it is known, these antennas can work over a limited frequency band (e.g. X band, Ku band etc.). It has already been mentioned in the earlier chapters that we basically take $IFFT$ of the frequency-domain reflection coefficient data and for the proper functioning of $IFFT$ routing or the inverse Fourier transform method, the values of the spectral-domain function over a wide frequency band starting from dc or very low frequency are required. But using our present setup, we are able to measure the reflection coefficient data either in X band or Ku band only, hence the $IFFT$ routines don't seem to function quite well. The problem is that due to the limited bandwidth the resolution of the reconstruction in the space-domain is not very good. This resolution problem can possibly be solved in two ways. The first way is to use some special antennas which can work over a wide frequency band. In this case the directivity or gain of the antennas should also be high so that enough power is able to reach the material under test under the far-field condition. The second way is probably to take the thicker samples (in our case it was 1.5 cm only) for measurements. If we take thick samples, then high resolution would not be required in the spatial domain and hence low-band antennas can be used. But as mentioned earlier we also require the large transverse dimension (1×1 meter) to minimize the diffraction problem and if we make these samples thicker, then the materials would be quite bulky and difficult to handle. Hence from the above

discussion, it can be concluded that under practical situations it might be difficult to characterize the dielectric materials very accurately using the free-space method, but the overall technique works in principle and it can definitely be used to image the dielectric objects qualitatively if not quantitatively. The other advantage of our method as compared to e.g. [99] is that our setup works for thick as well as thin samples, and hence it can also be used to image the multi-layer dielectric media provided the calibration and the measurement are done very accurately. It may also be mentioned here that our setup for the free-space measurement uses only one horn antenna, along with the vector network analyzer and a coaxial-waveguide adapter, which is simpler than the setup used e.g. in [100].

It has already been mentioned that the vector network analyzer (VNA) model used in our setup has a time-domain facility, which was basically used to remove ripples in the spectral-domain measured data by means of time-domain gating. We have recently explored the possibility of using the time-domain measurements of VNA to determine the relative permittivity of single layer dielectric materials, and it works provided certain criteria are satisfied. These time-domain measurements seem to be specially advantageous in the band-limited case, where our proposed technique does not give good results. The overall idea of making use of these time-domain measurements is as follows. It can be readily proved that the reflection coefficient data measured over a frequency band e.g. in *X*-band is equivalent to exciting the device under test (DUT) with a sinc pulse. The width of this pulse depends upon the bandwidth of the spectral domain signal in such a way that higher the bandwidth, the lower the pulse-width. This means that when we measure the

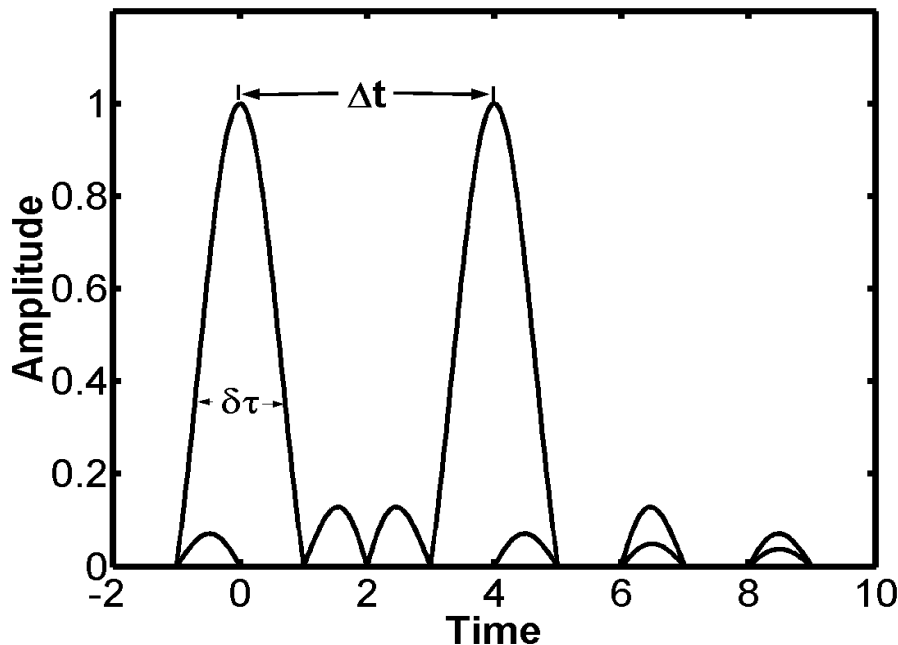


Figure 5.66: The approximate shape of the spectral domain function in time-domain

dielectric material using e.g. a horn antenna (which is band-limited) and observe the reflection coefficient data on VNA in the time-domain, then a typical graph may look like as shown in Fig. 5.66. The width $\delta\tau$ in this figure depends upon the bandwidth as mentioned earlier, and the spacing between two peaks Δt will basically

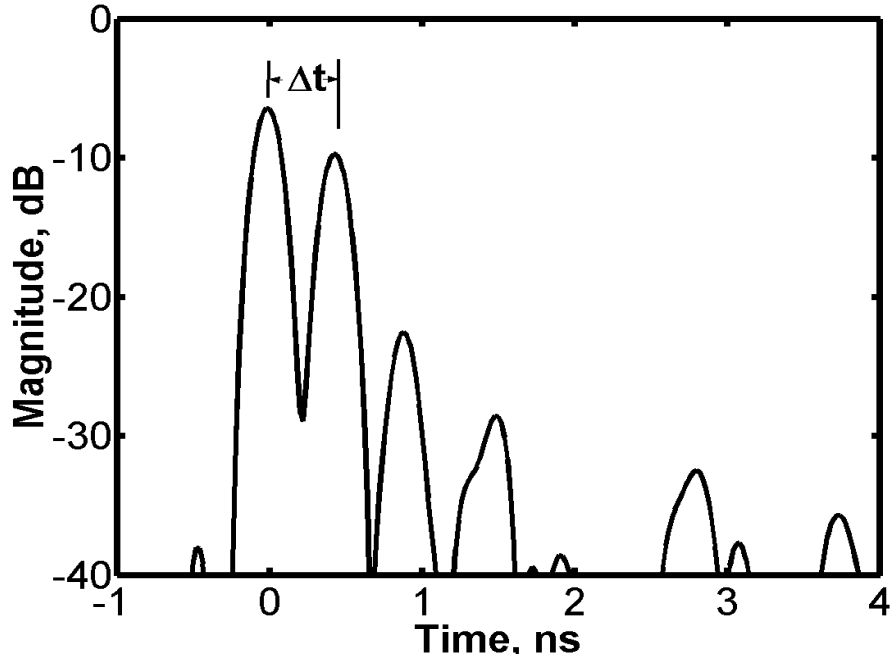


Figure 5.67: The measured reflection coefficient of a 5 cm thick sample in time-domain

correspond to the electrical length of the dielectric material under test (MUT), i.e.,

$$\Delta t = \frac{\Delta x \sqrt{\epsilon_r}}{c} \quad (5.9)$$

where Δx and ϵ_r are the thickness and the relative permittivity of the MUT respectively. Hence if we are able to measure Δt , then the permittivity ϵ_r can be determined from this equation provided the thickness of the material Δx is known. However, this whole method can work only if the width of the sinc pulse $\delta\tau$ is much smaller than the time interval Δt , so that we can observe very sharply the reflection from the two edges of the dielectric sample in the time-domain.

To satisfy this criterion, either the spectral bandwidth should be large enough to make the width $\delta\tau$ quite small, or the dielectric MUT of higher thickness should be chosen in order to make Δt larger. This can be also explained with respect to Fig. 5.61, where we have plotted the time-domain reflection coefficient data of the teflon sample (1.6 cm thick) as seen on VNA for the *Ku* band. We can see only one peak in this curve because this sample is quite thin. For the permittivity of the order of 2.0 the value of Δt as per (5.9) comes out to be around 0.076 ns, which is much less than the pulse-width (≈ 0.62 ns) of the sinc function in this figure.

For the proper application of the proposed time-domain method, we also measured some thicker dielectric samples. The time-domain measurement of one of these samples, which is approximately 5 cm thick is shown in Fig. 5.67. The two peaks can be clearly seen in this figure and Δt in this case is very accurately determined with help of two markers (the facility available in the VNA). After computing Δt , the relative permittivity is determined with the help of (5.9) and this has been plotted in Fig. 5.68 along with its exact value. We also measured the time-domain reflection coefficient data for another dielectric sample, which is 5.30 cm thick. The

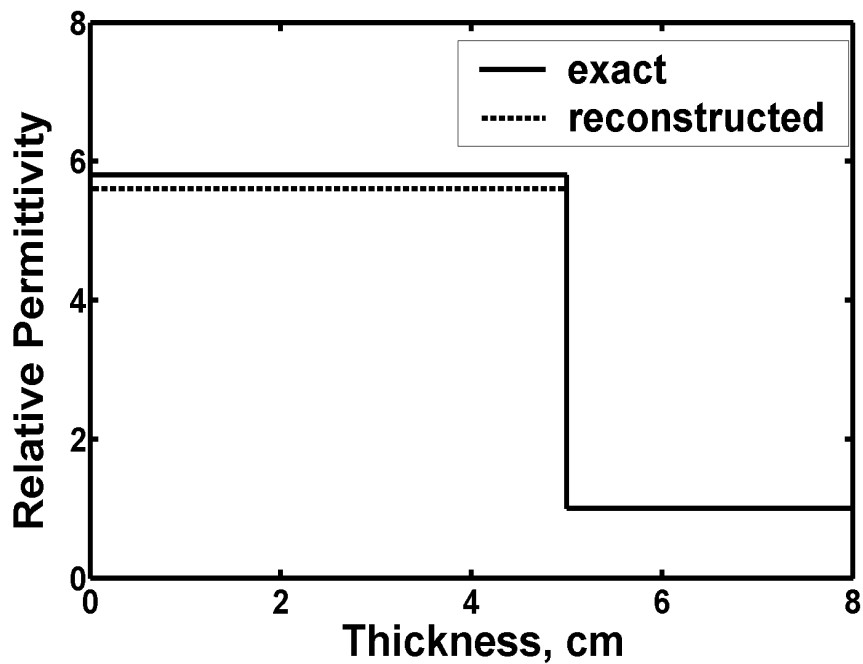


Figure 5.68: The reconstructed value of relative permittivity from the time-domain reflection coefficient data

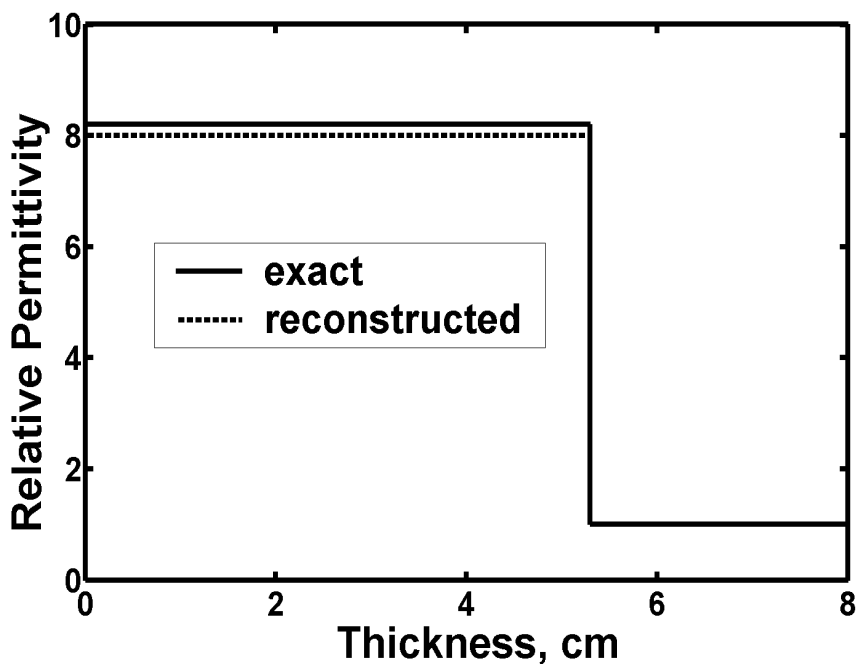


Figure 5.69: The reconstructed value of relative permittivity from the reflection coefficient data measured in time-domain

exact and reconstructed profile for this case has been shown in Fig. 5.69. It can be seen from both figures that this simple time-domain technique works in principle as long as the sample is reasonably thick. However, it is to be noted here that for this technique to work, we should know accurately the thickness of the dielectric material in advance and hence this method cannot work for the inhomogeneous or

multi-layer dielectric media. Another reason for the unsuitability of this method in case of multi-layer media is that it cannot take into account the effect of multiple reflections. Finally, it may be mentioned that the TDR method used in the previous section for the time-domain airline measurement, does not seem to work for free-space measurement. The reason is that because of the presence of the horn antenna in our measurement setup, not enough power is probably able to pass through this band-pass antenna and hence the effect of dielectric material placed in the far-field of antenna cannot be observed on the screen of TDR.

Chapter 6

Summary

In this thesis, a new method for the reconstruction of one-dimensional depth dependent permittivity profiles in planar and non-planar dielectric objects has been presented. The reconstruction of permittivity profiles is a basic problem in the field of microwave imaging and remote sensing. The determination of depth-dependent inhomogeneity of dielectric objects is generally the most difficult part of the microwave imaging process as these measurements cannot be carried out *in-situ*. The cross-sectional dielectric image of the object, on the other hand, can be obtained by means of lateral scanning if a number of high-directivity antennas are used. Hence our technique in combination with the lateral scanning methods can provide a complete image of any arbitrary shaped dielectric object. We have shown in this work that the resolution of the reconstructed image in the spatial domain can be quantitatively controlled by varying the bandwidth of the spectral domain reflection coefficient data. A unique solution can be obtained using our method as it isolates the non linearity associated with inverse problems into a simple algebraic transformation. On the other hand, the method is not based on the so-called Born approximation and hence it can be used to reconstruct dielectric objects of higher contrasts as well.

For the implementation of our proposed scheme, we have first considered an inhomogeneous dielectric object in the Cartesian coordinate system. The direct problem has been formulated for this kind of geometry taking into account multiple reflections between different layers of the dielectric object. The formulation is in the form of nonlinear Riccati differential equations relating the spectral domain reflection coefficient to the inhomogeneous permittivity profile for different polarizations. An improved renormalization technique has been presented for the solution of these nonlinear differential equations representing the one-dimensional inverse scattering problems. Accordingly a closed-form expression has been obtained to determine the one-dimensional permittivity profile in terms of an inverse Fourier transform of the spectral domain reflection coefficient data. The permittivity profile is generally reconstructed starting from its value at the air-dielectric interface. Hence two methods have also been presented to determine the value of the permittivity at the air-dielectric interface from the reflection coefficient data. This whole process of determining the permittivity profile from the reflection coefficient data is generally called the Riccati-differential-equation (*RDE*) approach, as the overall technique is based on the inversion of this *RDE* making use of the frequency-dependent reflection coefficient data.

The above mentioned RDE approach was applied till now only to planar objects. We have generalized this *RDE* approach so that they can be applied to analyze the one-dimensional inhomogeneity of non-planar structures as well by simply relaxing the functional form of the transform kernel. After extending the applicability of *RDE* technique to the general one-dimensional case, we have numerically validated the theory in the case of cylindrical and spherical coordinate systems. For this purpose, the Riccati-similar nonlinear differential equations for different *TE* and *TM* illuminations have first been derived in these non-planar coordinate systems. They relate the one-dimensional radially varying permittivity profile in each case to the appropriately defined frequency-dependent reflection coefficient data. The formulations have been started with the lower order illumination for the radially directed waves in cylindrical and spherical structures, and then have been generalized for arbitrary order *TE* and *TM* modes. A linearized version of these differential equations has been introduced in terms of a virtual reflection coefficient, and an optimum algebraic transformation between the actual and the virtual reflection coefficient has been found. The introduced linear equations have been solved using an appropriate boundary condition to obtain an integral form of the spectral domain reflection coefficient function in each case. For the proper and accurate inversion of these equations, a coordinate transformation in the spatial domain has also been introduced, which converts the real space variable into a virtual time variable. One of the aims of this coordinate transformation is to take into account the change in wavelength as the wave travels inside the dielectric inhomogeneous media. After incorporating the above variable transformation, the spectral domain reflection coefficient acquires the form of an integral equation whose kernel is a function of the angular frequency and the *virtual time*-variable. At this stage, a suitable integral transform¹ has been introduced to convert the reflection coefficient function from the spectral domain into a spatial domain. The kernel of this transform has been combined with the kernel of the spectral domain reflection coefficient function determined earlier to obtain the form of a sampling function for each particular case. The shape of this sampling function has been plotted for various lower and higher order *TE* and *TM* modes in both cylindrical and spherical coordinate systems. Interestingly this function has always been found to be pulse-shaped possessing all the characteristics as proposed by us in the theory. After ascertaining the shape of the sampling function for each case, the virtual-time domain permittivity profile function in each coordinate system has been reconstructed in terms of the spatial domain reflection coefficient data. Finally, the one-dimensional radially varying permittivity profile in both cylindrical and spherical coordinate system has been determined from the *virtual-time* domain permittivity function using a numerical algorithm.

To validate our technique, several examples (both simulated and experimental) have been considered in this thesis. In the case of planar Cartesian media, the simulated reflection coefficient have been obtained by either numerically solving the exact non-linear Riccati differential equation, or by using the the transmission-matrix formulation. The permittivity profile for both continuous and layered dielectric media have been reconstructed from these simulated frequency-domain reflection coefficient data using our technique. The error between the actual and reconstructed permit-

¹The form of this integral transform is the Hankel transform in the case of cylindrical geometry, while it is the spherical Fourier-Bessel transform in the case of spherical geometry.

tivity profile has been found to be less than 1% in the case of continuous media, and less than 2% in case of layered media. The larger deviation between the actual and reconstructed permittivity profile in the case of layered media is mainly due to a step change in the permittivity values from one layer to another. For cylindrical and spherical structures, the reflection coefficient data have been generated by solving numerically our derived Riccati-similar nonlinear differential equations for a number of linearly and non-linearly varying permittivity profiles in their respective coordinate systems. The radially varying permittivity profiles in both cylindrical and spherical coordinate system have been reconstructed from these simulated reflected coefficient data using our method with an accuracy of less than 2%. In the case of cylindrical media, the layered structures have also been considered using the radial transmission line theory and the deviation between the actual and the reconstructed permittivity profiles in this case has been found to be 5%. This larger deviation in the case of cylindrical stratified media has been mainly due to a high rate of change of the permittivity profile. Finally, the effect of noise has also been considered and it has been observed that even a 2 – 5% error in the simulated reflection data does not affect the reconstructed profile to a large extent. This is specially advantageous in the real time measuring condition, where few percent error in the measurement data is unavoidable.

To validate our method experimentally, reflection coefficient data of some dielectric samples have been measured in the coaxial airline and in free-space using the vector network analyzer (VNA). The coaxial airline media gives the reflection coefficient data over a wide frequency band. On the other hand, the free-space measurements simulate more accurately real-time applications such as the imaging of dielectric bodies or the characterization of dielectric materials used for radar applications. In the case of coaxial airline, both single and multi-layered dielectric materials have been used and the permittivity profile in each case has been reconstructed with a deviation of less than 2%. In the free-space, a simple setup has been used to calibrate the VNA and measure the reflection coefficient data. The accuracy here has not been good enough as compared to transmission line measurements due to the problem of correctly positioning the reference plane and the edge-diffraction. The spectral domain reflection coefficient data of two dielectric samples in X and Ku bands have been measured in free-space using the above mentioned setup. The permittivity values of these samples have been determined using the proposed method. Time-domain measurements have also been carried out for some dielectric samples in free-space, and the permittivity values of these materials from the time-domain curves have been determined using a very simple method. It has been observed that these time-domain data can be used to determine the relative permittivity of single-layer dielectric materials even under very hostile measuring conditions. The typical accuracy in the determination of relative permittivity of dielectric materials from the free-space reflection coefficient measured data has been found to be about 5%.

Appendix A

The solution of two simultaneous differential equations having a common factor

Let x be an independent variable and we have a set of equations defined as follows

$$g_1 f = \frac{\partial}{\partial x} (g_2 f) \quad (\text{A.1a})$$

$$g_3 f = \frac{\partial}{\partial x} (g_4 f) \quad (\text{A.1b})$$

where f , g_1 , g_2 , g_3 , and g_4 are all implicit functions of x . Our task here is to solve both equations (A.1a) and (A.1b) simultaneously in order to eliminate the common function f . This is done in following steps.

First, we expand the right hand sides of (A.1) to obtain

$$g_1 f = g_2 \frac{\partial f}{\partial x} + f \frac{\partial g_2}{\partial x} \Rightarrow \frac{\partial f}{\partial x} = \frac{(g_1 - \frac{\partial g_2}{\partial x}) f}{g_2} \quad (\text{A.2a})$$

$$g_3 f = g_4 \frac{\partial f}{\partial x} + f \frac{\partial g_4}{\partial x} \Rightarrow \frac{\partial f}{\partial x} = \frac{(g_3 - \frac{\partial g_4}{\partial x}) f}{g_4} \quad (\text{A.2b})$$

In the next step, the expressions of $\frac{\partial f}{\partial x}$ from both (A.2a) and (A.2b) are combined together to yield

$$\frac{(g_1 - g_2') f}{g_2} = \frac{(g_3 - g_4') f}{g_4} \quad (\text{A.3})$$

where g_2' and g_4' represent derivatives of g_2 and g_4 respectively with respect to the independent variable x . Finally, the above equation is further simplified after eliminating the common function f from both sides of (A.3) to obtain the following expression

$$(g_1 - g_2') g_4 = (g_3 - g_4') g_2 \quad (\text{A.4})$$

which is the required solution obtained after solving both (A.1a) and (A.1b) simultaneously.

Appendix B

The derivatives of the spherical Hankel functions

B.1 The first order derivative

The recurrence formula involving the first order derivative of the *standard* spherical Hankel function of order n and argument z is given by [91]

$$\frac{d}{dz} [h_n^{(p)}(z)] = \frac{1}{(2n+1)} \left[n h_{n-1}^{(p)}(z) - (n+1) h_{n+1}^{(p)}(z) \right] \quad p = 1 \quad \text{or} \quad 2 \quad (\text{B.1})$$

The above equation can be used for the derivation of the first order derivative of a spherical Hankel function defined by (3.107) as given below

$$\begin{aligned} \frac{d}{dz} [\hat{H}_n^{(p)}(z)] &= h_n^{(p)}(z) + z \frac{n}{(2n+1)} h_{n-1}^{(p)}(z) - z \frac{(n+1)}{(2n+1)} h_{n+1}^{(p)}(z) \\ &= \frac{1}{(2n+1)} \left[(2n+1) h_n^{(p)}(z) - z h_{n+1}^{(p)}(z) + n z h_{n-1}^{(p)}(z) - n z h_{n+1}^{(p)}(z) \right] \\ &= \frac{1}{(2n+1)} \left[z h_{n-1}^{(p)}(z) + n z h_{n-1}^{(p)}(z) - n z h_{n+1}^{(p)}(z) \right] \end{aligned} \quad (\text{B.2})$$

Hence our final formula for the first order derivative of the spherical Hankel function of order n reduces to

$$\frac{d}{dz} [\hat{H}_n^{(p)}(z)] = \frac{1}{(2n+1)} \left[(1+n) \hat{H}_{n-1}^{(p)}(z) - n \hat{H}_{n+1}^{(p)}(z) \right] \quad (\text{B.3})$$

B.2 The second order derivative

The first order derivative of the *standard* spherical Hankel function of order n and argument z , in terms of the corresponding function of a lower order is given by [91]

$$\frac{d}{dz} [z^{n+1} h_n^{(p)}(z)] = z^{n+1} h_{n-1}^{(p)}(z) \quad p = 1 \quad \text{or} \quad 2 \quad (\text{B.4})$$

Now for our definition of the spherical Hankel function defined by (3.107), the above equation reduces to

$$\begin{aligned} \frac{d}{dz} \left[z^n \hat{H}_n^{(p)}(z) \right] &= z^n \hat{H}_{n-1}^{(p)}(z) \quad p = 1 \quad \text{or} \quad 2 \\ \Rightarrow \frac{d}{dz} \left[\hat{H}_n^{(p)}(z) \right] &= \hat{H}_{n-1}^{(p)}(z) - \frac{n}{z} \hat{H}_n^{(p)}(z) \end{aligned} \quad (\text{B.5})$$

For obtaining the second order differential of the spherical Hankel functions, the above equation can be differentiated again to obtain

$$\frac{d^2}{dz^2} \left[\hat{H}_n^{(p)}(z) \right] = \frac{d}{dz} \left[\hat{H}_{n-1}^{(p)}(z) \right] - n \frac{d}{dz} \left[\frac{\hat{H}_n^{(p)}(z)}{z} \right] \quad (\text{B.6})$$

The terms on the right hand side of (B.6) may be individually computed as

$$\begin{aligned} \frac{d}{dz} \left[\hat{H}_{n-1}^{(p)}(z) \right] &= \hat{H}_{n-2}^{(p)}(z) - \frac{(n-1)}{z} \hat{H}_{n-1}^{(p)}(z) \\ n \frac{d}{dz} \left[\frac{\hat{H}_n^{(p)}(z)}{z} \right] &= \frac{n}{z} \frac{d}{dz} \left[\hat{H}_n^{(p)}(z) \right] - \frac{n}{z^2} \left[\hat{H}_n^{(p)}(z) \right] \\ &= \frac{n}{z} \left[\hat{H}_{n-1}^{(p)}(z) \right] - \frac{n(n+1)}{z^2} \left[\hat{H}_n^{(p)}(z) \right] \end{aligned} \quad (\text{B.7})$$

where we have made use of (B.5) to compute the first derivatives for orders n and $n - 1$. In the next step, both the individual terms of the above equation are substituted in (B.6) to obtain

$$\frac{d^2}{dz^2} \left[\hat{H}_n^{(p)}(z) \right] = \frac{n(n+1)}{z^2} \left[\hat{H}_n^{(p)}(z) \right] + \hat{H}_{n-2}^{(p)}(z) - \frac{(2n-1)}{z} \left[\hat{H}_{n-1}^{(p)}(z) \right] \quad (\text{B.8})$$

Now we can use another recurrence formula of the spherical Hankel functions given as [91]

$$\frac{(2n+1)}{z} \hat{H}_n^{(p)}(z) = \hat{H}_{n-1}^{(p)}(z) + \hat{H}_{n+1}^{(p)}(z) \quad (\text{B.9})$$

The above equation for the spherical Hankel functions of order $n - 1$ reduces to

$$\hat{H}_{n-2}^{(p)}(z) - \frac{(2n-1)}{z} \hat{H}_{n-1}^{(p)}(z) = -\hat{H}_n^{(p)}(z) \quad (\text{B.10})$$

The above equation can be finally combined with (B.8) to obtain

$$\frac{d^2}{dz^2} \left[\hat{H}_n^{(p)}(z) \right] = \left[\frac{n(n+1)}{z^2} - 1 \right] \hat{H}_n^{(p)}(z) \quad p = 1 \quad \text{or} \quad 2 \quad (\text{B.11})$$

which is the required formula for the second order derivative of the spherical Hankel function.

Appendix C

Integral containing two Hankel functions

C.1 The cylindrical Hankel functions

The Wronskian formula for the cylindrical Hankel functions of order n is given by [90]

$$H_n^{(1)}(z) H_n^{(2)'}(z) - H_n^{(2)}(z) H_n^{(1)'}(z) = -\frac{4j}{\pi z} \quad (\text{C.1})$$

where the prime ' indicates the first order derivative. The above equation can be rewritten as

$$\frac{1}{H_n^{(2)}(z)} \frac{d}{dz} [H_n^{(2)}(z)] - \frac{1}{H_n^{(1)}(z)} \frac{d}{dz} [H_n^{(1)}(z)] = -\frac{4j}{\pi z H_n^{(1)}(z) H_n^{(2)}(z)} \quad (\text{C.2})$$

Now, when $z = \omega t$, then the above equation will be modified to

$$\begin{aligned} \Rightarrow \frac{1}{H_n^{(2)}(\omega t)} \frac{d}{dt} [H_n^{(2)}(\omega t)] - \frac{1}{H_n^{(1)}(\omega t)} \frac{d}{dt} [H_n^{(1)}(\omega t)] &= -\frac{4j * \omega}{\pi \omega t H_n^{(1)}(\omega t) H_n^{(2)}(\omega t)} \\ \Rightarrow \frac{d}{dt} [\ln H_n^{(2)}(\omega t)] - \frac{d}{dt} [\ln H_n^{(1)}(\omega t)] &= -\frac{4j}{\pi t H_n^{(1)}(\omega t) H_n^{(2)}(\omega t)} \\ \Rightarrow \frac{d}{dt} \left\{ \ln \left[\frac{H_n^{(1)}(\omega t)}{H_n^{(2)}(\omega t)} \right] \right\} &= \frac{4j}{\pi t H_n^{(1)}(\omega t) H_n^{(2)}(\omega t)} \end{aligned} \quad (\text{C.3})$$

If we integrate the above equation, then it will reduce to

$$\int_t \frac{4j}{\pi t H_n^{(1)}(\omega t) H_n^{(2)}(\omega t)} dt = \ln \left[\frac{H_n^{(1)}(\omega t)}{H_n^{(2)}(\omega t)} \right] \quad (\text{C.4})$$

which is the required formula for the integral containing two cylindrical Hankel functions of order n .

C.2 The spherical Hankel functions

The Wronskian formula for the spherical Hankel functions of order n is given by [101]

$$h_n^{(1)}(z) \frac{d}{dz} h_n^{(2)}(z) - h_n^{(2)}(z) \frac{d}{dz} h_n^{(1)}(z) = -\frac{2j}{z^2} \quad (\text{C.5})$$

In this thesis, we have used a special type of spherical Hankel functions defined as

$$\hat{H}_n^{(p)}(z) = z h_n^{(p)}(z) \quad p = 1 \text{ or } 2 \quad (\text{C.6})$$

The Wronskian formula for this type of spherical Hankel function can be derived as follows

$$\begin{aligned} \hat{H}_n^{(1)}(z) \frac{d}{dz} \hat{H}_n^{(2)}(z) - \hat{H}_n^{(2)}(z) \frac{d}{dz} \hat{H}_n^{(1)}(z) &= \\ z h_n^{(1)}(z) \left[h_n^{(2)}(z) + z \frac{d}{dz} h_n^{(2)}(z) \right] - z h_n^{(2)}(z) \left[h_n^{(1)}(z) + z \frac{d}{dz} h_n^{(1)}(z) \right] &= \\ = z^2 \left[h_n^{(1)}(z) \frac{d}{dz} h_n^{(2)}(z) - h_n^{(2)}(z) \frac{d}{dz} h_n^{(1)}(z) \right] &= -2j \end{aligned} \quad (\text{C.7})$$

where we have substituted the value of (C.5) to arrive at the last expression of (C.7). When $z = \omega t$, then the above equation will be modified into

$$\begin{aligned} \hat{H}_n^{(1)}(\omega t) \frac{d}{dt} \hat{H}_n^{(2)}(\omega t) - \hat{H}_n^{(2)}(\omega t) \frac{d}{dt} \hat{H}_n^{(1)}(\omega t) &= -2j * \omega \\ \Rightarrow \frac{1}{\hat{H}_n^{(2)}(\omega t)} \frac{d}{dt} \hat{H}_n^{(2)}(\omega t) - \frac{1}{\hat{H}_n^{(1)}(\omega t)} \frac{d}{dt} \hat{H}_n^{(1)}(\omega t) &= \frac{-2j \omega}{\hat{H}_n^{(1)}(\omega t) \hat{H}_n^{(2)}(\omega t)} \quad (\text{C.8}) \\ \Rightarrow \frac{d}{dt} \left\{ \ln \left[\frac{\hat{H}_n^{(1)}(\omega t)}{\hat{H}_n^{(2)}(\omega t)} \right] \right\} &= \frac{2j \omega}{\hat{H}_n^{(1)}(\omega t) \hat{H}_n^{(2)}(\omega t)} \end{aligned}$$

The above equation can be integrated to obtain

$$\int_t \frac{2j \omega}{\hat{H}_n^{(1)}(\omega t) \hat{H}_n^{(2)}(\omega t)} dt = \ln \left[\frac{\hat{H}_n^{(1)}(\omega t)}{\hat{H}_n^{(2)}(\omega t)} \right] \quad (\text{C.9})$$

which is the required formula for the integral containing two spherical Hankel functions of order n .

Appendix D

The spherical Fourier-Bessel transform

The 3-dimensional Fourier-transform and its corresponding inverse can be given by

$$F(k_x, k_y, k_z) = \int_{-\infty}^{\infty} \int_{-\infty}^{\infty} \int_{-\infty}^{\infty} f(x, y, z) e^{-j(k_x x + k_y y + k_z z)} dx dy dz \quad (\text{D.1a})$$

$$f(x, y, z) = \frac{1}{8\pi^3} \int_{-\infty}^{\infty} \int_{-\infty}^{\infty} \int_{-\infty}^{\infty} F(k_x, k_y, k_z) e^{j(k_x x + k_y y + k_z z)} dk_x dk_y dk_z \quad (\text{D.1b})$$

where k_x , k_y and k_z are the wavenumbers along the three coordinate axes x , y and z respectively. The above 3-dimensional transform can be converted to the spherical coordinate system using the following coordinate transformation

$$\begin{aligned} x &= r \sin \theta \cos \phi, & y &= r \sin \theta \sin \phi, & z &= r \cos \theta \\ dx dy dz &= r^2 \sin \theta dr d\theta d\phi \end{aligned} \quad (\text{D.2})$$

The corresponding spectral domain coordinate transformation is given by

$$\begin{aligned} k_x &= \beta \sin \alpha \cos \gamma, & k_y &= \beta \sin \alpha \sin \gamma, & k_z &= \beta \cos \alpha \\ dk_x dk_y dk_z &= \beta^2 \sin \alpha d\beta d\alpha d\gamma \end{aligned} \quad (\text{D.3})$$

where β , α , and γ are the equivalent spectral components in the spherical coordinate system. We can use (D.2) and (D.3) to evaluate the kernel of (D.1) into the spherical coordinate system

$$\begin{aligned} k_x x + k_y y + k_z z &= \beta r [\sin \alpha \sin \theta \cos \gamma \cos \phi + \sin \alpha \sin \theta \sin \gamma \sin \phi + \cos \theta \cos \alpha] \\ &= \beta r [\sin \alpha \sin \theta \cos(\phi - \gamma) + \cos \theta \cos \alpha] \end{aligned} \quad (\text{D.4})$$

The above equation along with (D.2) and (D.3) can be substituted in (D.1a) to obtain

$$F(\beta, \alpha, \gamma) = \int_{\phi} \int_{\theta} \int_r f(r, \theta, \phi) e^{-j\beta r \sin \alpha \sin \theta \cos(\phi - \gamma)} e^{-j\beta r \cos \theta \cos \alpha} r^2 \sin \theta dr d\theta d\phi \quad (\text{D.5})$$

For objects, which are symmetrical in the ϕ direction, (D.4) will reduce to

$$k_x x + k_y y + k_z z \cong \beta r [\sin \alpha \sin \theta + \cos \theta \cos \alpha] = \beta r \cos(\theta - \alpha) \quad (\text{D.6})$$

The above equation can be substituted in (D.5), which yields

$$F(\beta, \alpha) = 2\pi \int_r \int_\theta f(r) e^{-j\beta r \cos(\theta - \alpha)} r^2 \sin \theta dr d\theta \quad (D.7)$$

The exponential function in (D.7) can be evaluated in terms of its series expansion [91]

$$e^{-j\beta r \cos(\theta - \alpha)} = \sum_{n=0}^{\infty} (2n+1) j^n P_n[\cos(\theta - \alpha)] j_n(-\beta r) \quad (D.8)$$

where P_n is the *Legendre polynomial*, and j_n represents the spherical Bessel function of order n . The value of the exponential can be substituted from (D.8) into (D.7)

$$\begin{aligned} F(\beta, \alpha) &= 2\pi \int_r \int_\theta f(r) \sum_{n=0}^{\infty} (2n+1) j^n P_n[\cos(\theta - \alpha)] j_n(-\beta r) r^2 \sin \theta dr d\theta \\ &= 2\pi \int_0^\infty f(r) r^2 \sum_{n=0}^{\infty} \left\{ (2n+1) j^n \left[\int_0^\pi P_n[\cos(\theta - \alpha)] \sin \theta d\theta \right] j_n(-\beta r) \right\} dr \end{aligned} \quad (D.9)$$

The above equation can be simplified using the following property of the *Legendre* function integral [91]

$$\begin{aligned} &\int_0^\pi P_n(\cos \theta) \sin(m\theta) d\theta \\ &= \begin{cases} 2 \frac{(m+n-1)(m+n-3)\cdots(m-n+1)}{(m+n)(m+n-2)\cdots(m-n)}; & \text{if } n < m \text{ and } (m+n) \text{ is odd} \\ = 0; & \text{otherwise} \end{cases} \end{aligned} \quad (D.10)$$

We have made use of the above equation to compute the inner integral

$$\int_0^\pi P_n[\cos(\theta - \alpha)] \sin \theta d\theta \quad (D.11)$$

of (D.9).

After comparing (D.11) with (D.10), we find that in our case $m = 1$ and hence the integral (D.11) will be *non-zero* if and only if $n = 0$ and for all other values of n the value of this integral will be zero as per (D.10). Hence for the integral (D.11), we can write

$$\int_0^\pi P_n[\cos(\theta - \alpha)] \sin \theta d\theta = \begin{cases} \int_0^\pi \sin \theta d\theta = 2; & \text{if } n = 0 \\ = 0; & \text{otherwise} \end{cases} \quad (D.12)$$

where we have made use of the fact that $P_0[\cos(\theta - \alpha)] \equiv 1$ [91]. We can substitute the value of integral (D.12) into (D.9) and this yields

$$\begin{aligned} F(\beta, \alpha) &\equiv F(\beta) = 2\pi \int_0^\infty 2 f(r) r^2 j_0(-\beta r) dr \\ &= 4\pi \int_0^\infty f(r) r^2 j_0(\beta r) dr \end{aligned} \quad (D.13)$$

where the relationship $j_0(-z) = j_0(z)$ is used.

Now, to compute the second integral (D.1b), we can follow the same procedure as for computing (D.1a) and going by this convention we can rewrite (D.1b) in the following form

$$f(r, \theta) = \frac{1}{4\pi^2} \int_0^\infty \int_0^\pi F(\beta) e^{j\beta r \cos(\theta - \alpha)} \beta^2 \sin \alpha d\beta d\alpha \quad (\text{D.14})$$

If we compare the above equation with (D.7), then it is observed that both equations have similar form and hence the procedure used for simplifying (D.7) can also be used here to reduce (D.14) to the following form

$$f(r) = \frac{1}{2\pi^2} \int_0^\infty F(\beta) \beta^2 j_0(\beta r) d\beta \quad (\text{D.15})$$

Let us now try to scale (D.13) and (D.15) by a common factor as follows

$$\bar{F}(\beta) = \frac{F(\beta)}{\sqrt{2}\pi}; \quad \bar{f}(r) = \sqrt{2}\pi f(r) \quad (\text{D.16})$$

With the scaling factor defined above, equations (D.13) and (D.15) can be rewritten as

$$f(r) = \int_0^\infty F(\beta) j_0(\beta r) \beta^2 d\beta, \quad \text{and} \quad (\text{D.17a})$$

$$F(\beta) = \frac{2}{\pi} \int_0^\infty f(r) j_0(\beta r) r^2 dr \quad (\text{D.17b})$$

Equations (D.17a) and (D.17b) are called spherical Fourier-Bessel transform pairs in a more general sense. It may be mentioned here that in (D.17a) and (D.17b), the variables r and β may always be replaced by t and ω without any loss of generality. The orthogonality of the above kernel can be ascertained by the following closure relationship [92]

$$\frac{2a^2}{\pi} \int_0^\infty j_n(ar) j_n(br) r^2 dr = \delta(a - b) \quad (\text{D.18})$$

Hence it can be concluded that the spherical Fourier-Bessel transform given by (D.17a) and (D.17b) can be used for the analysis in the spherical coordinate system in a similar way as that of Hankel transform and the Fourier transform used in the cylindrical and the cartesian coordinate system respectively.

Bibliography

- [1] L. Tsang and J. A. Kong, "Application of strong fluctuation random medium theory to scattering from vegetation-like half space," *IEEE Trans. Geodic. Remote Sensing*, vol. GRS-19, pp. 62–69, 1981.
- [2] M. A. Karam, A. K. Fung, and Y. M. M. Antar, "Electromagnetic wave scattering from some vegetation samples," *IEEE Trans. Geodic. Remote Sensing*, vol. GRS-26, pp. 799–807, Nov. 1988.
- [3] M. O. Knothole, "Scattering from dielectric cylinders having radially layered permittivity," *J. Electromag. Waves Applicat.*, vol. 6, pp. 235–259, 1992.
- [4] H. Baltes, W. Goepel, and J. Hesse, *Sensors Update, Vol. 7*. Germany: Wiley-Vch, 2000.
- [5] T. Habashy and R. Mittra, "Review of some inverse methods in electromagnetics," *J. Opt. Soc. Amer. A, Opt. Image Sci.*, vol. 4, pp. 281–291, Jan. 1987.
- [6] D. K. Ghodgaonkar, O. Gandhi, and M. J. Hagmann, "Estimation of complex permittivities of a three-dimensional inhomogeneous biological bodies," *IEEE Trans. Microwave Theory Tech.*, vol. MTT-31, pp. 442–446, June 1983.
- [7] N. Joachimowicz, C. Pichot, and J.-P. Hugonin, "Inverse scattering: An iterative numerical method for electromagnetic imaging," *IEEE Trans. Antennas Propagat.*, vol. 39, pp. 1743–1752, Dec. 1991.
- [8] N. Joachimowicz, J. J. Mallorqui, J.-C. Bolomey, and A. Broquetas, "Convergence and stability assessment of newton-kantorovich reconstruction algorithm for microwave tomography," *IEEE Trans. Med. Imag.*, vol. MI-17, pp. 562–570, Aug. 1998.
- [9] V. Mikhnev, Y. Maksimovitch, and P. Vainikainen, "Microwave reconstruction of underground targets using frequency domain measurements," in *Proc. 30th European Microwave Conference*, vol. 3, (Paris), pp. 237–240, Oct. 2000.
- [10] A. G. Yarovoy, P. van Genderen, and L. P. Ligthart, "Experimental multi-sensor gpr system for humanitarian demining," in *Proc. 31st European Microwave Conference*, vol. 2, (London), pp. 91–94, Sep. 2001.
- [11] J. M. Rius, C. Pichot, L. Jofre, J. C. Bolomey, N. Joachimowicz, A. Broquetas, and M. Ferrando, "Planar and cylindrical active microwave temperature imaging: Numerical simulations," *IEEE Trans. Med. Imag.*, vol. MI-11, pp. 457–469, Dec. 1992.

- [12] R. Maini, M. F. Iskander, and C. H. Durney, "On the electromagnetic imaging using linear reconstruction techniques," *Proc. IEEE*, vol. 68, pp. 1550–1552, 1980.
- [13] E. C. Fear, S. C. Hagness, P. M. Meaney, M. Okoniewski, and M. A. Stuchly, "Enhancing breast tumor detection with near-field imaging," *IEEE microwave magazine*, vol. 3, pp. 48–56, Mar. 2002.
- [14] A. Broquetas, J. Romeu, J. M. Rius, A. R. Elias-Fuste, A. Cardama, and L. Jofre, "Cylindrical geometry: A further step in active microwave tomography," *IEEE Trans. Microwave Theory Tech.*, vol. MTT-39, pp. 836–844, May 1991.
- [15] W.-M. Boerner, A. K. Jordan, and I. W. Kay, "Introduction to the special issue on inverse methods in electromagnetics," *IEEE Trans. Antennas Propagat.*, vol. AP-29, pp. 185–189, Mar. 1981.
- [16] R. F. Harrington, *Time-Harmonic Electromagnetic Fields*. New York:McGraw-Hill, 1961.
- [17] K. I. Hopcraft and P. R. Smith, *An Introduction to Electromagnetic Inverse Scattering*. The Netherlands: Kluwer Academic Publishers, 1992.
- [18] K. Chadan and P. C. Sabatier, *Inverse Problems in Quantum Scattering Theory*. Springer-Verlag, 1977.
- [19] T. Habashy and R. Mittra, "On some inverse methods in electromagnetics," *Journal of Electromagnetic waves and applications*, vol. 1, pp. 25–28, 1987.
- [20] E. Wolf, "Three-dimensional structure determination of semi-transparent objects from holographic data," *Optical Communications*, vol. 1, pp. 153–156, 1969.
- [21] A. J. Devaney, "A computer simulation study of diffraction tomography," *IEEE Trans. Biomed. Eng.*, vol. BME-30, pp. 377–386, 1983.
- [22] S. X. Pan and A. C. Kak, "A computational study of reconstruction algorithms for diffraction tomography: Interpolation vs. filtered backpropagation," *IEEE Trans. Accous., Speech and Signal Processing*, pp. 1262–1275, Oct. 1983.
- [23] M. Slaney, A. C. Kak, and L. E. Larsen, "Limitations of imaging with first-order diffraction tomography," *IEEE Trans. Microwave Theory Tech.*, vol. MTT-32, pp. 860–873, Aug. 1984.
- [24] T. Chu and K. Lee, "Wide-band microwave diffraction tomography under born approximation," *IEEE Trans. Antennas Propagat.*, vol. 37, pp. 515–519, Apr. 1989.
- [25] W. Tabarra, "Reconstruction of permittivity profiles from a spectral analysis of the reflection coefficient," *IEEE Trans. Antennas Propagat.*, vol. AP-27, pp. 241–248, Mar. 1979.

- [26] J. Bolomey, D. Lesselier, C. Pichot, and W. Tabarra, "Spectral and time domain approaches to some inverse scattering problems," *IEEE Trans. Antennas Propagat.*, vol. AP-29, pp. 206–212, Mar. 1981.
- [27] D. B. Ge, D. L. Jaggard, and H. N. Kritikos, "Perturbational and high frequency profile inversion," *IEEE Trans. Antennas Propagat.*, vol. AP-31, pp. 804–808, Sep. 1983.
- [28] P. R. Smith, K. I. Hopcraft, and R. E. Smith, "A novel method for determining dielectric inhomogeneity from scattered electromagnetic radiation," *Inverse Problems*, vol. 4, pp. 235–248, 1988.
- [29] T. H. Chu and N. H. Farhat, "Frequency-swept microwave imaging of dielectric objects," *IEEE Trans. Microwave Theory Tech.*, vol. MTT-36, pp. 489–493, Mar. 1988.
- [30] K. I. Hopcraft and P. R. Smith, "Geometrical properties of backscattered radiation and their relation to inverse scattering," *J. Opt. Soc. Am. A.*, vol. 6, pp. 508–515, Apr. 1989.
- [31] I. M. Gelfand and B. M. Levitan, "On the determination of a differential equation from its spectral measure function," *Am. Math. Soc. 1*, vol. 1, pp. 253–304, 1955.
- [32] A. K. Jordan and H. N. Kritikos, "An application of one-dimensional inverse-scattering theory for inhomogeneous regions," *IEEE Trans. Antennas Propagat.*, vol. AP-21, pp. 909 – 911, Nov. 1973.
- [33] S. Ahn and A. K. Jordan, "Profile inversion of simple plasmas and nonuniform regions: Three-pole reflection coefficient," *IEEE Trans. Antennas Propagat.*, vol. AP-24, pp. 879 – 882, Nov. 1976.
- [34] G. N. Balanis, "The plasma inverse problem," *J. Math. Phys.*, vol. 13, pp. 1001–1005, 1972.
- [35] D. L. Jaggard and K. E. Olson, "Numerical reconstruction for dispersionless refractive profiles," *J. Opt. Soc. Am. A.*, vol. 2, pp. 1931–1935, 1985.
- [36] D. L. Jaggard and P. V. Frangos, "The electromagnetic inverse scattering problem for layered dispersionless dielectrics," *IEEE Trans. Antennas Propagat.*, vol. AP-35, pp. 934 – 946, Aug. 1987.
- [37] M. H. Reilly and A. K. Jordan, "The applicability of an inverse method for reconstruction of electron-density profiles," *IEEE Trans. Antennas Propagat.*, vol. AP-29, pp. 245 – 252, Mar. 1981.
- [38] A. Roger, "Newton-kantorovitch algorithm applied to an electromagnetic inverse problem," *IEEE Trans. Antennas Propagat.*, vol. AP-29, pp. 232 – 238, Mar. 1981.

- [39] A. G. Tijhuis and C. van der Worm, "Iterative approach to the frequency-domain solution of the inverse-scattering problem for an inhomogeneous lossless dielectric slab," *IEEE Trans. Antennas Propagat.*, vol. AP-32, pp. 711–716, Jul. 1984.
- [40] P. V. Frangos and D. L. Jaggard, "The reconstruction of stratified dielectric profiles using successive approximations," *IEEE Trans. Antennas Propagat.*, vol. AP-35, pp. 1267 – 1272, Nov. 1987.
- [41] T. Uno and S. Adachi, "Inverse scattering method for one-dimensional inhomogeneous layered media," *IEEE Trans. Antennas Propagat.*, vol. AP-35, pp. 1456 – 1466, Dec. 1987.
- [42] T. Habashy, W. C. Chew, and E. Y. Chow, "Simultaneous reconstruction of permittivity and conductivity profiles in a radially inhomogeneous slab," *Radio Science*, vol. 12, pp. 635–645, 1986.
- [43] M. Moghaddam and W. C. Chew, "Study of some practical issues in inversion with the born iterative method using time-domain data," *IEEE Trans. Antennas Propagat.*, vol. AP-41, pp. 177 – 184, Feb. 1993.
- [44] R. D. Murch and T. K. K. Chan, "Improving microwave imaging by enhancing diffraction tomography," *IEEE Trans. Microwave Theory Tech.*, vol. MTT-44, pp. 379–388, Mar. 1996.
- [45] K. Belkebir, R. E. Kleinman, and C. Pichot, "Microwave imaging - location and shape reconstruction from multifrequency scattering data," *IEEE Trans. Microwave Theory Tech.*, vol. MTT-45, pp. 469–476, Apr. 1997.
- [46] A. E. Souvorov, A. E. Bulyshev, S. Y. Semenov, R. H. Svenson, A. G. Nazarov, Y. E. Sizov, and G. P. Tatsis, "Microwave tomography: a two-dimensional newton iterative scheme," *IEEE Trans. Microwave Theory Tech.*, vol. MTT-46, pp. 1654–1659, Nov. 1998.
- [47] R. Pierri, A. Brancaccio, and F. D. Blasio, "Multifrequency dielectric profile inversion for a cylindrically stratified medium," *IEEE Trans. Geodic. Remote Sensing*, vol. GRS-38, pp. 1716–1724, Jul. 2000.
- [48] A. G. Tijhuis, "Iterative determination of permittivity and conductivity profiles of a dielectric slab in the time domain," *IEEE Trans. Antennas Propagat.*, vol. AP-29, pp. 239 – 245, Mar. 1981.
- [49] C. L. Bennett, "Time domain inverse scattering," *IEEE Trans. Antennas Propagat.*, vol. AP-29, pp. 213 – 219, Mar. 1981.
- [50] S. Caorsi, G. L. Gragnani, and M. Pastorino, "A multiview microwave imaging system for two-dimensional penetrable objects," *IEEE Trans. Microwave Theory Tech.*, vol. MTT-39, pp. 845–851, May 1991.
- [51] M. M. Ney, "Method of moments as applied to electromagnetic problems," *IEEE Trans. Microwave Theory Tech.*, vol. MTT-33, pp. 972–980, Oct. 1985.

- [52] H. Harada, D. J. N. Wall, T. Takenaka, and M. Tanaka, "Conjugate gradient method applied to inverse scattering problem," *IEEE Trans. Antennas Propagat.*, vol. AP-43, pp. 784 – 792, Aug. 1995.
- [53] A. Franchois, A. Joisel, C. Pichot, and J. C. Bolomey, "Quantitative microwave imaging with a 2.45-ghz planar microwave camera," *IEEE Trans. Med. Imag.*, vol. MI-17, pp. 550–561, Aug. 1998.
- [54] T. A. Maniatis, K. S. Nikita, and N. K. Uzunoglu, "Two-dimensional dielectric profile reconstruction based on spectral-domain moment method and nonlinear optimization," *IEEE Trans. Microwave Theory Tech.*, vol. MTT-48, pp. 1831–1840, Nov. 2000.
- [55] E. C. Fear and M. A. Stuchly, "Microwave detection of breast cancer," *IEEE Trans. Microwave Theory Tech.*, vol. MTT-48, pp. 1854–1863, Nov. 2000.
- [56] P. M. Meaney, M. W. Fanning, D. Li., S. Poplack, and K. D. Paulsen, "A clinical prototype for active microwave imaging of the breast," *IEEE Trans. Microwave Theory Tech.*, vol. MTT-48, pp. 1841–1853, Nov. 2000.
- [57] F. Bolinder, "Fourier transforms in the theory of inhomogeneous transmission lines," *Proc. IRE*, vol. 38, pp. 1354–1355, 1950.
- [58] D. M. Pozar, *Microwave Engineering*. New York: John Wiley and Sons Inc., second ed., 1998.
- [59] D. L. Jaggard and Y. Kim, "Accurate one-dimensional inverse scattering using a nonlinear renormalization technique," *J.Opt.Soc.Am.A.*, vol. 2, pp. 1922–1930, 1985.
- [60] T. J. Cui and C. H. Liang, "Reconstruction of the permittivity profile of an inhomogeneous medium using an equivalent network approach," *IEEE Trans. Antennas Propagat.*, vol. 41, pp. 621–626, Dec. 1993.
- [61] T. J. Cui and C. H. Liang, "Nonlinear differential equation for the reflection coefficient of an inhomogeneous lossy medium and its inverse scattering solutions," *IEEE Trans. Antennas Propagat.*, vol. 42, pp. 621–626, May. 1994.
- [62] M. J. Akhtar and A. S. Omar, "Reconstructing permittivity profiles using an improved renormalization technique," in *Microwave Symposium Digest*, vol. 4, (USA), pp. 1815–1818, IEEE MTT-S International Microwave Symposium, 1999.
- [63] A. D. Poularikas, *The Transforms and Applications Handbook*. USA: CRC Press, Inc., 1996.
- [64] J. A. Stratton, *Electromagnetic Theory*. McGraw-Hill Book Company, Inc., 1941.
- [65] A. S. Omar and M. J. Akhtar, "A *Hankel* transform reconstruction technique for radially dependent permittivity profiles in cylindrical objects," in *European Microwave Conference Proceedings*, (Munich, Germany), Oct. 1999.

- [66] M. J. Akhtar and A. S. Omar, "Reconstructing permittivity profiles using integral transforms and improved renormalization techniques," *IEEE Trans. Microwave Theory Tech.*, vol. 48, pp. 1385–1393, Aug. 2000.
- [67] M. J. Akhtar and A. S. Omar, "Reconstruction of permittivity profiles in cylindrical objects illuminated by higher order modes," in *Microwave Symposium Digest*, vol. 2, (USA), pp. 1085–1088, IEEE MTT-S International Microwave Symposium, 2000.
- [68] M. J. Akhtar and A. S. Omar, "Microwave imaging of radially inhomogeneous cylindrical bodies," in *Proceedings IEEE AP-S International symposium*, vol. 1, (USA), pp. 304–307, 2000.
- [69] M. J. Akhtar and A. S. Omar, "Reconstruction of permittivity profiles in cylindrical objects illuminated by higher order TE_{mn} and TM_{mn} modes," *IEEE Trans. Microwave Theory Tech.*, vol. 48, pp. 2721–2729, Dec. 2000.
- [70] M. J. Akhtar and A. S. Omar, "An analytical method for the microwave imaging of cylindrically stratified media," in *Microwave Symposium Digest*, (USA), pp. 2005–2008, IEEE MTT-S International Microwave Symposium, 2002.
- [71] M. J. Akhtar and A. S. Omar, "Profile inversion of spherical objects illuminated by TE and TM -polarized waves," in *Proceedings IEEE AP-S International symposium*, vol. 3, (USA), pp. 1764–1767, 2000.
- [72] M. J. Akhtar and A. S. Omar, "Wide band microwave imaging of spherically shaped biological bodies," in *Proceedings 30th European Microwave Conference*, vol. 3, (Paris), pp. 185–189, Oct. 2000.
- [73] M. J. Akhtar and A. S. Omar, "Estimation of inhomogeneous permittivity profiles of spherical objects from noisy scattering data," in *Proceedings IEEE AP-S International symposium*, vol. 2, (USA), pp. 670–673, 2001.
- [74] M. J. Akhtar and A. S. Omar, "Nondestructive imaging of dielectric objects using band-limited noisy scattering data," in *Proceedings 31st European Microwave Conference*, vol. 3, (London), pp. 413–416, Sep. 2001.
- [75] J. C. Maxwell, *A Treatise on Electricity and Magnetism*. N.Y.: Dover, 1954.
- [76] R. S. Elliott, *Electromagnetics: history, theory, and applications*. NJ: The IEEE/OUP Series on Electromagnetic Wave Theory, 1993.
- [77] A. von Hippel, *Dielectrics and Waves*. Boston: Artech House, 1995.
- [78] R. E. Dubroff, S. V. Marshall, and G. G. Skitek, *Electromagnetic concepts and applications*. NJ: Prentice Hall, 1996.
- [79] R. E. Collin, *Foundation for Microwave Engineering*. New York: McGraw-Hill, 1966.
- [80] L. C. Andrews and B. K. Shivamoggi, *Integral Transforms for Engineers and Applied Mathematicians*. New York: Macmillan Publishing Company, 1988.

- [81] J. W. Cooley and J. W. Turkey, "An algorithm for the machine calculation of complex fourier series," *Math. Comp.*, vol. 19, pp. 297–301, Apr. 1965.
- [82] J. Hadamard, *Lectures on Cauchy's Problem in Linear Partial Differential Equations*. New Haven: Yale University Press, 1923.
- [83] A. Kirsch, *An Introduction to the Mathematical Theory of Inverse Problems*, vol. 120 of *Applied Mathematical Sciences*. Berlin: Springer-Verlag, 1996.
- [84] D. Colton and R. Kress, *Inverse Acoustic and Electromagnetic Theory*, vol. 93 of *Applied Mathematical Sciences*. Berlin: Springer-Verlag, second ed., 1998.
- [85] C. W. Groetsch, *Inverse Problems*. USA: The Mathematical Association of America, 1999.
- [86] V. A. Morozov, "Choice of parameter for the solution of functional equations by the regularization method," *Sov. Math. Doklady*, vol. 8, pp. 1000–1003, 1967.
- [87] L. Landweber, "An iteration formula for fredholm integral equations of the first kind," *Am. J. Math.*, vol. 73, pp. 615–624, 1951.
- [88] L. B. Felsen and N. Marcuvitz, *Radiation and Scattering of Waves*. New York: IEEE Press, 1994.
- [89] *Microwave Studio getting started*. CST GmbH, Darmstadt, Germany, version 3 ed., 2001.
- [90] G. N. Watson, *A Treatise on the Theory of Bessel Functions*. Cambridge: University Press, 1966.
- [91] P. M. Morse and H. Feshbach, *Methods of Theoretical Physics*. New York: McGraw-Hill Book Company, Inc., 1953.
- [92] G. Arfken, *Mathematical Methods for Physicists*. London: Academic Press, Inc., 1985.
- [93] S. A. Schelkunoff, *Electromagnetic Waves*. Princeton, N.J.: D. van Nostrand Company, Inc., 1943.
- [94] T. J. Cui and C. H. Liang, "Novel application of an approximate profile inversion for one-dimensional medium," *IEEE Trans. Antennas Propagat.*, vol. 43, pp. 308–312, Mar. 1995.
- [95] B. J. Rice and J. D. Strange, *Ordinary Differential Equations : with applications*. Pacific Grove, Calif. : Brooks/Cole Pub. Co., 1994.
- [96] T. J. Akai, *Applied Numerical Methods for Engineers*. John Wiley and Sons, Inc., 1993.
- [97] V. A. Mikhnev and P. Vainikainen, "Two-step inverse scattering method for one-dimensional permittivity profiles," *IEEE Trans. Antennas Propagat.*, vol. 48, pp. 293–298, Feb. 2000.

-
- [98] *User's Guide HP 8719D/20D/22D Network Analyzer*, 1996.
- [99] M. H. Umari, D. K. Ghodgaonkar, V. V. Vardan, and V. K. Varadan, "A free-space bistatic calibration technique for the measurement of parallel and perpendicular reflection coefficients of planar samples," *IEEE Trans. Instrum. Meas.*, vol. 40, pp. 19–24, 1991.
- [100] F. C. Smith, B. Chambers, and J. C. Bennett, "Calibration techniques for free space reflection coefficient measurements," *IEE Proceedings-A.*, vol. 139, pp. 247–253, Sep. 1992.
- [101] M. Abramowitz and I. A. Stegunan, *Handbook of mathematical functions with formulas, graphs, and mathematical tables*. Washington DC: United States Department of Commerce, 1972.

Curriculum Vitae

Name Md. Jaleel Akhtar
Date of Birth March 26, 1971 in Gaya
Naionality Indian
Address Reinhold-Frank-Str. 48 C
76133 Karlsruhe, Germany
E-mail jaleel@gmx.de

Education

May 1984 Secondary School Certificate, Gaya, India
June 1986 Senior Secondary School Certificate, AMU, Aligarh, India
October 1990 Bachelor of Science in Electronics Engineering
AMU, Aligarh, India
June 1993 Master of Engineering in Electronics and Communication,
Birla Institute of Technology, Ranchi, India

Work Experience

Sep. 93 - Dec. 97 Scientist, Central Electronics Engineering
Research Institute, Pilani - India
Jan. 98 - Oct. 98 Research Assistant, Arbeitsbereich Hochfrequenz-
technik, TU Hamburg-Harburg, Germany
Nov. 98 - Jul. 03 Research Assistant, Chair of Microwave and
Communication Engineering, University
of Magdeburg, Germany

Magdeburg, 03.09.2003

(Md. Jaleel Akhtar)